

2013

IDENTIFICATION OF CONCRETE FRACTURE PARAMETERS USING DIGITAL IMAGE CORRELATION AND INVERSE ANALYSIS

Wafa Polies Asmaro
University of Windsor

Follow this and additional works at: <http://scholar.uwindsor.ca/etd>

 Part of the [Civil and Environmental Engineering Commons](#)

Recommended Citation

Polies Asmaro, Wafa, "IDENTIFICATION OF CONCRETE FRACTURE PARAMETERS USING DIGITAL IMAGE CORRELATION AND INVERSE ANALYSIS" (2013). *Electronic Theses and Dissertations*. Paper 4952.

This online database contains the full-text of PhD dissertations and Masters' theses of University of Windsor students from 1954 forward. These documents are made available for personal study and research purposes only, in accordance with the Canadian Copyright Act and the Creative Commons license—CC BY-NC-ND (Attribution, Non-Commercial, No Derivative Works). Under this license, works must always be attributed to the copyright holder (original author), cannot be used for any commercial purposes, and may not be altered. Any other use would require the permission of the copyright holder. Students may inquire about withdrawing their dissertation and/or thesis from this database. For additional inquiries, please contact the repository administrator via email (scholarship@uwindsor.ca) or by telephone at 519-253-3000ext. 3208.

IDENTIFICATION OF CONCRETE FRACTURE PARAMETERS USING DIGITAL
IMAGE CORRELATION AND INVERSE ANALYSIS

By

Wafa Polies Asmaro

A Dissertation
Submitted to the Faculty of Graduate
Studies through Civil and Environmental Engineering
in Partial Fulfillment of the Requirements for
the Degree of Doctor of Philosophy at the
University of Windsor

Windsor, Ontario, Canada

2013

© 2013 Wafa Polies

IDENTIFICATION OF CONCRETE FRACTURE PARAMETERS USING DIGITAL
IMAGE CORRELATION AND INVERSE ANALYSIS

By

Wafa Polies

APPROVED BY:

P. Leger, External Examiner
Ecole Polytechnique Montreal, University of Montreal

D. Green, Outside Department Reader
Department of Mechanical, Automotive & Materials Engineering

A. El Ragaby, Department Reader
Department of Civil and Environmental Engineering

M. Madugula, Department Reader
Department of Civil and Environmental Engineering

F. Ghrib, Principal Advisor
Department of Civil and Environmental Engineering

S. Cheng, Co-Advisor
Department of Civil and Environmental Engineering

June 14, 2013

DECLARATION OF ORIGINALITY

I hereby certify that I am the sole author of this dissertation and that no part of this dissertation has been published or submitted for publication.

I certify that, to the best of my knowledge, my dissertation does not infringe upon anyone's copyright nor violate any proprietary rights and that any ideas, techniques, quotations, or any other material from the work of other people included in my dissertation, published or otherwise, are fully acknowledged in accordance with the standard referencing practices. Furthermore, to the extent that I have included copyrighted material that surpasses the bounds of fair dealing within the meaning of the Canada Copyright Act, I certify that I have obtained a written permission from the copyright owner(s) to include such material(s) in my thesis and have included copies of such copyright clearances to my appendix.

I declare that this is a true copy of my dissertation, including any final revisions, as approved by my dissertation committee and the Graduate Studies office, and that this thesis has not been submitted for a higher degree to any other University or Institution.

ABSTRACT

Concrete is one of the oldest materials used for construction, yet it still poses fundamental problems for engineers and researchers. The most critical problem is the propagation of cracks in concrete structures, but the mere presence of cracks does not necessarily mean that the concrete structure has reached the limit of its service life; however, instability caused by the propagation of these defects could result in the failure of a concrete structure. Thus, the focus of fracture mechanics is on assessing the stability of a structure, rather than detecting the presence of cracks.

An accurate analysis of the progress of a fracture is required for assessing the integrity of a concrete structure and to predict its future performance. Accordingly, finite element analysis was used to model the performance of cracked concrete structures using available damage models, which require accurate evaluation of the mechanical and fracture properties. While concrete's mechanical properties are well known, the identification of concrete's fracture parameters poses an ongoing challenge.

Concrete is a heterogeneous material with complicated fracture patterns. Therefore, sensors attached directly to the specimen to measure the crack opening do not provide accurate measures. The objective of this research is to develop a new methodology to study a cracked concrete structure's performance using a non-contact technique to monitor the development of the fracture process zone without causing interference during fracture. Consequently, Digital Image Correlation was chosen and

applied successfully to the Wedge Splitting Test to study a cracked structure's response, represented by the mean of the load-crack tip opening displacement.

Since the WST is an indirect fracture test, the experimental data was used to identify concrete fracture parameters by means of inverse analysis based on the cohesive crack model. The associated forward problem is based on the cracked hinge model, which is capable of accounting for the softening phenomenon.

The use of Digital Image Correlation made it possible to study the dynamics of crack propagation. Experimental observations are thoroughly discussed, with special attention being placed on the monitoring of the crack's evolution, and the variation of dissipated energy and tensile damage along the crack path.

DEDICATION

TO MY LOVELY CHILDREN

RITA, RIVA & RYAN

This would not have been possible without your love, patience, and
understanding.

ACKNOWLEDGEMENTS

First and foremost, I would like to thank God who gave me strength and patience while guiding me in the work of this Dissertation. Without His blessings, this research work could not have been completed.

This project has been carried out under the supervision and guidance of Dr. Faouzi Ghrib to whom I am grateful for his endless constructive commentary, valuable suggestions, and continuous support in making this study a success. I am also grateful to my co-advisor, Dr. Shaohong Cheng, for all her support.

I was privileged and honored to have Dr. Pierre Leger as the external examiner. I am in appreciation for his acceptance of this invitation and I am also grateful for the time and effort he dedicated in making valuable recommendations for this dissertation.

I would like to express my sincere gratitude to the Outside Department Reader, Dr. Daniel Green, for his encouragements, and the time and effort he dedicated to read this dissertation and provide constructive suggestions. Dr. Daniel Green supplied the ARAMIS system that was crucial to this research work.

I would like to thank Dr. Amr El Ragaby, the Department Reader, for the time he dedicated in reading and reviewing this dissertation and also for his support, valuable advices, and recommendations.

I would like to thank Dr. Murty Madugula, the Department Reader, for his time in reviewing this dissertation and also for his valuable recommendations.

Completion of this doctoral dissertation would not have been possible without the technical staff: Lucian Pop, Patrick Seguin, and Matthew St. Louis. Their assistance during laboratory work is crucial and much appreciated.

I would like to also thank my colleagues Mena Bebawy, Li Li, Nori Saady, and Muhsin Hamdoon for their constant support. A special thanks is extended to Jan Skoček, from the Technical University of Denmark, for his valuable advice regarding the wedge splitting test set-up.

A special appreciation is also extended to the faculty and staff of the Department of Civil and Environmental Engineering including the Faculty of Engineering and the Faculty of Graduate Studies and also to the Leddy Library of the University of Windsor.

Finally, I would like to express my deepest gratitude to my husband, Laith, for his understanding and encouragements and also to my lovely children: Rita, Riva, and Ryan for their love, patience, and sacrifices.

To all of those people, I would like to say God bless you.

TABLE OF CONTENTS

DECLARATION OF ORIGINALITY	iii
ABSTRACT	iv
DEDICATION	vi
ACKNOWLEDGEMENTS	vii
LIST OF TABLES	xii
LIST OF FIGURES	xiii
CHAPTER	
I. INTRODUCTION	
1.1 General	1
1.2 Problem Definition	2
1.3 Research Objectives and Scope	8
1.4 Thesis Contents and Organization	11
II. BACKGROUND AND LITERATURE REVIEW OF CONCRETE FRACTURE MECHANICS	
2.1 Introduction	13
2.2 History of Fracture Mechanics	14
2.3 Mechanical Properties of Concrete	17
2.4 Fracture Properties of Concrete	20
2.5 Deficiencies in Concrete Structure	23
2.6 Linear Elastic Fracture Mechanics (LEFM)	24
2.7 Nonlinear Fracture Mechanics (NLFM)	27
2.8 Application of Fracture Mechanics to Concrete Material	29
2.9 Fracture Mechanisms and Structural Design	31
2.10 Modeling Concrete Fracture Behaviour	35
2.11 Simulation of Concrete Structural Damage and Cracking	41
2.12 Experimental Techniques for Concrete Fracture Characterization ..	53
2.12.1 Experimental Determination of Concrete Fracture Parameters	53
2.12.2 Experimental Investigations of the FPZ and Crack Evolution	68
2.13 Conclusion	76

III. APPLICATION OF DIGITAL IMAGE CORRELATION ON THE WEDGE SPLITTING TEST

3.1	Mechanical Properties of Concrete	83
3.2	Fracture Properties of Concrete.....	88
3.3	Wedge Splitting Test (WST).....	91
3.4	Mix Design and Mixing Procedure	98
3.5	Experimental Investigation of the Wedge Splitting Test (WST) ...	100
3.6	Experimental Findings for the Traditional Technique	103
3.7	Experimental Investigation of an alternative approach: Digital Image Correlation (DIC).....	112
3.7.1	Specimen Preparation	117
3.7.2	ARAMIS System Calibration Process	118
3.7.3	Testing Procedures.....	122
3.7.4	Experimental Results using the DIC Technique.....	124
3.8	Comparison of the Experimental Results for the Traditional and DIC Technique	130
3.9	Experimental Investigation of Crack Evolution and Development of the FPZ using the DIC Technique	135
3.9.1	Evaluation of Toughening Mechanisms in the FPZ.....	136
3.9.2	Assessing the Variation of FPZ Size and Crack Evolution with DIC.....	142
3.9.3	Energy Dissipation along the Crack Path	159
3.9.4	Assessment of the Development of the <i>FPZ</i> using the DIC Technique.....	164
3.10	Advantages of the DIC Technique	176
3.11	Summary of the Findings for the Application of DIC to the Study of the Fracture Behaviour of Plain Concrete	179
3.12	Conclusions	187

IV. INVERSE ANALYSIS AND NUMERICAL SIMULATION

4.1	An Inverse Problem Formulation for the Identification of the Fracture Properties of Concrete	194
4.1.1	Fictitious Crack Model (FCM)	196
4.1.2	Description of the Cracked Hinge Model (CHM)	200
4.2	Application of Inverse Analysis to the Wedge Splitting Test	210
4.3	Inverse Analysis Results.....	222
4.4	Finite Element Analysis (FEA).....	234
4.4.1	Finite Element Modeling and Concrete Fracture Behaviour.....	235
4.4.2	Application of Finite Element Analysis (FEA)	237
4.4.3	Damage-based Mechanics Model (ABAQUS, 2010).....	240
4.4.4	The Application of FEA to the WST.....	245
4.5	Finite Element Analysis (FEA) Results.....	247
4.6	Conclusion	267

v.	CONCLUSIONS AND RECOMMENDATIONS	
5.1	General Observations.....	269
5.2	Conclusions.....	271
5.3	Recommendations for Future Research.....	274
	BIBLIOGRAPHY.....	277
	VITA AUCTORIS	284

LIST OF TABLES

Table 3.1: Concrete Mix Design	99
Table 3.2: Experimental findings for the WST using traditional methods	112
Table 3.3: Experimental results from the WST using DIC	130
Table 3.4: Variation of the FPZ length with the splitting load	156
Table 3.5: Development of the traction free zone	158
Table 4.1: Comparison between the input and output bilinear softening parameters	224
Table 4.2: Comparison of the input and output parameters of the inverse analysis	225
Table 4.3: Comparison of the input and output parameters of the inverse analysis.....	226
Table 4.4: Comparison of the input and output parameters of the inverse analysis	227
Table 4.5: Softening curve parameters extracted from inverse analysis	229
Table 4.6: The fracture energy (G_F) and initial fracture energy (G_f) obtained from experimentation and inverse analysis simulation	232
Table 4.7: Comparison of the fracture energy (G_F) and initial fracture energy (G_f) obtained from the experimental studies and inverse analysis simulations	233
Table 4.8: Material properties of the plasticity-damage coupled model (traditional)	246
Table 4.9: Material properties of the plasticity-damage coupled model (DIC)	246
Table 4.10: Concrete fracture energy (comparison study)	264

LIST OF FIGURES

Figure 2.1: Different types of material response under uniaxial stress and deformation	15
Figure 2.2: The three basic modes of cracking	16
Figure 2.3: Mode I crack opening in a gravity dam	17
Figure 2.4: Description of the fracture energy	22
Figure 2.5: Distribution of internal stress at the tip of a sharp crack	25
Figure 2.6: The size of the nonlinear zone in different materials	28
Figure 2.7: The compact three-point-bending test and the WST	59
Figure 2.8: The bi-linear softening curve with four parameters	60
Figure 3.1: Compressive Strength Test and Split Cylinder Test	85
Figure 3.2: Stress distribution on concrete cylinder during splitting test	86
Figure 3.3: Yield lines of the assumed plastic failure mode	87
Figure 3.4: Fracture energy estimated from the area under the P-w curve	90
Figure 3.5: Wedge splitting specimen as a “compact” three-point-bending test	92
Figure 3.6: Schematic view of the WST-setting	95
Figure 3.7: Principle of wedge-splitting test (WST)	96
Figure 3.8: Geometry of the WST-specimen incorporating the band width model and loading	98
Figure 3.9: WST-specimen steel mold, and casting the WST-specimen	99
Figure 3.10: Clip-on Gauge (MTS Systems Corporation)	101
Figure 3.11: Clip-on Gauge, knife-edges, and positioning	102
Figure 3.12: Experimental set-up of the WST	103
Figure 3.13: The WST-specimen (WST6) after failure	105
Figure 3.14: Experimental results from the WST using clip gauge (CG)	106
Figure 3.15: Experimental results from the WST at different ages using clip gauge	108
Figure 3.16: Experimental results from the WST using clip gauge (CG)	109
Figure 3.17: The effect of the angle of rotation on COD reading	111
Figure 3.18: The hardware components of the ARAMIS DIC system	116
Figure 3.19: Preparing specimen for measurement with the ARAMIS system, and macro-image facets	117
Figure 3.20: Calibration Panel	119
Figure 3.21: Calibration process for the ARAMIS system	121

Figure 3.22: Experimental set-up for the WST with the ARAMIS and DIC	123
Figure 3.23: ARAMIS cameras and WST-specimen	124
Figure 3.24: The position of the notch tip and clip gauge	125
Figure 3.25: WST-specimen after failure and magnified view of the notch tip	125
Figure 3.26: Displacement calculation (d_s) using the ARAMIS DIC system	126
Figure 3.27: Screen-shot from ARAMIS during project computation and ARAMIS report after finalizing computation	126
Figure 3.28: Experimental results from the WST obtained using DIC	128
Figure 3.29: P_{sp} -COD curves from WST on concrete specimens	133
Figure 3.30: Evolution of the crack path and toughening mechanisms	138
Figure 3.31: The WST-specimen (WST2) supplemented with ARAMIS	140
Figure 3.32: Toughening mechanisms on the surface of the WST-specimen	141
Figure 3.33: Computational domain for the WST-specimen (WST2)	143
Figure 3.34: Crack tip opening displacement (CTOD) at various loading stages	145
Figure 3.35: Crack opening displacement-positions along the crack path	147
Figure 3.36: Crack opening displacement along the crack path (COD-Y)	147
Figure 3.37: Concrete crack and <i>FPZ</i> boundaries	148
Figure 3.38: Splitting load-Crack tip opening displacement (P_{sp} -CTOD)	150
Figure 3.39: Development of the <i>FPZ</i> and crack tip during loading	151
Figure 3.40: Development of the <i>FPZ</i> and crack during the post-peak phase	153
Figure 3.41: Development of the <i>FPZ</i> and the traction free zone	155
Figure 3.42: Variation of the <i>FPZ</i> length with the splitting load	156
Figure 3.43: Growth of the traction free zone	159
Figure 3.44: ARAMIS DIC system, screen shot (WST4)	161
Figure 3.45: Splitting load-crack opening displacement (P_{sp} -COD) curves	162
Figure 3.46: The dissipated energy and the crack opening displacement	163
Figure 3.47: The tensile damage along the crack path	164
Figure 3.48: Strain distribution over the WST-specimen's (WST6) surface	165
Figure 3.49: Splitting load-Crack tip opening displacement (P_{sp} -CTOD)	166
Figure 3.50: Strain distribution on the WST-specimen (WST6) surface	167
Figure 3.51: Location of internal cracks detected for different loads	167

Figure 3.52: Strain distribution and initiation of localized damage	168
Figure 3.53: Strain distribution and damage localization on the WST-specimen	169
Figure 3.54: Strain distribution and damage localization on the WST-specimen	170
Figure 3.55: Strain distribution on the WST-specimen at peak load	171
Figure 3.56: Strain distribution during the post-peak stage	172
Figure 3.57: Strain distribution during the post-peak phase	173
Figure 3.58: Strain distribution during the post-peak stage	174
Figure 3.59: Strain distribution during the post-peak stage	175
Figure 3.60: Variation in the crack path for the WST-specimen	176
Figure 4.1: The bi-linear softening curve with four parameters	176
Figure 4.2: Geometry of the WST-specimen	196
Figure 4.3: Cohesive crack in front of the notch and stress-crack opening curve	199
Figure 4.4: Principles of the fictitious crack model (FCM)	200
Figure 4.5: Stress-strain relationship (pre-cracked state), and Stress-crack opening relationship assuming a bi-linear softening curve for the cracked state	203
Figure 4.6: Geometry and loading and deformation characteristics with incorporation of the hinge element to a WST-specimen	204
Figure 4.7: The phases of stress distribution in the hinge	206
Figure 4.8: Geometry and loading of the WS-specimen	211
Figure 4.9: Load-crack tip opening displacement curve and normalized stress-crack opening displacement curve for WST5	224
Figure 4.10: Load-crack tip opening displacement curve (P_{sp} -CTOD) and normalized stress-crack opening displacement curve for WST6	225
Figure 4.11: Load-crack mouth opening displacement curve and normalized stress-crack opening displacement curve for WST5	226
Figure 4.12: Load-crack mouth opening displacement curve (P_{sp} -CMOD) and normalized stress-crack opening displacement curve for WST6	227
Figure 4.13: Normalized stress-crack opening displacement curves for WST5	230
Figure 4.14: Normalized stress-crack opening displacement curves for WST6	230
Figure 4.15: Response of concrete to uniaxial loading	242
Figure 4.16: Concrete tension stiffening with G_F option	244
Figure 4.17: Finite element meshing on the WST model	247
Figure 4.18: Load-crack tip opening displacement curve (P_{sp} -CTOD)	249

Figure 4.19: Tensile damage (d_t) and the crack's path derived using DIC output	250
Figure 4.20: FEA result using DIC output	251
Figure 4.21: Maximum principal stress (S_p) and strain (ϵ_p) at failure	253
Figure 4.22: FEA results using DIC output	254
Figure 4.23: The dissipated energy along the crack path	255
Figure 4.24: Load-crack tip opening displacement curve	257
Figure 4.25: Tensile damage in the cracked specimen and the crack's path	258
Figure 4.26: Maximum principal stress, displacement and principal stress-CTOD curve crack initiation using CG inverse analysis output	259
Figure 4.27: Maximum principal stress (S_p) and strain (ϵ_p) at failure	260
Figure 4.28: FEA results: using CG inverse analysis output	261
Figure 4.29: FEA results using CG inverse analysis output	262
Figure 4.30: Comparison of FEA results for the CG and DIC experimental data	265
Figure 4.31: FEA results for variation in tensile strength and dissipated energy along the crack path of a WST-specimen	266

CHAPTER I

INTRODUCTION

1.1 General

Concrete is the most widely produced construction material. Structures made of concrete can have a long service life making them more environmentally friendly. However, its low tensile strength capacity is considered to be one of concrete's major disadvantages. As a result of low tensile strength, cracks often develop in concrete structures, and are usually controlled by providing steel reinforcement to the tension zones; however, in large concrete structures, such as massive concrete dams, providing adequate steel reinforcement is uneconomical.

The presence of cracks is not in itself an indication of the end of a structure's service life; however, investigations of cracking are required for the assessment of structural integrity. Accurate modelling of cracking is important for studying concrete structural behaviour; accordingly, finite element analysis, which simulates cracking behaviour, is needed to model the performance of cracked structures using available damage models, but requires accurate assessment of mechanical and fracture properties. While concrete mechanical properties that characterize the behaviour of concrete before cracking are well known, and can be determined using standard material tests, the identification and evaluation of concrete fracture parameters poses an ongoing challenge for engineers and researchers. Concrete fracture properties are also necessary for the

accurate prediction of the probability of crack stability or propagation in concrete structures.

Many experimental techniques to identify fracture parameters have been discussed in the literature; however, they have many limitations. Furthermore, the fracture behaviour of concrete is greatly influenced by the *fracture process zone* (FPZ), the zone in which the material undergoes softening damage. Therefore, it is of interest not only to understand the conditions underlying crack initiation, but also crack evolution. Consequently, the need for an accurate technique that is capable of monitoring the *FPZ* and measuring crack displacement is recognised by many researchers. To the best of this author's knowledge, no experimental investigation has been reported that focused on changes in concrete properties along the crack path during various fracture stages while also recording crack opening displacement, including: variations in dissipated energy, tensile damage, and size of the *FPZ* and traction free zone.

1.2 Problem Definition

Concrete is a heterogeneous material filled with defects and micro-cracks that are capable of propagating. The study of fracture mechanisms in concrete, initiated by Kaplan in 1961, is very important for thorough investigation of the performance of concrete structures, particularly concrete dams that were built decades ago. A common question that highlights the focus of much of the concrete-related research conducted today is: what size of crack can be tolerated at an expected service load?

Assuming that modern structures have achieved a satisfactory level of safety means that the code applied to attain the required safety level is satisfactory, and requests for the evaluation of these structures are unnecessary. However, the increasing demand for structural evaluation reveals the limitations of this view of the applied methodology.

There are over 13,000 dams classified as having high hazard potential, which means that the consequences of the dam's failure will likely include loss of human life and significant downstream property damage. Failure of the Silver Lake Dam in Michigan in 2003 resulted in \$100 million of damage, including \$10 million in damage to utilities, \$4 million to the environment, \$3 million to roads and bridges, and the flooding of 20 homes and businesses. Big Bay Lake Dam in Mississippi, which produced \$2.5 million of damage, failed in 2004 destroying 48 homes, damaging 53 homes, 2 churches, 3 businesses and a fire station, as well as washing out a bridge (The Association of State Dam Safety Officials (ASDSO), 2011). These catastrophes are current reminders of the potential consequences of unsafe dams. These cases of failure, among many other cases, highlight the need to evaluate existing concrete structures and to develop new design methodology that takes the fracture mechanics of concrete into consideration for both economic reasons and for the wellbeing of humans in their vicinity.

According to the Canadian Council for Public Private Partnerships in 2009, Canada's infrastructure deficit is \$125 billion, and is in fact growing annually by \$2 billion. The ASCE report (2005) indicated that the percentage of the nation's 590,750 bridges rated structurally deficient between the period of 2000 and 2003. To address all

of the current bridge deficiencies, an estimated budget of \$9.4 billion a year for 20 years would be required. The ASCE report also indicated that the number of unsafe dams has risen by 33% since 1998 to more than 3,500 hazardous dams. The number of dams identified as unsafe is increasing at a faster rate than those being repaired. A budget of \$10.1 billion will be required over the next 12 years to address all of the critical non-federal dams, which pose a direct risk to human life and property.

Moreover, most of the design procedures currently in use are based on strength of materials concepts where continuity is assumed. Concrete is full of cracks; thus, the singularity of the stress concentrations at the crack tips, notches, around holes, and in connections, require more sophisticated design procedures as these stresses can exceed the strength of the materials. If concrete was a perfectly brittle material, any small crack or flaw in the regions containing tensile stresses, f'_t , would lead to crack propagation, which might lead to a catastrophic failure. However, concrete is quasi-brittle and is characterized by softening behaviour before failure, which means it can sustain some deformation before failure. Therefore, the question is: how much energy is needed to overcome this deformation at a specific stage of fracture? Evaluation of concrete fracture parameters, in particular the dissipated energy during the fracture process, could provide an answer to this question. An accurate analysis of the fracture progress is required for assessing the integrity of a concrete structure and to predict its future performance. Unfortunately, despite a great deal of research, fracture mechanics concepts are still seldom used in the design of concrete structures, particularly in North America (Mindess, 2002).

A strong structure is one that is designed properly to resist various modes of failure, such as: elastic instability, large elastic deformation, yielding (plastic deformation), necking (tensile instability), and fracture (Saouma, 2003). However, in structural engineering, the practical design procedures covered by safety codes is simplified by including some material parameters (usually the compressive strength and elastic modulus), and giving some emphasis to experience. Consequently, simplified numerical functions are often used in the design of structures. However, continuous research development in recent decades indicates that the limits of such an approach have been reached.

Concrete is a mixture of aggregates, cement, and water. The properties of all of these compounds, which may differ from one place to another, influence the final properties and performance of concrete. Furthermore, the properties of the cement paste used in making concrete depend on the method of hydration that took place, and this can be affected by moisture, temperature, mixing conditions, etc. Concrete properties are constantly evolving, depending on the chemical composition of the cement paste, environmental conditions, mechanisms active during setting, and hardening. Although concrete has been the most widely used material for a long period of time, accurate modeling of existing concrete structures is still needed. Fracture is one of the major concerns in the modeling of engineering materials; therefore, knowledge about post-cracking parameters is necessary for structural integrity assessment as these parameters depict crack initiation and propagation.

The safety of some structures, such as gravity dams, depends on the tensile toughness of concrete. The presence of cracks can be considered as a defect rather than a failure. Therefore, as already mentioned, cracks in concrete do not necessarily mean that the structure has reached the limit of its useful life. However, propagation of these defects could result in the failure of a structure; with the development of fracture mechanics, the question is not whether a crack exists or not, but whether the crack is stable or not. Therefore, ongoing examination of the performance of concrete structures is a constant and essential requirement for determining the lifespan of concrete structures.

In structural applications, conclusions about a structure's performance are often driven by surface assessment or overall observation and measurement. However, the fracture behaviour of concrete is greatly influenced by the *fracture process zone* (FPZ), the zone in which the material undergoes softening damage. The mechanical behaviour and fracture process of concrete is governed by the stability of internal cracks and flaws, which are greatly influenced by the concrete composition and by the microstructural changes in concrete material. Consequently, thorough investigation of the FPZ's properties and toughening mechanisms such as bridging, crack deflection, and the evolution of the crack path during various loading stages is required. Most previous investigations of the FPZ included general examination and/or characterization of this zone (e.g. size, shape). Some experimental techniques considered the FPZ; for example, the impregnation technique successfully obtained the crack profile. However, due to its destructivity, this technique failed to depict crack evolution. Another method, acoustic emission (AE), did not succeed in characterizing the crack profile and traction free zone.

To the best of this author's knowledge, no investigation focused on the changes in concrete properties that occur during various loading stages, such as alterations in dissipated energy or crack opening along the crack path. Therefore, an innovative technique is needed for comprehensive investigation of the *FPZ*, and is explored in addition to the main goal of this research which was to determine structural response under loading (load-deformation) from a single test.

Crack propagation in concrete structures is usually controlled by providing steel reinforcement to the tension zones in order to supply adequate tensile strength; however, in some structures, such as massive concrete dams, providing steel reinforcement is not economically feasible. Unreinforced concrete structures are the most sensitive to fracture. Consequently, the focus of discussion of many researchers and engineers is on how the safety level of new structures can be made compatible with economic considerations, with an emphasis on deriving scientific bases for code and standard requirements. American Concrete Institution (ACI) 446.3R-97 stated: "It makes sense to study the analysis of unreinforced concrete structures, because these provide the most severe tests of fracture behaviour, and because the results of these analyses can add insight into the more complex behaviour evidenced in reinforced concrete structures". In addition, if fracture mechanics are considered, design engineers can determine the relative importance of stress, materials toughness, and flaw size during the design rather than during fracture analysis of a structure that has already cracked, and so requires assessment to investigate its condition.

1.3 Research Objectives and Scope

Despite the fact that concrete is one of the oldest construction materials, there are still fundamental problems and questions about this material for researchers and structural engineers to resolve. The challenge is to develop concrete structures that are economical, and also meet the safety and serviceability requirements for higher performance and/or to find an innovative technique for assessing the integrity and monitoring the health of existing concrete structures.

Cracks are inevitable in concrete, and fracture is an important mode of deformation in both plain and reinforced concrete structures. Fracture mechanics is a field concerned with the study of crack propagation using analytical solid mechanics to characterize a material's resistance to fractures. It is an important tool for improving the mechanical performance of materials, in which the theories of elasticity and plasticity are applied to the microscopic defects found in real materials in order to predict the macroscopic mechanical failure of a structure. Fracture mechanics techniques are essential for many engineering applications, such as preventing failures during service life and developing concrete design codes.

Although the deformation response is an important aspect of the analysis of a reinforced concrete structure under loading, prediction of crack formation and propagation is also required. Therefore, the experimental technique that is chosen must be able to identify the location of a new crack tip and crack width along the crack path during crack propagation and up to failure. The intention of the research presented in this

thesis is to illustrate the use of such technology for the identification of concrete fracture parameters, including specimen deformation, estimation of the variation of dissipated energy, tensile damage, and the crack opening displacement along the crack path while also monitoring the crack tip opening displacement (CTOD) to identify the fracture energy and other fracture parameters.

The main objective of this research is to develop a new technique to identify concrete fracture parameters, which are needed to model concrete structures subjected to extreme loading such as earthquakes, flood, wind, and storm. The need for an accurate non-contact and non-disturbing technique that is capable of monitoring the *FPZ*, as well as the crack opening, is recognised by many researchers. The approach chosen for this research is based on the development of digital camera resolutions that allow the tracking of a structure's deformation under loading on a macroscopic scale and the extraction of accurate material properties that can describe the fracture behaviour of the tested materials. A non-contact digital image correlation (DIC) technique using the ARAMIS system was chosen to perform experimental measurements. Due to the difficulties associated with the direct uniaxial test (UTT) that yields the concrete *softening curve* ($\sigma-w$), the indirect wedge splitting test (WST) was chosen; therefore, inverse analysis was required to generate the $\sigma-w$ curve and other fracture parameters. The results of inverse identification were confirmed using finite element analysis (FEA) along with the fracture energy values that were obtained. The concrete damaged-plasticity coupled constitutive law was implemented to simulate the progressive accumulation of mechanical damage in the WST-specimens.

The objectives of this research can be summarized in two main categories:

Application of the digital image correlation (DIC) technique to the WST:

- To remotely obtain the load-crack opening (P_{sp} -COD) relationship at the crack tip and any location on the WST-specimen's surface.
- To examine the ability of the DIC technique to perform a complex investigation of the micromechanics of concrete fracturing due to mode I fracture.
- To investigate the physical phenomena of fracture initiation and propagation in concrete with respect to its microstructure using innovative non-contact DIC techniques, including toughening mechanisms present during fracture without interference and/or the impact of machine vibrations during loading.
- To investigate the ability of DIC techniques to provide insights into a failure scenario, including *FPZ* properties, change in the crack tip position (size of the traction free zone), and the evolution of the crack profile (which is difficult to investigate using the traditional clip-gauge technique).
- To investigate the development of the dissipated energy and tensile damage along the crack path.

Inverse analysis and numerical simulation

- To examine if the DIC results can be employed for the determination of the *softening curve* (σ - w) by using them to solve an inverse problem based on the

cracked hinge model, leading to accurate estimation of the fracture properties of concrete, such as the *tensile strength* (f_t) and *fracture energy* (G_F)

- To develop realistic numerical models of concrete and compare structural responses from numerical models to those observed in the original concrete material during testing
- To examine whether Inverse Analysis is capable of evaluating the input parameters necessary for a FEA from measurements obtained from only one test.
- To study the ability of the coupled damage-plasticity model to capture the evolution of strain localization in the WST.

1.4 Thesis Contents and Organization

The research presented here was conducted in three main stages. The first stage involved an experimental study using the wedge splitting test (WST), which was carried out utilizing the digital image correlation (DIC) technique to monitor tensile fracture in concrete in comparison to measures obtained with the classical direct technique using a clip-gauge. Mathematical modeling was conducted in the second stage using an inverse analysis based on the cracked hinge model. Lastly, finite element analysis (FEA) using ABAQUS was conducted to validate these findings. This thesis is organized in five chapters.

The present chapter introduces the thesis topic and research objectives. Chapter II presents general background about concrete fracture mechanics and includes a

comprehensive literature review relevant to the topics in this thesis. Chapter III investigates the fracturing processes in concrete, and describes the experimental component of the research, including the application of the DIC technique and the classical method, using a clip-gauge, to the WST. Furthermore, a thorough investigation of the *FPZ* and crack path is reported in detail in order to understand the complicated mechanisms of concrete fracture during different fracture stages. Chapter IV focuses on the numerical approach to obtaining concrete fracture parameters, including determination of the softening curve using inverse analysis of the DIC results based on a cracked hinge model. To validate the findings obtained with this approach, the fracture parameters obtained by inverse analysis were confirmed by FEA utilizing the coupled damage-plasticity constitutive law for concrete. Lastly, the conclusions drawn from this research, findings and recommendations for future studies are presented in Chapter V.

CHAPTER II
BACKGROUND AND LITERATURE REVIEW OF CONCRETE FRACTURE
MECHANICS

2.1 Introduction

Most engineering materials contain some defects. Concrete is one of these materials; however, concrete also offers many advantages, such as low cost, good weather and fire resistance, formability, and good compressive strength. Therefore, worldwide, concrete is the most widely used material in the construction of many structures (e.g. buildings, bridges, and dams).

Concrete is a heterogeneous material that contains mainly cement, aggregate and water. Due to shrinkage of the cement paste, micro-cracks occur in concrete prior to loading; therefore, cracks are inevitable in concrete structures. The presence of cracks is not an indication of the end of the structures' service life; however, investigation and assessment is required to classify the existing cracks, and to decide whether or not they are stable. The mechanical behaviour and fracture processes of concrete subjected to different loading conditions are governed by the stability of these internal cracks and flaws during loading.

Fracture mechanics is a failure theory that uses energy criteria, possibly in conjunction with strength criteria, to account for failure propagation through a structure (ACI Committee 446.1 R-91). Fracture mechanics is a general analysis of structural

failure considering existing flaws; this approach examines the behaviour and response of a structure to crack initiation and propagation by employing the fracture parameters used in design, modeling and failure analyses. According to Broek (1986), fracture mechanics should be able to answer the following questions:

- What is the residual strength of the structure as a function of crack size?
- What size of crack can be tolerated at the service load?
- How long does it take for a crack to grow from a specific initial size to the critical size for failure?
- What size of pre-existing flaw can be permitted at the moment the structure starts its service life?
- How often should the structure be inspected for cracks?

2.2 History of Fracture Mechanics

The mechanical behaviour of a structure is influenced by the materials used in the structure. Most engineering materials can be classified as brittle, ductile, or quasi-brittle, depending on the schematic material tensile stress-deformation response as shown in Figure 2.1.

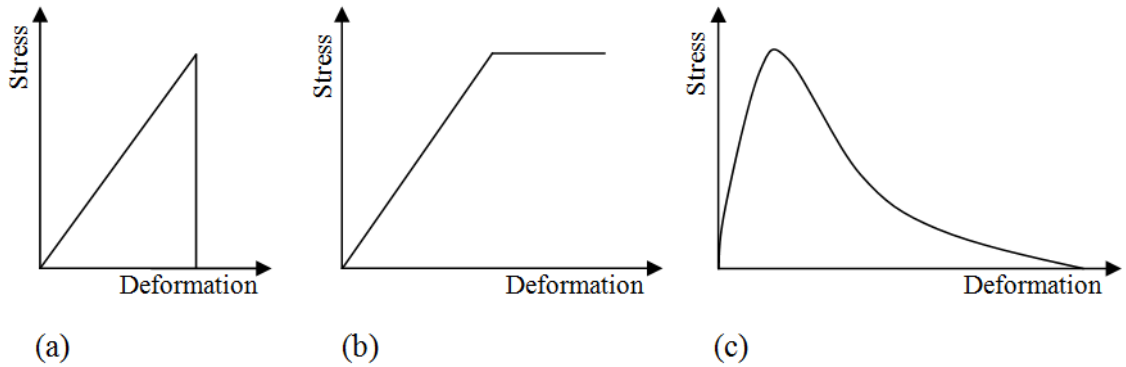


Figure 2.1: Different types of material response under uniaxial stress and deformation (a) elastic-brittle material, (b) elastic-plastic material, (c) elastic-quasi-brittle material (adapted from Shah et al., 1995)

Figure 2.1(a) represents the development of the stress-deformation curve for perfectly brittle materials (i.e., elastic-brittle), such as glass. When elastic-brittle material is used, it can be assumed that the structure will fail catastrophically with less deformation when the maximum stress is equal to the tensile strength of the material. For ductile material, however, the stress remains constant when the level of applied stress causes the structure to yield; the structure withstands a large amount of deformation before failure. The yielding region for ductile materials often accounts for most of the stress-deformation curve; the deformation of ductile material provides warning prior to failure as shown in Figure 2.1 (b). Quasi-brittle material is characterized by gradually decreasing stress levels after the application of peak load; a softening (stress-deformation) curve is usually observed for quasi-brittle materials as shown in Figure 2.1(c).

Three fundamental modes for the opening of a crack have been defined in fracture mechanics: Mode I, Mode II and Mode III. Mode I cracking is caused by normal stress applied to the crack faces. Mode II cracking is due to shear stresses along the crack faces; since these forces are parallel to the crack, one of these forces pushes one half of the crack while the other pulls the other half, but both of them are applied along the same line (in-plane shear mode). Both Mode I and II cracking are in-plane modes. Mode III cracking is an out-of-plane shear mode caused by tearing loading, where the forces are transverse to the crack; this causes the material to slide along itself, and move out of its original plane (out-of-plane shear mode). These three basic fracture modes are shown in Figure 2.2.

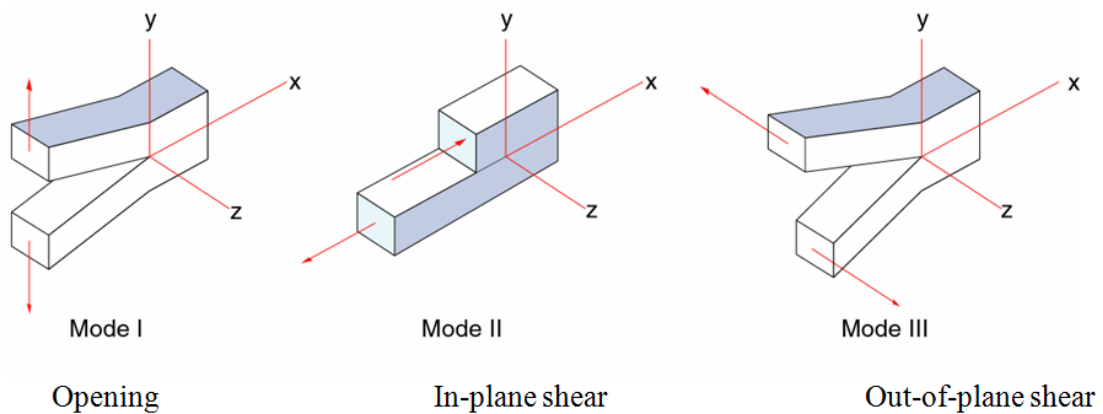


Figure 2.2: The three basic modes of cracking: (a) Mode I opening, (b) Mode II in-plane opening, (c) Mode III out-of-plane opening

Mode I opening is very common, and takes place, for example, in concrete gravity dams as shown in Figure 2.3. If there is an existing crack on the upstream side, water can penetrate and open the crack.

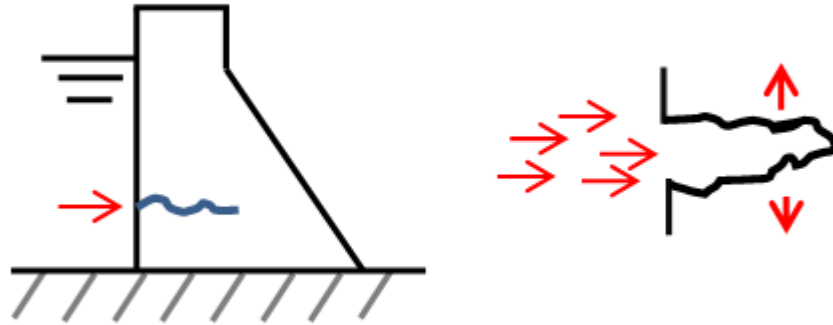


Figure 2.3: Mode I crack opening in a gravity dam

2.3 Mechanical Properties of Concrete

Standard material tests are carried out to determine the values of material properties, such as compressive strength (f'_c), tensile strength (f_t), Young's modulus (E), and Poisson's ratio (ν).

Compressive strength (f'_c) is the capability of a material or structure to resist axial pressure. In the other words, it represents the maximum stress that a material can sustain under compression. This property is one of the most common mechanical parameters of concrete since it is used in structural analysis and design. In addition, this parameter can be used to estimate the tensile strength, Young's modulus, and cohesiveness of concrete. Improving concrete f'_c depends primarily on adjustments to the water-cement ratio

(W/C), type of cement, admixtures, and curing conditions; however, the disadvantage of increasing this parameter is associated with reducing the ductility of the concrete structure. The value of f'_c can be determined by following the ASTM C873-10 standard test protocol using concrete cylinders after curing for 28 days. The failure of concrete during compression can be described by means of the theory of plasticity.

The tensile strength (f'_t) is one of the most important parameter of concrete, even though it is not clearly used in design. This is due to the fact that its importance has been poorly understood and/or methods for taking f'_t into account have been lacking; however, f'_t is indirectly used in the shear design of beams (Hillerborg, 1985). Without f'_t , concrete would not be able to form any geometrical shape (e.g. beams, columns, walls, slabs, etc.). The role of f'_t in the behaviour of concrete structures at fracture is also important; f'_t predicts crack initiation and propagation in a concrete structure since it is assumed that cracking will occur when the stress at the crack tip reaches the f'_t of the material. The safety of some concrete structures, such as gravity dams and slabs, depends on the tensile toughness of concrete. If concrete was a perfectly brittle material, any small crack or flaw in a region exposed to tensile stresses would cause crack propagation, which might lead to a catastrophic failure. Nevertheless, the f'_t of concrete is neglected in most of the serviceability and limit state calculations making it difficult to model the effects of cracks. It is well known that concrete is weak (with respect to tension) and filled with flaws and micro-cracks that propagate if the f'_t is reached during loading, which occurs in the range of approximately 8 to 15% of its compressive strength (f'_c) for normal concrete and 5 to 7% of the f'_c of high-strength concrete. Crack propagation in concrete structures

is usually controlled by providing steel reinforcement in the tension zones; however, in some structures, such as massive concrete dams, providing steel reinforcement is uneconomical. Therefore, accurate modelling of fracture progression is required for assessing the structure's performance.

The parameter termed Young's modulus (E) is named after the 19th century British scientist Thomas Young, and represents the stiffness of an elastic material. However, the concept was initially developed by Leonhard Euler in 1727; the first experiment that used the concept of E in its current form was performed by the Italian scientist, Giordano Riccati, in 1782. E of concrete is a function of the values of E of the aggregates and cement matrix, and their relative proportions. For concrete, E is defined as the ratio of the uniaxial stress over the uniaxial strain in the range of stress in which Hooke law holds; E can be calculated experimentally utilizing the stress-strain curve where it is equal to the slope of the tangent of the initial linear part of the curve. The value of E can also be estimated theoretically according to the standard, CSA A23.3 (8.6.2.3). The initial elastic stiffness (E_o) is relatively constant at low stress levels, but starts decreasing with increased loading indicating damage evolution associated with stiffness degradation. The degradation of the tensile elastic stiffness after the peak stress (softening stage) is represented by d_t ; consequently, according to the concrete damaged plasticity model, the reduction of the elastic modulus is given in terms of a scalar degradation variable d as: $E = (1-d_t) E_o$.

The Poisson's ratio (ν), named after Siméon Poisson (1781-1840), is a measure of the Poisson effect where the material tends to expand in the two directions perpendicular to the direction of the applied compressive load. Accordingly, ν is the ratio of the lateral expansion to the longitudinal contraction of the specimen under uniaxial compressive loading. The value of ν must be known in order to generalize 2D finite element modelling. The estimated value of ν for various materials is reported in the literature, and for concrete this value is approximately equal to 0.2.

2.4 Fracture Properties of Concrete

Fracture properties are essential material parameters that are important for the assessment of structural integrity since they can be utilized to depict crack initiation and propagation. Analysing the cracking process assists engineers to investigate how safe a crack would be at a specific stage of propagation. In addition, fracture properties are used for modeling concrete structures where prediction of a potential crack can be specified. Furthermore, modeling results may be used to improve the structural design, so that cracking will be controlled and the properties of the material to be used can be selected appropriately. The fracture of concrete can be characterized by the stress-crack opening relationship (σ - w), fracture energy (G_F), and characteristic crack length (l_{ch}).

The stress-crack opening (σ - w) relationship, which is called the *softening curve*, illustrates the development and the degradation of the stress-carrying capacity of concrete during the fracture process; this curve is directly linked to G_F , the energy absorbed (per

unit area of the fracture surface) within the damage zone. In addition, other material properties, such as the f_t , can be extracted from this relationship. The *softening curve* ($\sigma-w$) and G_F are the main fracture properties that govern crack propagation. The total energy, according to Hillerborg (1985), can be divided into two parts corresponding to the two curves shown in Figure 2.4. This figure illustrates the stress-deformation behaviour of concrete. As the deformation increases, the stress increases until a maximum stress level is reached where softening phenomena appear (post-peak stage). The decrease in stress observed under increasing deformation of quasi-brittle material is called *strain softening*. This softening takes place within a narrow zone of the specimen, the *FPZ* or *damage zone*. After the *FPZ* starts to develop, the strain will no longer be evenly distributed along the specimen since the deformation increases within the damage zone, but decreases within the rest of the specimen. At this stage, the stress-deformation of the material cannot be described generally by a single curve since the shape of this curve will depend on the length over which the deformation is measured. A general description of the stress-deformation properties of concrete can be given by two curves; the first is the stress-strain ($\sigma-\varepsilon$) curve, including unloading branches, and the second is the stress-deformation ($\sigma-w$) curve describing the additional deformation within the damage zone. Consequently, two types of energy are involved: 1) the energy absorbed by the whole specimen, representing the energy per unit volume, can be calculated from the area under the ($\sigma-\varepsilon$) curve before tensile stress is reached; and 2) G_F absorbed within the damage zone only, which is equal to the area below the ($P_{sp}-w$) curve divided by the projected fracture area on a plane perpendicular to the splitting load direction (ligament length x specimen width), and can be estimated as shown in Figure 2.4.

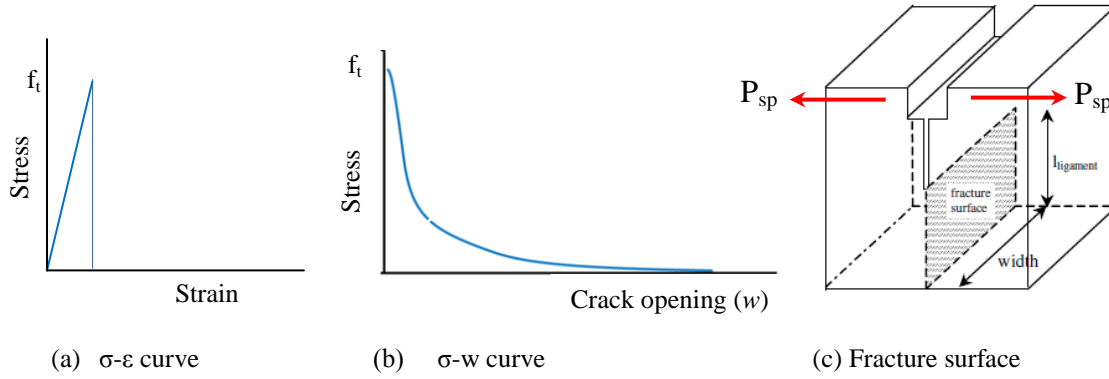


Figure 2.4: Description of the fracture energy: (a) fracture energy before reaching tensile strength, (b) G_F absorbed within the damage zone, (c) fracture area for the WST-specimen

The parameters G_F and σ - w depend on the composite structure of the material, which is essentially governed by the mechanical interaction of the aggregates with the cement-based matrix (Wittmann, 2002). Furthermore, G_F alone does not suffice to characterize the brittleness of concrete. In 1976, Hillerborg introduced the concept of *characteristic length* (l_{ch}) to define the influences of the material and the size of the structure as a function of the brittleness number (β), which can be calculated from Equation 2.1:

$$\beta = \frac{\text{Elastic Energy}}{\text{Fracture Energy}} = \frac{f_t^2 L}{G_F E_c} = \frac{L}{l_{ch}} \quad (2.1)$$

$$l_{ch} = \frac{G_F E_c}{f_t^2} \quad (2.2)$$

The elastic energy is the potential mechanical energy stored in the configuration of a material as work is performed to distort its volume or shape. L is a structural dimension, and l_{ch} is a material parameter that represents a measure of the elastic strain energy needed for one unit area of crack propagation. The parameter, l_{ch} , can be interpreted as the length that stems from the comparison of the elastic stored energy and G_F , and that characterizes the brittleness for complete fracture (RILEM TC 187-SOC 2007). This measure has been used to quantify the brittleness of concrete, rock, glass and other materials, and was used for concrete by Hilsdorf and Brameshuber (1991), Zhou et al. (1995) and Tasdemir et al. (1996). The value of l_{ch} for concrete is approximately 200-400 mm (Patterson, 1981). Zhou et al. (1995) reported values of l_{ch} ranging from 80 to 330 mm for concrete with compressive strengths ranging from 81 to 115 MPa. In general, l_{ch} decreases with the structure's age, indicating increased brittleness (RILEM TC 181, 2002). According to the fictitious crack model, l_{ch} is proportional to the length of the *FPZ*. The *FPZ* length for concrete is on the order of $0.3 l_{ch}$ to $0.5 l_{ch}$ at complete separation of the initial crack tip, and is purely a material property (Shah et al, 1995).

2.5 Deficiencies in Concrete Structure

For many reasons, flaws, such as cracks, voids, weld defects, and design discontinuities, may appear in a structure. Brittle materials exhibit notch sensitivity; the presence of a notch causes a change in the net section strength (σ_{net}) of the materials, which can be calculated on the basis of the reduced cross section (net cross section) of the elastic-brittle material without considering the stress concentration effect at the notch.

Structural failure occurs as the result of propagation of the initial defects of the materials. Conventional strength-based design approaches consider the influence of these defects by introducing a *stress concentration factor* (K_t). K_t approaches infinity for a sharp crack, which means that the internal stress reaches infinity at the crack tip; however, no material can sustain infinite stress.

$$\sigma_{\max} = K_t \sigma_{net} \quad (2.3)$$

2.6 Linear Elastic Fracture Mechanics (LEFM)

The field of fracture mechanics developed in 1913 when Inglis studied the elastic solution for the state of stresses at the vertex of an ellipse hole, and observed that as an ellipse approaches a line crack, the stress concentration tends to infinity (Figure 2.5). Subsequently, the first explanation of the mechanism of fracture in brittle materials, such as glass, was given by Griffith (1920-1924) and was based on the analysis of a thin plate with a sharp crack. He concluded that when a crack appears, the fracture process of brittle materials cannot be governed by any strength criteria, since the stress at the crack tip, from applying a very small load, approaches infinity in an elastic continuum. Consequently, any structure containing a crack should fail, no matter how small the crack or how light the load. This led Griffith to propose an energy criterion of failure (i.e., a thermodynamic approach), which forms the basis of classical linear elastic fracture mechanics (LEFM). This criterion states that the crack will propagate if the available energy is equal to the energy required to extend the crack by a unit surface area.

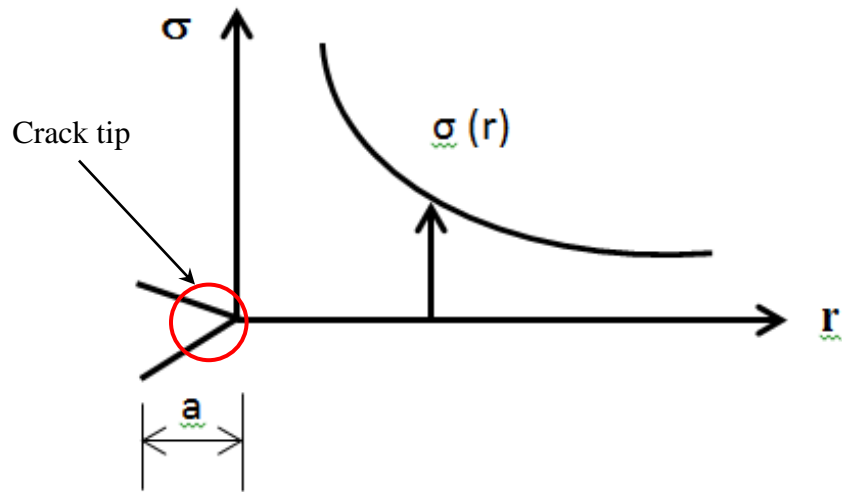


Figure 2.5: Distribution of internal stress at the tip of a sharp crack
[adapted from Shah et al., 1995]

Since infinite stress cannot develop in real materials, a specific zone of inelasticity must exist at the crack tip. For metallic materials, this inelastic zone is considered as a *yielding zone*. Westergaard (1934) was the first to apply the concepts of fracture mechanics to concrete beams. In 1939, Westergaard developed a linear elastic description for the stress field around the crack tip using stress functions in the complex domain. The development of elastic fracture mechanics occurred during the period of 1940-1970, and was inspired by confusing failures due to the fracture splitting of the hulls of Liberty ships in the U.S. Navy during World War II. Consequently, the accomplishments of theoretical, numerical, and experimental activities brought LEFM to its present state, a mature scientific discipline, by linking the *energy release rate* to the elastic stress and strain fields.

Irwin (1957) proposed that the presence of a plastic zone at the crack tip reduces the stiffness of the structure to that of a structure containing a longer crack. He introduced the concept of the stress intensity factor (K) as a parameter denoting the intensity of stresses that are close to the crack tip, and related this factor to Young's modulus (E) and the *energy release rate* (G). This relationship describes the energy needed to break the bonds in the material microstructure and create a unit area of new surface, which can be determined from the following equation:

$$G = \frac{K^2}{E} \quad (2.4)$$

It is clear that LEFM characterizes the local crack-tip stress field in a linear elastic material using a single value for K , which depends on the applied stress, the size and placement of the crack, and the geometry of the specimen. The determination of K is described in any fracture mechanics hand book (e.g. Tada, et al., 1985).

Irwin (1957) also introduced the critical energy release rate (G_c), which can be determined experimentally, and represents the work required to produce a unit increase in crack area. Since any propagation of an initial crack in a structure made of linearly elastic materials means catastrophic failure, the critical condition under which the crack propagates is when G equals the critical value, G_c , causing a global failure. Consequently, $G = G_c$ can be used as the failure criterion for linear elastic materials. Thus, the tensile stress needed to propagate the initial crack was calculated using the following equation:

$$\sigma_c = \sqrt{\frac{EG_c}{\pi a}} \quad (2.5)$$

where E is the Young's modulus, a is the initial crack length and G_c is the critical energy release rate (i.e., the toughness of the material).

2.7 Nonlinear Fracture Mechanics (NLFM)

Higgins and Bailey (1976) conducted a three point bend beam test (TPBT) with concrete samples constructed of the same material, but with different depths and found the values of the critical stress intensity factor (K_c) to be size dependent when LEFM concepts were used to describe the results. The LEFM approach is based on the assumption that the size of the plastic zone is small compared to the size of the actual crack, and that the energy is dissipated from a small area while the remainder of the structure is considered elastic. This means that the LEFM approach does not take the stable crack growth associated with the *FPZ* into consideration. In other words, according to LEFM, the initial crack length, rather than the sum of the initial crack length and the length of the crack extension where various types of toughening mechanisms take place, is used to determine the critical stress intensity factor. Since an inelastic zone (instead of a yielding zone) exists at the crack tip in quasi-brittle material, this material does not exhibit a yielding limit for increasing load, which limits the validity of LEFM to large structures only. Furthermore, the size of the inelastic zone (*FPZ*) in quasi-brittle materials is usually not smaller than the initial crack, where the dissipative processes take place (Figure 2.6). Therefore, the principles of NLFM, represented by the strain energy release

rate, should be used to describe stable crack propagation, and for modeling concrete fracture (Shah et al, 1995).

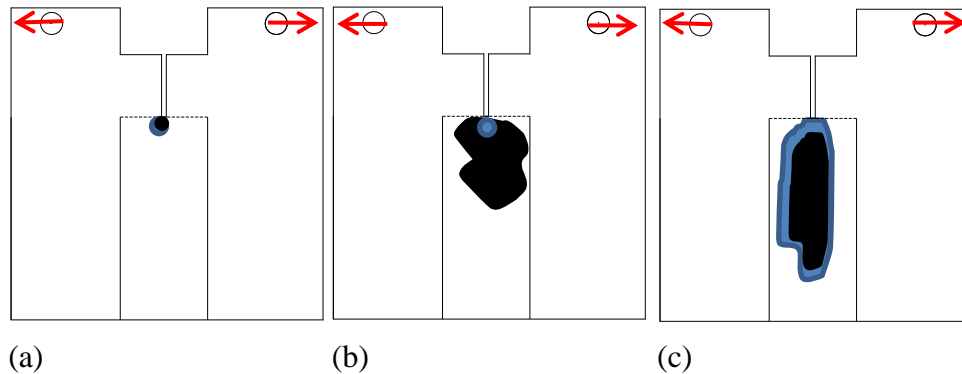


Figure 2.6: The size of the nonlinear zone in different materials: (a) brittle material, (b) elasto-plastic material and (c) quasi-brittle material (adapted from Karihaloo, 1995).

Griffith proposed assuming the closure of smooth crack faces to overcome this problem. The first attempt to include cohesive forces to close the crack was undertaken by Barenblatt (1959), who assumed that large cohesive forces of unknown distribution act in a small region, the cohesive zone, near the crack tip. In 1960, Dugdale suggested a similar approach for elastic-plastic materials with cohesive forces acting in a narrow cohesive zone; because of the yield limit and high ductility of these materials, the distribution of cohesive forces could be determined. Due to the fact that cracks in heterogeneous materials are not smooth and straight, but are rough and tortuous, and are accompanied by micro-cracking, frictional slip, and plasticity in a sizable zone around the tip, this localized damage zone consumes part of the energy provided by the applied load, and induces nonlinearity into the response as shown in Figure 2.1 (c). Consequently, the

energy required for the propagation of an initial crack (of a unit length with a unit thickness) in a structure made with this material is larger than G_c , and is called the energy release rate for quasi-brittle material (G_q).

Since crack propagation always involves the dissipation of energy, consideration of energy factors plays an important role in the study of fracture mechanics, including crack propagation problems. By considering fracture from an energetic point of view, crack growth criteria can be assumed in terms of energy release rate. This approach offers an alternative to the K -based fracture criteria, and supports the connection between global and local fields in fracture problems. Accordingly, the energy release rate is considered to be a global parameter, while the stress intensity factor is considered to be a local (crack-tip) parameter.

2.8 Application of Fracture Mechanics to Concrete Material

Concrete is a heterogeneous material consisting of different phases, and the inelastic zone around the crack tip is dominated by different crack arrest mechanisms. For example, crack shielding, which is randomly oriented, consumes some of the external energy due to the applied load. Crack deflection occurs when the path of least resistance is around a relatively strong particle or along a weak interface. Bridging occurs when the crack has advanced beyond an aggregate that continues to transmit stresses across the crack until it ruptures or is pulled out. If there is some contact between the cracked rough faces, energy dissipation occurs through friction and through some of the bridging across

the crack. Crack tip blunting by voids requires additional energy to propagate the crack with its new blunt tip. Furthermore, due to the heterogeneity of concrete, the crack could propagate into several branches, and more energy is needed to form new crack branches. These are examples of the inelastic toughening mechanisms that appear around a concrete crack tip when it propagates. The presence of these mechanisms generally deters the application of LEFM principles to concrete structures. The influence of all of these mechanisms in combination is taken into account by the conceptual Fracture Process Zone (*FPZ*). In order to apply the concepts of fracture mechanics to concrete, it is important to understand and determine the nature of this *FPZ*, especially its size and how it changes with the propagation of a crack.

The application of the principles of fracture mechanics to concrete by Neville in 1959 was followed by Kaplan (1961) who worked on crack propagation. Since the publication of Kaplan's work, many attempts have been made to apply fracture mechanics to concrete. Initially, concrete research was associated with LEFM; however, Kesler et al. (1971) indicated that the LEFM approach could not be applied to concrete. Shah and McGarry (1971) also realized that, due to the presence of the sizable *FPZ*, LEFM cannot be directly applied to concrete. Therefore, nonlinear fracture mechanics models were developed, and thousands of papers have been published on this topic. A comprehensive review of the related problems was published by Mindess et al. (1983).

As the discipline of fracture mechanics developed over the course of the nineteenth century, and continues to develop, it became clear that the correct analysis and design of many concrete structures must include the ideas of fracture mechanics.

2.9 Fracture Mechanisms and Structural Design

A healthy structure is a structure that is designed properly to resist various modes of failure, such as elastic instability, large elastic deformation, yielding (plastic deformation), necking (tensile instability), and fracture (Saouma, 2003).

Concrete design has already witnessed two revolutions. The first, which made the technology of concrete structures possible, was the development of the elastic no-tension analysis during 1900-1930. The second revolution, based on a theory considered essential during the 1930's, was due to the introduction of plastic limit analysis during 1940-1970. There are now good reasons to believe that the introduction of fracture mechanics to the design of concrete structures might be the third revolution. The theory, formulated primarily after 1980, finally appears to be ripe (Bazant, 1992).

The question of the applicability of the classical strength theories to concrete was explored long ago, beginning with Kaplan (1961) and others, but the answer was negative (e.g. Kesler et al., 1972). Since engineers cannot be totally sure that concrete is flaw-free, it is common practice to assume that a flaw of some size will be present. In addition, the maximum stress depends not only on the properties of the materials, but also on the

structural geometry and boundary conditions. The strength failure criterion in terms of nominal stress is not always appropriate and can result in un-conservative designs. Furthermore, when defects do exist in a structure, the conventional strength-based design approaches consider the influence of these defects by introducing a *stress concentration factor* (K_t), which depends on the geometry of the hole; with the conventional approach, K_t reaches infinity for a sharp crack. As was noted previously, the behaviour of concrete cannot be described or predicted according to classical ideas about the strength of materials or LEFM. This is mainly due to one or more of the following reasons: (1) The *FPZ* is assumed to be small compared to the size of the structure. This is not the case for concrete, where this zone may be more than 100 mm long at maximum load. (2) The stress within the *FPZ* is assumed to increase or to remain constant as the load increases. This is also not true for concrete, where the stress within this zone decreases as the load increases. (3) Conventional fracture mechanics only deals with what happens to an already existing crack. For practical application to concrete, it is essential that the formation of a crack can also be analysed (Hilleborg, 1976).

When finite element analysis (FEA) was used to model cracking behaviour (including the strain-softening response), it was found that use of a strength criterion for failure yields results that are not realistic with respect to the size of the FE mesh used (Bazant et al. 1980). In a concrete structure, elastic and inelastic energy in the *FPZ* should be considered. Accordingly two energy criteria are usually needed to completely describe the failure of this type of structure. The energy criteria for the fracture mechanics of structures provides the level of control that is necessary for a numerical

approach that assures stable and convergent solutions, which can be established using the principles of nonlinear fracture mechanics. Therefore, from a numerical modeling standpoint, the need for a fracture mechanics approach is mandatory for applications to concrete structures (Shah et al., 1995).

Most of the design procedures currently in use are based on concepts about the strength of materials where the assumption of continuity applies. However, the singularity of the stress concentrations (present at the crack tips, notches, and within connections, etc.) requires the use of more sophisticated design procedures. Unfortunately, despite a great deal of research, design concepts based on fracture mechanics are seldom used in the design of concrete structures, particularly in North America. For instance, they are not even mentioned in the current ACI 318 Building Code Requirements for Structural Concrete or in the Canadian CSA Standard A23.3 Design of Concrete Structures (Mindess, 2002). If fracture mechanics is considered, the designer can determine the relative importance of various parameters (e.g. stress, materials toughness and flaw size) during the design stage, rather than during failure analysis.

The ACI Committee 446.1 R-91 listed five important reasons for using the fracture mechanics approach for the design of concrete structures, which are:

- Energy required for crack formation: the actual formation of cracks requires a certain energy, which can be studied based on energy criterion while strength criterion can be used for crack initiation only;

- Objectivity of calculations: numerical calculation and modeling precede experimental verification; accordingly, a theory found to be unrealistic or lacking in objectivity must be rejected. For example, the results from the smeared cracking model showed dependency on mesh size. To obtain reliable results that are independent of element size, consideration of the energy dissipated through cracking is required;
- Lack of a yield plateau: in quasi-brittle materials, which exhibit softening behaviour where the failure process does not result in the formation of plastic hinges, but takes place due to the propagation of a fracture zone throughout the structure;
- Energy absorption capability and ductility: the area under a load displacement curve for a structure loaded to failure represents the energy consumed during the failure process. For quasi-brittle material, the post-peak response represents the absorbed energy and determines the ductility of the structure, which cannot be determined using limit state analysis since this approach does not consider tension softening;
- Size effect: describes the decrease in stress at failure with increasing member size. This effect is directly attributable to the fact that fracture is governed by fracture parameters that depend on the dimensions of the crack, which are related to structure size and some measure of stress. The size effect represents the dependence of stress on the structure's size; this effect can be predicted using fracture mechanics, but not by the use of concepts based on strength criteria.

2.10 Modeling Concrete Fracture Behaviour

When a crack propagates in any material, a concentration of strain appears ahead of the crack tip, extending the FPZ. For plastic materials, the nonlinear zone is dominated mainly by plastic deformation until failure; however, for quasi-brittle materials such as concrete, only a small amount of plastic strain can be sustained before failure. As was mentioned previously, the nonlinear zone of concrete consists of a narrow band of damaged material with micro cracks and zones bridged by aggregates; therefore, LEFM is unsuitable for analysing the behaviour of concrete structures. The current state-of-the-art in fracture mechanics includes a wide variety of models to simulate concrete behaviour. The Dugdale and Barenblatt concept was used by Hillerborg (1976), who proposed the fictitious or cohesive crack model (FCM or CCM) for quasi-brittle materials such as concrete. In this model, it is assumed that prior to crack initiation, the material exhibits linear elastic behaviour. After crack initiation, stresses may be transmitted across the crack; hence, the crack is termed a “fictitious crack”. The crack-bridging stresses are taken to be a function of the crack opening, and are given by the stress-crack opening (σ - w) relationship. In this model a narrow band of partially broken material is idealized as a crack, a line in two dimensions or a surface in three dimensions. The *softening curve* (σ - w) is assumed to be a material property that is independent of structural geometry and size. The FCM assumes that the initial crack propagates when the principal tensile stress reaches the tensile strength of the material, f_t . The σ - w curve can be completely determined if f_t and G_F are known, and the shape of the curve (σ - w) is defined in advance (e.g. linear, bi-linear, trilinear, or exponential, etc.). The parameters, f_t and G_F , can be

combined into a property termed characteristic length, $l_{ch} = EG_f / f_t^2$. Based on the FCM, l_{ch} is a material property, which is proportional to the length of the *FPZ*. Bazant and Oh (1983) proposed the Crack Band Model (CBM) to model the *FPZ* in a band of uniformly and continuously distributed micro-cracks with a fixed width where a stable crack propagates. This width was estimated as three times the maximum aggregate size for concrete.

Experimental techniques to estimate the σ - w curve have been reported in the literature. The uniaxial direct tension test (UTT), which is believed to give the best estimate of concrete softening and f_t , is not commonly used due to difficulties in performing a stable and representative test (Hordijk, 1989). Instead, several indirect methods have been developed. These methods yield a load-deformation curve, from which the σ - w relationship may be generated using a proper inverse analysis. Many approaches for obtaining concrete fracture properties using inverse analysis have been developed and reported (Skoček and Stang, 2008). These approaches can be divided into two main categories: The first group involves inverse analyses that determine the following point of the already defined one on the *softening curve* by minimizing the discrepancy between the computed value at the following point and the corresponding experimental measurement on the load-displacement curve. The poly-linear method introduced by Kitsutaka et al. (1997) is an example of the approach used by the studies in this group; the poly-linear method involves a step-by-step extension of the *softening curve* as the following point on the curve is obtained by minimization of the difference between the computed and the measured load corresponding to the crack opening

investigated. In general, the main advantage of this method is that no assumptions need to be made in advance of modeling or testing, such as assuming the shape of the softening curve. However, the *softening curve* determined in this way is influenced by accumulative errors; therefore, the value of the calculated load is a function of all the previously determined points on the *softening curve*. In addition, the f_i and the initial part of the *softening curve* may not be determined accurately (Uchida and Barr, 1998 and Planas et al. 1999). The second category includes approaches that determine the fracture parameters by describing the *softening curve*; its shape is assumed in advance of modeling or testing. Within this group of studies, two approaches have been reported in the literature: one requires some material parameters to be known in advance, while the other approach is capable of predicting all of the parameters from the data obtained in a single experiment. In this case, the type of softening curve has to be defined in advance (i.e., as linear, bi-linear, tri-linear, exponential, etc.). However, the bi-linear softening curve is usually used to approximate the softening behaviour of cementation materials, and seems to provide sufficiently accurate results for a wide range of materials, including concrete, fibre-reinforced concrete, cement mortar or rock; therefore, the bi-linear softening curve is widely used (Skocek 2008). A global optimization process is conducted involving several measured points. This optimization procedure can be performed by determining all of the variables at once; however, a sequence of sub-optimizations that determine selected variables one after another is more robust due to the lower risk of reaching local minima. This approach requires knowledge of some of the concrete parameters, such as f_i . Østergaard (2003) applied this technique, and the parameters that can describe the power softening law were determined.

The fracture behaviour of concrete was estimated by many researchers using inverse analysis and the FCM. Olesen (2001) developed a nonlinear cracked hinge model (CHM) for a three point bending beam (based on the concepts of fracture mechanics for the FCM) similar to that of Ulfkjær et al. (1995). The conceptual basis of the hinge model is to consider the crack as a local discontinuity in the overall stress and strain field, which disappears outside of a specific band width. Cracking is assumed to be confined to this band, while the rest of the structure is modelled using an appropriate elastic model. The simplified nature of the CHM allows an efficient method to evaluate analytically the load-crack opening displacement (P-COD) curve. The advantage of this model is related to its ability to provide a closed-form analytical solution for the crack opening displacement (COD) for a given load on the hinge. In order to apply the CHM, in addition to information about the shapes of the σ - w and P-COD relationships, concrete material properties, such as f_t and E , are required. These can be estimated from the experimental results obtained from testing concrete samples (More details about the CHM are given in chapter four). Olesen (2001) chose the bi-linear σ - w curve to model crack propagation in a fibre-reinforced beam. The analysis of the crack propagation through the elastic layer was conducted without considering the overall behaviour of the beam. The elastic layer was regarded as a nonlinear hinge for which the solution could be expressed in terms of the overall hinge deformation. Olesen's study was not restricted to the case of a bilinear σ - w opening relationship, but also covered the multi-linear case. Closed-form solutions were presented for the moment-rotation relationship of the hinge as a crack propagated. The hinge solution was also developed using two special shapes (i.e., drop-linear and drop-horizontal) for the stress-crack opening relationship; these

were treated separately, and based on the aforementioned model, CHM, an approximate solution was developed. The applicability of the hinge model was illustrated through analysis of the bending fracture process in the case of a three-point bending beam and an infinitely long beam on a Winkler foundation, with the latter analysis comprising the effect of a constant tensile normal force. Oleson's analysis revealed a deficiency of the hinge model; it does not have a distinct unloading branch that models the closure of an open crack.

Østergaard (2003) determined the σ - w curve for early age and mature high strength concrete. The wedge splitting test (WST) was chosen to produce the crack mouth opening displacement (P-CMOD) curve; by developing a new inverse analysis algorithm utilizing the nonlinear CHM based on the FCM, the σ - w curve was determined. This analytical model was used to describe concrete fracture behaviour, and the results were confirmed with FEA. The author found that G_F increased with age, and was accompanied by increased f_t and E , but the ductility of the concrete (in terms of l_{ch}) was found to decrease. The researchers also found that the analytical hinge model and the FEA were closely correlated. Furthermore, splitting tensile strength (f_{sp}) was determined using the split cylinder test (SCT); it was found that $f_t \cong (0.7-0.8) f_{sp}$ for mature concrete, but the test was not well suited for early age concrete. Therefore, these authors recommended using other test methods.

Østergaard et al. (2004) demonstrated that the non-linear CHM developed by Olesen (2001) could be applied to the WST. Their investigation showed that this model

was well suited for the interpretation of the WST results (represented by the P-w curve) in terms of the σ -w relationship. The authors found that the WST and the hinge model formed a solid basis for inverse analysis. They also found that there was good agreement between the hinge model and the FEA. To verify the precision of the 2D model, a 3D model was created; the authors claimed that the differences were minor, and concluded that the 2D FEA was sufficiently accurate. Østergaard et al. (2004) stated that the FEA produced a lower CMOD for a given crack depth, which they attributed to differences in the stress distribution for the hinge model compared to the FEA, and to the fact that the hinge element has no shear stiffness.

Skocek and Stang (2008) investigated the performance of the inverse analysis algorithm proposed by Østergaard (2003) when increasing the number of segments in the multi-linear softening curve. They showed that the algorithm was strong enough to be able to determine the parameters of softening curves consisting of up to four segments. When the simulations for poly-linear, bi-linear, tri-linear, and quad-linear softening curves were compared, the authors found that the most widely used bi-linear softening curve could be replaced by the tri-linear curve, or even the quad-linear curve, with the advantage of decreasing the total discrepancy between the experimental and the simulated results. Skocek and Stang (2008) claimed that the problem with local minima occurred, and the algorithm was not able to reach the convergence criteria when a multi-linear softening curve with 5 lines was chosen. In addition, this study investigated the sensitivity of the inverse analysis to the initial softening estimations for two variables. First, the shapes of the initial softening curves were changed, and then the initial values

of the uniaxial tensile strength and of the critical COD were changed for a given shape. The inverse analysis was found to be much more sensitive to the initial values of the uniaxial tensile strength and the critical COD. In addition, the initial shape of the softening curve did not play an important role if the initial approximations for uniaxial tensile strength and critical crack opening were valid. The authors concluded that the WST is capable of providing measures of both elastic and fracture properties with high reliability, and that the hinge model is a useful tool for simulation requiring only minimal computational costs. In order to verify the results obtained, the authors simulated the WST using the FE software application, DIANA. The results obtained from the hinge model-based inverse analysis were used as the material input for the FE simulation. The data predicted by the FE simulation compared favourably with the data measured experimentally.

2.11 Simulation of Concrete Structural Damage and Cracking

Early FEA models did not take fracture mechanics into account, yet proved satisfactory. It is possible that the published studies included only the problems with the most successful outcomes, while poor results related to the fracture sensitivity of the modelled structures were not reported (ACI 446.3R-97). Nevertheless, almost all concrete structures have cracks and flaws, and some of these structures are fracture sensitive; therefore, in some cases it will be necessary to use a reliable and accurate fracture model for the FEA. Accordingly, the modelling of damage and cracks in concrete structures has been the subject of very intense research scrutiny in structural

engineering (Choi and Shah, 1998). In addition, understanding the fracture behaviour of concrete structures is important for structural analysis under loading conditions. The classical strength-based mechanics of materials approach has proven to be inadequate for handling severe discontinuities, such as cracks. Furthermore, it is necessary to model existing damage in a structure prior to the application of any strengthening and rehabilitation systems, in order to predict its fracture behaviour and ensure the appropriateness of planned reinforcements.

The mechanical behaviour of structures made from cementation materials has been successfully modeled using non-linear fracture mechanics in recent decades. For example, the nonlinear elastic models and plasticity-based models were employed by De Borst (1987). The FEA technique is a powerful tool for structural analysis, but requires the use of advanced material modelling methods, such as fracture mechanics, to simulate true cracking behaviour. Plain and reinforced concrete structures have been extensively analysed using this approach. A great deal of research on the numerical modelling of concrete cracking behaviour has been conducted in recent decades. As a result, many concrete crack propagation models have been developed and applied in concrete cracking analyses (Cai and Robberts, 2006).

Hillerborg et al. (1976) proposed a method of combining fracture mechanics and FEA of the formation and propagation of a crack by assuming that the concrete is linear-elastic until f_i reached. The crack was assumed to propagate when the stress at the crack tip reaches f_i . It was also assumed that when the crack opens, the stress will not

immediately fall to zero, but will decrease linearly with increasing crack width, w . Moreover, FEA was used to determine the energy release rate in an energy balance approach to the problem. The authors claimed that this approach enabled them to use a coarse mesh since no stress singularity was experienced and the amount of absorbed energy was not very sensitive to the mesh size. Furthermore, the study examined an unreinforced concrete beam with a rectangular cross-section loaded by a pure bending moment. The tensile stress reached f_t at the bottom fibre of any specific bending moment (i.e., M_0). Since the authors assumed that concrete cannot take higher tensile stresses than f_t , the crack started to open at the extreme bottom point, while M increased above M_0 . By proceeding in this way, a relationship between the crack depth and the applied moment was found. With continuous loading, at the point that the crack propagates, the corresponding bending moment reaches a maximum value (M_{max}), and then starts decreasing. The authors found that the behaviour of the beam depends on the h/l_{ch} ratio (Hillerborg et al., 1976), where h represents the depth of the beam and l_{ch} represents the *characteristic length* (ACI 446.3R-97).

Researchers have investigated different simulation methods for modelling cracking and damage in concrete structures. Three major modelling techniques were proposed: the discrete crack method, the smeared crack method, and the element-free Galerkin (EFG) method. However, it was found that all of these methods work well under specific, limited conditions.

The discrete crack model treats a crack as a geometrical entity. In this model, the crack is considered as a discrete gap along the inter-element boundary that involves additional nodes, and so influences element connectivity and the stiffness matrix. Cracking is assumed to occur as soon as the stress at nodes normally at the element boundaries exceeds the maximum tensile stress that can be sustained. New degrees of freedom at these node locations are created, and a geometrical discontinuity is assumed to occur between the old node and the newly created node (De Borst, 1987). Clough (1962) was the first to apply FEA to the cracking of concrete structures, followed by the research of Scordelis, Nilso and Ngo (1967-1968). Ngo and Scordelis modeled a discrete crack, but did not address the problem of crack propagation. Had they done so, they would have found many problems with their model, starting with the fact that the stresses at the tips of cracks increase as the element size is reduced, so no convergence (of crack tip stresses) would have been obtained for a satisfactory solution. Nilson (1967) was the first to use FEA to represent the propagation of discrete cracks in concrete structures, using a strength-based criterion. At an early stage in the application of FEA to concrete structures (Rashid 1968), it became clear that it is often much more convenient to represent cracks by changing the constitutive properties within the finite element model than by changing the structure of the finite element grid. The earliest procedure involved dropping the material stiffness to zero in the direction of the principal tensile stress. Once the stress was calculated to exceed the tensile capacity of the concrete, the stresses were simultaneously released and re-applied to the structure as residual stress (ACI 446.3R-97). After Hillerborg et al. (1976) found that a crack in concrete has a gradual softening region of significant length at its tip, and realized that it is inaccurate to model cracks by

applying LEFM, the development and application of FEA of NLFM to a discrete fracture was introduced by Goodman et al. (1968). Cohesive stress may develop within the *FPZ* of inelastic material. These traction responses are generally thought of as nonlinear functions of the relative displacements between the two sides of the crack. The capability of FEA to compute stress intensity factors was demonstrated, and the linear elastic model of crack propagation was used to apply the principles of fracture mechanics. This technique was applied to concrete by Ingraffea (1977), who continued investigating this approach with his coworkers (Ingraffea and Manu, 1980; Saouma, 1981; Gerstle, 1982; 1986; Wawrzynek and Ingraffea, 1986; and Swenson and Ingraffea, 1988). A predefined crack path is sometimes required to describe the orientation of the crack planes (Cai, Robberts, 2006); however, when the crack path is known in advance, discrete cracks are usually modeled by altering the mesh to accommodate the propagating cracks and the boundaries along the newly created cracks. Re-meshing techniques for discrete crack models were developed by Ingraffea and Saouma (1985) and Carter et al. (1995) using a LEFM technique; the algorithm requires the knowledge of crack direction, then the formation of a new mesh in which the crack has propagated over a specific distance. Since the maximum stress at the crack tip depends on element size, the results were mesh-dependent, and consequently the algorithm was not an objective depiction of an actual crack. In 1991, Swenson and Ingraffea demonstrated that unstable cracking in reinforced piers caused the sudden collapse of New York's Schoharie Creek Bridge during a flood in 1987. They adopted a discrete crack model, and included linear and NLFM to evaluate the initiation, stability, and propagation profile of the crack that caused the failure. Shi et al. (2001) extended the discrete crack model to the numerical

analysis of multiple cracks in an actual-size tunnel specimen. The discrete crack model offers the advantage of tracing each individual crack; however, as mentioned previously, the model may require substantial re-meshing to accommodate arbitrary crack geometry and to incorporate the boundaries along newly created cracks. Re-meshing is usually time-consuming, even with the use of modern fast computers. In addition, the details of the crack pattern and crack propagation in this model are rather vague and imprecise because of the arbitrary nature of the crack orientation along the element boundaries (Yang et al., 2008). Although the fictitious crack model was utilized in the development of FEA of nonlinear discrete fracture, this approach was inadequate for modeling realistic concrete behavior in the *FPZ* in some situations. In these cases, the smeared crack model is an alternative (ACI 446.3R-97).

In the smeared crack model, the fracture is represented in a smeared manner; an infinite number of parallel cracks of infinitely small openings are distributed (smeared) over the finite element (Bazant et al. 1988). In this approach, the cracking process is grouped into integration points within the elements, where the stress-strain relationship is modified to account for the stiffness and strength degradation that accompanies cracking (De Borst, 1987). The smeared crack mode gained a great deal of popularity in the 1970s, when comprehensive efforts were devoted to developing constitutive models in a smeared setting, which could reproduce the experimental results for the stress-strain characteristics of concrete. With respect to cracking, the two main modifications introduced with this approach were the shear retention factor (Suidan and Schnorich, 1973) and the replacement of the sudden stress drop due to crack initiation with a

descending branch in the tensile stress-strain relationship to represent the contribution of the stiffness between the cracks of reinforced concrete (tension-stiffening). Cope et al. (1980) recognized that the introduction of a shear retention factor causes the principal stresses at a cracked integration point to rotate upon further loading. In 1987, De Brost studied the modeling of non-orthogonal cracks using the smeared crack model, and showed that the model obeys the principle of material frame-indifference and included some conclusions about possible stress-strain laws within a smeared crack. The instability due to the appearance of spurious kinematic modes was observed by Rots (1988). The cracks are usually modelled within a fixed finite element mesh. Their propagation is simulated by the reduction of the stiffness and strength of the material. The constitutive laws, defined by stress–strain functions, are nonlinear and show a decrease in stress under increasing deformation (strain softening), which takes place within a narrow zone in the specimen (*FPZ*). This approach was pioneered with fixed crack orthotropic secant models and rotating crack models. FEA of cracking in concrete using a smeared crack model was presented by Valente (2003) using a crack band model to analyse, statically and dynamically, the collapsed baroque Noto Cathedral in Italy. Dabbagh and Foster (2006) developed the cracked membrane model using a smeared crack model for the FEA of orthogonally reinforced structural elements under plane stress.

The investigation of crack widths is difficult using the smeared crack model. In addition, due to the relationship between element size and crack band width, this approach may show mesh dependency. Furthermore, this approach involves non-continuous modeling of the crack path, which detracts from the application of this model

when localized crack growth is required; however, remeshing has been used as an adjustment tool for modeling crack growth (Bouchard, et al. 2000, 2002, Patzák and Jirásek 2004). Nevertheless, remeshing requires the projection of variables to different meshes. Consequently, some objections have been raised against the smeared crack model. The main concern is that this modeling approach inherently introduces mesh sensitivity into the solutions, in the sense that the FEA results do not converge to a unique result. For example, since cracking is associated with strain softening, mesh refinement will lead to narrower crack bands (Sluys and Borst, 1992). Accordingly, a continuous non-mesh sensitive model is required.

A coupled damage-plasticity continuum model for concrete based on thermodynamic principles is implemented by the ABAQUS (Dassault Systèmes Simulia Corp.) application. This model is based on the proposals of Lubliner et al. (1989) and Lee and Fenves (1998). The coupled damage-plasticity model includes the constitutive relations for the elastic-plastic response coupled with the stiffness degradation response, which makes the model attractive for effective numerical implementation. This model requires a definition of cohesion in the yield criteria, and utilizes the Lubliner yield criterion that has been adopted by many investigators and the commercial FE program, ABAQUS. This criterion has achieved great success, especially in the modelling of plane stress states. The concrete damaged-plasticity model is primarily intended to provide general capability for the analysis of concrete structures under cyclic and/or dynamic loading. The model is also suitable for the analysis of quasi-brittle materials, such as rock, mortar and ceramics. Under low confining pressures, concrete behaves in a brittle

manner where the main failure mechanisms are cracking from tension and crushing from compression. The brittle behavior of concrete disappears when the confining pressure is sufficiently high to prevent crack propagation. In these circumstances, failure is driven by the consolidation and collapse of the concrete microporous microstructure, leading to a macroscopic response that resembles that of ductile material with work hardening (ABAQUS documentation). This constitutive theory aims to capture the effects of irreversible damage associated with the failure mechanisms that occur in concrete and other quasi-brittle materials under fairly low confining pressures. These effects manifest as the following macroscopic properties: different yield strengths for tension and compression, with the initial yield stress for compression being a factor of 10 or more higher than the initial yield stress for tension; softening behavior for tension as opposed to initial hardening followed by softening for compression; different degradation characteristics of the elastic stiffness for tension and compression; stiffness recovery effects during cyclic loading.

The Element-Free Galerkin Method (EFG) method, which has the ability to deal with arbitrary geometry, was developed by Belytschko et al. (1994). The main advantage of this method is that it requires only nodal data, and no information about element structure is necessary. The principle underlying this method is to derive equivalent shape functions using least-square approximations, which move along a given/fixed number of nodes. These shape functions are then used to construct a weak formulation of the force balance and other equations in a similar manner to conventional FEA. These approximations require a lot of computational effort, especially in the approximation of

interface regions, loading boundaries and crack zones (Sukumar, 1997). The major disadvantage of the EFG method is that the essential boundary conditions cannot be applied directly. Instead, modified variation forms or multiplier methods are used to implement these essential boundary conditions. Although the EFG method seems quite promising, most of the existing studies that used the EFG method have focused on the propagation of a single crack or a few major cracks in a brittle material, so can model crack growth. However, due to major differences from standard FEA, the EFG method cannot be directly implemented with existing FEA code.

There is no general rule for choosing the most appropriate method for a given crack simulation, and this is particularly true in the situation of reinforced concrete structures. De Borst (1997) reviewed some of the most important aspects of numerical modelling of cracking in concrete using discrete crack models, smeared representations and lattice models. Yang et al. (2005) carried out a comparison study by implementing the three major numerical methods for the simulation of crack formation in a concrete beam. Accordingly, the nonlinear modeling approach showed that the smeared crack model gave the best results for a limited number of cracks (less than 40) and when the number of elements was less than 2000, while the discrete element model gave the best results for multiple cracks (up to 100). For a moderately large number of elements with arbitrary geometry, the element-free Galerkin model seems to be superior. The advantage of this method lies in its simplicity and cost-effectiveness, since the topology of the FE mesh remains unchanged and no restrictions are imposed on the orientation of the crack. However, the tendency to produce diffused crack patterns, along with the directional bias

and stress-locking that can develop, are the main disadvantages of this approach. Another comparison study was conducted by Yang et al. (2008) to highlight the strengths and weaknesses of the various methods. This comparison focused on four main issues: computational time and efficiency for a given simulation; the robustness of each method; the ability to trace cracks; and flexibility for dealing with external and internal reinforcement. The simulations showed that the smeared crack model was computationally very efficient, but was unable to deal directly with crack propagation, especially in the case of multiple crossover cracks. Furthermore, the interpretation of crack width was difficult, and often showed mesh dependency. The authors found that the discrete crack model could trace the crack geometry, but required re-meshing and thus, the computation time was usually greater than that required for the smeared crack model. This study found that the EFG method had the ability to deal with internal and external reinforcement, different reinforcement bond conditions, arbitrary beam geometry, tracing of individual cracks, and most importantly, was more efficient than the other two methods. This comprehensive comparison also showed that in the analysis of the flexural behaviour of reinforced concrete beams where the number of cracks is limited, all three methods gave a good indication of the crack pattern. However, the smeared crack model was moderately faster than the discrete crack model, while the EFG model was superior to the other two methods and found to be 60–80 times faster than the discrete crack method at obtaining the solution for a given number of nodes. The capability of each method to deal with individual cracks, and the implications for simulating CFRP-strengthened concrete structures was also studied by these researchers (Yang et al.2008).

This comparison provided insight into the strengthening behaviour of a beam with dapped ends, and helped to facilitate the choice of appropriate numerical tools for the design and analysis of such structures. Researchers used a series of small line segments in the model to provide an indication of the crack location and orientation, which were then applied to the smeared crack model. For the discrete crack model, the authors used actual crack boundaries to display the actual crack shape and orientation, and then applied these to the model. Both of these representations of the crack were used as inputs for the EFA, depending on the circumstances of the simulation.

Although the deformation response is important for analyses of reinforced concrete structures under loading, prediction of crack formation and propagation is required for the purposes of analysis, structure monitoring and integrity assessment. Therefore, the chosen concrete cracking model must be able to identify the location of crack initiation, and model the localization and propagation of the crack, including its width along the crack path, up to failure; furthermore, the model's outcomes should be independent of mesh size. In the application of FEA to model cracking behaviour, including the strain-softening response, the use of a strength criterion for failure yields results that are inadequate depending on the size of the FE mesh used (Bazant et al., 1980). Many of the problems related to the service state and strength state design may be addressed by using energy criteria based on fracture mechanics. For studies conducted on crack growth analysis and remaining life prediction using LEFM principles, a difference of 12% was found between predicted results and experimental observations. This difference in predicted and actual results can be attributed to lack of consideration of the

tension-softening effect in the analysis. Therefore, in order to produce reliable and valid predictions, the softening effect should be considered in the analysis using NLFM principles (Murthy et al., 2006). Accordingly, the energy criteria of fracture mechanics provide the level of control necessary to assure stable and convergent solutions.

2.12 Experimental Techniques for Concrete Fracture Characterization

The common test methods used to investigate the failure of concrete, before the concepts of fracture mechanics were introduced to the analysis of concrete structures, were compression or splitting tests of cylinders or cubes or bending tests of beams. These tests were sufficient for strength of materials analyses; however, since the assumptions made with respect to stress distribution in the specimen are violated in the case of concrete (because of the inhomogeneity and the nonlinearity of concrete), none of these tests can really characterize the failure mechanisms or fracture properties of concrete.

2.12.1 Experimental Determination of Concrete Fracture Parameters

Concrete structures can sustain high compressive load, but are not made to carry tension. The tensile cracking of concrete limits the efficiency of several types of concrete structures. Therefore, the formulation of the behaviour of concrete under tension is needed. Concrete tensile strength (f_t ; described in Section 2.2) is employed as a parameter indicating crack initiation. Cracking in concrete occurs when the maximum principle stress at any point is equal to f_t at the same point and in the same direction. The necessity

of using a standard method for the determination of concrete f_t was indicated by Malhotra in 1970; however, Chen (1970) stated that the f_t of concrete is usually determined from indirect tests, such as splitting cylinder tests (SCT) or flexural tests on beams, rather than from a direct tension test. In order to apply the concepts of fracture mechanics to concrete structures, it is necessary to find an experimental technique for the determination of the fracture properties of concrete, just as there are experimental methods for the determination of strength. The ACI report (Committee 224, 1986) indicated that direct tension and indirect tension test methods can be used to determine the f_t of plain concrete. Due to difficulties in performing a stable and representative direct tensile test on a plain concrete specimen, no standard test was recommended; i.e., the UTT may be the most straightforward approach to estimating the f_t of concrete material. Winter and Nilson (1991) stated that these difficulties are caused by minor misalignments and the stress concentration at the gripping devices. Østergaard (2003) noted that the difficulties are due to problems with the self-weight of the specimen in the upright position while a specimen that is laid down horizontally is influenced by friction against the sub-base. The difficulties associated with direct tensile test were also mentioned by Neville, Wang and Salmon (year), who stated that neither the SCT nor the modulus of rupture is the proper test to determine the f_t of concrete.

Van Mier (1995) stated that differences in the rotational freedom of the loading platen led to different crack growth processes. He also claimed that when the platens can rotate freely, a single crack-zone crosses the specimen from one side to the other, whereas for a specimen tested between fixed platens, two interacting cracks develop from

two sides of the specimen. The crack growth process under fixed loading platens typically leads to a bump in the descending branch. Van Mier concluded that, from an experimental point of view, size and boundary condition effects have deep consequences for the softening diagram. Furthermore, the UTT can be considered a reliable method for assessing f_t when the stresses are uniformly distributed over the cross-section of the specimen during the entire test, and when the specimen's geometry has no effect on the obtained $\sigma-w$ curves needed to accurately derive material properties. Unfortunately, the most elaborate UTT cannot exclude all of the effects of geometry due to particular test set-ups. Therefore, the $\sigma-w$ curve obtained from UTT is always affected by a combination of material and structural properties. Although adjustments proposed by Akita et al. (2003) to control specimen rotation may provide the most uniform deformation distribution over the cross-section of the specimen, it is not fully clear how these adjustments affect crack development. Therefore, the test set-up required for UTT is too elaborate to be recommended for consideration as a standard test (RILEM TC 187-SOC 2007).

It is evident that it is very difficult to conduct a perfect UTT; consequently, several indirect methods have been developed, such as the three point bending test (TPBT), the split cylinder tensile test (SCT), and the wedge splitting (WST) test. These methods are indirect and yield a load-deformation curve from which a proper analysis, the $\sigma-\varepsilon$ relationship may be generated.

A fracture mechanical interpretation of the TPBT, in combination with a method for f_t extraction (by inverse analysis), was suggested by Wittmann, Roelfstra, Mihashi, Huang & Zhang (1987). However, most of the TPBT were performed on relatively small beams of 200 mm depth, but the self-weight compared to the fracture area was large. Therefore, the effect of self-weight on fracture properties must be carefully considered with this test. In addition, since the TPBT-specimen cannot be drilled from an existing structure, it is difficult to use this test for structural integrity assessment. These drawbacks, and the large amount of elastic energy stored in the beam, led to the formation of Subcommittee B within RILEM (International Union of Laboratories and Experts in Construction Materials, Systems, and Structures - TC 89-FMT) with the main task of proposing a testing method as an alternative to the TPBT. Accordingly, a simple “compact” specimen shape, such as a cube, was recommended as an alternative testing method (Figure 2.7).

Another indirect test is the SCT, also known as the Brazilian splitting test, which is widely accepted as a standard test method for assessing the tensile strength of concrete and similar materials. SCT was first described by Carneiro & Barcellos (1949), and is performed by loading a cylindrical specimen along diametrically opposed generators until failure. Timoshenko & Goodier (1970) showed that the diametrical loading of the cylinder induces an almost uniform tensile stress normal to the plane of loading, and the failure load is interpreted as the load at which these tensile stresses reach the uniaxial tensile strength of the material. The tensile strength based on this interpretation is known as the splitting tensile strength. For a perfectly brittle material, the splitting tensile

strength would coincide with the uniaxial tensile strength. However, concrete is not a perfectly brittle material, but is a so-called quasi-brittle material. The load is usually distributed over a small strip, which results in a disturbance of the stress field; this results in the well-known fact that, for normal strength concrete, the splitting tensile strength overestimates the true uniaxial tensile strength. The failure of a split cylinder specimen is characterized by a splitting crack beginning at the center line and propagating towards the loading points. If the material is sufficiently brittle, the splitting will continue until the specimen is divided into two pieces. In this case, the ultimate load is governed by the tensile strength as well as the tension softening behaviour of the material. However, if the material is not sufficiently brittle, the splitting process will not be completed before a compressive crushing/sliding failure develops, which then governs the ultimate load. Concrete failing during compression may be modelled as a rigid-plastic material with a Mohr-Coulomb friction yield criterion (Nielsen 1999*b*). Upper-bound solutions exist for the rigid-plastic failure of the split cylinder test. These solutions are characterized by the formation of wedge-like regions under the loading strips, which simultaneously split the rest of the specimen.

The wedge-splitting test (WST) is another test suitable for assessing the fracture of concrete, which is similar to the compact tension test used for metals. The WST was utilized for investigations of concrete by Hillemier and Hilsdorf (1977); the final shape of the test specimen is shown in Figure 2.7 (b). The specimen is characterized by a starter notch and groove, which can be either moulded or sawn. Linsbauer and Tschegg (1986) proposed the WST specimen's geometry, which was originally designed for the

determination of the G_F . The test was subsequently improved by Bruhwiler (1988) and Bruhwiler and Wittmann (1989), who conducted over 300 tests on normal concrete, dam concrete and other cementations material at the Swiss Federal Institute of Technology. Very large wedge splitting specimens, with sizes up to 1.5 m, were tested by Saouma, Broz, Bruhwiler and Boggs (1989) at the University of Colorado to study the size effect in concrete dams. The WST was adopted by RILEM as a stable fracture mechanics test for concrete (RILEM TC 89-FMT, 1991). The methodology of this test, which is a special form of the compact tension test shown in Figure 2.7 (a), is to split a small cube with a groove and a starter notch into two pieces while monitoring the load and CMOD without the need for an additional sensor to measure the deflection. This method is indirect, and yields a global P_{sp} - w curve from which a proper analysis the σ - w relationship may be generated.

The simplicity, stability and small dimensions of a WST-specimen make WST a favoured experimental method. In addition, the WST-specimen can easily be prepared under laboratory conditions or cored directly from an existing structure for further assessment. More details about the WST can be found in chapter three of this thesis.

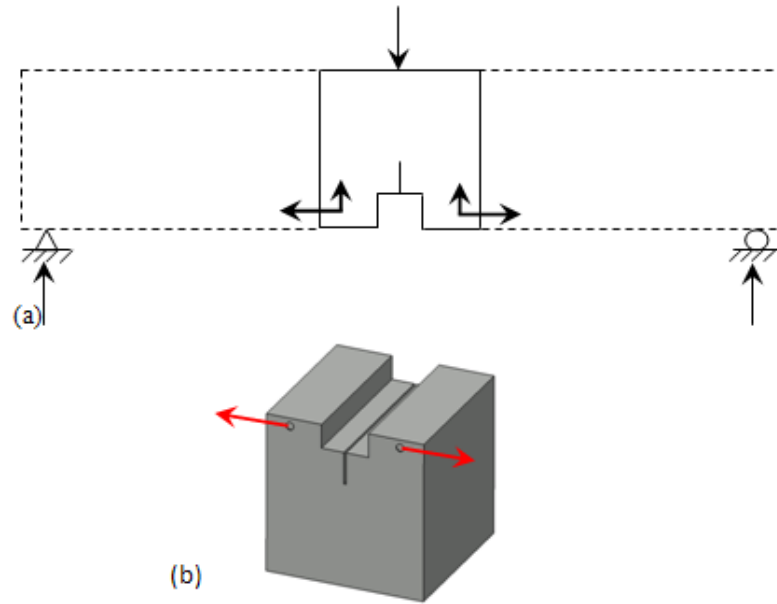


Figure 2.7: (a) The compact three-point-bending test (TPBT), (b) The wedge splitting test (WST)

RILEM TC 89-FMT (1991) obtained the tensile softening diagram from fracture mechanics tests; the experimental P_s -CMOD curves from the WST were numerically analysed using the SOFTFIT program (Roelfstra and Wittmann, 1986). This program is based on the FCM, and was used to determine a bilinear softening diagram from an experimentally obtained P_s -CMOD curve by means of a data fitting procedure, so that the square of the difference between the experimental and the calculated curves were minimized. The fracture test was simulated numerically using an initial specified softening diagram (i.e., bilinear), and then the calculated P_s -CMOD curve was compared to the experimental curve. The parameters of the softening diagram were corrected (i.e., optimized), and the analysis was repeated until there was good agreement between the calculated and the experimental curves. The parameters of the bilinear softening diagram are the f_t , the stress σ_l at the break point (approximately equal to one third of f_t according

to Hillerborg, 1976), the fictitious crack width (w_1) at the break point, and the maximum fictitious crack width (w_2) (Figure 2.8).

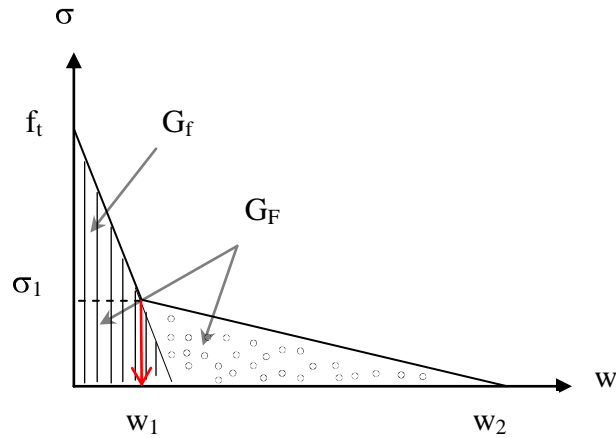


Figure 2.8: The bi-linear softening curve with four parameters

The main characteristics of the CCM or FCM (described in section 2.9), which is generally accepted as the best simple fracture model for concrete, are f_t and also the fracture energies G_F and G_f . G_F represents the area under the entire σ - w curve (Hillerborg et al., 1976) while G_f represents the area under the initial tangent of this curve (Elices and Planas, 1992). Bažant et al. (2003) stated that G_f and G_F are two different material characteristics that are only weakly correlated as $G_F/G_f \cong 2.5$, and should both be used for calibrating the initial slope and the tail of the softening curve of the CCM.

For infinite-size specimens, the cohesive stress at the notch tip under maximum load vanishes; thus, the maximum load is decided by G_F rather than G_f (Bažant and Kazemi, 1991). The predictions of the entire post-peak softening load-deformation curve

of a specimen or structure depend strongly on the tail of the σ - w curve for the CCM, and thus, on G_F . In practice, for normal-size fracture specimens and most concrete structures, the maximum load of notched fracture specimens is determined by G_f since these specimens are not large enough for the cohesive stress at maximum load to be reduced to zero at the notch tip. Various experimental methods for measuring the fracture properties of concrete are described in the literature; according to Bažant et al. (2003), these methods can be classified as *peak load methods*, *peak region methods* and *complete-curve methods*. The first two methods rely on measurements that are taken in the maximum load region; the *peak load* method relies on the application of maximum loads and can only be used to measure G_f , while the *peak region* method needs the application of more than the maximum load to be measured. The *complete-curve* method assesses the complete load-deformation curve, and therefore is used to measure G_F . The *peak load* methods include the Notched-Unnotched method (NUM) described by Guinea et al. (1994), which requires testing a notched fracture specimen and an unnotched specimen (e.g. the SCT), and the Size Effect method (SEM) described by Bazant and Kazemi (1990), which considers a series of geometrically similar structures of different sizes, but with constant initial crack length to beam depth ratios and constant thickness. The Two-Parameter Fracture Model (TPFM) described by Jenq-Shah (1985) is an example of the *peak region methods* that require measurements of the unloading compliance and of the crack-tip opening displacement, δ_{CTOD} . This method is based on the exact solution of the bilinear-CCM; however, since the identification of material fracture parameters from test data involves two random variables, f_t and G_f , statistical regression procedures should be applied. The *complete-curve method*, which measures the entire load-deformation curve

of the specimen, includes the direct tensile test method and the work of fracture method (Hillerborg et al., 1976). The complete-curve method is based on measuring the work done in fracturing the whole ligament of a notched specimen. Hillerborg's work of fracture method, the Jenq-Shah TPFM, and the Bazant and Kazemi SEM were adopted in the RILEM international standard recommendations (RILEM, 1985, 1990a,b); however, in the early-1990s, it was realized that the last two methods (TPFM and SEM) yield a different fracture energy (G_f) than the work-of-fracture method (G_F). In addition, the Jenq-Shah method (TPFM) suffers from a theoretical inconsistency and from being more complex than Guinea et al.'s method (NUM). The disadvantage of the SEM, which is experimentally simple, is that it needs the casting of differently sized specimens; even so, its accuracy in determining G_f is not very high unless large specimens are used. Lastly, the direct tensile test method is associated with many difficulties, but the work-of-fracture method, which gives a clear result for G_F , is well understood as discussed in RILEM (1990) (Bažant et al., 2003).

Brokenshire and Barr (1995) determined the fracture energy, G_F , from a notched TPBT with cylinders subjected to either torsional or flexural loading using a closed-loop machine. The P- δ curves and the torque-rotation (T- ϕ) curves that were obtained were used to determine the G_F of concrete. The G_F was determined from the P- δ curves, (or torque-rotation (T- ϕ) curves in the case of cylinders in torsion), according to the RILEM recommendations. The authors found that the ratio of the G_F values obtained from P- δ and from (P-CMOD) approximately 1.1. Brokenshire and Barr claimed that if all of the results obtained from the P-CMOD curves were scaled up by a factor of 1.125, then the

real G_F values would be obtained. Therefore, they suggested that the P-CMOD curves can be used as an indirect method for evaluating G_F values; they also claimed that the shapes of the *softening curves* obtained from the P- δ and P-CMOD curves are identical.

Xiao et al. (2004) investigated the fracture behaviour of ultra-high strength concrete (UHSC) with and without coarse aggregates for six cubical specimens in the WST. The fracture parameter, such as G_F , and crack opening displacement (COD), were experimentally determined, while the l_{ch} and the fracture toughness (K_I) were estimated numerically where $l_{ch} = G_F.E/f_t^2$ and $K_I = (G_F.E)^{1/2}$. The authors found that the G_F for concrete with crushed basalt coarse aggregates was over 100% higher than that of concrete without coarse aggregates, and the coarse aggregates were more efficient during post-peak than pre-peak behaviour. In addition, the authors claimed that the ductility might be improved by increasing the non-homogeneity of concrete by adding coarse aggregate. This suggestion was a result of their ability to increase the values of l_{ch} and K_I in the UHSC specimens containing coarse aggregate. The ratio of G_f (the area beneath the curve from peak COD to ultimate COD) to total G_F (the area beneath the curve from zero COD to ultimate COD) was found to be 0.6 for UHSC. The authors also demonstrated that although the f_t of UHSC is much higher than that of normal high strength concrete, the G_F decreased while K_I increased in UHSC without coarse aggregates. For UHSC with coarse aggregates, with a maximum diameter of only 5 mm, both the G_F and K_I values were improved compared with normal concrete. The authors simulated the relationships between P_{sp} and COD using FEA - CEB-FIP (Comité Euro-International du Béton (CEB) and the Fédération International de la Précontrainte (FIP)) Model Code. Linear and

bilinear models for closing force versus crack width were suggested for UHSC with and without coarse aggregates. The result was then verified by comparison to experimental findings, and indicated that the bilinear model of the softening curve may be adopted to simulate the fracture behaviour of UHSC with coarse aggregates using the finite element method, whereas the linear model is more suitable for modeling the behaviour of UHSC without coarse aggregates. Furthermore, Xiao et al. (2004) found that the contribution of coarse aggregates markedly improved the COD, l_{ch} , and K of UHSC. Nevertheless, the fracture behaviour of UHSC was not ideal, and depicted great brittleness despite its high compressive strength. The authors recommended that coarse aggregates, even with a small diameter, should be mixed into the UHSC to improve its fracture behaviour, and suggested using fine aggregates as well to enhance confinement and increase non-homogeneity in order to obtain satisfactory ductility behaviour.

Karihaloo et al. (2005) determined that the deterministic size effect on the strength of cracked concrete structures is a result of stress discontinuities introduced by the crack. The strength of three concrete mixes was measured in geometrically similar TPBT and WST (i.e., various initial crack to depth ratios with a constant span to depth ratio of 4 for TPBT). The authors found that the value of the specific fracture energy varies with the size (depth) and the notch to depth ratio, so the specific fracture energy decreased when the initial crack increased and increased when the depth of the beam increased. To consider the boundary effect on the local fracture energy distribution in the *FPZ*, the authors assumed a bilinear energy distribution in the ligament ahead of the pre-existing crack and concluded that, in general, the ligament size for a notched TPBT-

beam or WST-specimen is always larger than the slope of the first segment of the bilinear curve. The inverse analysis procedure of Olesen (2001), which is based on a nonlinear hinge model, was used to identify the bilinear curve parameters. Karihaloo et al. (2005) revisited the published formulation of this model with a view to predict the observed nominal strength of TPBT and WST specimens made from normal and high strength concrete using various geometries. The results were used to predict the nominal strength of the test specimens using the FCM of Hillerborg et al. (1976). The theoretical/computational results were represented by computational studies based on FCM, which used a simple strength size effect formula that took into consideration energy and asymptotic behaviour. The proposed formula had three unknown coefficients that depended only on the size of the crack, and was obtained by testing geometrically similar specimens of different sizes. Three material parameters needed to be measured independently for this formula, namely: E , f_t , and G_F . The comparison of the test results with the theoretical predictions was studied. The proposed formula improved the prediction of the strength size effect. The authors of this study concluded that: (a) it is not possible to test WST-specimens with very small initial crack/specimen depth ratios (smaller than around 0.15) because they tend to fail prematurely at the re-entrant corners, and (b) a nonlinear theory of fracture is essential for structures of small size, but large concrete structures with cracks can be analysed using LEFM theory. Lastly, the authors concluded that a deterministic size effect exists for the strength of cracked concrete structures due to the stress redistribution introduced by the presence of cracks in the *FPZ*, and that this effect becomes stronger as the size of the cracked structure increases, and

weaker as the size of the crack decreases relative to the size of the structure; this was confirmed by theoretical studies based on the FCM.

Zhao et al. (2008) studied the size effect on G_F . The TPBT for a notched beam and wedge splitting tests (WST) were performed on ten different types of concrete with specimens of different sizes and geometry. A data averaging method was used for companion specimens, and the G_F was calculated from the averaged data of the load-CMOD curve obtained for each specimen. The authors found that the G_F increases with increased specimen size, especially in the WSTs, but that asymptotic behaviour for the effect of size is observed in some concretes. In addition, G_F increased with an increase of the maximum aggregate size, but there was no systematic trend associated with the water to binder ratio or with the test method. The authors claimed that 40% of the observed size dependency of G_F was caused by friction between the supports and the specimen, crushing near the supports, energy dissipation in the bulk of the materials near the crack, and the energy represented by the unmeasured tail segment of the load-deflection curve. Additionally, they noted that these experimental errors can be avoided if the WST is used because the vertical load is not applied to the specimen, and so only lateral force acts through the wedge and roller; therefore, the energy dissipation not associated with crack propagation (such as friction with the supports and crushing near the supports) can be minimized. Consequently, the beam test results may include more experimental error compared to the WST results. The researchers concluded that the G_F of concrete depends on the specimen's size, and the observed size effect for G_F can be attributed to the differing shapes of the *FPZ* in accordance with the specimen's size and geometry. Zhao

et al. (2008) indicated a need for more investigation of the size effect on the softening curve in order to identify the mechanisms acting in the *FPZ*, which are still not fully understood.

Cedolin et al. (2008) studied the identification of concrete fracture parameters through indirect methods based on size effect approach and cohesive crack law (CCL) approach with the TPBT. These methods use the size effect curve (structural strength versus structural size) associated with specific specimen geometry to identify f_t and G_f . These two parameters were used to characterize the peak and the initial post-peak slope of the CCL. The authors reviewed two approaches involving polynomial interpolation of numerically calculated structural strengths of geometrically similar specimens of different sizes followed by investigation of the relationship between the two approaches. A new procedure to identify f_t using the SEL was proposed and several sets of experimental results were analyzed with both approaches in order to assess their range of applicability and accuracy in the identification of the two fracture parameters (f_t and G_f). The researchers stated that the classical Bazant's size effect law (SEL) is equivalent to the asymptotic behaviour predicted for large size structures by the cohesive crack model (CCL). Exploiting this equivalence made it possible to establish a unique relationship between the parameters of the SEL and of the CCL, which can be used either to compute f_t from the identified SEL parameters or the equivalent crack extension from the identified CCL parameters. From this relationship, the authors used the SEL not only for the identification of G_f , but also for the identification of f_t . The analysis of the TPBT experimental results showed, however, that the two models are applicable only if the

specimens are characterized by values of D/l_{ch} (where D is the depth of the beam) lying in the range 2–5 (on the CCL scale). For D/l_1 less than 2 (where l_1 is the characteristic length related to the initial fracture energy, G_f , and E , so that $l_1 = EG_f/f_t^2$), the SEL asymptotic behaviour cannot be captured, and the CCL predictions appeared to be unacceptable. Furthermore, when D/l_1 is greater than 5, both models departed from their range of validity because the stress profile in the *FPZ* cannot be predicted accurately by assuming a linear cohesive law. Therefore, Cedolin et al. (2008) concluded that there was no justification for favouring the CCL over the SEL for the identification of G_f and f_t . The SEL appeared to be more appealing because it only requires a linear regression analysis, which can account for the effects of the specimen geometry and boundary conditions automatically.

2.12.2 Experimental Investigations of the FPZ and Crack Evolution

The fracture behaviour of concrete is greatly influenced by the *FPZ*, the zone in which the material undergoes softening damage as described in Chapter 3. Various experimental techniques for measuring the *FPZ* have been described, including surface holographic measurements, dye penetration, acoustic emission (AE), laser holographic interferometry, laser speckle technique, vacuum impregnation technique, scanning electronic microscope, digital image cross-correlation, X-rays, optical fiber technology, scanning computer vision, and CT-scan. These methods vary in their ability to provide detailed measures of the *FPZ* and crack profile under all conditions. For example, in addition to the measurement of the *FPZ*, the crack profile was obtained by the

impregnation technique. However, due to its destructive nature, this technique is unable to provide information about crack evolution during loading of a single specimen. Although the crack tip position can be determined approximately by acoustic emission, the crack profile and its traction free opening cannot be characterized. While optical fiber technology using fiber bragg grating successfully detected the *FPZ*, this technique has some major drawbacks because the fibers are very sensitive to environmental temperatures, vibrations and air drafts (Denarie et al., 2001). Furthermore, strain measurements obtained with this technique can be unreliable because of fiber damage or the presence of an adjacent aggregate, which shields the material from strains. Therefore, the position of the optical fiber needs to be specified before the test, and more than one gauge should be installed as some of them may be positioned outside of the actual *FPZ*. Furthermore, since the fracture pattern of concrete is naturally complicated because of its internal heterogeneity, gauges attached directly to the specimen do not provide accurate data.

The dye penetration technique was developed by Swartz and Go (1984), and modified by Swartz and Refai (1989) who found that the crack length on the notched-beam surface of a TPBT-specimen was greater than within its interior. The same technique was used by Kan and Swartz (1989) to study variation in the thickness of the *FPZ*; they found that the crack length varies with beam thickness. Castro-Montero et al. (1990) studied experimentally surface crack propagation on cementation plate using laser holographic interferometry; the authors found that the crack surfaces were not free from traction since tension was transmitted across the crack. This outcome was observed using

the laser light incident on the plate as the light transmitted through the plate was reflected by the mirror. In 1991, Van Mier used vacuum impregnation techniques to test single-edge-notched concrete plates subjected to uniform boundary displacement. The results revealed that concrete fracturing is a 3D growth process, and that cracking starts at the surfaces of a specimen due to non-uniform drying out and related tensile stress near the specimen's surface. In 1993, Krstulovic-Opara obtained similar results by means of a scanning electron microscope. Similar observations were also reported for other quasi-brittle materials (Sakai et al., 1988; and Homeny and Baughn, 1990). An acoustic emission technique was utilized to study the nature and magnitude of damage in quasi-brittle material (Maji et al., 1990; and Ouyang et al., 1991). Acoustic emission is a localized, rapid release of strain energy in a stressed material. The energy release causes waves of stress to propagate through the specimen, which can be detected to deduce the magnitude and the nature of damage presented by the material. The acoustic emission technique indicates that the *FPZ* may have a noticeable width.

Van Mier (1991) used vacuum impregnation to investigate cracking in single-edge-notched concrete plates subjected to uniform boundary displacement. This researcher found that macroscopic structural effects, such as non-uniform opening and non-uniform drying out, obviously influenced specimen behaviour. It was found also that macrocracks are discontinuous cracks with debonding near larger aggregates and intact material bridges between them. According to these findings, when the average crack opening is larger than 50 μm , the load carrying capacity of a tensile specimen can be explained by the distributed crack interface grain bridging where failure is a process

involving bending and frictional pull-out. Therefore, the flexural (post-peak load) capacity for coarse grained mix was explained by the larger size of the crack interface grain bridges. In addition, the maximum aggregate size had significant effects on the softening behaviour of all of the specimens. According to these findings, in order to obtain a realistic fracture model for cement-based composites, micro-structural observations of cracking and localization are recommended.

Krstulovic-Opara (1993) assessed microcracks in the *FPZ* of compact tension mortar specimens using a high-magnification scanning electron microscope (SEM). He reported that the microcracks were randomly oriented with respect to the main crack plane, and that the density of the microcracks decreased with increasing distance from the face of the main crack.

Choi et al. (1997) examined the application of computerized visual technology to study concrete fracture; this technique uses different sub-images to measure displacements on specimen pieces that were broken into multiple parts by cracks. A non-destructive displacement evaluation system using a digital image cross-correlation scheme was developed to conduct microscopic examinations of fracture processes in concrete under compressive loads. The values of the cross-correlation coefficients, which define the level of similarity between two sub-images, were set to be larger than 0.7; this level was reasonable to eliminate poor matches due to local discontinuities. A full-field assessment method that was accurate within the micron range was chosen for the examination of a 100 mm x 75 mm viewing area. Friction-reducing material was applied

between the specimen and loading platens to reduce the impact of frictional shear constraints. In order to apply correlation matching between the same site in different images, black paint was lightly sprayed directly on to the surface of concrete specimens in order to create unique patterns on the specimen surface for matching. Different methods were used to estimate the value of the measurements. A closed-loop servo-controlled testing machine was used in conjunction with a suitable feedback signal that combined the lateral and axial deformations to provide a well-balanced imaging rate both before and after the application of peak load. A large number of measurement nodes were selected in order to obtain detailed information for the displacement contour maps. The development of non-uniform displacements in concrete was depicted with displacement contour maps obtained at various loading stages. Cracks that circumvented the aggregates and propagated parallel to the loading direction in the matrix were well illustrated. Mode I cracks were observed in the matrix area, but both Mode I and Mode II cracks were observed around aggregate interfaces. The processes of fracture in concrete were well defined at different deformation levels using this image-based technique.

Lawler et al. (2001) investigated the fracture process under compressive loading in concrete rectangular prisms (38.1 mm x 12.7 mm x 12.7 mm) containing sand or graphite aggregates. Two techniques were used; a 2D digital image correlation (DIC) technique was used to study surface cracking and a 3D technique, x-ray microtomography (XMT), was used to study internal cracking. The tested specimens were cut from larger specimens, exposing aggregate on the specimens' surface where the DIC measurements were performed. The displacements evaluated by DIC were analyzed with

an algorithm that determines the existence of cracking based on the magnitude of the difference observed in adjacent displacement vectors. DIC and XMT depicted cracks occurring in concrete specimens in different ways, and both techniques provided useful information regarding the development of fractures in concrete. The DIC technique measured surface displacement and depicted cracks as discontinuities in the displacement field, while the XMT technique utilized 3D maps to locate cracks that appeared in contrast to the surrounding materials. Nevertheless, a strong correspondence was observed for the crack patterns illustrated at the specimen surface when these two methods were applied simultaneously and compared. The authors concluded that crack propagation appears to proceed simultaneously on the surface of the specimen and internally, and that each technique is best suited to describe crack behaviour at different resolutions. DIC required much less time and was more effective than XMT at determining crack width and the location of small cracks (under 30 μm), but was disrupted by the occurrence of large cracks where a high degree of correlation was impossible. Conversely, XMT depicted the shape of larger cracks more successfully than DIC and could show the influence of internal features on the fracture process. The different properties of aggregate material heavily influenced the type of crack behaviour observed, which affected the material response of the specimen as a whole. The crack shapes observed in the specimens containing graphite aggregate exhibited distributed and more tortuous cracking, which slowed the growth of any localized crack system leading to a more ductile specimen. Cracks in the specimens containing sand aggregate were vertically oriented and were more direct and smoother in nature, enabling a crack to

propagate quickly through the specimen once initiated, leading to swift crack propagation and overall, more brittle behaviour in these specimens.

Wittmann (2002) studied the influence of concrete strength on concrete fracture properties and crack evolution. He noted that the width of the damaged zone in normal concrete increased at the beginning of loading, then remained constant as the crack ran along the ligament, and finally decreased again. For high strength concrete, the peak load was increased, compared to the peak load for normal concrete, while the material became more brittle; cracks ran through any aggregates as the matrix and the aggregates were mechanically very similar, so a comparatively narrow crack band was formed. Wittmann concluded that the fracture energy (G_F) is not equally distributed over the length of a crack, which leads to the size effect phenomena, according to Duan et al (2006). Wittmann also studied the influence of maximum aggregate size on the fracture energy, and found that G_F increases with increasing maximum aggregate size, if the size distribution remains similar.

Schlangen (2008) investigated the use of a CT-scanner with image processing software to measure the 3D microstructure of a concrete material in order to perform fracture simulations, to measure fracture properties and to determine the particle arrangements inside the material used to model the behaviour of the material. The tests (UTT) were conducted on cylindrical specimens (55 mm x 70 mm) composed of mortar, regular concrete with maximum aggregate size of 8-16 mm, and model concrete produced with special plastic sphere aggregates with a diameter of 12 mm and a very low

bond with the cement paste. A notch with a depth of 4 mm was made at half height. The model concrete showed more micro-cracking, a more tortuous crack path, lower tensile load and less brittle behaviour compared to the findings for mortar and regular concrete. Schlangen claimed that the opening of the crack was more uniform when the material heterogeneity increased, which resulted in further stable fracture. Almost the same peak loads were observed for mortar and regular (8-16 mm aggregate) concrete (close strength); however, the mortar specimens were more brittle. Some of the tests on mortar showed snap-back behaviour; however, these specimens had strength values that were three times higher than those of the model concrete specimens. Disorder was observed in the mortar material followed by snap-back in the $P-\delta$ curve, and it was not possible to determine the full softening curve. This was due to non-uniform opening of the specimens caused by the heterogeneity of the concrete material itself, even though the specimens were glued between non-rotating steel platens. The disorder was greater in the specimens made of model concrete, which led to non-linear opening with no snap-back behaviour. The CT-scan of the regular (8-16 mm aggregate) concrete did not provide enough detail since the image processing tools were unable to distinguish between the aggregates and the matrix because of the close density of the aggregates and cement matrix. Schlangen concluded that the opening of the crack is more uniform when the material heterogeneity is increased, which results in improving stability during fracture.

Wu et al. (2011) used the DIC technique to investigate the properties of the *FPZ* (for Mode I cracking of concrete) in the TPBT with a span to height ratio of 4. Attention was focused on the direction perpendicular to the crack path, while displacement along

the crack surface was neglected. The length of the *FPZ* increased during crack propagation and decreased after full development of the *FPZ*, which occurred when the ratio of the crack extension length to ligament length was 0.91; the ratio was lower at peak load, and the crack extension length at the peak load was about 0.25 times the ligament length. In addition, the maximum *FPZ* length and its length at the peak load increased with increased specimen height, but decreased when the notch depth to specimen height ratio increased. The authors concluded that the strain field determined cannot be quantitatively accurate; however, the strain field was used to judge the crack path.

2.13 Conclusion

Fracture is an important aspect of deformation and damage in both plain and reinforced concrete structures. The low tensile strength of concrete leads to cracking, which is usually, controlled by providing steel reinforcement to the tension zones; however, in structures such as massive concrete dams, providing steel reinforcement is uneconomical, so the accurate modelling of cracking is important for assessing the structure's behaviour. The Finite Element Analysis (FEA) is a powerful tool for structural analysis, but requires the use of advanced material modelling to simulate cracking behaviour. In order to accurately predict fracture behaviour using FEA, it is essential to choose a consistent and accurate fracture model of the material's properties. A variety of non-linear models have been developed to describe the fracture and failure of concrete in order to ensure the integrity and safety of concrete structures. These models require the

determination of parameters that are obtained experimentally from the testing of concrete samples.

The uniaxial tensile test (UTT) gives the best estimates of concrete's tensile strength and its softening curve; however, this test is not commonly used due to difficulties in performing a stable and representative test. Therefore, several indirect methods have been developed. The simplicity, stability and small dimensions of the wedge splitting test (WST) make it a favoured experimental method. This method yields a load-crack opening (P_{sp-w}) curve from which proper data reduction and inverse analysis can generate the *softening curve* and other concrete parameters. The preliminary results derived from the P_{sp-w} curve can be interpreted using the nonlinear cracked hinge model, which is based on the cohesive crack model that takes into consideration concrete toughening mechanisms, such as aggregate bridging and crack deflection. RILEM (TC 187-SOC 2007) includes the following statement:

“...the present contribution is closed, in Section 4, with an outline of the explicit data reduction technique that allows determination of a bilinear approximation of the stress-crack opening curve from results of diametric splitting tests and stable three-point-bending tests of notched beams. A similar procedure could be devised for other fracture specimens, such as the wedge-splitting specimen, but the computational effort required to support such a method has not been carried out yet.”

Investigation and characterization of the *fracture process zone* (FPZ), including its size and how it changes with crack propagation, is important for the application of

concrete fracture mechanics as the *FPZ* is associated with various mechanisms that occur during fracture. To the best of this author's knowledge, most of the investigations published in the literature included characterization of the *FPZ* (e.g. size, shape, and variation of the *FPZ*) along the specimen's length and/or general study of the fracture processes in concrete. No investigation focused on changes in concrete properties along the crack path during various fracture stages, such as variations in dissipated energy and tensile damage, the sizes of the *FPZ*, traction free zone and crack opening, or provided insight about toughening mechanisms while monitoring the crack opening from a single test.

Furthermore, the traditional method of assessing concrete deformation using a clip-gauge and the experimental techniques for measuring the *fracture process zone* are reported to have many limitations. Therefore, the need for an accurate non-contact and non-disturbing technique that is capable of monitoring the *FPZ* and measuring displacement is recognised by many researchers. Digital image correlation (DIC), a non-contact method, measures the surface displacement and reveals cracks as a discontinuity in the displacement field without producing any corresponding environmental effects on the specimen during testing. The following chapter present the application of the non-contact and non-disturbing DIC techniques to the WST.

CHAPTER III

APPLICATION OF DIGITAL IMAGE CORRELATION ON THE WEDGE SPLITTING TEST

Concrete is a quasi-brittle material; when cracked its behaviour is characterized by the presence of a *fracture process zone* (FPZ), where the material undergoes softening damage, ahead of the crack tip. Investigation of the FPZ and crack opening displacement are essential for characterizing the stability of concrete structure. Various experimental techniques for measuring the FPZ have been described, and include the use of: scanning electronic microscope (Mindess and Diamond, 1982 and Krstulovic-Opara, 1993), surface holographic measurements (Jacquot and Rastogi, 1983 and Raiss et al., 1990), dye penetration (Swartz and Go, 1984 and Swartz and Refai, 1989), acoustic emission (Maji and Shah, 1988 and Mihashi et al., 1991), laser holographic interferometry (Castro-Montero et al., 1990), laser speckle technique (Horii and Ichinomiya, 1990), vacuum impregnation technique (Mier, 1991), digital image cross-correlation (Choi and Shah, 1997), CAT scan (Landis and Nagy, 1998), X-rays (Otsuka and Date, 2000), optical fiber technology (Rossi and Le Maou, 1989, Leung et al., 1998, Denarie et al., 2001, and Hadjab et al., 2004), scanning computer vision (John and Shah, 2002), and CT-scan (Schlangen, 2008).

These methods vary in their ability to provide detailed measures of the FPZ and crack profile under all conditions. For example, in addition to measurement of the FPZ, the crack profile was obtained by the impregnation technique. Due to destructivity, this technique cannot provide information about crack evolution during loading (Jan and

Stang, 2010). On the other hand, the approximate crack tip position determined by acoustic emission, which provides an estimation of the dissipated energy, failed to characterize the crack profile. Although optical fiber technology using fiber bragg grating successfully detected the *FPZ*, a major drawback was that the fibers are very sensitive to environmental temperatures, vibrations and air draft (Denarie et al., 2001). Furthermore, strain measurements obtained with this technique could be unreliable because of the fiber damage or the presence of an adjacent aggregate shielding the material from strains. Consequently, the position of the optical fiber needs to be specified before the test when more than one gauge should be installed, as some of them may be positioned outside of the actual *FPZ*.

The traditional method for assessing concrete cracks uses a clip-gauge mounted directly on to the crack mouth to generate the load-crack mouth opening relationship (P_{sp} -CMOD) that is essential for characterising a fracture. This method has many limitations, such as: (a) the clip-gauge has to be attached to the specimen directly, so the results could be affected by the vibration of the testing machine and/or the cracked concrete specimen itself; (b) the displacement measurement's position needs to be specified in advance (e.g. at crack mouth), therefore it is impossible to assess crack evolution; and (c) since the displacement is measured at the crack mouth, evaluation of the fracture energy from this measurement leads to overestimation compared to the determination of fracture energy based on displacement measurement at the crack tip. Consequently, other techniques have been used to measure crack opening displacement in concrete structures, which include laser interferometry, stereo imaging, acoustic emission, CT-scan, and ultrasonic

and computerized tomography. These methods suffer either from high sensitivity to the vibrations from testing machines, low measurement accuracy, or laborious post-processing (Choi and Shah, 1997). In addition, it can be difficult under ordinary laboratory conditions to perform these techniques.

Moreover, to the best of the author's knowledge, most of these investigations included characterization of the *FPZ* (e.g. size, shape, and variation of the *FPZ*) along the specimen's length, and/or general study of the fracture processes in concrete. No investigation focused on changes in concrete properties, such as crack opening or dissipated energy along the crack path during various loading stages in a single test.

The state of the art for current understanding of the general performance of concrete at the *FPZ* seems to be adequate, but remains deficient from a fundamental perspective. That is, there are some essential questions that need to be answered, such as questions about the variation of dissipated energy and crack opening displacement along the crack path, the position of the newly formed crack tip, and a closer understanding of the toughening mechanism. Furthermore, since the fracture pattern of concrete is naturally complicated because of its internal heterogeneity, gauges attached to the specimen do not provide accurate data.

Therefore, the need for an accurate non-contact and non-disturbing technique that is capable of monitoring the *FPZ* is recognised by many researchers. The main objective of this chapter is to illustrate the use of such technology for the identification of concrete

fracture parameters, including: an estimation of the variation of the dissipated energy and the crack opening displacement along the crack path, the monitoring of the crack propagation process, and an accurate method for determining the crack tip opening displacement (CTOD) at the notch tip, which is important for identifying the fracture energy and other parameters.

Optical techniques have proven valuable for characterizing the properties of advanced materials, especially those exhibiting inhomogeneity. For example, Digital Image Correlation (DIC) is an optical technique used to visualize surface deformations that is based on the processing of data encapsulated in digital images. Furthermore, DIC is a non-disturbing and non-contact measurement technique of displacement and strain. When DIC is used for the assessment of concrete, it is possible to monitor the development of the *FPZ* without interference during the fracture and/or when machine vibrations are present during testing; image recognition is used to analyze and compare digital images obtained from the surface of a substrate. This technique is not restricted to a single axis or to specific points on the surface, so is capable of providing richer data than gauge-based measurement techniques as images of the entire surface of the specimen are recorded, and then processed conveniently after the test.

For all of the aforementioned reasons, and the ability to obtain undisturbed data during the failure process as well as data from any point on the specimen's surface, the DIC technique was chosen to generate the load-crack opening displacement (P_{sp} -CTOD)

curve from the analysis of digital images obtained while the *FPZ* is monitored during loading.

The present experimental study deals with Mode I fracture behaviour of plain concrete. Experimental result from the WST with the crack mouth opening displacement (CMOD) measured using a clip-on gauge was used as reference points. This result was subsequently compared to the result obtained from DIC using the ARAMIS system.

3.1 Mechanical Properties of Concrete

The mechanical properties or parameters, which characterize the behaviour of concrete before cracking, are needed in order to model its performance. In this study, standard material tests were carried out to determine the values for *compressive strength* (f'_c), *tensile strength* (f'_t), and *Young's Modulus* (E), while the Poisson's ratio was estimated.

f'_c is one of the most common mechanical properties of concrete. To determine this parameter, an ASTM C873-10 standard test (Figure 3.1(a)) was carried out using concrete cylinders (D x H =100 mm x 200 mm), which were cast in PVC molds, capped for 24 hours, and then cured in water at room temperature for one month. In order to have concrete that was representative of the concrete used in the WST-specimens, the same environment was provided for all cylinders during and after casting. Compressive strength was determined using the following equation:

$$f_c = \frac{P}{r^2 \pi} \quad (3.1)$$

where P stands for the load at failure, and r stands for the radius of the concrete cylinder.

The uniaxial direct tension test (UTT), which is believed to give the best estimate of the tensile strength of concrete, is not commonly used due to difficulties in performing a stable and representative test (Hordijk, 1989). Instead, several indirect methods have been developed; the most familiar one is the split cylinder tensile test (SCT) suggested by Fernando Carneiro (1943), and known as the Brazilian test (Neville, 1981).

The split cylinder test is a widely accepted method for estimating f_t of concrete. The determination of the splitting tensile strength (f_{sp}) of concrete was carried out according to ASTM C496 standard test procedures, as shown in Figure 3.1(b). A concrete cylinder (of the same type as that used in the compression test) was placed, with its axis horizontal, between the platens of the testing machine, and then the load was increased at a constant rate until failure occurred. The concrete cylinder split into two halves along the vertical diameter, due to the indirect tensile stress generated by the Poisson's effect.

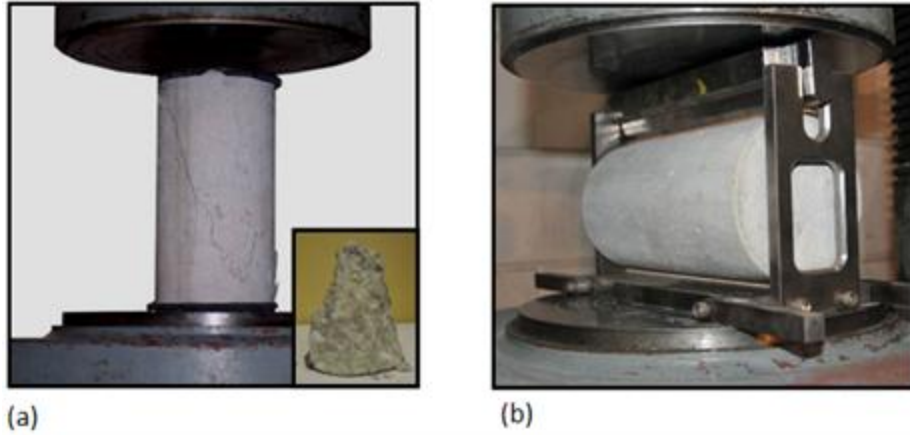


Figure 3.1: (a) Compressive Strength Test, (b) Split Cylinder Test

To estimate the f'_t of concrete, we proceeded by assuming that the concrete behaviour remains elastic up to the point of complete failure. The elastic solution for relating the splitting stress and the applied force is given by Timoshenko & Goodier (1970). Uniform lateral tensile stress acting along the vertical plane causes the failure of the specimen, as shown in Figure 3.2. The splitting tensile strength at failure, f_{sp} can be calculated from the following equation:

$$f_{sp} = \frac{2P}{\pi LD} \quad (3.2)$$

where P stands for the load at failure, D and L stand for the concrete cylinder diameter and length, respectively.

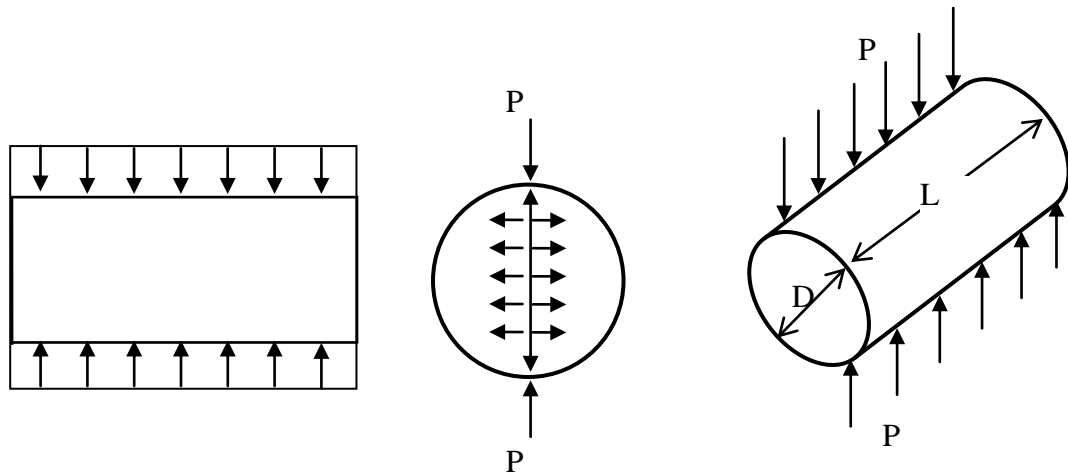


Figure 3.2: Stress distribution on concrete cylinder during splitting test

The quasi-brittle behaviour of concrete and the size of the related fracture mechanics effect induce a difference between the conventional splitting tensile strength, f_{sp} and the true f'_t . The former depends on the material, as well as the size and geometry of the tested specimen, and the testing procedure, whereas the latter is regarded as a material fracture parameter.

The interpretation of this indirect test, which relies on a linear elastic formula, overestimates the true f'_t . Therefore, this evaluation should be combined with a correction factor. According to Neville (1981), the splitting strength is 5 to 12 percent higher than direct measures of tensile strength. Furthermore, taking the size effect into consideration, another reduction factor of 5% should be applied as smaller (100 mm x 200 mm) cylinders were used instead of the recommended cylinder size (150 mm x 300 mm) (Blanks and McNamara, 1935).

In addition, high compressive stresses are induced locally on the specimen. To allow uniform distribution of the applied load and to reduce the magnitude of the high compressive stresses near the loading axis, strips of plywood (3 mm thick) were placed between the specimen and the loading platens of the testing machine. Under these conditions, the load is distributed evenly over loading strips of $2a$ (25 mm) width, as shown in Figure 3.3. According to Tang (1994), this phenomenon affects the stress state; therefore, the f_{sp} solution should be modified as in the following expression:

$$f_{sp} = \frac{2P}{\pi LD} \left[1 - \left(\frac{2a}{D} \right)^2 \right]^{2/3} \quad (3.3)$$

where P stands for the load at failure, D and L stand for the concrete cylinder diameter and length, respectively, and $2a$ stands for the strip width.

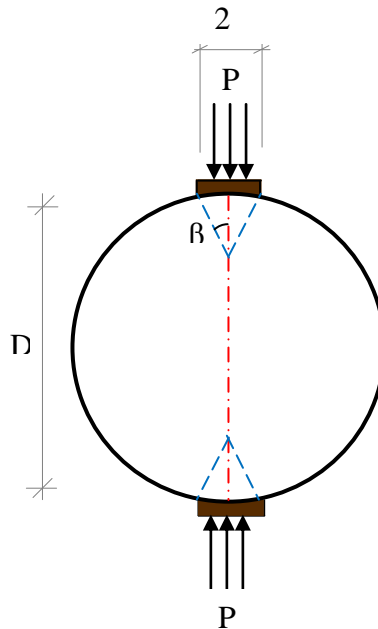


Figure 3.3: Yield lines of the assumed plastic failure mode

The Young's modulus (E) is a measure of the stiffness of an elastic material. It is defined as the ratio of the uniaxial stress over the uniaxial strain in the range of stress in which Hook's law holds. Young's modulus can be experimentally determined from the slope of a stress-strain curve conducted on a sample of the material; for this study; however, the E of concrete was estimated according to the standard, CSA A23.3 (8.6.2.3), shown in the following equation:

$$E_c = 4500\sqrt{f'_c} \quad (3.4)$$

The Poisson's ratio (ν) is the ratio of the lateral expansion to the longitudinal contraction of the specimen under uniaxial compressive loading. In this study, this value was estimated to be 0.2.

3.2 Fracture Properties of Concrete

The aforementioned properties describe the pre-cracking behaviour of concrete, and are used in analysis, design, and deformation computations; however, the fracture behaviour of concrete is greatly influenced by the *FPZ*, the zone in which the material undergoes softening damage.

Fracture is one of the major concerns in modeling engineering materials; the identification of concrete fracture properties poses an ongoing challenge for materials scientists. As noted in the second chapter of this dissertation, knowledge of the post-

cracking parameters is necessary for any structural integrity assessment as these parameters depict crack initiation and propagation. For example, the nonlinear fracture of concrete can be characterized by the stress-crack opening relationship ($\sigma-w$), fracture energy (G_F), and characteristic crack length (l_{ch}).

The stress-crack opening relationship ($\sigma-w$), also called the *softening curve*, illustrates the degradation of the stress-carrying capacity of concrete during the fracture process; this curve is directly linked to the fracture energy. In addition, other material properties can be extracted from this relationship, such as the f_t , which can be directly determined by conducting the uniaxial tension test. However, for the reasons mentioned in chapter two, the WST was chosen for the current research study, to measure $\sigma-w$ indirectly through numerical analysis as described in the next chapter.

By definition, the Fracture energy (G_F) represents the energy absorbed per unit area of crack. G_F can be measured from the area under the splitting load-crack opening displacement ($P_{sp}-COD$) curve divided by the projected fracture area on a plane perpendicular to the splitting load direction (ligament length x specimen width) as shown in Figure 3.4. This energy, according to Hillerborg (1976), can be divided into two parts corresponding to: 1) the ($\sigma-w$) curve, which represents the energy per unit volume absorbed by the whole specimen before the tensile stress is reached, and 2) the area below the ($P_{sp}-w$) curve, which represents the energy absorbed within the damage zone only, G_F .

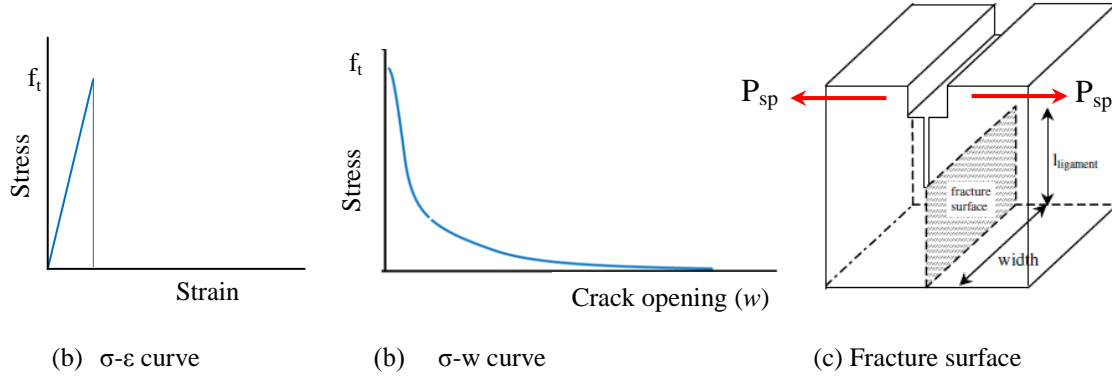


Figure 3.4: Fracture energy estimated from the area under the splitting load-crack opening

The fracture energy alone does not suffice to characterize the brittleness of concrete. In 1976, Hillerborg introduced the concept of l_{ch} to define the influence of the material and the size of the structure as a function of the brittleness number (β). The brittleness ratio is defined as:

$$\beta = \frac{\text{Elastic Energy}}{\text{Fracture Energy}} = \frac{f_t^2 L}{G_F E_c} = \frac{L}{l_{ch}} \quad (3.5)$$

The elastic energy is the potential mechanical energy stored in the configuration of a material as work is performed to distort its volume or shape. L is a structural dimension, and l_{ch} is a material parameter known as the characteristic length, which denotes this theoretical parameter (β) in a dimensionless form that represents a length that stems from the comparison of the elastic stored energy and the total energy that the crack can absorb, and characterizes the brittleness for complete fracture (RILEM TC 187-SOC 2007). The value of l_{ch} for concrete is approximately 200-400 mm (Patterson, 1981). In

general, the characteristic length decreases with a structure's age, indicating increased brittleness. This parameter, l_{ch} , may be interpreted as a measure of the elastic strain energy needed for one unit area of the crack propagation, which can be calculated from the following equation:

$$l_{ch} = \frac{G_F E_c}{f_t^2} \quad (3.6)$$

The characteristic length, based on the fictitious crack model, is proportional to the length of the *FPZ*. The *FPZ* length for concrete is on the order of $0.3 l_{ch}$ to $0.5 l_{ch}$ at complete separation of the initial crack tip, and is a purely material property (Shah et al, 1995).

3.3 Wedge Splitting Test (WST)

The uniaxial tension test is recognized as the most direct method for the determination of the stress-crack opening relationship ($\sigma-w$); however, due to the difficulties associated with this test (Lamond and Pielert 2006), other methods are preferred. The three points bending test (TPBT) and WST are often used when determining concrete fracture properties. These methods are indirect and yield a load-deformation curve from which a proper analysis, $\sigma-w$ may be generated. Østergaard (2003) compared different testing geometries to identify the concrete fracture properties at an early age using the SCT, WST, TPBT, and UTT. The author found that it is

possible to determine very similar relationships for $\sigma-w$ with the aforementioned test methods. Moreover, he stated that the results obtained from the indirect methods (SCT, WST, and TPBT) are valuable and close to the result obtained with the direct UTT method.

The WST-specimen's geometry proposed by Linsbauer and Tschegg (1986) was originally designed for the determination of G_F and was then improved by Brühwiler and Wittmann (1990), and finally adopted by RILEM as a stable fracture mechanics test for concrete (RILEM TC 89-FMT, 1991). The methodology of this test, which is a special form of the compact tension test (Figure 3.5), is to split a small cube with a groove and a starter notch into two halves while monitoring the load and CMOD.

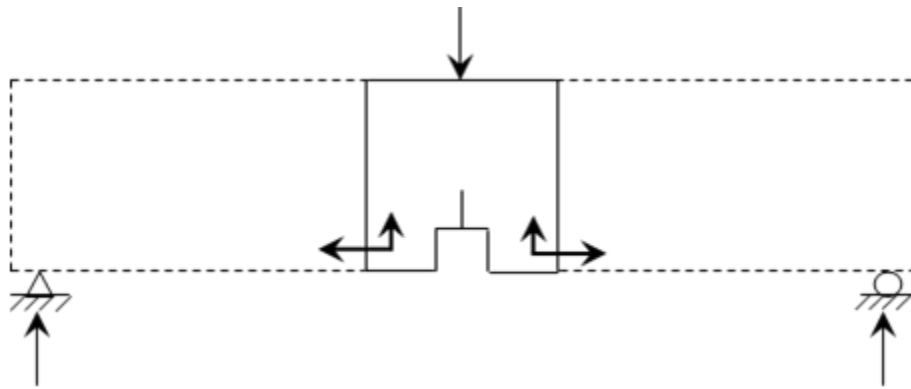


Figure 3.5: Wedge splitting specimen as a “compact” three-point-bending test

The WST was traditionally used for brittle materials as it is suitable for obtaining the P_{sp} -CMOD and for estimating G_F while ensuring post-cracking stability. The applicability of the WST was investigated, and the test proved to be reliable for the

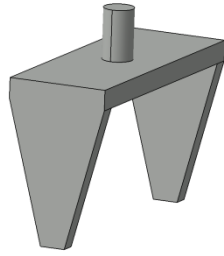
determination of the fracture properties of concrete. Harmuth (1995) used the WST to study the stability of the crack propagation associated with G_F . Que et al. (2002) employed the WST to investigate the numerical evaluation of cohesive fracture parameters, while Hanjari (2006) utilized the WST to investigate the fatigue behaviour of concrete, and WST applicability to the study of dynamic loading.

The determination of the fracture properties of concrete at an early age using the WST was investigated by Østergaard (2003) and Karihaloo et al. (2004). This test was also applied to polymer cement concrete (Harmuth, 1995), polypropylene fibre reinforced concrete (Elser et al., 1996), crushed limestone sand concrete (Kim et al., 1997), lightweight-aggregate concrete (Faust and Voigt, 1999), ultra high strength concrete (Xiao et al., 2004), high performance concrete (Østergaard et al., 2004), rock-concrete (Kishen et al., 2004), and steel fiber reinforced concrete (e.g. Löfgren, 2005), among others. The WST was also used for the determination of σ - w of interfaces between steel and concrete (Lundgren et al., 2005, and Walter et al., 2005), and the effect of size on the strength of cracked concrete structures (Karihaloo et al., 2005).

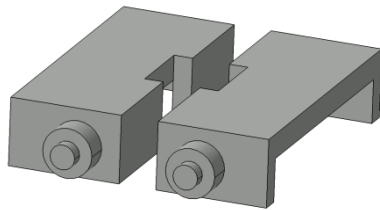
The schematic view of the WST is shown in Figure 3.6. The specimen is characterized by a groove and a starter notch, which can either be moulded or saw cut. During the test, the WST-specimen is placed on a line support fixed to the lower plate. Two massive steel loading devices equipped with roller bearings are placed on each side of the top of the specimen. A steel device with two identical wedges is mounted to the upper part of the loading frame. During testing, the actuator of the testing machine is

moved down, so that the wedge enters between the bearings rollers, which results in a horizontal splitting force component as shown in Figure 3.7.

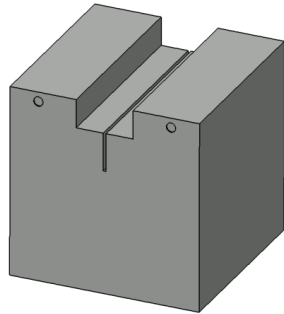
The fracture section of the specimen is essentially subjected to a bending moment. The load in the vertical direction (P_v) and the CMOD are monitored during the test. The splitting force (P_{sp}) is the horizontal component of the force acting on the bearings, which can be determined in terms of the wedge angle and frictional forces. Equilibrium of the forces on the wedge is shown in Figure 3.7, where φ is the wedge angle and μ is the coefficient of friction for the bearings roller.



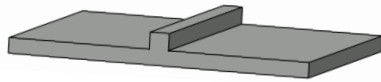
Wedge device



Steel loading device with roller bearing



WST-specimen



Linear support

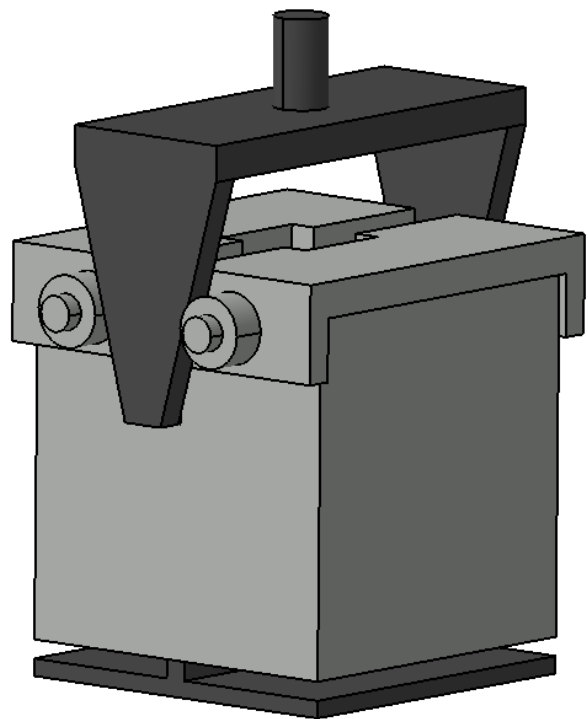


Figure 3.6: Schematic view of the WST-setting

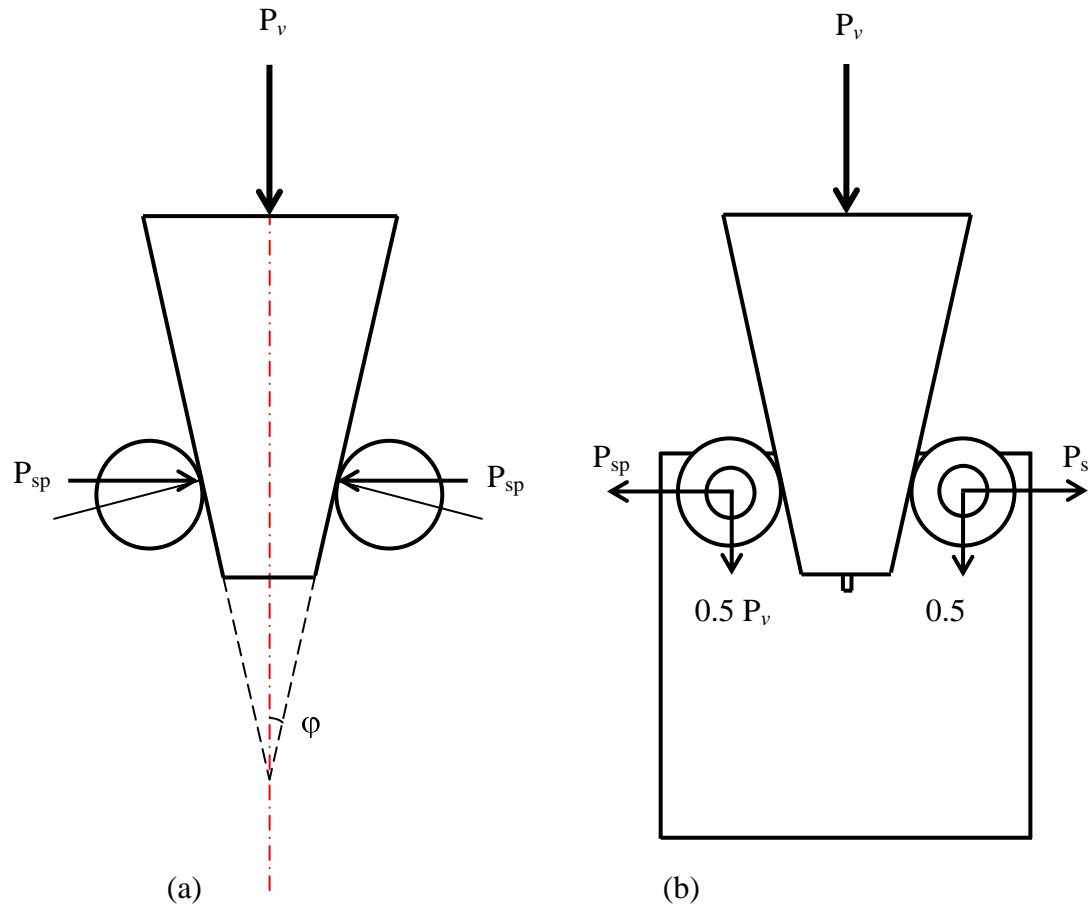


Figure 3.7: Principle of wedge-splitting test (WST): (a) forces acting on the WST, (b) specimen passing wedge between bearings rollers

A small wedge angle for the loading device increases the stiffness of the specimen-testing machine assembly and facilitates the control of the actuator displacement, which is perpendicular to the COD; however, by reducing this angle, the frictional force between the roller bearing and the loading device increases significantly. According to the International Union of Laboratories and Experts in Construction Materials, Systems, and Structures, RILEM TC 89-FMT (1991), a wedge angle of 15° is appropriate; the stiffness of the specimen-machine assembly is increased and control of the actuator displacement is facilitated. Consequently, the wedge angle, which enhances

the effect of the vertical force applied by the machine, also reduces the elastic energy stored in the testing device in comparison to the TPBT. Furthermore, the WST does not suffer from problems caused by the self-weight of the specimen, so the contribution of specimen weight is negligible in comparison to the splitting force. Due to the compressive stresses developed in front of the crack tip and the limited amount of elastic energy stored in the specimen, the crack extends in a stable manner during the WST. The WST-specimens can be easily fabricated in the lab or at a building site, so that they match the geometry of a standardized specimen of freshly poured concrete. WST-specimens can also be drilled from an existing structure, and the groove and notch should be sawed off of the specimen where there is no risk of breaking the specimens during handling. Lastly, according to RILEM 1991, the WST-specimen with a fracture ligament of 130 mm has a fracture area that is approximately 5.2 times larger than the fracture area of the beam, for the same volume of concrete.

In the current research, for all of the aforementioned reasons, the WST, with a wedge angle of 15° as recommended by RILEM, was carried out to obtain the concrete fracture parameters. The dimensions of the groove and the notch were also chosen according to RILEM recommendations, so that the crack would propagate in the vertical direction, and the specimen would split into two halves while the load and CMOD were monitored. The geometry of the WST-specimen, with dimensions of 200x200x200 mm, a notch length of 40 mm, and a ligament length of 130 mm, is shown in Figure 3.8.

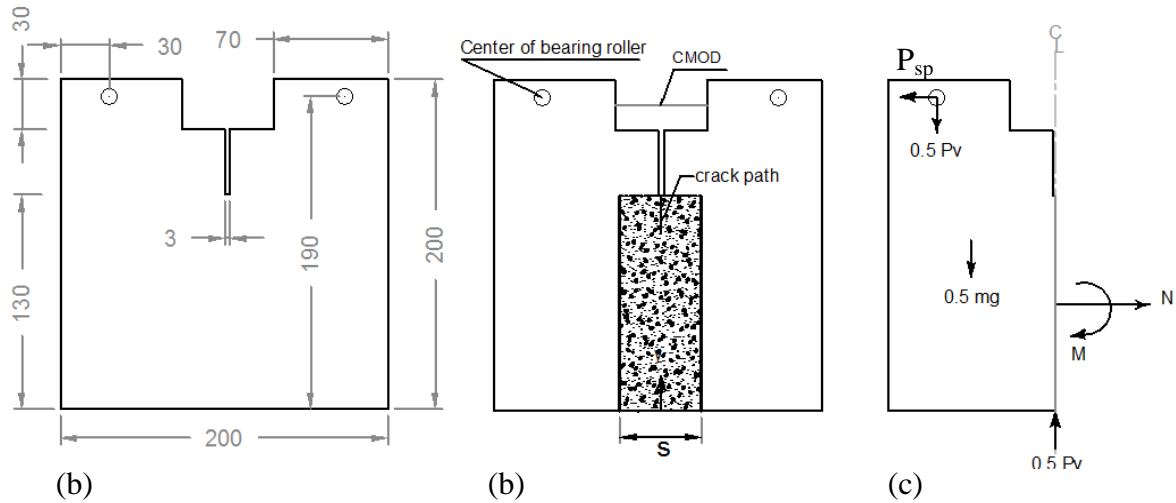


Figure 3.8: (a) Geometry of the WST-specimen, (b) Incorporation of the band width model, (c) Loading (CMOD: crack mouth opening displacement, P_v : vertical load, P_{sp} : splitting load, mg : specimen weight)

3.4 Mix Design and Mixing Procedure

The WST-specimens and concrete cylinders were cast and tested in the lab at different times after casting. High early strength cement (HE)-Type 30 (CSA Standard A5-M83) was used with a water to cement ratio (W/C) of 0.47. The aggregate was made of Blue chips (stone) with maximum aggregate size (d_{max}) of 9.5 mm. The concrete was mixed using a continuous pan mixer where the dry materials were first mixed for 2 min, then water was added while the mixing continued for another 3 min. The mix proportion by weight is given in Table 3.1. All of the WST-specimens were cast in steel molds; the groove and the notch were fabricated using a special steel device as illustrated in Figure 3.9. Special attention was paid to control water evaporation, knowing the detrimental effect of the moisture content, curing, and temperature on the tensile strength (Van der

Been, 1987). The cast specimen was compacted on a vibration table at 50 Hz for 2 min. All specimens were covered after casting with plastic sheets for 24 hours before demolding, and then cured in water at room temperature for one month.

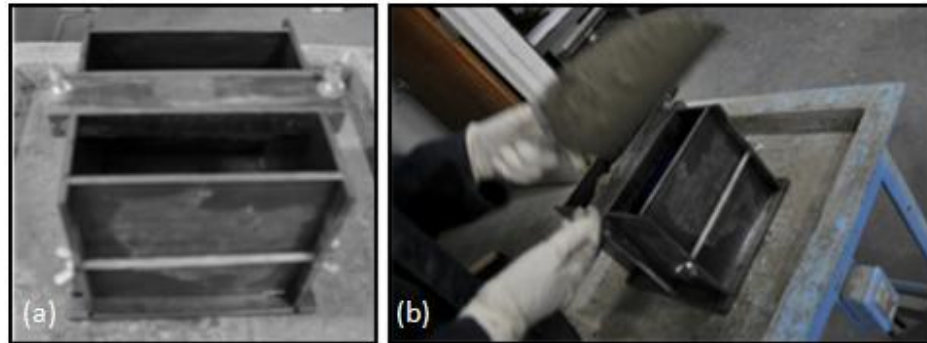


Figure 3.9: (a) WST-specimen steel mold, (b) Casting the WST-specimen on a vibration table

Table 3.1: Concrete Mix Design

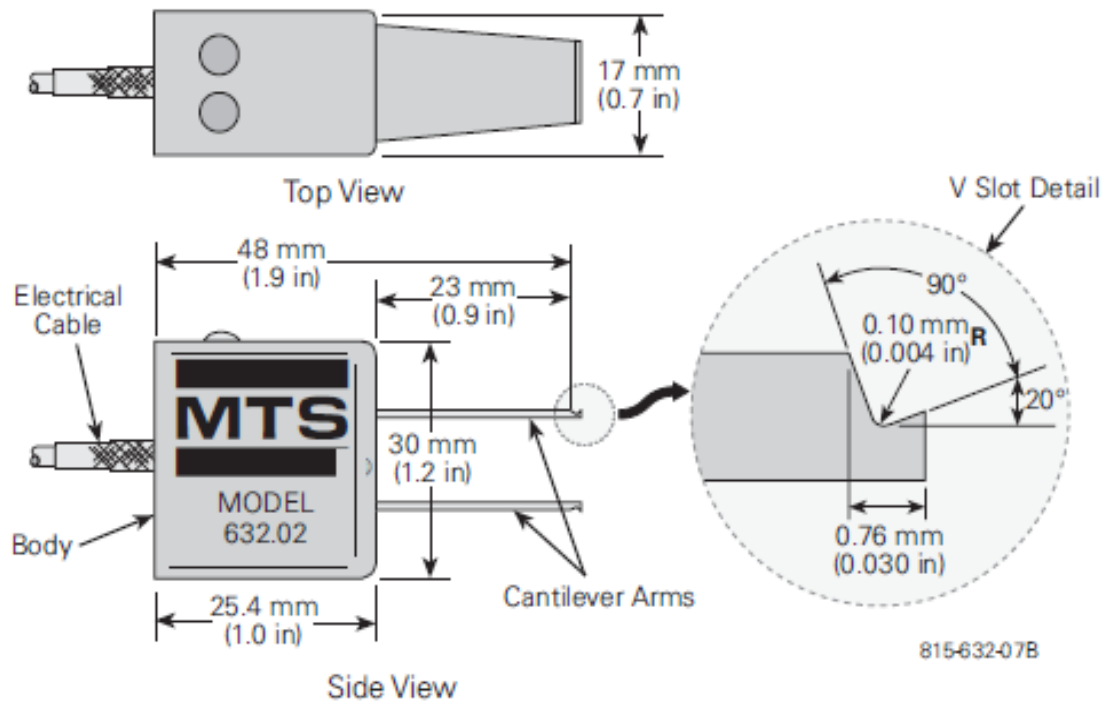
Concrete Material	Percentage of Mass
Aggregate	65
Cement	24
water	11

3.5 Experimental Investigation of the Wedge Splitting Test (WST)

This study deals with Mode I fracture behaviour of plain concrete. The experiment began with a WST following recommended protocols (RILEM, 1991). All of the WST were carried out in an electro-hydraulic closed-loop testing machine, INSTRON, with a load capacity of ± 100 kN; the load in the vertical direction and the CMOD were monitored.

During the test, the specimen was placed on a linear support resting on a spherical hinge (rotational joint) to allow the specimen to rotate about the loading axis. This setting prevents unwanted restraint and assures that the wedges fit between the bearing rollers, so that the load will be applied symmetrically to the loading plates, and then to the specimen. Two steel loading devices equipped with bearing rollers were placed on each side of the top of the specimen as shown in Figure 3.6. A stiff steel plate with two identical wedges angled at 15° was mounted to the upper part of the loading frame to reduce the dead load effect. To measure the CMOD under displacement control, a clip gauge with three points of contact (MTS CLIP-ON GAUGE-632.03F-20 with a 12 mm gauge length and a maximum travel of 4 mm as shown in Figure 3.10) was placed in the groove of the WST-specimen and mounted between two knife edges attached to the specimen (Figure 3.11). The CMOD was monitored with this clip-gauge, which was fixed at the level where the splitting force acts on the specimen. The test was performed with the INSTRON testing machine under CMOD control with a constant speed of 0.0005 mm/sec (as recommended by RILEM); the downward movement of the wedges placed between the bearing rollers created a splitting action. Brillwiler and Wittmann

(1990) found that the G_F determined using the TPBT and the WST increased as loading rate increased; this finding was also reported by Bazant et al. (1989). Therefore, the displacement rate was kept constant for all tests. The experimental setup for the WST is shown in Figure 3.12.



Model 632.02 Clip-on Gage

Figure 3.10: Clip-on Gauge (MTS Systems Corporation)

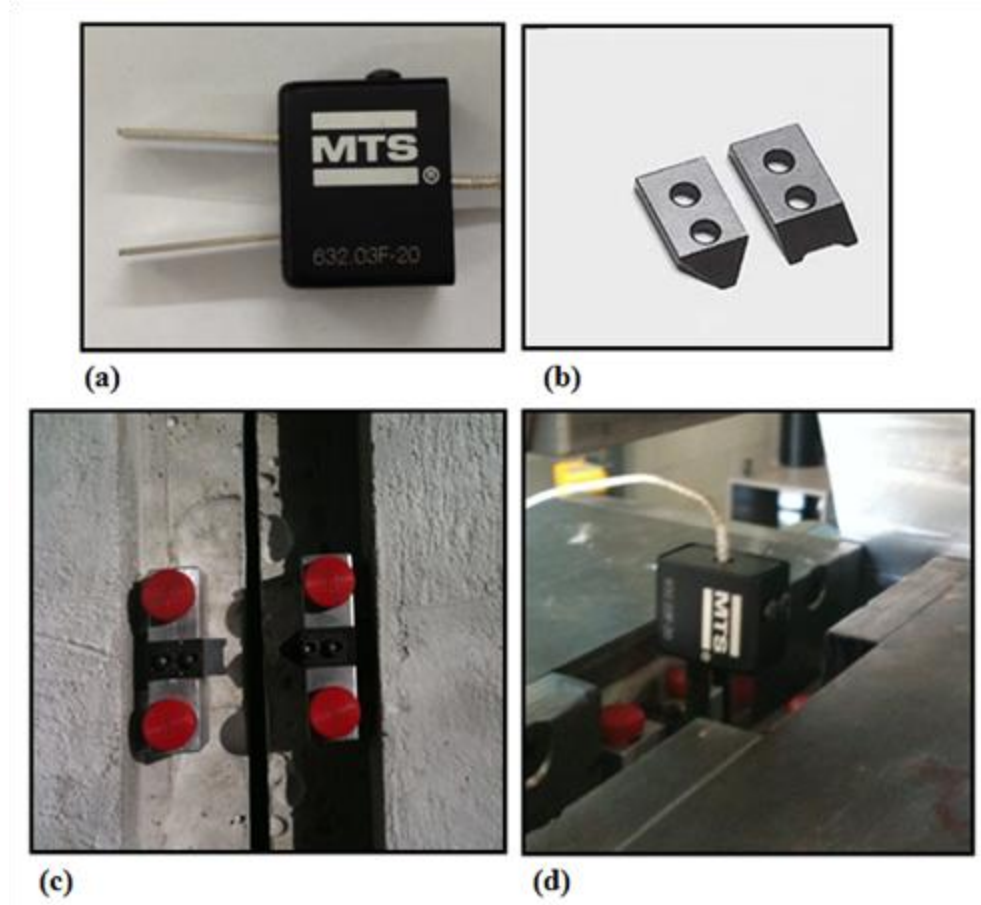


Figure 3.11: (a) Clip-on Gauge, (b) knife-edges, (c) knife-edges attached to the WST-specimen where the CMOD was measured, (d) Clip-on Gauge placed between the knife-edges in the groove of the WST-specimen

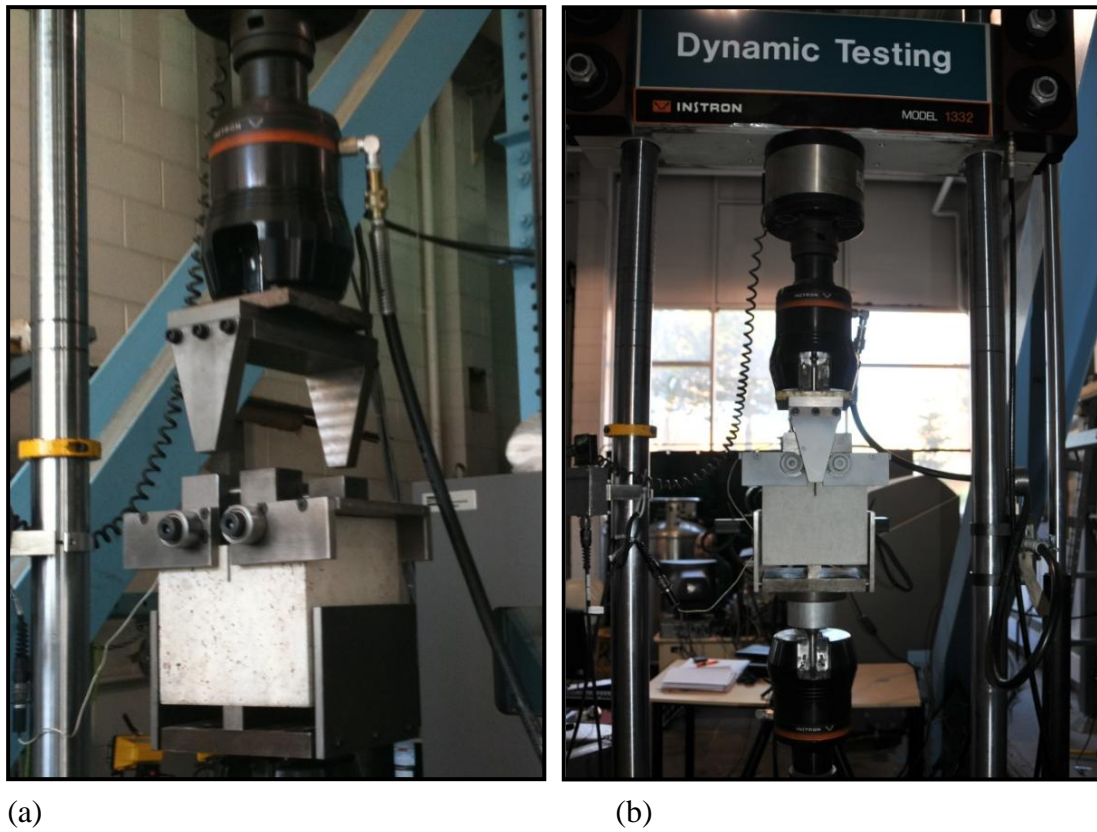


Figure 3.12: Experimental set-up of the WST. (a) the set-up preparation where the loading device (wedges) is mounted to the upper part of the loading frame, (b) the WST-specimen in place for testing

3.6 Experimental Findings for the Traditional (clip-gauge) Technique

The vertical load (P_v) and the CMOD were monitored during the test and extracted from the INSTRON data acquisition system. The test was stable and accurately covered the complete P_{sp} -CMOD diagram. The P_{sp} which is the horizontal component of

the force acting on the bearing as shown in Figure 3.7, was calculated from the applied P_v taking the wedge angle (φ) of 15° into consideration as follows:

$$P_{sp} = \frac{P_v}{2 \cdot \tan \alpha} \left(\frac{1 - \mu \cdot \tan \varphi}{1 + \mu \cdot \text{ctg} \varphi} \right) \quad (3.7)$$

Hillemeier (1976) experimentally determined on a calibrator a value for the coefficient of friction, μ , of 0.031% for a wedge loading set-up using hardened steel, an inclined wedge surface that was polished carefully, and bearing rollers. Accordingly, RILEM (1991) suggested that μ should be considered if it is larger than 0.5%. Therefore, in this study, μ was ignored as the effect of frictional forces between the wedge device and the roller was reduced using the set-up described above. Consequently, the splitting force can be computed from the vertical force according to the following expression:

$$P_{sp} = \frac{P_v}{2 \cdot \tan \alpha} \approx 1.866 \cdot P_v \quad (3.8)$$

Out of 26 WSTs, the experiment was successful for only six of them (i.e., the entire softening curve was generated and recorded during the WST). During the other 20 tests, sudden failure of the specimens occurred and/or snap-back behaviour was experienced at some point after the peak load was applied, which prevented generation of the complete softening curve. The reason for the high failure rate was that the settings used for the INSTRON machine were incompatible with the WST. This was the first time that this type of test was conducted in the University of Windsor's laboratories; however,

this series of unsuccessful tests played an important role in the development of a compatible experimental set-up for this application of the INSTRON technology.

During the current study, insight was gained through experimental work conducted for the purpose of better understanding of the failure mechanism. Depending on the bond strength of the aggregate, two crack mechanisms may potentially develop during the failure of cementation materials. If an aggregate is weaker than the bond strength, the crack can penetrate the aggregate and the interface properties will contribute little to crack resistance. Alternatively, a strong aggregate will deflect the crack through the interface, and a tortuous crack can develop (see Figure 3.13). In this figure, the effect of crack deflection is clearly illustrated; in addition, the fracture surface is rough as the crack ran around some aggregate particles and/or through voids within the matrix. The total energy dissipated may be affected by the crack scenario. In the first case, the fracture path is planar but the energy release rate is usually larger in comparison to the energy release rate for a crack path running along the aggregate interface and matrix. In the second case, the crack path is longer, and therefore may consume more energy. The experimental results represented by the P_{sp} -CMOD relationship are shown in Figure 3.14.

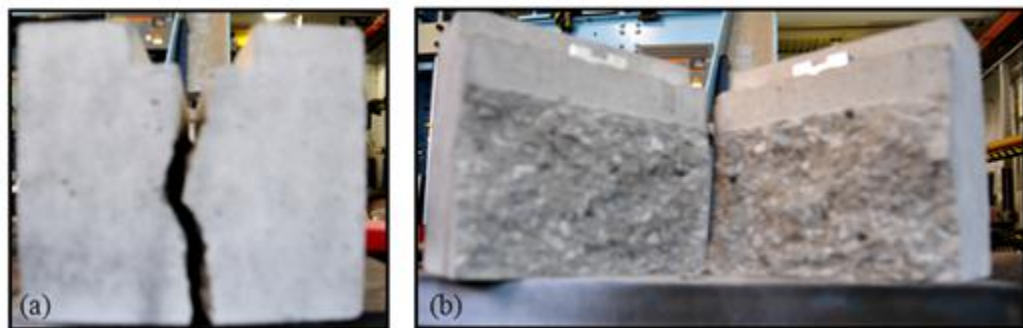


Figure 3.13: The WST-specimen (WST6) after failure (a) the cracked specimen, (b) the fracture surfaces

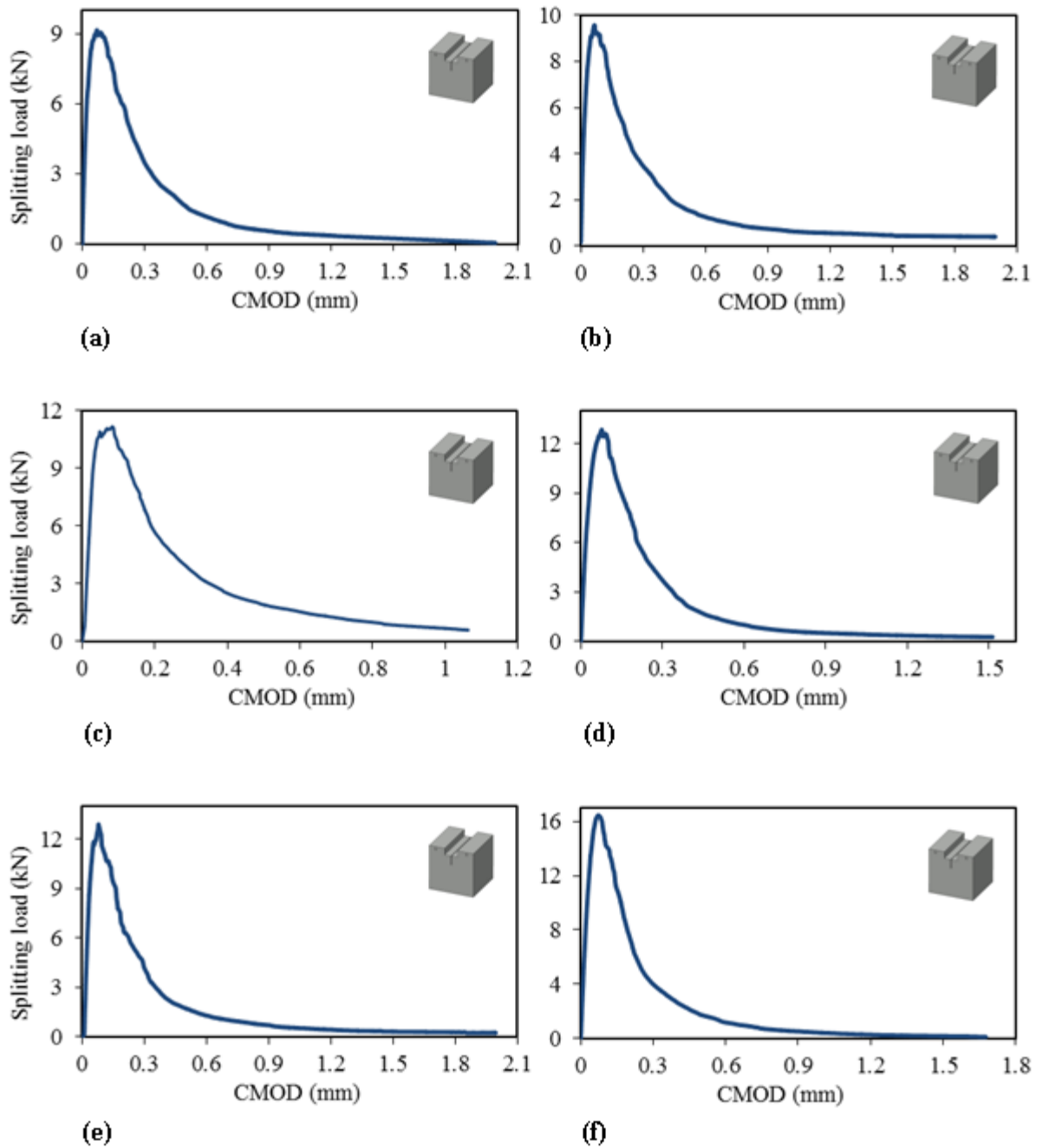


Figure 3.14: Experimental results from the WST using clip gauge (CG) at different ages (Figures a, c, and e are made from the same concrete batch) (a) WST1 at 81 days, (b) WST2 at 90 days, (c) WST3 at 80 days, (d) WST4 at 117 days, (e) WST5 at 97 days, (f) WST6 at 236 days

The above figure illustrates that the experimental set-up was capable of detecting the softening behaviour. At the initiation of loading, the specimen reacts quasi-linearly. However, by increasing the load, nonlinear behaviour develops; the fracture process reduces the specimen's resistance capacity and softening behaviour is observed.

The P_{sp} -CMOD relationship between splitting load and crack mouth opening displacement for WST-specimens of various ages (81 to 236 days after creation of the specimens) is shown in Figure 3.15. As expected, the peak load increases along with increases in concrete strength while concrete material reacts in a more brittle manner. The commonly accepted view of the mechanism of concrete deformation can be summarized as: when the load is applied to the WST-specimen, the effect of the initiation of internal cracks can be ignored. At approximately 30% of the ultimate stress, random propagation of the formation of micro-cracks occurs, and then major cracks begin to localize into macro-cracks at 80% of the maximum stress; these macro-cracks propagate critically at the peak load. These phenomena can be seen clearly in the magnified portion of Figure 3.15; observations for WST 1 and WST 2, which have the lowest tensile strength, start to deviate from the other specimens at approximately 82% of the peak load (see Shah et al., 1995). These findings could be interpreted as: the increase in tensile strength related to aging causes variation in the formation of macro-cracks, including their localization and distribution, according to the loading stage (expressed as a percentage of the maximum or peak load).

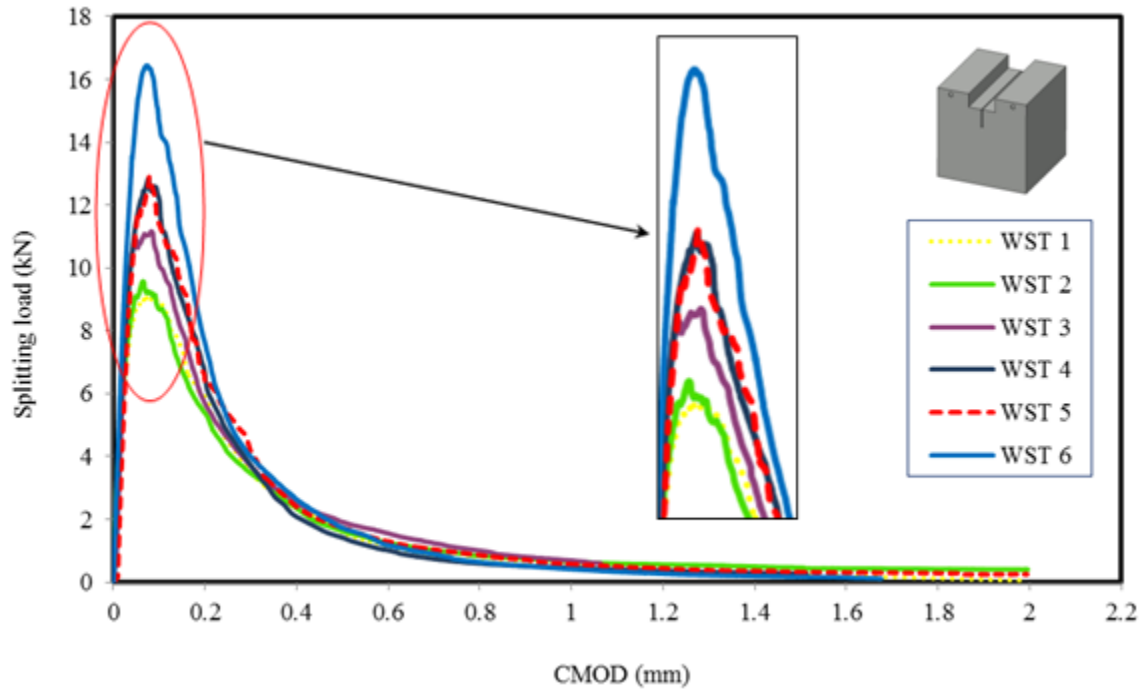


Figure 3.15: Experimental results from the WST at different ages using clip gauge (CG)

Figure 3.16 illustrates the P_{sp} -CMOD relationship for three specimens made from the same concrete batch and tested at different times. This figure shows that as the concrete strength increases with concrete age, the peak load increases. WST5, the strongest specimen, has a higher value for fracture energy as estimated from the area under the P_{sp} -CMOD curve. In addition, the slope of the first part of the softening curve increases as the specimen's strength increases; this indicates an increase in the brittleness of the material. All of the curves seem to converge asymptotically for large CMOD values, at the tail.

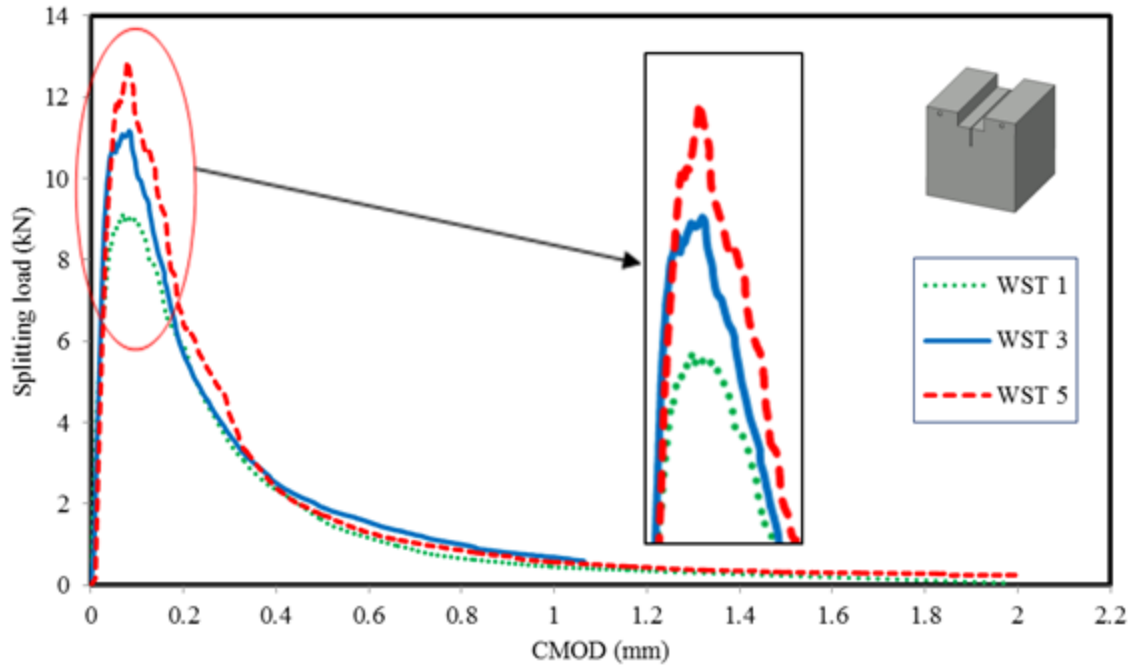


Figure 3.16: Experimental results from the WST using clip gauge (CG) at different ages for specimens made from the same concrete batch WST1 tested at 81 days, WST3 at 90 days, and WST5 at 97 days

Concrete fracture energy (G_F) is calculated by dividing the area under the P_{sp} -CMOD curve by the fracture surface (projected fracture area). The fracture surface in the WST-specimen is obtained by multiplying the ligament by the specimen's width (i.e., 130 mm x 200 mm as shown in Figure 3.4). The WST experiment usually ends before the P_{sp} fully declines to zero; therefore, the remaining area under the tail of the P_{sp} -CMOD curve is estimated using the following equation (Ulfkjaer and Brincker, 1995):

$$G_{F(tail)} = \frac{P_{sp1} \cdot w_1}{h \cdot t} \quad (3.9)$$

where P_{spl} stands for the splitting load at the end of the experiment; w_l stands for the corresponding crack opening on the P_{sp} -CMOD curve; and, h and t represent the ligament length and the specimen's thickness, respectively (i.e., fracture area).

However, in many circumstances, the structure fails before the crack is fully developed. In such a case, the response is as if the stress vs. crack opening curve were given by its initial linear approximation (RILEM TC 187, 2007) as shown by the dashed line in Figure 3.4.

According to the cohesive fracture model, G_F is defined as the energy required to overcome the cohesive stress when separating two surfaces, and can be calculated from the area under the P_{sp} -COD curve, measured at the initial crack tip (Shah et al, 1995). The traditional approach would overestimate the G_F unless it is calibrated. This is due to a higher estimate of the magnitude of the COD as measured at the position of the clip-gauge, above the crack tip. The variation between the two values is due to the distance between the clip gauge position and the notch tip position. In fact, the rate of variation increases as the rate of the crack opening increases. This is because the rotation angle that is formed between the two locations increases as the crack opening increases (Figure 3.17). Under these circumstances, this overestimated value for G_F could lead to a weak design.

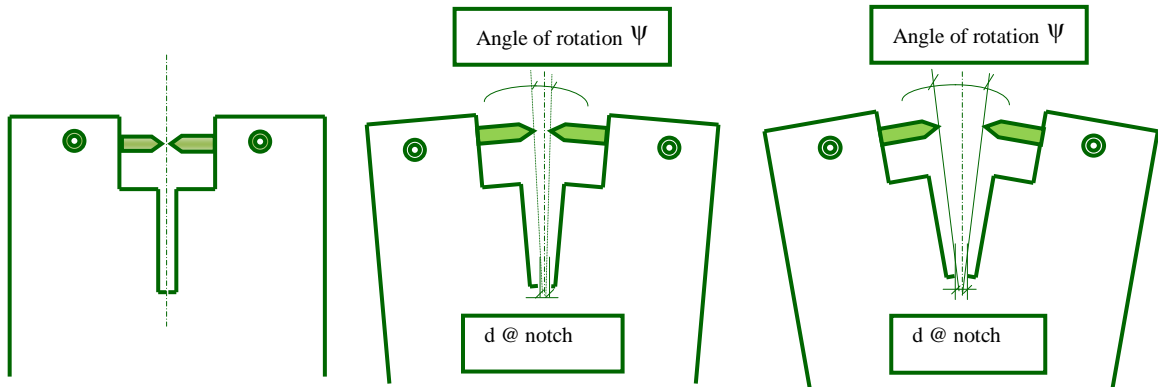


Figure 3.17: The effect of the angle of rotation on COD reading at the clip gauge and the notch tip

Table 3.2 summarises the concrete mechanical and fracture properties of the six specimens, including: the compressive strength, tensile strength, fracture energy, characteristic length, brittleness number, and Young's modulus, in addition to the CMOD at the peak load.

Table 3.2: Experimental findings for the WST using traditional methods
(clip gauge, CG)

WST	Age (days)	f_c (MPa)	E_c (MPa)	f_t (MPa)	G_F (N/mm)	l_{ch} (mm)	β	Peak Load (kN)	CMOD (mm) @ peak load
1	81	49	31500	2.8	0.115	462	0.43	9.0	0.092
2	90	49	31500	2.8	0.111	448	0.45	9.6	0.065
3	90	49	31500	2.9	0.100	374	0.53	11.2	0.083
4	116	50	31820	2.9	0.108	408	0.49	12.8	0.077
5	97	49	31500	2.9	0.119	446	0.45	12.9	0.078
6	236	52	32450	3.2	0.131	415	0.48	16.4	0.072

WST1, WST3, WST5 specimens are made from the same concrete batch

3.7 Experimental Investigation of an alternative approach: Digital Image Correlation (DIC)

An accurate measurement of the crack tip opening displacement (CTOD) is required to determine the fracture parameters of a concrete structure. Furthermore, detection of the development of the *FPZ* and crack evolution is not possible using traditional methods. In addition, as mentioned previously, G_F generated directly from the area under the P_{sp} -CMOD curve is overestimated. Several non-contact techniques have been used to measure COD, but suffer from low measurement accuracy, laborious post-processing, or high sensitivity to environmental temperature, air draft, or vibrations from testing machines. The demand for non-contact and non-disturbed deformation measurements has led to the development of a new technique based on optical

measurement that is capable of monitoring the *FPZ* and crack evolution, in addition to providing an accurate measurement of the CTOD.

Optical techniques have proven to be particularly promising tools for characterizing the properties of engineering materials, especially systems exhibiting inhomogeneity. DIC is an optical technique for visualizing surface deformations, and is based on post-processing of digital images which uses image recognition to analyze and compare digital images obtained from the surface of a substrate during testing. DIC provides a non-disturbing and non-contact measurement tool that is able to analyze the displacement and strain fields over an entire surface. Because DIC is a non-contact measuring technique, information about the displacement, strain, and detection of crack evolution and development of the *FPZ* are obtained without interference from the testing machine's vibration. Since the images of the specimen cover the entire area of interest, this technique is not restricted to a single axis measurement or to specific points as is the case with most gauge-based measurement techniques. Consequently, the displacement and strain can be measured at any point on the surface. In the case of fracture mechanics, the measurement of CTOD at the notch tip can be determined directly from analysis of the images. Utilizing direct measurement of the CTOD, accurate estimates of G_F can be made from a work-of-fracture test. By tracking the crack path, the variation of the dissipated energy and the crack opening along the crack path can also be estimated. Lastly, the quality of the images, which directly affects the accuracy of the results, can be checked before and after the test.

DIC was originally introduced in the early 1980's by researchers from the University of South Carolina (Peters and Ransom, 1982). Currently, DIC is widely used to examine the deformation of engineering materials, including concrete and related cement-based materials (Choi and Shah, 1997; and Lawler et al., 2001). More recently, the DIC method has been extended for use with two stereo cameras with different viewing angles, to measure 3D displacement fields.

The DIC technique is based on inferring the displacement of the material being tested, by tracking the deformation of a random speckle pattern on the specimen's surface. Mathematically, this is accomplished by finding a region in the image with a deformed configuration that maximizes a normalized cross-correlation score with a small subset of the reference image that was taken while no load was applied. By repeating this process for a large number of subsets, full-field deformation data can be obtained. A single camera DIC system is able to measure in-plane deformations, while a system with two cameras is needed to obtain a 3D measurement of the displacement and strain. Macro-image facets, which represent virtual gauges, are areas created throughout the image using sets of pixels (typically 5-20 pixels per side) distributed across the image, thus allowing sub-pixel accuracy (Tyson, 2001). The number of facets within an image depends on the cameras' resolution, as well as the defined size and overlap of the facets; however, it is possible to define thousands of facets across an image. A 13 x 13 pixel facet with a 2 pixel overlap allows for the formation of over 10,000 facets on an image with a resolution of 1280 x 1024. The ideal facet has several discrete pixels within it, the centre of each of these facets provides surface coordinates, and the locations of these

facets are tracked through a series of images called 'stages'. When a specimen is loaded, its surface image deforms in response to loading, and at each stage the displacement values can be obtained in relation to a reference stage. Typically, the initial image at zero loading is taken as the reference frame from which the reference measurements are taken. The accuracy of results obtained by DIC techniques depends on many factors, including the resolution and configuration of the cameras used, the quality of the light source, the accuracy of the calibration, and the quality of the surface pattern. In addition, the displacement sensitivity increases while increasing the field of view. High sensitivity can be obtained using DIC, with a displacement sensitivity on the order of 1/30,000 of the field of view (Tyson, 2001), while strain sensitivity is constant (50-100 Microstrain).

For this research study, an alternative approach to the evaluation of fracture tests based on optical measurements of displacements (using DIC) was conducted using the ARAMIS1.3M system (GOM mbH, Braunschweig, Germany), which is manufactured by Gesellschaft fur Optische Messtechnik (GOM), a global industry partner involved in developing and producing optical measurement solutions and technologies for 3D coordinate measurement and deformation analysis (GOM, 2012). ARAMIS is a commercial DIC deformation measurement system, which analyzes, calculates and documents material deformations. The data post-processing software provided with ARAMIS examines the correlation between stereo images of subsequent loading steps, and computes relative displacements of characteristic features or points on the digital images. The hardware in the ARAMIS DIC system includes a pair of cameras (mounted on a rigid bar to avoid relative motion of the cameras), a tripod, an extension arm, a

Rack-Mount computer with associated software to evaluate the deformation (displacement and/or strain), in addition to various calibration panels (ARAMIS, 2005). The DIC method does not require the use of lasers, and the specimen can be illuminated by means of a white-light source. Figure 3.18 illustrates the hardware components of the ARAMIS 3D system (setup with 2 cameras).



Figure 3.18: The hardware components of the ARAMIS DIC system (GOM mbH)

3.7.1 Specimen Preparation

To calculate the amount of displacement and deformation on the surface of a specimen with DIC, a random pattern is needed on the surface. This pattern can either exist naturally or can be applied to the specimen's surface. Among the many methods available for pattern application are self-adhesive, pre-printed patterns, stamps, and paint speckles applied with air-brushes or spray cans.

For our study, preparation of the WST-specimen involved grinding the surface, and then cleaning it with high levels of air pressure to remove all loose particles. A flat white paint was then applied to the WST-specimen's surface. After this step, a black speckle pattern was applied using spray paint in order to create a sharp contrast with the white surface coating, and to provide a surface pattern from which displacement measurements will be taken using the ARAMIS system (Figure 3.19).

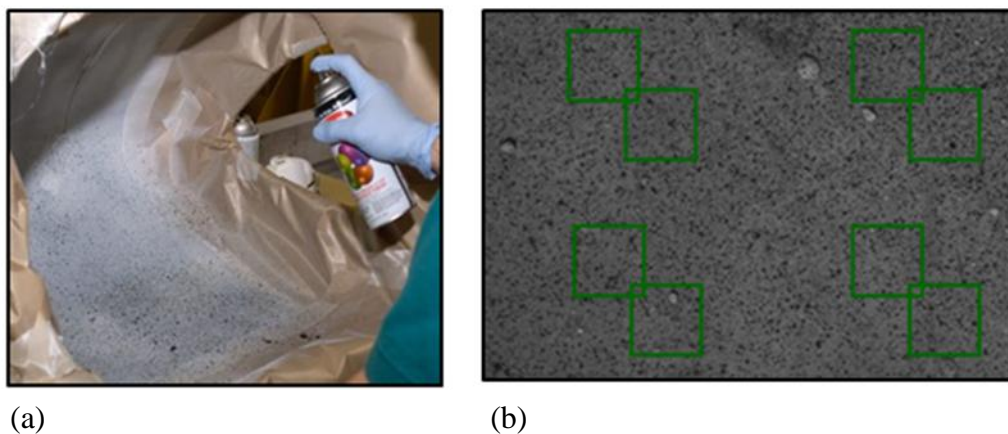


Figure 3.19: (a) Preparing specimen for measurement with the ARAMIS system, (b) Macro-image facets, or virtual gauge areas, are created throughout the image using sets of pixels.

3.7.2 ARAMIS System Calibration Process

Before starting the test, the ARAMIS 3D system needs to be calibrated. The measurement volume needs to be defined according to the size of the object to be measured (e.g. the size of the WST-specimen), which determines the optimal size for the calibration object (i.e., calibration panel). A prerequisite for successful calibration is the correct setup of the sensors, including the cameras' lenses; therefore, both cameras should be equipped with appropriate lenses, which correspond to the measuring volume (calibration panel). Due to the availability of optical lenses, the largest calibration panel that could be used in this study was 65 mm x 52 mm (Figure 3.20), which limits the area of the WST-specimen that can be measured.

In addition to determining the optimal set of lenses, the measuring volume controls the distance between the cameras and the distance between the sensors and the object specified by the supplier (GOM). The calibration procedure was provided by GOM, and involved taking a series of images of the center, front, and back boundaries of the calibration volume established with the calibration panels, using the two cameras together, and each camera individually. This calibration process determines the location of the calibrated volume with respect to each of the cameras, and allows the ARAMIS system to relate the digital image data obtained from each camera. This calibration procedure ensures that the DIC system will compute accurate displacement and strain measurements.

The camera angle was also adjusted by assuring that both cameras were focused on the same point on the surface of the object that would be measured in the live images. Then, the focus and shutter time were adjusted, so that no overexposed areas were visible, and a printed sheet of paper could be read easily at the selected measuring distance. The final adjustment was to the camera apertures after switching on the light source and setting the shutter time between 0.1 ms and 2 sec; the aperture should be closed as much as possible in order to achieve a good depth of field, ensuring that the images are free from overexposure (red pixels). The aperture of both cameras should be closed to approximately the same extent; this was checked by means of the false-colour mode of the video image, which should show approximately the same colour distribution in the images from each camera.



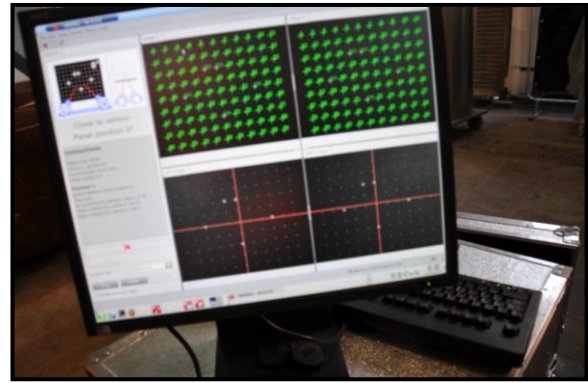
Figure 3.20: Calibration Panel (65 mm x 52 mm)

The first five calibration pictures establish the geometry of the camera setup and the absolute distance measurements as shown in Figure 3.21(a). Then, four pictures were taken with each camera separately in order to characterize the camera/lens combination throughout the field of view as shown in Figure 3.21(b).

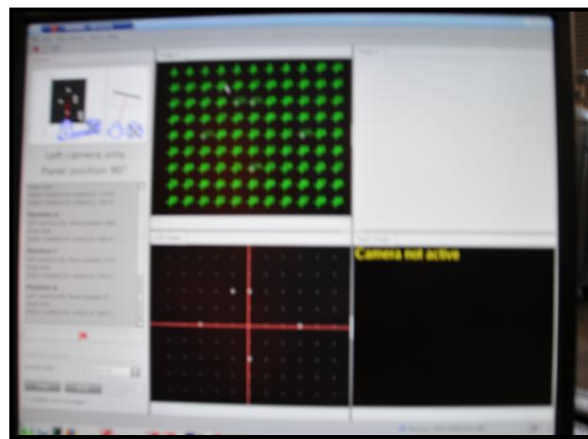
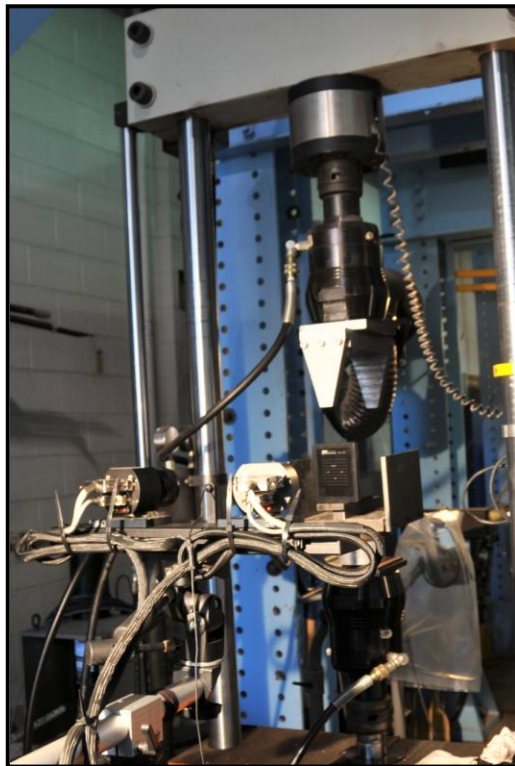
Upon completion of the calibration process, a calibration deviation value was determined by the ARAMIS system, which represents the average deviation between each camera throughout the calibration process. Based on a maximum calibration deviation value of 0.035 pixels, the limit used throughout testing for acceptable calibration was 0.04 pixels.

To further validate the calibration process and ensure that the quality of the speckle pattern applied to the surface of the WST-specimen was suitable for DIC, a series of images was taken before starting the test. Since no load was applied to the specimen, negligible displacement values were expected, and this was confirmed with DIC.

In addition, the recording mode of the DIC system requires that the area in the images to be evaluated and analyzed is not overexposed. Prior to image recording, a live image was checked to assure that the brightness distribution was suitable for DIC analysis. This was done by means of the false-colour setting; in this mode, no white or blue-black areas should be visible in the images.



(a)



(b) **Figure 3.21:** Calibration process for the ARAMIS system (a) using both cameras, (b) using left camera

3.7.3 Testing Procedures

After preparing the surface of the WST-specimen and calibrating the cameras as described in Sections 3.7.1 and 3.7.2, the painted specimen was placed on a linear support. The clip-on-gauge was mounted between two knife edges attached to the specimen (Figure 3.11), and the CMOD was controlled and measured, so that the data could be used as reference points for the purpose of comparison. Before starting any test, several baseline images were taken to confirm the quality of the paint pattern and to validate the calibration process with no load applied. During loading, images of the specimen were recorded at various loading stages. To ensure that both cameras were aimed at the same point on the specimen during the test, after the images were captured, but before performing the DIC analysis, a starting point or target was positioned on a specific speckle in the right image, which should be identified automatically by the ARAMIS system in the left image. As the WST-specimen was expected to separate into two pieces after failure, two starting points or targets were placed on the specimen's surface (one on each side), and their placement verified in all images. After these starting points were created and verified in all of the images captured during testing, the calculation aspect of the project was initiated through the DIC system's computation mode. When the computation was complete, the ARAMIS system automatically switched to evaluation mode for analysis of the system's performance.

The distortion of the pattern on the specimen's surface allows calculation of the displacement at the region of the crack/notch tip from each recorded image, and the CTOD was calculated from the resulting displacement values. The displacement at each

loading stage was measured with respect to the initial unloaded stage, defined as the first recorded image of the un-deformed specimen. To associate a particular stage (or image) to a specific load, the load values were measured by the INSTRON testing machine with an MTS controller, and recorded by the ARAMIS data acquisition system using a BNC connector cable. Figure 3.22 depicts the ARAMIS system during the test, including the computer screen showing a view of the WST-specimen; the crack-path taken by both cameras is visible. Figure 3.23 illustrates a specimen from a failed test.

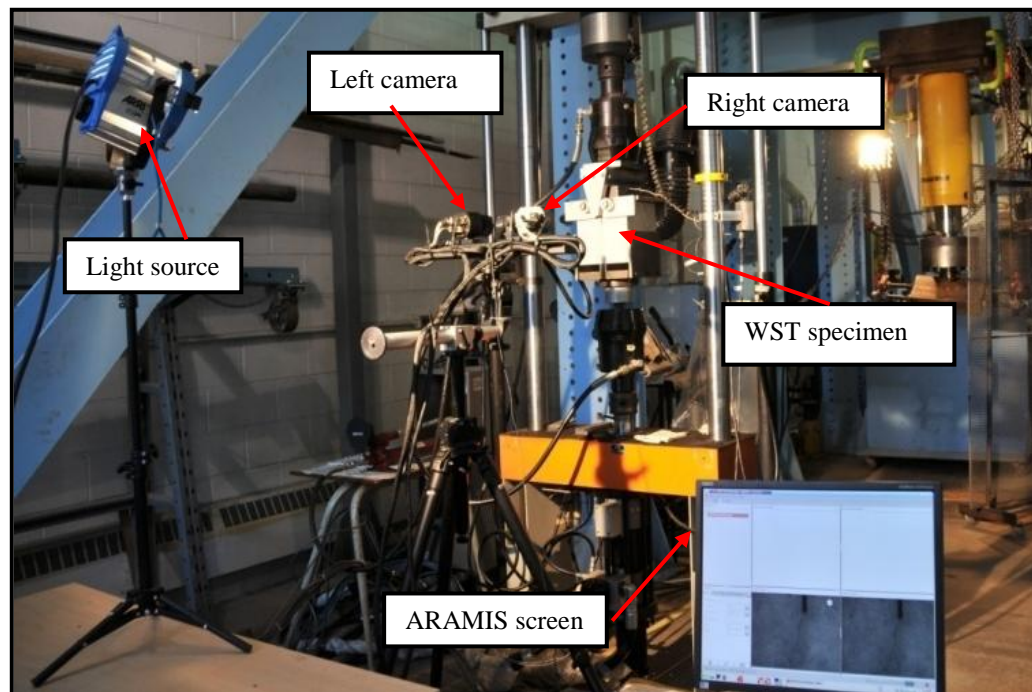


Figure 3.22: Experimental set-up for the WST with the ARAMIS data acquisition and DIC analytical system

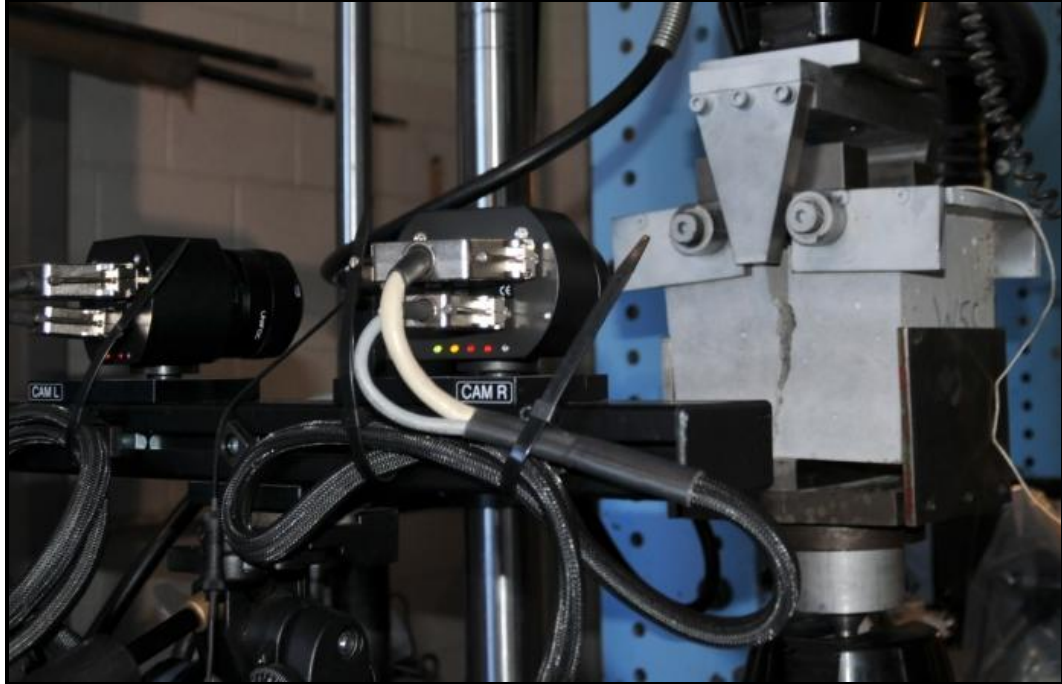


Figure 3.23: ARAMIS cameras and WST-specimen separated into two pieces after failure

3.7.4 Experimental Results using the DIC Technique

The CTOD was measured at the notch tip as shown in Figure 3.24. Using the ARAMIS system, the CTOD value was obtained by computing the length change of the horizontal segment created at the notch tip (Figure 3.25) for each loading stage with respect to the reference value from the zero load condition, as illustrated in Figure 3.26. Figure 3.27 shows a screen-shot from the ARAMIS system taken during the computation of CTOD, as well as the final report of the results.

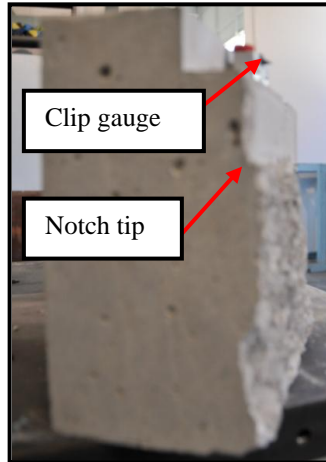


Figure 3.24: The position of the notch tip and clip gauge when the CTOD and CMOD were measured

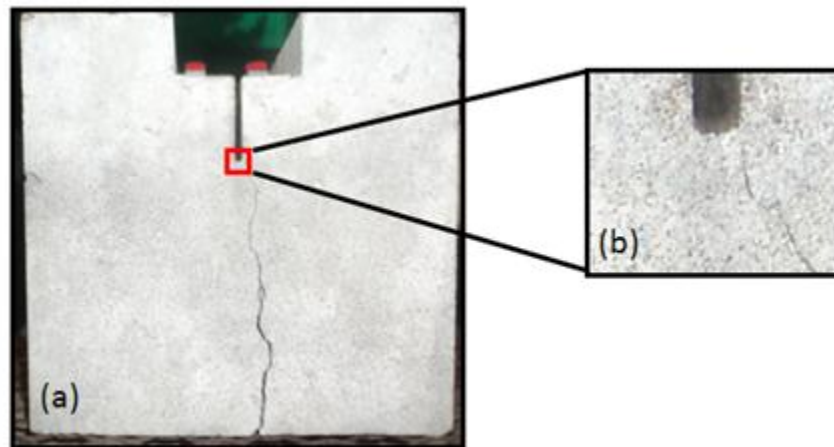


Figure 3.25: (a) WST-specimen after failure, (b) magnified view of the notch tip area (calibrated space)

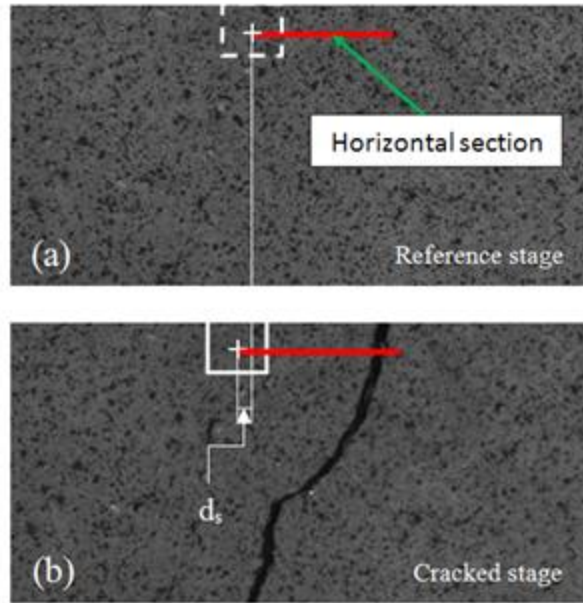


Figure 3.26: Displacement calculation (d_s) using the ARAMIS DIC system (a) reference stage (zero load), (b) loaded stage

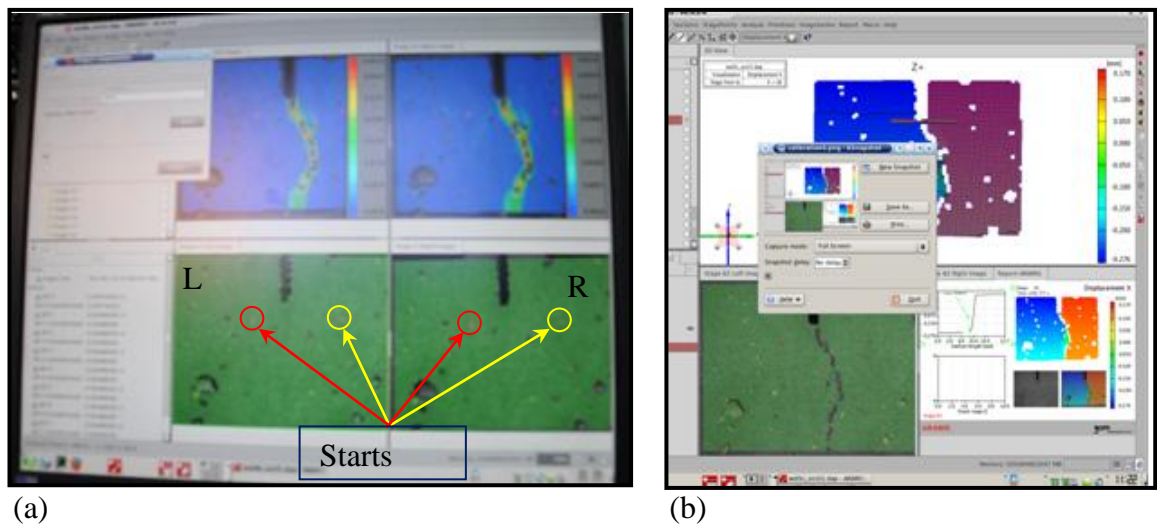


Figure 3.27: (a) Screen-shot from ARAMIS during project computation with the location of start points on each side of the specimen (b) ARAMIS report after finalizing the computation

Data was collected with a traditional clip-on gauge and with the DIC cameras simultaneously. The CTOD (from the same six WST-specimens used to measure CMOD with the traditional clip-on gauge technique; see Section 3.6) were determined using the DIC technique, and the results are shown in Figure 3.28. The experimental outcomes for the DIC analysis are represented by the splitting load-crack tip opening relationship (P_{sp} -CTOD).

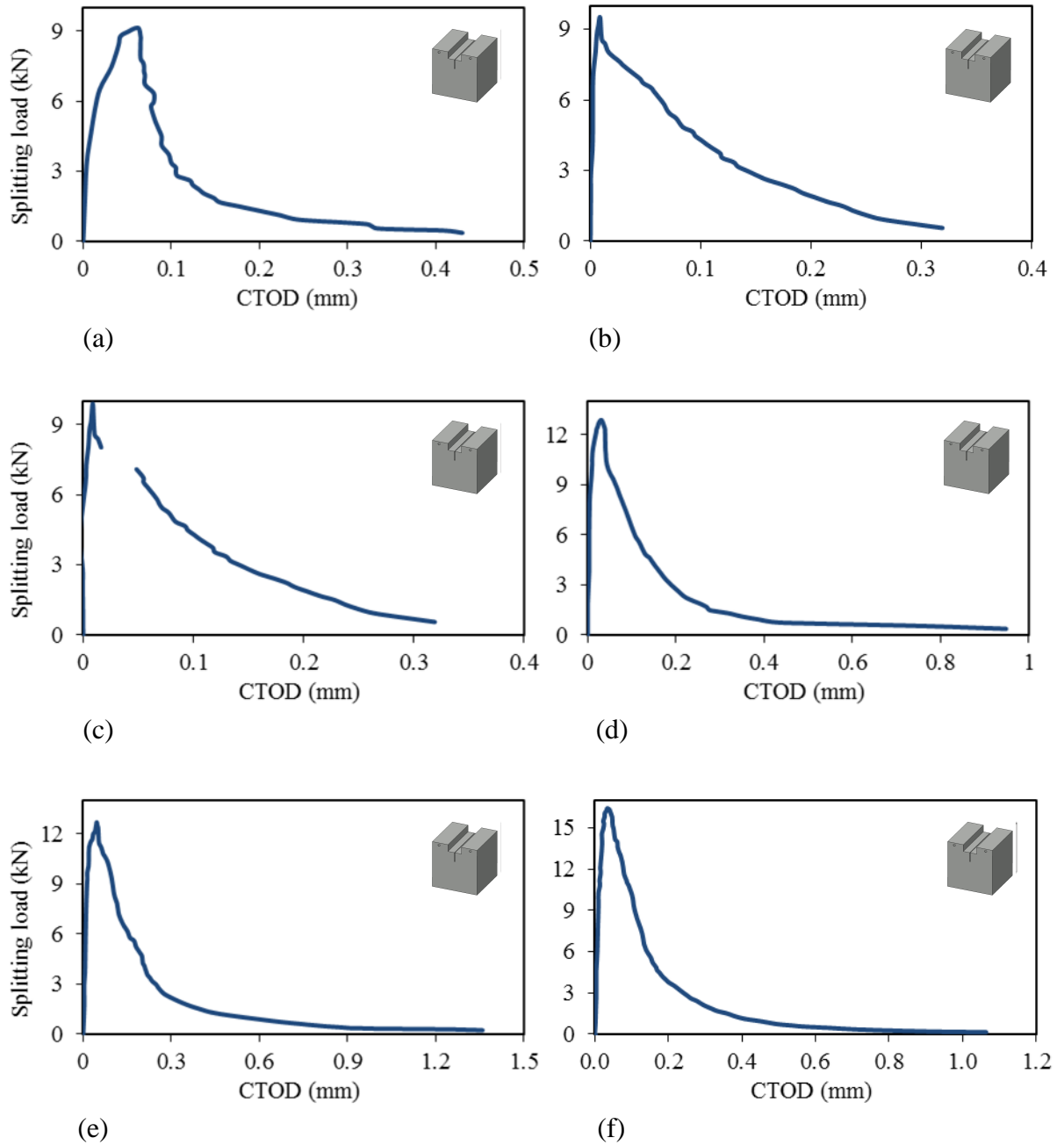


Figure 3.28: Experimental results from the WST obtained using DIC. (Figures a, c, and e are made from the same concrete batch). (a) WST1 at 81 days, (b) WST2 at 90 days, (c) WST3 at 90 days, (d) WST4 at 117 days, (e) WST5 at 97 days, (f) WST6 at 236 days

The above figure shows the softening behaviour of concrete specimens of different ages in the WST as measured using the DIC technique. Note that the tail of the softening portion of the P_{sp} -CTOD curve of specimens WST2, and WST3 are not fully demonstrated as it is for the other specimens, which was caused by a technical problem. The softening curve for specimen WST3 is incomplete. The missing portion may be due to a problem with the lighting.

Table 3.3 summarises the mechanical and fracture properties of the six concrete WST-specimens that were determined using the DIC technique. These properties include: the compressive strength (f_c), tensile strength (f_t), fracture energy (G_F), characteristic length (l_{ch}), brittleness number (β), Young's modulus (E_c), as well as the CTOD at the peak load. For the determination of the G_F and because the experiments ended before the load decreased to zero, the end portion (tail) of the P_{sp} -CTOD curve was estimated using the same equation as was used for the traditional method (Section 3.6, Equation 3.9).

Table 3.3: Experimental results from the WST using digital image correlation (DIC)

WST	Age (days)	f_c (MPa)	E_c (MPa)	f_t (MPa)	G_F (N/mm)	l_{ch} (mm)	β	Peak Load (kN)	CTOD (mm) @ peak load
1	81	49	31500	2.8	0.094	378	0.53	9.0	0.062
2	90	49	31500	2.8	0.05*	201*	0.99*	9.6	0.009*
3	90	49	31500	2.9	0.05*	187*	1.06*	11.2	0.007*
4	116	50	31820	2.9	0.081*	306	0.65	12.8	0.031
5	97	49	31500	2.9	0.099	371	0.54	12.9	0.046
6	236	52	32450	3.2	0.092	291	0.69	16.4	0.034

WST1, WST3, WST5 specimens are made from the same batch

*These values are considered unreliable, as explained above.

Table 3.3 indicates that the results obtained with the DIC technique seem to be more reliable than results obtained using the traditional ‘clip-on gauge’ method (apart from the incomplete test results for WST2 and WST3). This improved reliability is attributed to the new DIC technique’s capability of giving more accurate results (e.g. l_{ch} falls within the range of 100 mm to 400 mm described by Shah et al. (1995) for all specimens with complete results) because displacement at the crack opening was obtained at the crack tip (CTOD) rather than the crack mouth (CMOD). CTOD coincides with the definition of the G_F , and l_{ch} depends on G_F since $l_{ch} = G_F E_c / f_t^2$.

3.8 Comparison of the Experimental Results for the Traditional and DIC Technique

In this chapter, the experimental observations obtained during the WST using non-contact and non-disturbing optical measurements of displacements during loading

were investigated. In addition, experimental data from the WST specimens were collected, as a reference and for comparative purposes, using a traditional method involving direct contact with the specimen (Table 3.2); in this contact-based technique, the crack mouth opening displacement (CMOD) was measured using a clip-on gauge. [Note that COD is a general term for crack opening displacement at any position. In this study, COD is termed ‘CMOD’ when the displacement is measured near the crack mouth using a clip-on gauge; whereas, the term CTOD is used when the displacement is measured at the crack tip using the DIC technique]. Figure 3.29 shows that the crack opening displacement (COD) measured using DIC (i.e., CTOD) is generally lower than the displacement measured with the clip-on gauge (CG) (i.e., CMOD).

Prior to the propagation of micro-cracks, at approximately 30% of the peak load, the results for both CG- and DIC-derived curves are comparable; at that point, the discrepancy between the P_{sp} -COD curves (P_{sp} -CMOD, P_{sp} -CTOD) increases gradually with loading, until the peak load is reached. Beyond the peak load (i.e., where load declines while COD increases), the gap between the CG and DIC curves continues to increase until the P_{sp} -COD curves begin to tail off; at this point, the discrepancy is reduced, and the curves are approximately the same and tend to overlap. The discrepancies between the two curves are affected by the distance between the CG position (located near the crack mouth) and the crack tip (where the data for the DIC was extracted). In fact, the degree of variation between the curves increases as the crack opening widens because of the angle of rotation formed between the two locations (mouth and tip) on the opening crack (see Figure 3.17). Since the CMOD is very small

for light loads (applied loads $< 30\%$ of the peak load), the effect of the angle of rotation is negligible, so both the CG- and DIC-derived curves were comparable for this range of loads. The COD determined with the CG is overestimated; therefore, the G_F calculated from the area under the P_{sp} -CMOD curve is also overestimated using CG data. The traditional CG method overestimated the value of the G_F by more than 16% (compare Tables 3.2 and 3.3). Thus, accurate values for G_F can be calculated using DIC measures without the need for further calibration of the results (such as that required for the traditional method's CG results). The same conclusion can be extended to other derived properties, such as l_{ch} and β , since these properties are also functions of the G_F (see Equations 3.5 and 3.6).

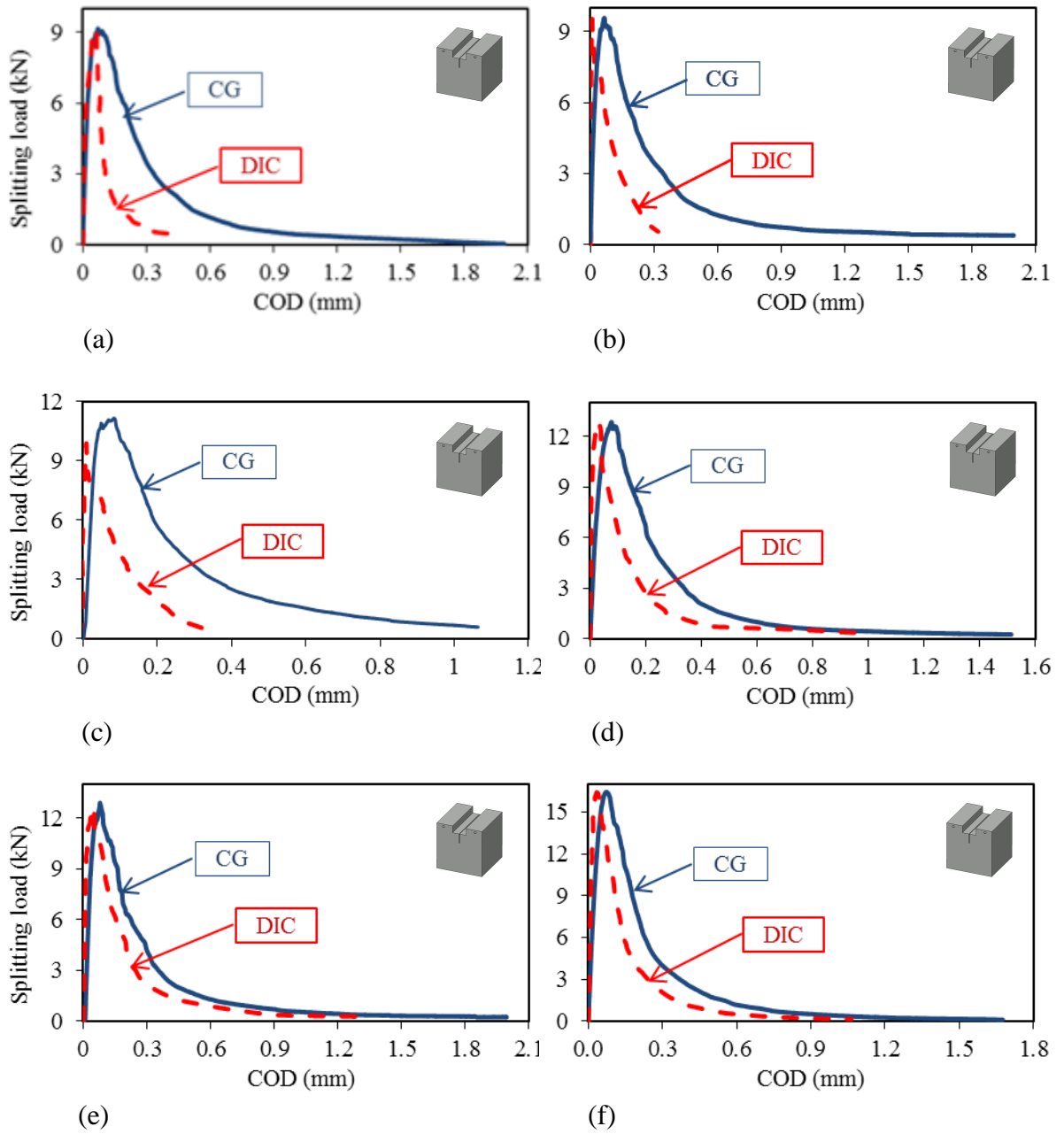


Figure 3.29: P_{sp} -COD curves from WST on concrete specimens of various ages, obtained by contact (CG) or non-contact (DIC) measurement techniques (a) WST1 at 81 days, (b) WST2 at 90 days, (c) WST3 at 80 days, (d) WST4 at 117 days, (e) WST5 at 97 days, (f) WST6 at 236 days

Despite the differences between the CG and DIC results illustrated in Figure 3.29, there is no doubt that it is possible to determine the P_{sp} -COD relationship with different techniques, and that the CG and DIC findings are comparable for small loads (<30% of the peak load). Nevertheless, the non-contact DIC method is useful over the full range of applied test loads, and the results obtained with DIC are more accurate than those obtained with the traditional CG method, as DIC is: 1) not affected by the distance between the position of the sensor and the crack tip throughout the test (i.e., angle of rotation; Figure 3.17), and 2) is not affected by machine vibration and/or instability caused by cracking of the specimen or other effects of direct contact between the sensor (e.g. CG) and the specimen. Furthermore, the COD can be measured without restriction at any position of interest on the surface of the specimen (e.g. CTOD, CMOD, etc.).

Consequently, the P_{sp} -COD curves obtained with both measurement techniques (CG or DIC) agreed reasonably well with each other as long as the differences between the measuring positions for the two methods are considered when deriving properties from the experimental data; in this study, the CG measures were obtained near the crack mouth, while the DIC measures were extracted from the crack tip. Nevertheless, comparison of the two techniques supports the use of the non-contact DIC method over traditional contact methods such as CG, for the reasons outlined and illustrated in this chapter. This study of the WST on specimens of various ages shows that DIC is capable of monitoring crack propagation on the surface of concrete structures, and can do so more accurately and without the limitations of traditional methods.

3.9 Experimental Investigation of Crack Evolution and Development of the FPZ using the DIC Technique

It is well established that prior to any loading, concrete already contains naturally distributed internal defects. When loading starts and during concrete fracture, a state of high-stress near the crack tip causes micro-cracking at these flaws. The mechanical behaviour of concrete subjected to different loading conditions is governed by the initiation and propagation of these internal cracks and flaws during loading (Shah et al. 1995). The micro-cracking region in front of the traction-free crack tip in concrete is referred to as the *FPZ* (Hillerborg et al., 1976). The fracture behaviour of concrete is influenced by the *FPZ* in the front of the crack tip. As realized by Shah and McGarry (1971), Linear Elastic Fracture Mechanics (LEFM) cannot be directly applied to concrete due to the presence of this sizable zone. Other difficulties for using fracture mechanics to describe concrete performance include: the tortuous crack path, and the difficulty of determining the location of the crack tip in concrete due to aggregate bridging, and the *FPZ* size that is closely related to the G_F (Wittmann and XZ, 1991). Consequently, in addition to the crack tip opening displacement (CTOD), an accurate description of concrete fracture should include the following features: the tortuous crack path, the position of the crack tip, the dissipated energy along the crack path, the length of the *FPZ*, and the 3D aspects of the crack profile (i.e., variation of the crack path and *FPZ* along the thickness dimension).

The experimental identification of the *FPZ* in concrete is difficult because the localized deformation around the crack tip cannot be measured accurately by

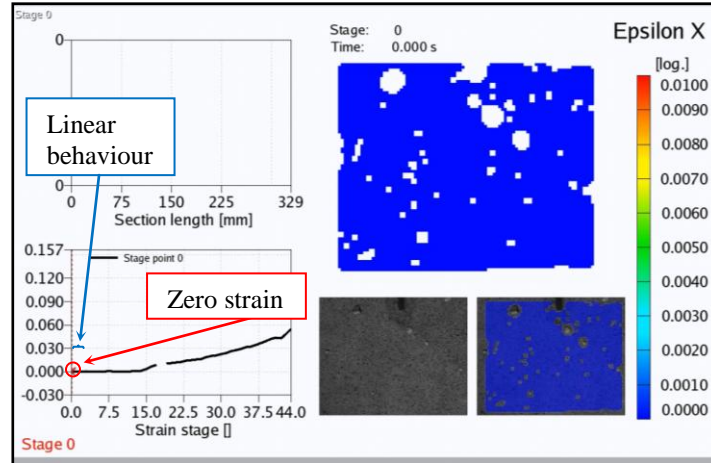
conventional gauges. However, the development of a *FPZ* associated with stable crack growth in the WST can be monitored using a non-contact measurement technique such as DIC. In this section, the author proposes to exploit the capability of DIC to measure local displacement and strain around the crack tip to study the extension and size of the *FPZ*. DIC makes it possible to study the dynamics of crack propagation by monitoring the evolution of energy dissipation during the fracture process. Attention is also paid to the changes in the crack tip position associated with the evolution of the crack path, toughening mechanisms in the *FPZ*, and variation in the energy dissipated along the crack path.

3.9.1 Evaluation of Toughening Mechanisms in the *FPZ* with DIC

The mechanisms underlying the deformation of concrete that occurs during loading and beyond the proportional limit, f_y , are not clearly understood (Shah et al. 1995); the commonly held views about the reasons for the mechanical deformation that occurs beyond f_y were summarized in Chapter Two. In order to provide clearer and more detailed information about the mechanisms producing this deformation, the output that was obtained using the DIC technique is discussed in this section.

Figure 3.30 shows the strain distribution, assessed using DIC, over an area of interest around the initial crack tip of a WST-specimen (WST2). The ARAMIS system's report in Figure 3.30 (a) includes the WST-specimen prior to loading with zero strain, and the linear behaviour of the concrete up to 21% of the peak load (f_y of 2 kN). The

white spots represent holes on the concrete specimen's surface and/or the surface areas that were poorly lit, so were not recognized by the DIC process. Figure 3.30 (b) Stage 6 shows that micro-cracks started propagating at loads $> f_y$ with a slight increase in strain. The aggregation of micro-cracks into a localized major crack (macro-crack) began at loading of approximately 8.8 kN (92% of the peak-load) as shown in Figure 3.30 (c) Stage 9.



(a) The WSt-specimen (WST2) prior to loading and DIC report

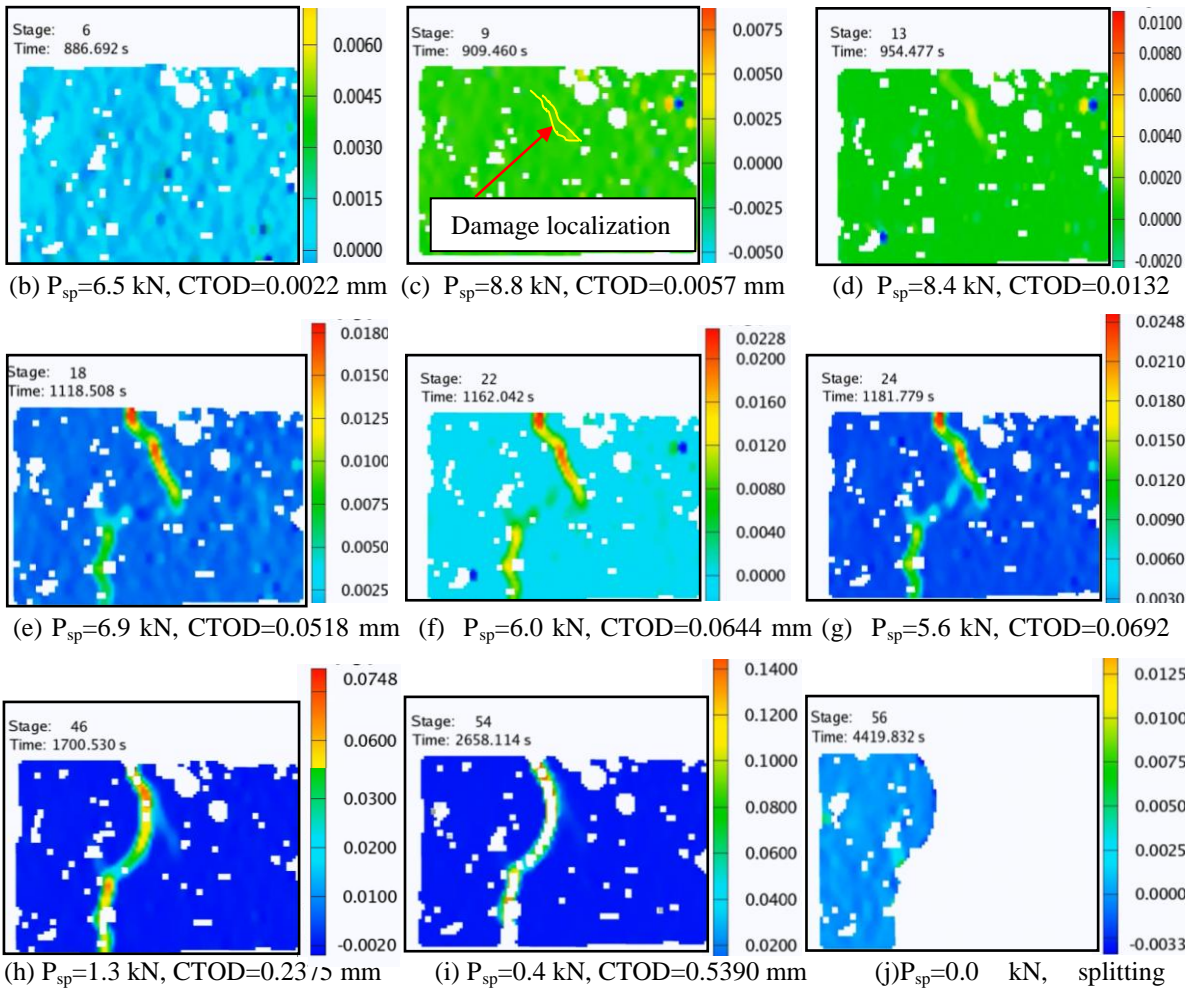


Figure 3.30: Evolution of the crack path and toughening mechanisms assessed using DIC in the WST2. Stages 0 to 9 present the strain distribution before the peak load was applied, and the post-peak or softening behaviour is illustrated from Stages 13 to 56.

The softening behaviour of concrete is evident in the steady state propagation of the crack in the *FPZ*, which is due to concrete's toughening mechanisms, such as aggregate bridging and crack deflection. The displacement observed during the post-peak stages consisted of the opening of a major crack accompanied by gradual unloading of the rest of the specimen as the strain value starts to decrease; this is obvious in Stage 46 where the strain is localized around the *FPZ*, and there is almost zero strain outside this area.

Toughening mechanisms related to concrete heterogeneity that appeared in the *FPZ* were detected using DIC. One of the important toughening progressions in concrete is aggregate bridging, which could be seen between Stages 18 and 46 (Figure 3.30). Although the crack had advanced beyond the aggregated concrete particles, the aggregate continued to transmit stress across the crack until it either ruptured or pulled loose. Since the crack surfaces were still in contact, they continued to sustain some tensile stress as characterized by the material σ - w relationship. During either aggregate pull out or opening of the tortuous crack (as demonstrated in Stages 18 to 46 of Figure 3.30), and because of the interlock between the crack faces, a small strain at the aggregate bridging area was detected in comparison to the strain on the crack path. This phenomenon was accompanied by a small increase in the CTOD, followed by a sudden increase in CTOD when the aggregate's rupture was complete as can be seen in Figure 3.30 (i). This jump occurred because of the sudden dissipation of the energy required to rupture the aggregated particles, accompanied by the opening of new crack surfaces to complete the crack path, as illustrated in Stage 54 of Figure 3.30.

Crack branching through the development of a secondary crack is shown in Stage 24 of Figure 3.30. However, this branch started closing during the rupture of the aggregate particles as can be seen in Stages 46 to 54 of Figure 3.30. The secondary crack, which was dissipating some of the energy, was closed by the complete rupture of the aggregate particles. It is interesting to note that the time needed to split the specimen was 3994 seconds, which is approximately thirty times the time needed to reach the peak load (134 seconds). This gives an indication that the test was stable which was controlled by a constant rate of crack opening.

The traction free zone for specimen WST2 was introduced at 25% of the peak-load during the post-peak phase (Figure 3.31), with 5 mm crack extension and CTOD equal to 0.173 mm.

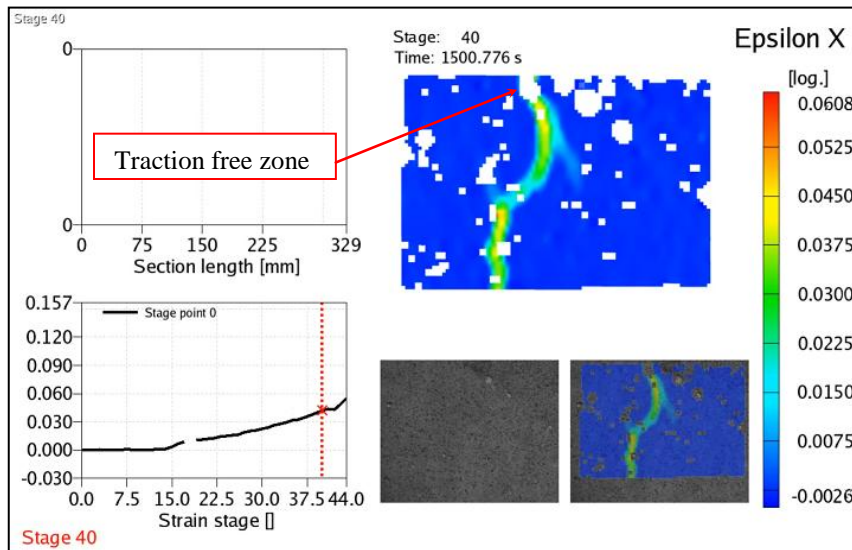


Figure 3.31: The WST-specimen (WST2) supplemented with ARAMIS system’s report at 2.4 kN during the post-peak phase (25% of the peak load) with CTOD = 0.173 mm

Figure 3.32 shows the effect of crack deflection on the WST-specimen when the path of least resistance was around a relatively strong aggregate or along a weak interface. Crack bridging is also evident in this figure when the crack had advanced beyond an aggregate that continued to transmit stress across the crack until it ruptured. These mechanisms cause energy dissipation during aggregate rupture or the opening of a tortuous crack path as some interlock occurs between the cracked faces. Crack branching through the development of a secondary crack is also demonstrated in this figure, but this secondary crack closed during the final stage (at failure) due to the crack surface roughness-induced closure mechanism (Pokluda, 2005).

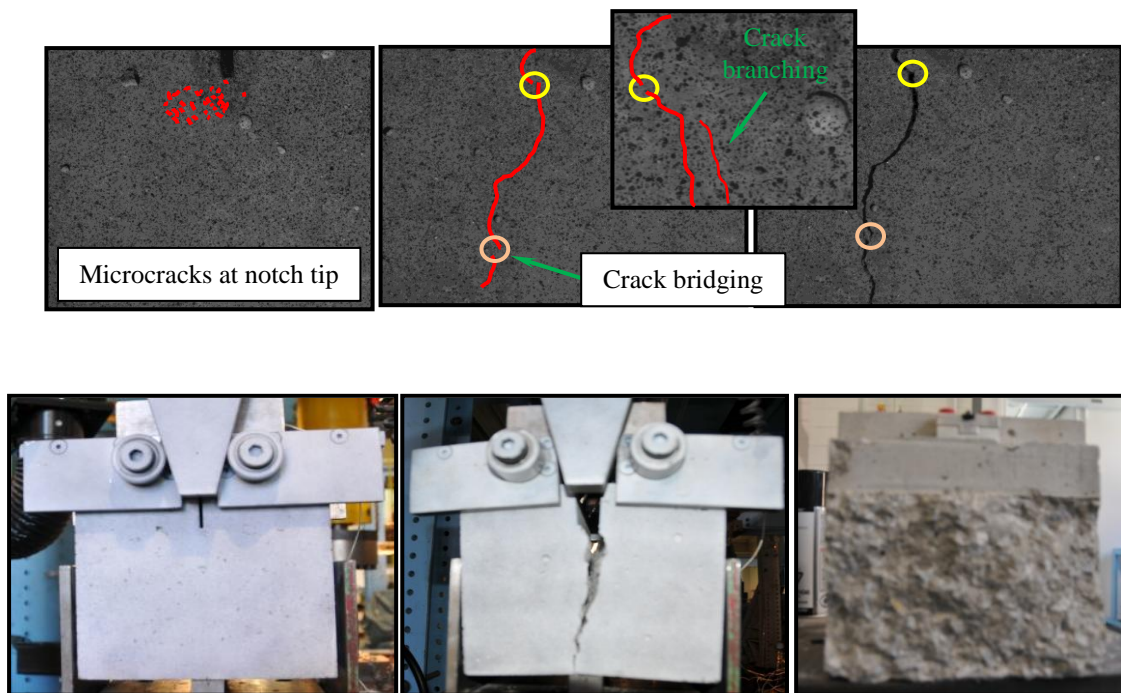


Figure 3.32: Toughening mechanisms on the surface of the WST-specimen

3.9.2 Assessing the Variation of FPZ Size and Crack Evolution with DIC

Accurate assessment of the length of the *FPZ* is essential for predicting the failure of concrete members and for selecting the appropriate dimensions for test specimens (Li and Marasteanu, 2010). As noted earlier (Section 3.9.1), one of the difficulties encountered when investigating the development of the *FPZ* in concrete, including its length, is the determination of the crack tip's precise position due to the impact of aggregate bridging and variation of the crack path across the structure's depth.

The WST-specimen, WST2, was chosen to illustrate the DIC procedure used to determine the *FPZ* length and the measurement of the COD along the crack path. Figure 3.33 shows the computational domain at the crack tip that includes part of the ligament length of the WST-specimen where the *FPZ* was tracked using DIC. The size of this computational domain was limited by the size of the calibration panel that controls the size of the measuring volume (Section 3.7.2); a larger calibration panel and different lenses, (not available for this study), are required to cover the whole specimen (crack path). It should be noted, however, that the accuracy of the computation declines with increased measuring volume. Thus, parallel sections were assigned along the crack path and used to assess the fracture within the assigned computational domain. To ensure that the crack passes through the mid-points of all sections comprising the computational domain, all of the sections were assigned after the crack path was revealed and the experimental observations were computed and evaluated by the ARAMIS DIC system.

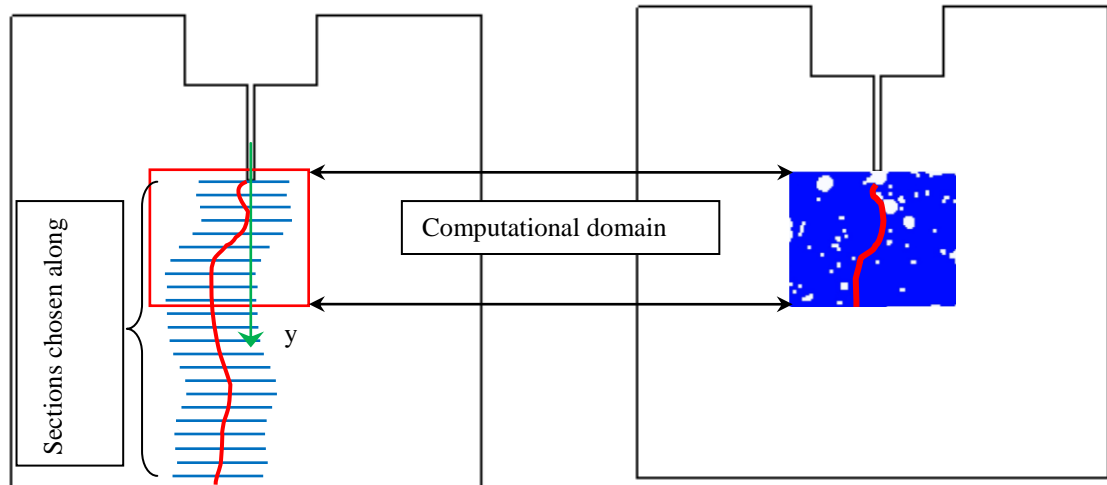
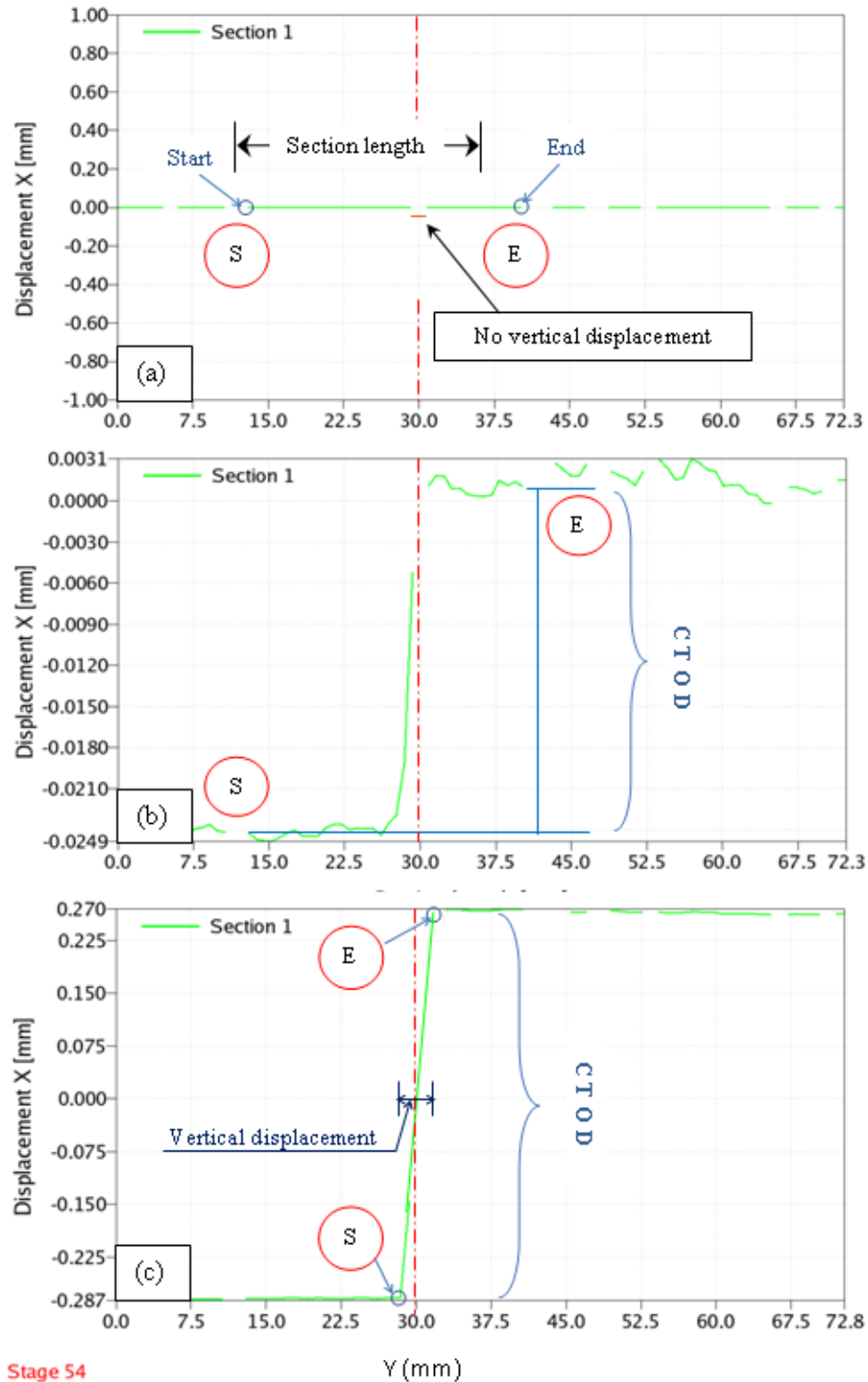


Figure 3.33: Computational domain for the WST-specimen (WST2), including the sections along the crack path

The COD along the crack path can be obtained by computing the length change of the parallel sections (segments) created on the WST-specimen surface corresponding to each loading stage in comparison to the reference stage of zero loading (see Section 3.7.4 and Figure 3.26). The COD can also be obtained by calculating the horizontal displacement of each section during the stages of loading in which the value of vertical displacement (along the Y-direction) is small enough to be ignored (as this study concentrates on mode I fracture mechanics). The latter method is illustrated in Figure 3.34, where line S-E represents the start and end points of the first horizontal section assigned at the crack/notch tip. For example, the displacement (CTOD) at Stage 54 can be calculated from the summation of the positive and negative displacement (the displacement to the right, $u(E)$ and to the left $u(S)$ of the section's mid-point as depicted in Equation 3.10 and Figure 3.34(c)), which is equal to 0.56 mm. As can be seen, in

Figure 3.34 (b) and (c), the CTOD increases with continued loading; however, there is marked vertical displacement.

$$CTOD = |u(E)| + |u(S)| \quad (3.10)$$



Stage 54

Figure 3.34: Crack tip opening displacement (CTOD) at various loading stages: (a) zero loading, (b) 80% peak-load in the post-cracking phase, (c) 4% peak-load in the post-cracking phase

The calculated values for crack opening displacement along the crack path (COD-Y) for various loading stages in the pre-peak and post-peak phases are shown in Figures 3.35 and 3.36, respectively. These results are limited to the area within 50 mm of the original crack/notch. This limit is imposed by the size of the calibration panel used (65 mm x 52 mm), which controls the size of the field of view. During the post-peak phase, the curve's shape changed so that two zones could be distinguished. The first zone (represented by the dotted curves in Figure 3.36) ended at approximately 37.2% of the peak-load, and the second zone (represented by the dashed curves in the same figure mentioned above) started at 21.6% of the peak-load (after the initiation of a traction-free zone); the interaction between these two zones is represented by the solid curves (Figure 3.36). This phenomenon supports the use of the bilinear softening model (Roelfstra and Wittmann, 1986; Guinea et al., 1994; Sousa and Gettu, 2003; RILEM, 2007) to estimate the strain softening behaviour of concrete in the *FPZ*. The popularity of the bilinear model's approximation of the tension softening diagram stems from the fact that the model captures the impact of two major mechanisms responsible for the tension softening observed in concrete, namely micro-cracking and aggregate interlock. The initial, steep branch of the tension softening diagram depicted by the bilinear model is a result of micro-cracking, whereas the second, shallow branch is a result of aggregate interlock (Abdalla and Karihaloo, 2004).

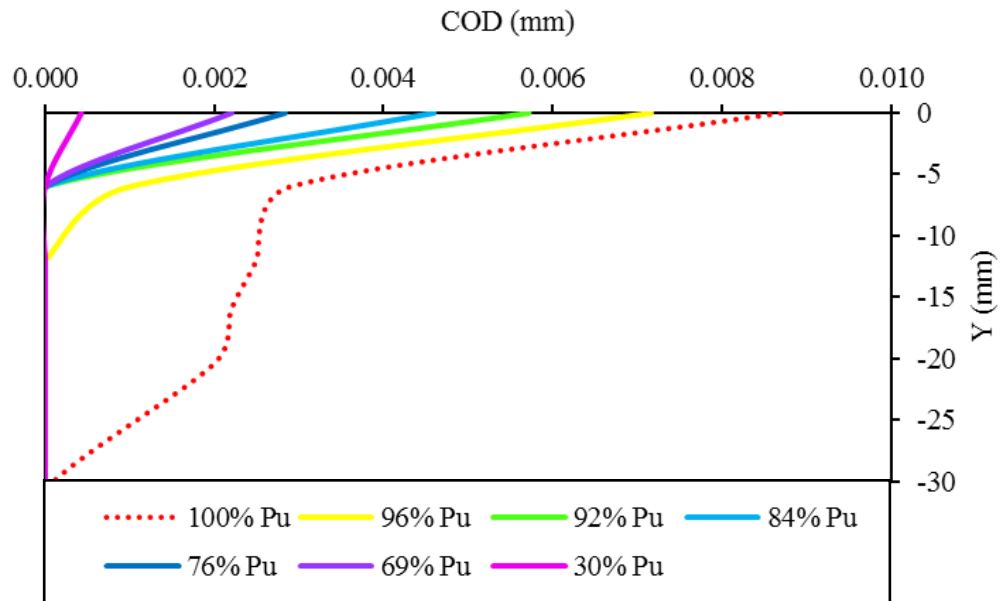


Figure 3.35: Crack opening displacement-positions along the crack path (COD-Y) during the pre-peak load phase, (P_u is the peak load)

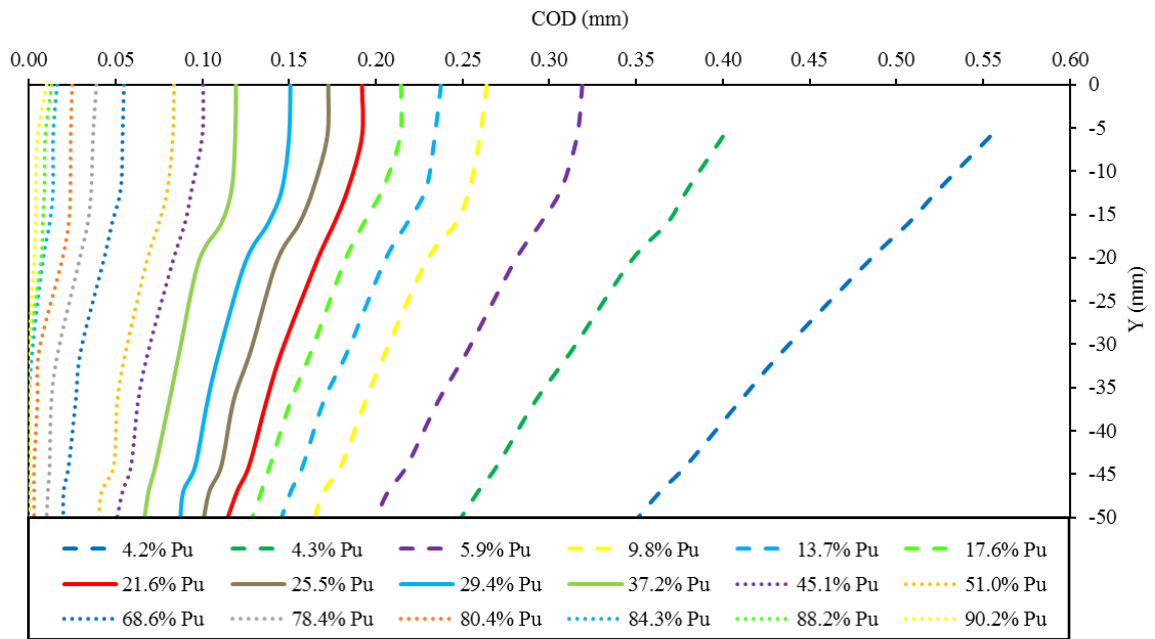


Figure 3.36: Crack opening displacement along the crack path (COD-Y) at various post-peak loading stages, (P_u is the peak load)

The main crack was used to examine the behaviour of the *FPZ* in the WST-specimens. As the crack extended, new crack surfaces formed ahead of the initial crack tip/notch; however, these new surfaces may be in contact with each other as a consequence of the toughening mechanisms described earlier (Section 3.9.1), which are behind the concrete strain softening phenomenon. Therefore, the newly formed crack surfaces may continue to sustain some tensile stress, which gradually increases from the crack tip to the end of the *FPZ*, where it reaches the tensile strength of the concrete material. For this study, however, both the position of the fictitious crack tip and the length of the *FPZ* at each loading stage are defined at the point where the crack opening is zero; in other words, the effect of micro-cracks in front of the newly formed fictitious crack tip was ignored when the *FPZ* length was estimated, as shown in Figure 3.37.

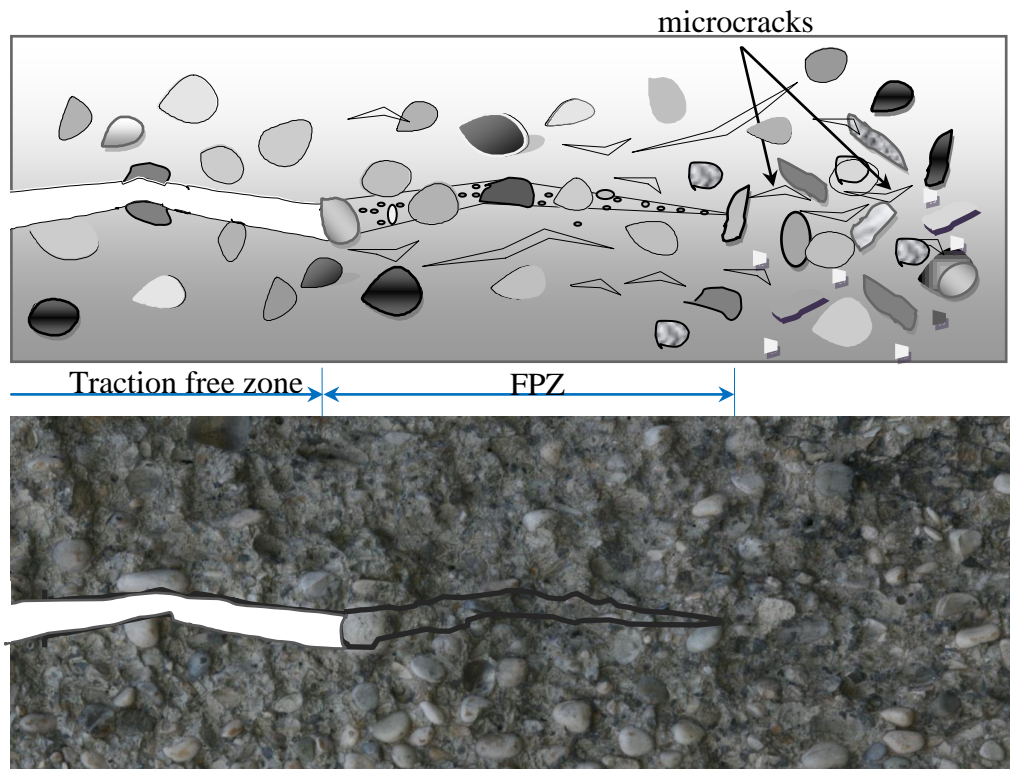


Figure 3.37: Concrete crack and *FPZ* boundaries (microcracks at the newly-formed crack tip are not included in the *FPZ*)

The *FPZ* was evaluated at the ten loading stages shown in Figure 3.38. As shown in Figure 3.39, at 2.0 kN, illustrated in Panel (a) (i.e., 22% of the peak load), the *FPZ* was 2 mm in length (i.e., 1.5% of the ligament length). The CTOD was 0.0004 mm and micro-cracks were distributed across the whole field of view. As the load increased to 8.0 kN or 84% of the peak load (Figure 3.39 Panel (b)), the *FPZ* length increased to 6 mm (i.e., 4.6% of the ligament length) and the CTOD was 0.0046 mm. In Panel (c) where the load is 9.1 kN (i.e., 96% of the peak load), the *FPZ* length was 12 mm (i.e., 9.2% of the ligament length) and the CTOD was 0.0072 mm. At the peak load (Panel (d)), the *FPZ* length reached 28 mm (i.e., 21% of the ligament length) and the CTOD was 0.0087 mm. During the post-peak phase, at 90% of the peak load (Panel (e); 8.6 kN), the *FPZ* length was 30 mm (23% of the ligament length) and the CTOD was 0.01 mm. From these results, we can see that the *FPZ* length developed very slowly during the pre-peak phase until 96% of the peak load was applied, and then the length of the *FPZ* suddenly increased.

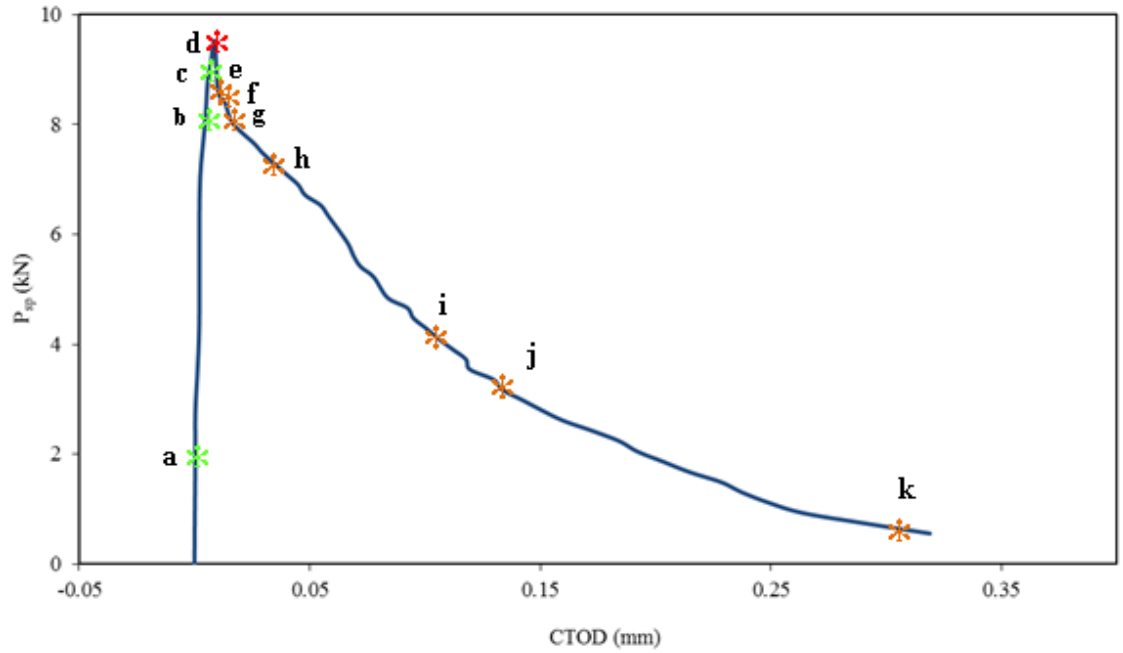


Figure 3.38: Splitting load-Crack tip opening displacement (P_{sp} -CTOD) relationship associated with different cracking stages in the WST-specimen (WST2), and assessed using DIC.

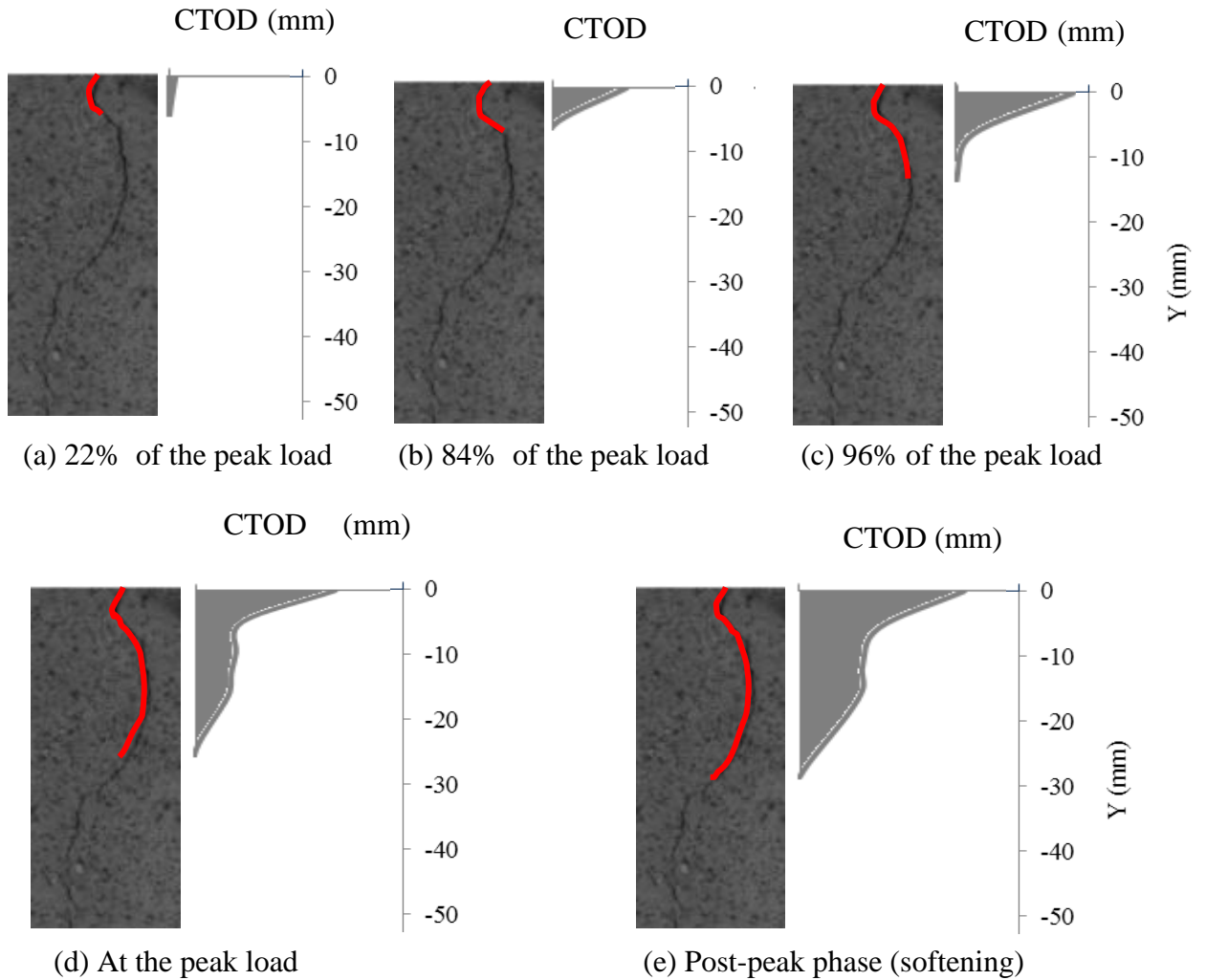
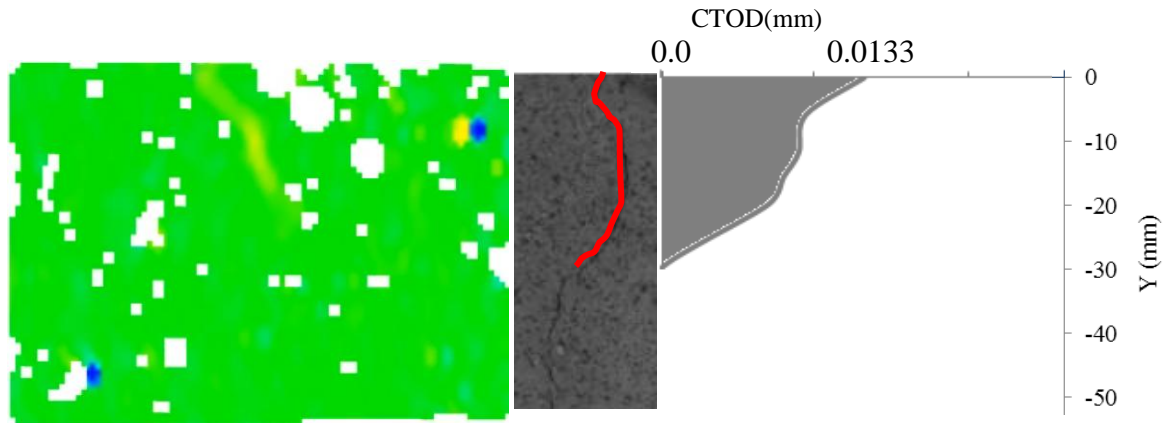


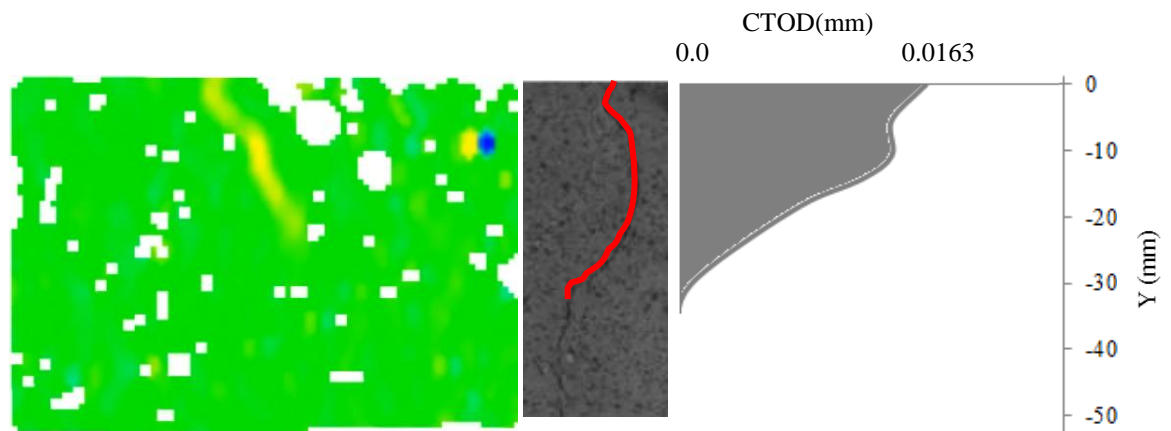
Figure 3.39: Development of the *FPZ* and crack tip during loading from 22% of the peak load during the pre-peak phase to 90% of the peak load during the post peak phase - (a) Point a in Figure 3.38, (b) Point b in Figure 3.38, (c) Point c in Figure 3.38, (d) Point d in Figure 3.38, (e) Point e in Figure 3.38.

Figure 3.40 illustrates the development of the *FPZ* during the post-peak phase (Figure 3.38, Panels (f) to (h)) along with the strain distribution on the surface of the specimen. At Point (f), 88% of the peak load (8.4 kN) was applied; the *FPZ* length was 31 mm (i.e., 24% of the ligament length) and the CTOD was 0.0133 mm, while the strain

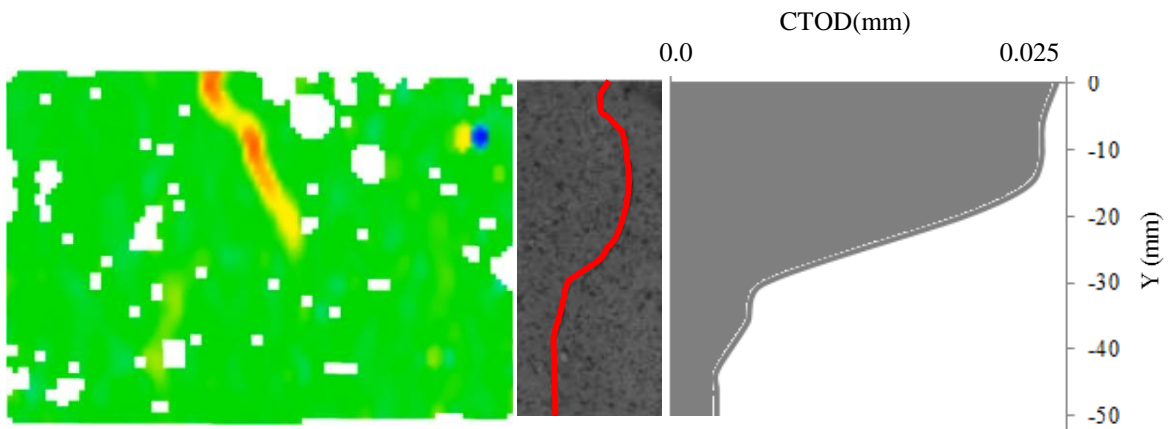
value was less than 0.006 (Figure 3.40 Panel (f)). During this stage, crack localization and propagation was evident, and was accompanied by a decrease in the *FPZ* width. At Point (g) of Figure 3.38, P_{sp} was 84% of the peak load (8 kN), and the *FPZ* length was 36 mm (i.e., 28% of the ligament length) and the CTOD was 0.0163 mm (Panel (g) of Figure 3.40). When P_{sp} was 80% of the peak load (7.6 kN; Figure 3.38, Panel (h)), the *FPZ* length exceeded 50 mm (i.e., 40% of the ligament length) and the CTOD was 0.0133 mm (Figure 3.40 Panel (h)).



(a) Post-peak phase (softening), 88% of the peak



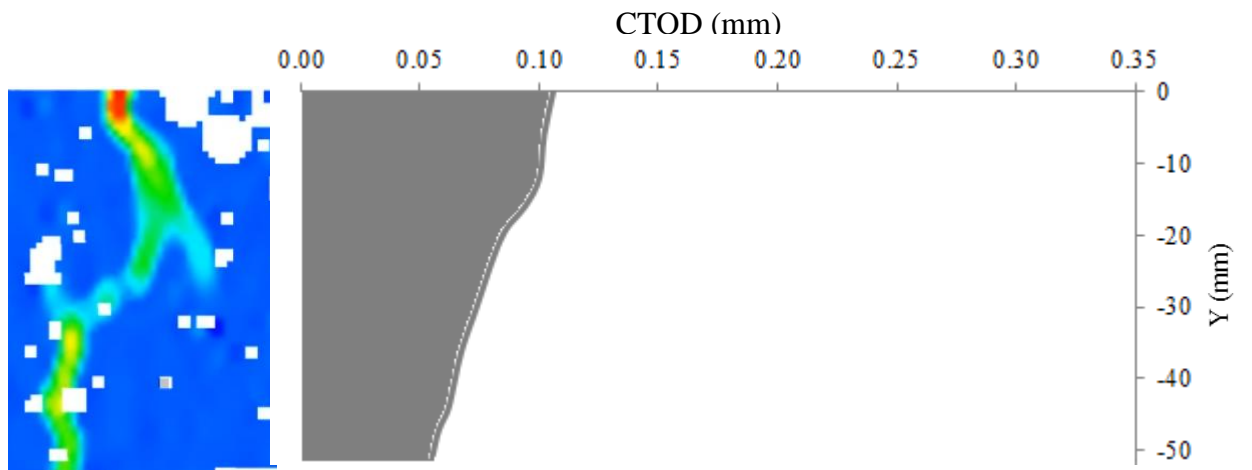
(b) Post-peak phase (softening), 84% of the peak load



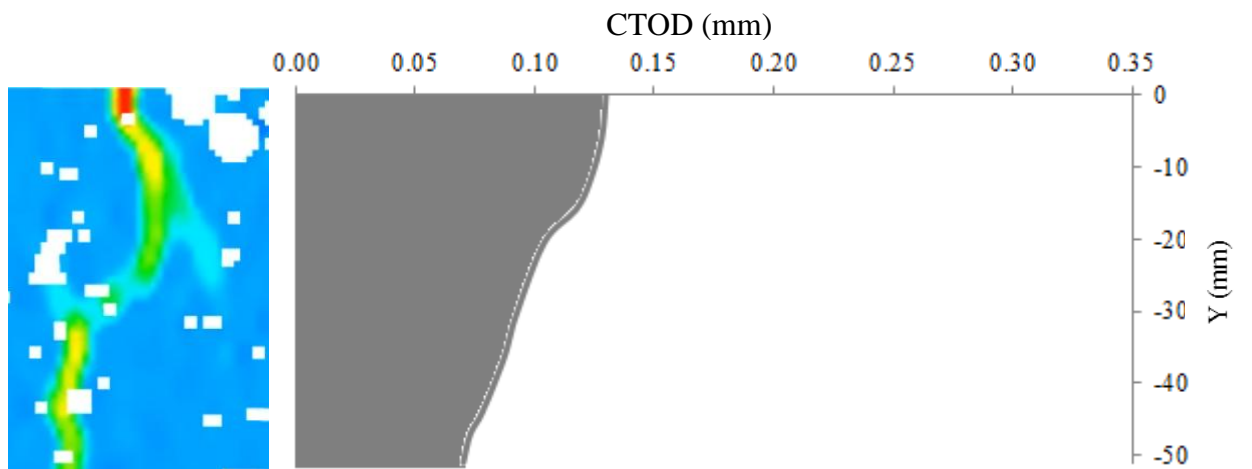
(c) Post-peak phase (softening), 80% of the peak load

Figure 3.40: Development of the *FPZ* and crack during the post-peak phase - (a) Point f in Figure 3.38, (b) Point g in Figure 3.38, (c) Point h in Figure 3.38.

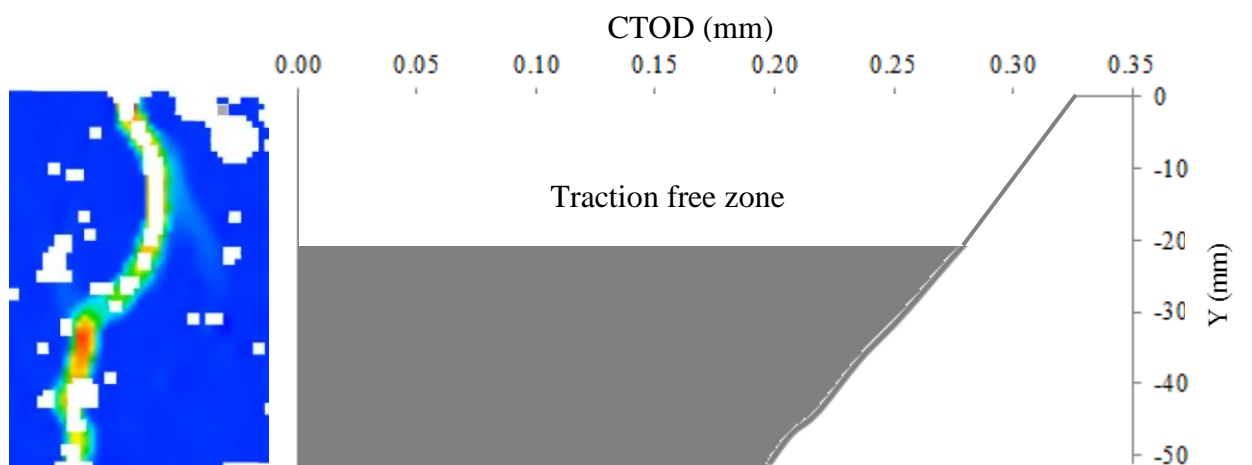
Figure 3.41 illustrates the development of the *FPZ* during the post-peak phase (Points (i) to (k) in Figure 3.38), along with the strain distribution on the specimen's surface at these loading stages. It is evident that the slope of the CTOD-Y curve along the crack path shown in Panel (k) (i.e., after the initiation of the traction free zone) differs from the slopes of the curves depicting stages prior to the initiation of the traction free zone (Figure 3.41 (i) (43% peak-load) and (j) (35% peak-load)). This could be related to the two major mechanisms responsible for the tension softening observed in concrete (see Section 3.9.2): the micro-cracking (steep part of the softening curve) and aggregate interlock (shallow part or tail of the softening curve), and provides further support for the use of the bilinear softening model to estimate the strain softening behaviour of concrete.



(a) Post-peak region (softening), 43% of the peak load



(b) Post-peak region (softening), 35% of the peak load



(c) Post-peak region (softening), 6% of the peak load

Figure 3.41: Development of the *FPZ* and the traction free zone during the post-peak phase (a) Point i in Figure 3.38, (b) Point j in Figure 3.38, (c) Point k in Figure 3.38

The variations in the length of the *FPZ* associated with the splitting load are summarized in Table 3.4 and Figure 3.42. Although the length of this zone increased with continuous loading, the rate of this increase was higher from stage (c) (96% peak load) to stage (d) (100% peak load) followed by slow growth within the post-peak phase.

Table 3.4: Variation of the *FPZ* length with the splitting load

Points Fig. (3.38)	Splitting load P_{sp} %	<i>FPZ</i> length L_{FPZ} (mm)	<i>FPZ</i> length/Ligament length %
	0	0	0
a	22	2	2
b	84	6	5
c	96	12	9
d	100	28	21
e	90	30	23
f	88	31	24
g	84	36	28

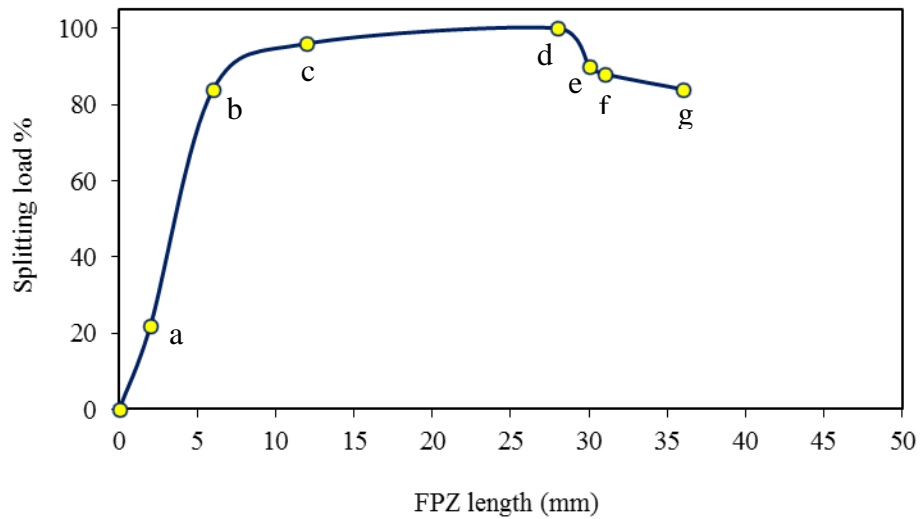


Figure 3.42: Variation of the *FPZ* length with the splitting load (P_{sp} ; % of peak load)

These findings indicate that the width of the *FPZ* increased continuously as loading increased, but then began to decrease when the localization of micro-cracks began at 88% of the peak-load within the pre-peak phase. The *FPZ* length also increased gradually with loading until 96% of the peak-load was applied; at this point the zone exhibited a sudden increase in its length followed by smaller growth (see Table 3.4). Further development of the *FPZ* could not be monitored, however, because at 80% of the peak-load during the post-peak phase, the *FPZ* extended beyond the field of view. (The extent of the field of view was limited by the measuring volume established during calibration of the DIC system; see Section 3.7.2 and Figure 3.42 for details).

Greater detail about the development of the traction free zone during the post-peak phase is provided in Table 3.5 and illustrated in Figure 3.43. The traction free zone initially grew slowly (from 2 to 8 mm; an increase of 6 mm) as the post-peak P_{sp} decreased sharply from 25.5 % to 9.8% of peak load, a change of over 16%. The length of the traction free zone grew another 6 mm as the load declined from 9.8% to 7.8%, a change of less than 2%. At this point, the size of the traction free zone continued to grow despite little change in the post-peak P_{sp} , which leveled off at slightly less than 5% while the traction free zone extended an additional 38 mm to reach a length of 52 mm.

Figure 3.43 illustrates the growth of the traction free zone (x-axis) as the post-peak splitting load declines in the direction of the red arrow on the y-axis. The traction free zone initially grew slowly from 2 to 8 mm (an increase of 6 mm) despite a large decrease in the post-peak load (from 25.49% to 9.8%; a change of over 15%) as

illustrated by the shallow slope of the curve at the right of the figure. The length of the traction free zone grew another 6 mm (from 8 mm to 14 mm) despite only a small decrease in load (from 9.8% to 7.84%; a change of less than 2%) as shown by a moderate slope in the middle segment of the curve. At this point, the post peak splitting load stabilized at slightly less than 5% of peak load, but the traction free zone continued to expand, so the slope became very steep as the size of the traction free zone increased from 23 to 52 mm, but the load declined from only 4.51% to 4.22% (a change of <0.3%; shown on the left side of the figure).

Table 3.5: Development of the traction free zone in relation to decreased splitting load during the post-peak phase (softening phase)

Traction Free Zone (mm)	Post-peak splitting load P_{sp} %
2	25.49
7	16
8	11.76
8	9.8
14	7.84
21	5.88
23	4.51
25	4.29
31	4.25
52	4.22

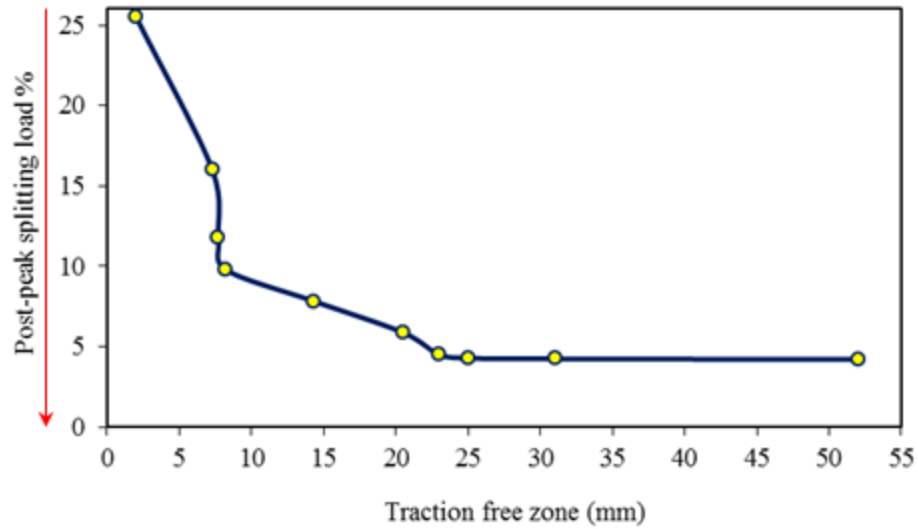


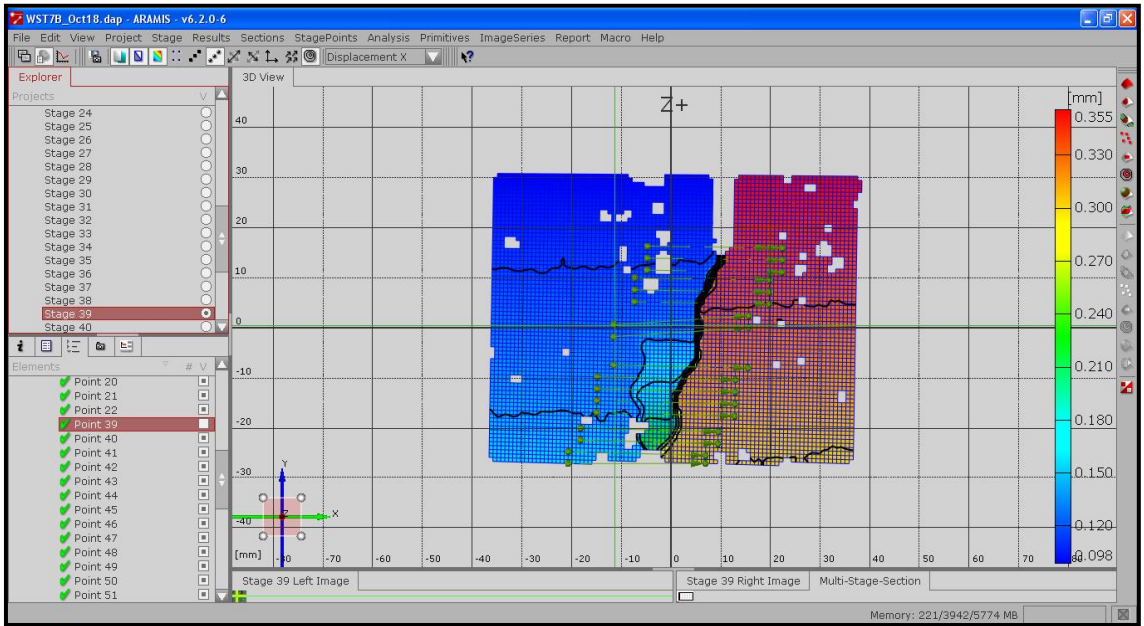
Figure 3.43: Growth of the traction free zone as the splitting load (P_{sp} %) decreases during the post-peak phase (softening phase)

3.9.3 Energy Dissipation along the Crack Path

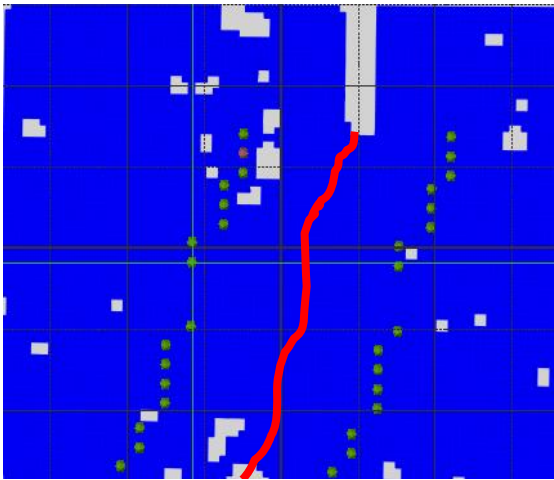
Bazant and Oh (1983) proposed a model for the *FPZ* based on a smeared crack, which assumes that there is a band of uniformly and continuously distributed micro-cracks within a fixed width, h_c , called the crack band; h_c is assumed to be a material fracture parameter. $h_c = n_a d_a$, where d_a is the maximum aggregate size and n_a is an empirical constant estimated to be 3 for concrete (Shah et al., 1995). Recently, Østergaard (2003) suggested that h_c has a width of approximately one-fifth of the ligament length (i.e., $0.2h$) of the WST-specimen (Figure 3.44). Consequently, for the current research, the value of h_c was estimated to be 26 mm. Figure 3.44 (a) shows a screen shot taken when the post-peak P_{sp} was 2.71 kN, reached after the peak load of 12.85 kN was applied (i.e., during the softening stage). The amount of energy required to

propagate the crack a specified distance along the crack path was obtained directly using DIC without the need for numerical calculation, calibration, and/or finite element calibration. To calculate the dissipated energy along the crack path, the P_{sp} -COD curves for various locations along the crack path are required. Therefore, the COD for all loading stages must be calculated at various locations along the crack path. This can be done by computing the amount of change in the length of each of the horizontal sections within the digital image of each loading stage, with respect to the reference image of the zero loading stage (see Figure 3.26). In this study, sections with a width of approximately 26 mm (i.e., $h_c = 0.2h = 26\text{mm}$) were chosen along the crack path as shown in Figure 3.44. The COD was then determined for these sections at each loading stage, and used to calculate the dissipated energy at various distances, y , from the crack/notch tip. Figure 3.45 demonstrates the P_{sp} -COD for various locations along the crack path.

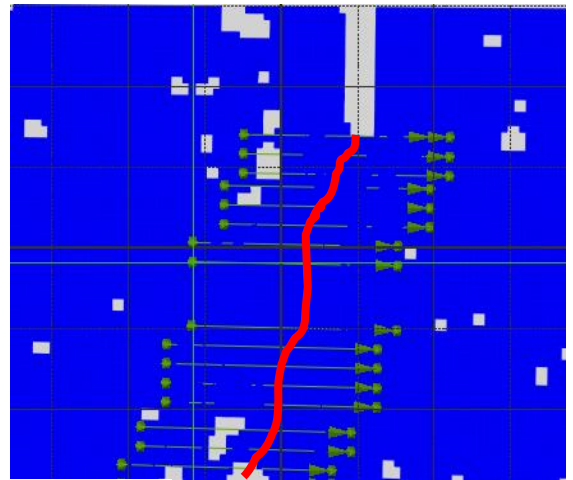
The energy required to propagate the crack to a point along the crack path that is a specific distance, y , from the crack/notch tip, is shown in Figure 3.46. The value for this energy was calculated by dividing the area under the P_{sp} -COD curve obtained for each location, y , during the post-peak phase (Figure 3.45), by the fracture area. Note that in the current study, this finding is limited to the amount of energy dissipated at locations that are within 50 mm from the crack/notch tip; this limitation is imposed by the calibration panel used (65 mm x 52 mm), which controlled the size of the field of view.



(a)

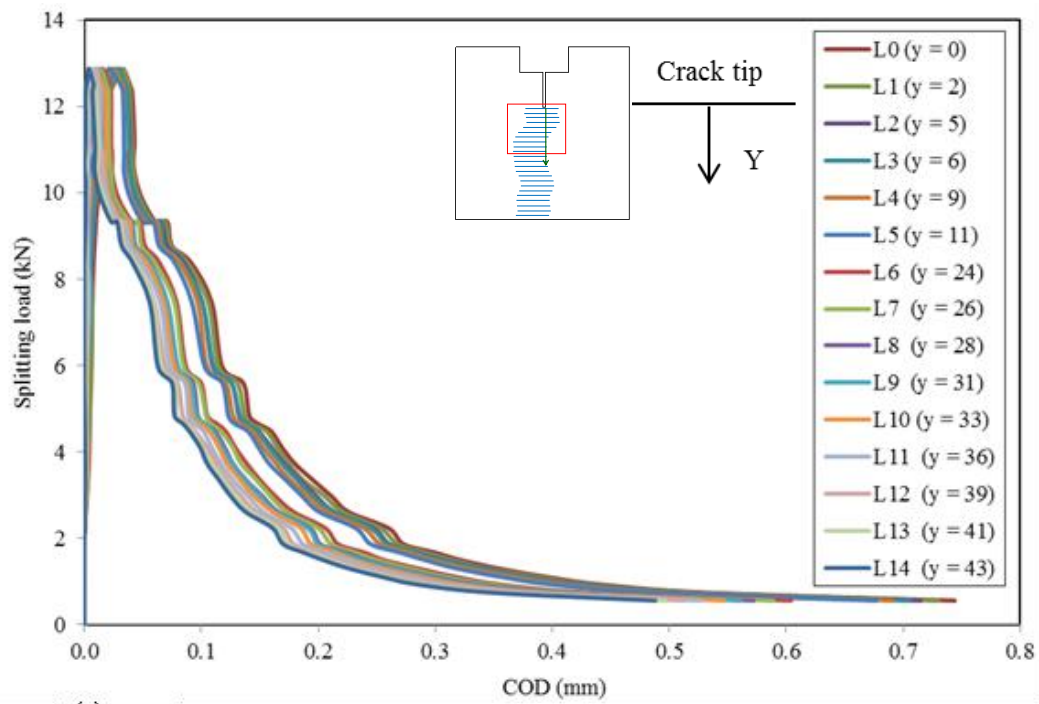


(b)

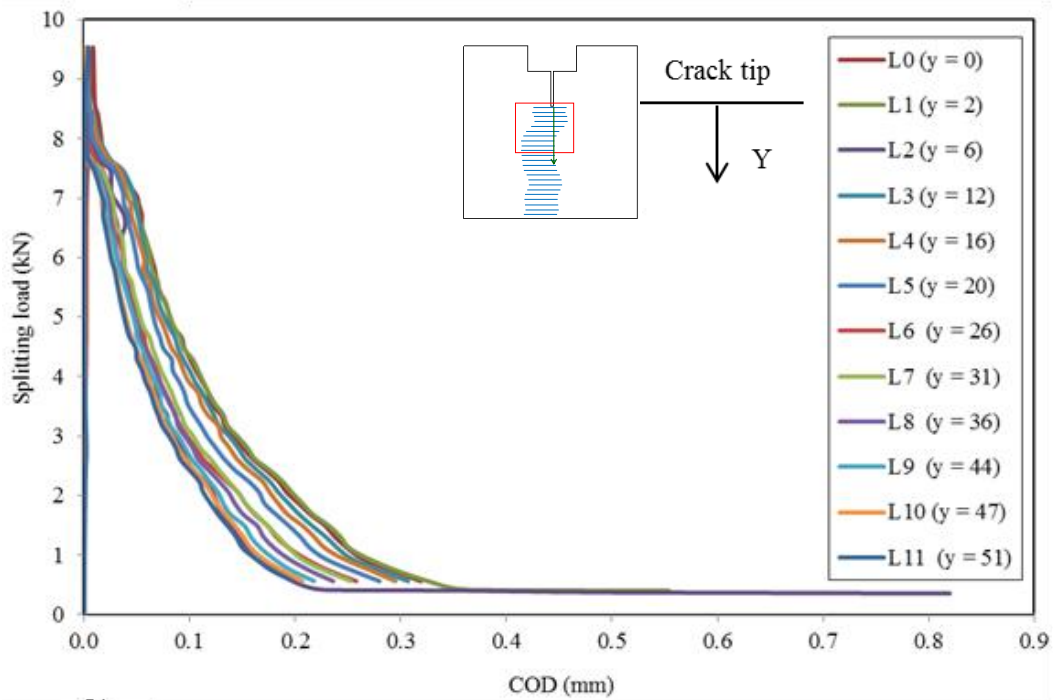


(c) $\leftarrow h_c \rightarrow$

Figure 3.44: ARAMIS DIC system, screen shot (WST4): (a) at stage 39, with P_{sp} of 2.71 kN during the post-peak phase with COD of 0.033 mm; (b) schematic placing of pairs of points (solid circles) along the crack path where the deformation was measured during post-test processing; (c) estimated band width, h_c of 26 mm, at different locations along the crack path where the dissipated energy was calculated.



(a)



(b)

Figure 3.45: Splitting load-crack opening displacement (P_{sp} -COD) curves calculated for various positions along the crack path, at a distance, y , from the crack/notch tip. Specimens: (a) WST2, (b) WST4

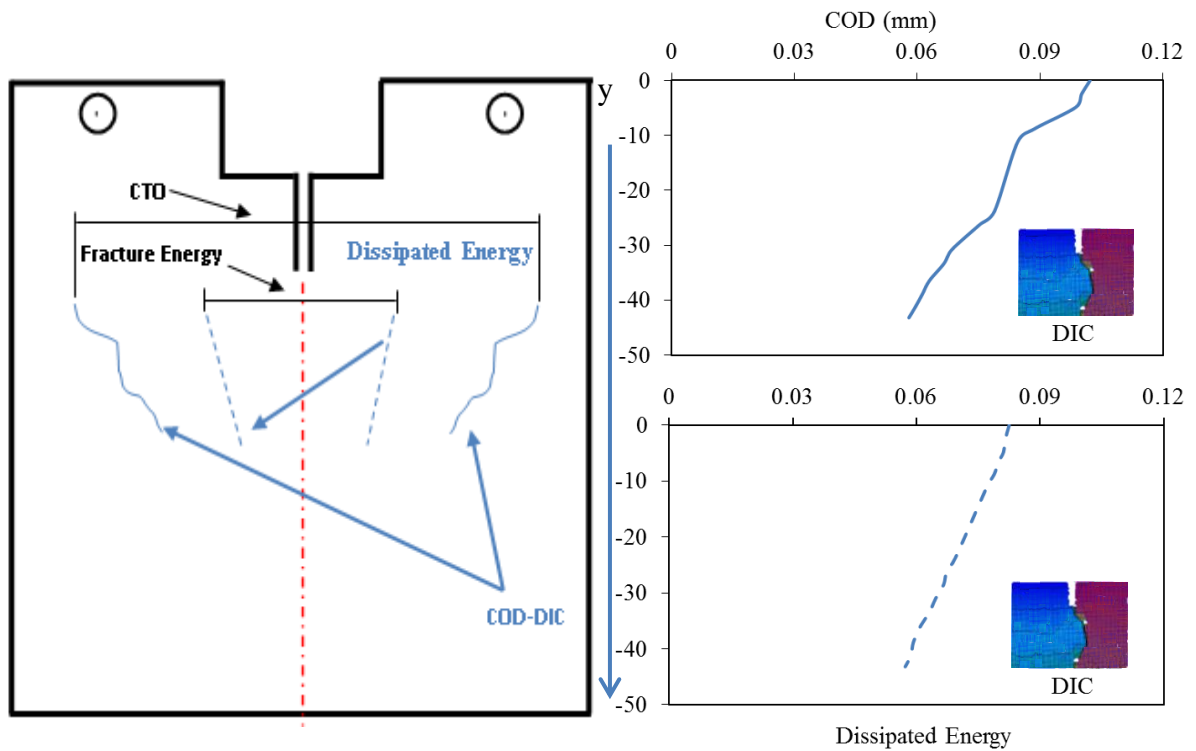


Figure 3.46: The dissipated energy and the crack opening displacement (COD) along the crack path measured using digital image correlation (DIC) for WST4

The stress causes energy consumption in highly stressed regions, such as the *FPZ*. Therefore, energy dissipation is influenced by the size of this zone, which changes during loading. The width of the damaged zone (*FPZ*) increases from the beginning of loading until the peak-load is applied. During the post-peak phase, the width of the *FPZ* starts decreasing and then remains constant as the crack runs along the ligament (Figure 3.42 in Section 3.9.2). This means that the dissipated energy is not equally distributed along the ligament; this is evident in Figure 3.47, which shows variation in the amount of tensile damage along the crack path, leading to a pronounced size effect (Duan et al., 2006) as observed in this investigation.

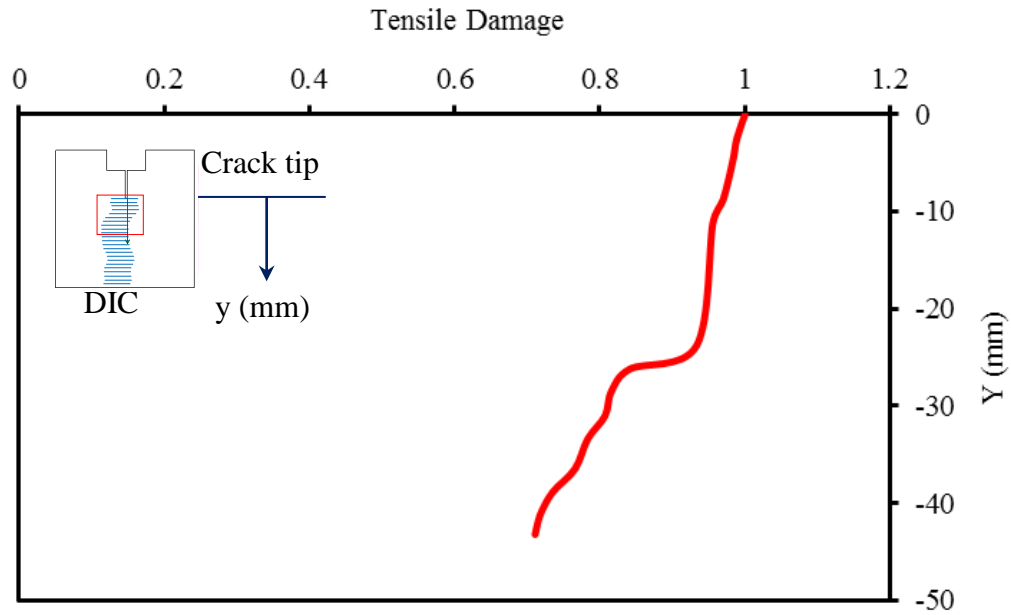


Figure 3.47: The tensile damage along the crack path assessed using digital image correlation (DIC)

3.9.4 Assessment of the Development of the FPZ using the DIC Technique

During concrete fracture, the high-stress state near the crack tip causes micro-cracking defects. Mindess and Diamond (1982) detected the crack tip in concrete using a scanning electron microscope; they reported that the crack surface is tortuous, and that the crack process in concrete is complicated. During the research activities presented in this thesis, we paid attention to the development of cracks and strain in the *FPZ* using DIC technique. Specimen WST6 was chosen to demonstrate the outcomes of this investigation.

Figure 3.48(a) illustrates the strain distribution over a limited area around the crack tip of specimen WST6 at 22% of the peak load; while Figure 3.48 (b) depicts the strain distribution at proportional limit, f_y , of 34% of the peak load (Point A in Figure 3.49). As can be seen in Figure 3.48, the initiation of internal cracks was detected at this stage; micro-cracks were concentrated at the crack tip, and are represented by a light spot indicating the *FPZ*. The recorded P_{sp} was 5.6 kN and the CTOD was 0.006 mm, while the tensile strain at the *FPZ* was about 0.0015. In Figure 3.49, at loading stages prior to Point A, the specimen behaves elastically with negligible distributed tensile strain at the crack tip during all loading stages. This observation is demonstrated in Figure 3.50 (a), and is consistent with observations made by Shah et al. (1995) using acoustic emission measurement, which indicated that the initiation of internal cracks is negligible before the proportional limit is reached.

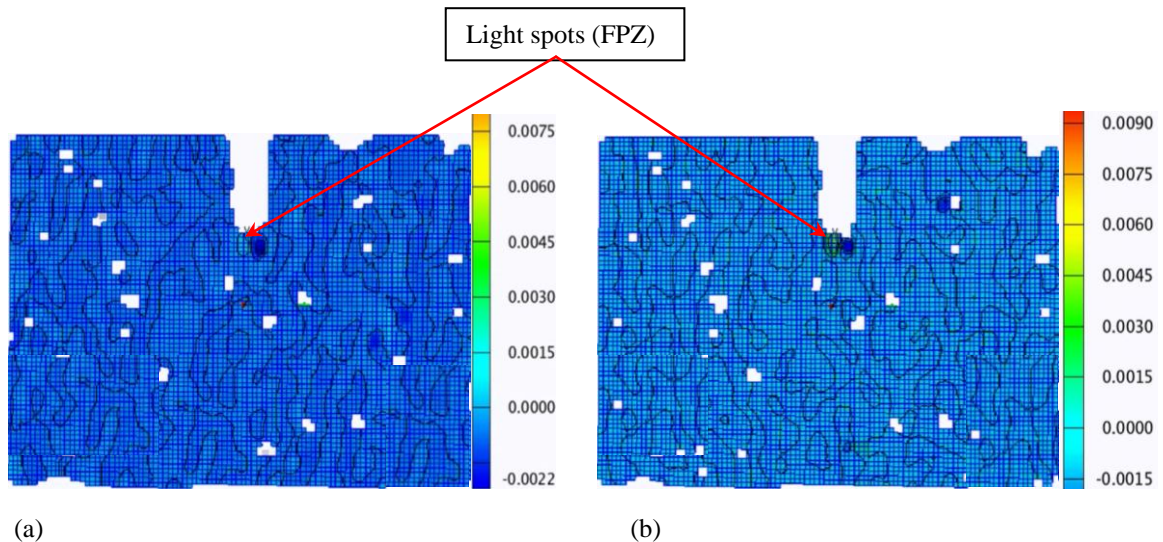


Figure 3.48: Strain distribution over the WST-specimen's (WST6) surface assessed using DIC: (a) at 22% of the peak load ($P_{sp} = 3.7$ kN and $CTOD = 0.004$ mm), (b) at 34% of the peak load (f_y) ($P_{sp} = 5.6$ kN and $CTOD = 0.006$ mm) – Point A in Figure 3.49

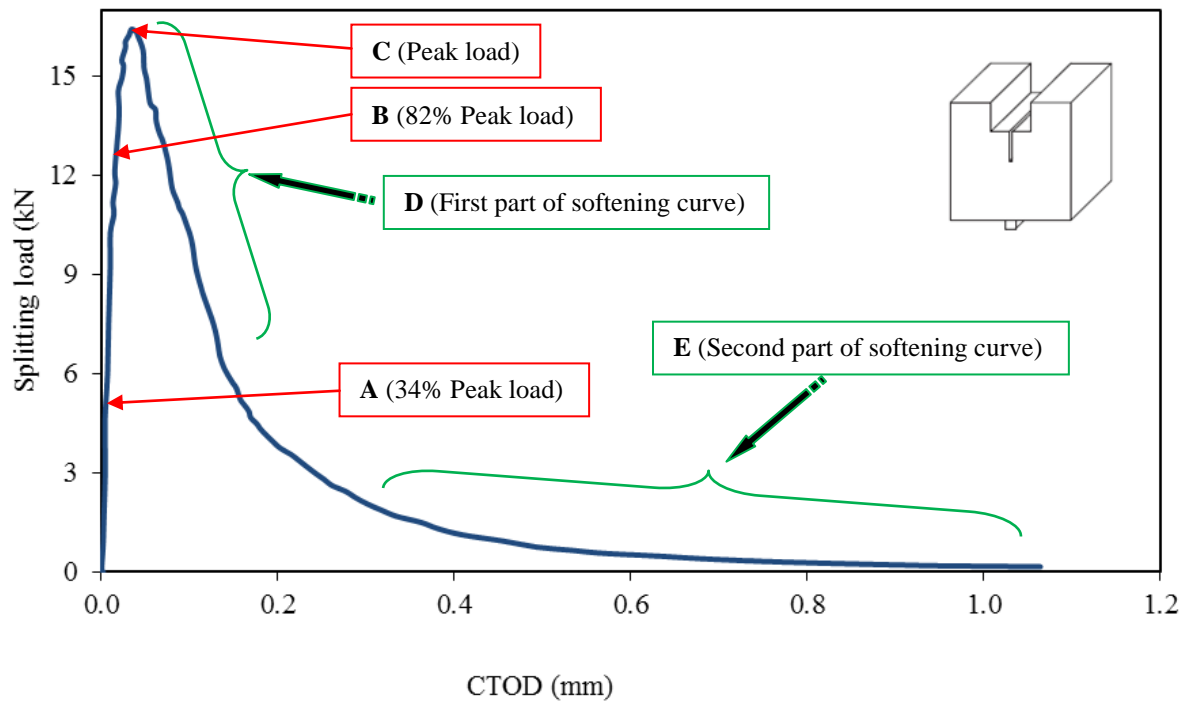


Figure 3.49: Splitting load-Crack tip opening displacement (P_{sp} -CTOD) associated with different cracking stages for the WST-specimen (WST6), assessed using DIC

As the load increased beyond Point A (Figure 3.49), more internal cracks were detected and the area around the crack tip started to exhibit some changes; however, this was accompanied by a slight increase in tensile strain and CTOD (Figure 3.50). When this new cracking stage started, the isolated internal cracks continued to spread randomly over the specimen without any particular localization (see Figure 3.51), while the strain value remained less than 0.002 until reaching 82% of the peak-load at Point B in Figure 3.49.

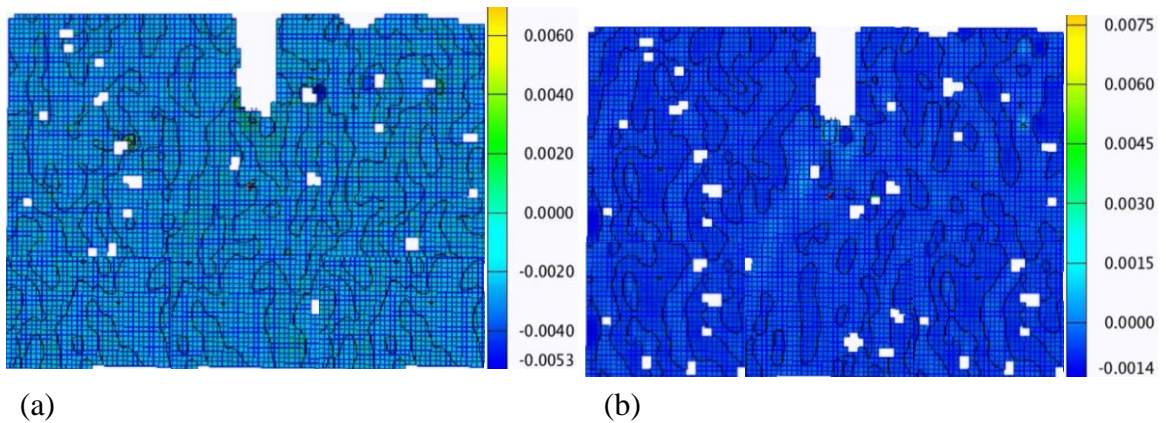


Figure 3.50: Strain distribution on the WST-specimen (WST6) surface assessed using DIC: (a) at 46% of the peak-load ($P_{sp} = 7.46$ kN and CTOD = 0.008 mm), (b) at 57% of the peak-load ($P_{sp} = 9.3$ kN and CTOD = 0.01 mm)

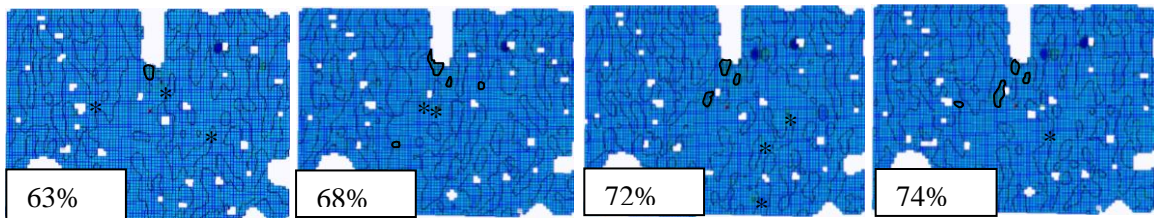


Figure 3.51: Location of internal cracks detected for different loads between stages A and B in Figure 3.49 using DIC

A new cracking stage was detected when 82% of the peak-load was applied, as shown in Figure 3.52(a); the load at this stage was 13.4 kN and the CTOD was 0.019 mm. The internal cracks that were concentrated at the crack tip exhibited an increase in strain which is approximately 0.003. At this loading point (B in Figure 3.49), the new cracking stage (Point B) was characterized by the appearance of a narrow band of internal cracks (Figure 3.52(a)) indicating that the damage had started to localize. This is equivalent to a continuous major crack starting to form where the band of microcracks is

located. This band continued to propagate in a stable manner until the peak-load was applied. As loading slightly increased, more internal cracks appeared, particularly in the area around the band and at the crack tip (Figure 3.52 (b)); there was also a small increase in tensile strain. After loading point B shown in Figure 3.49, the length of the band of microcracks continued increasing and became more clearly defined, indicating that the major crack was propagating (compare (a) at $P_{sp}=15.4\text{kN}$ and (b) at 15.5kN , in Figure 3.53). This phenomenon, however, was accompanied by increased strain within the band only. Based on the distribution of the microcracks and the strain across the specimen's surface shown in Figure 3.53, the length of the *FPZ* was estimated to be approximately 20 mm at 94% of the peak-load.

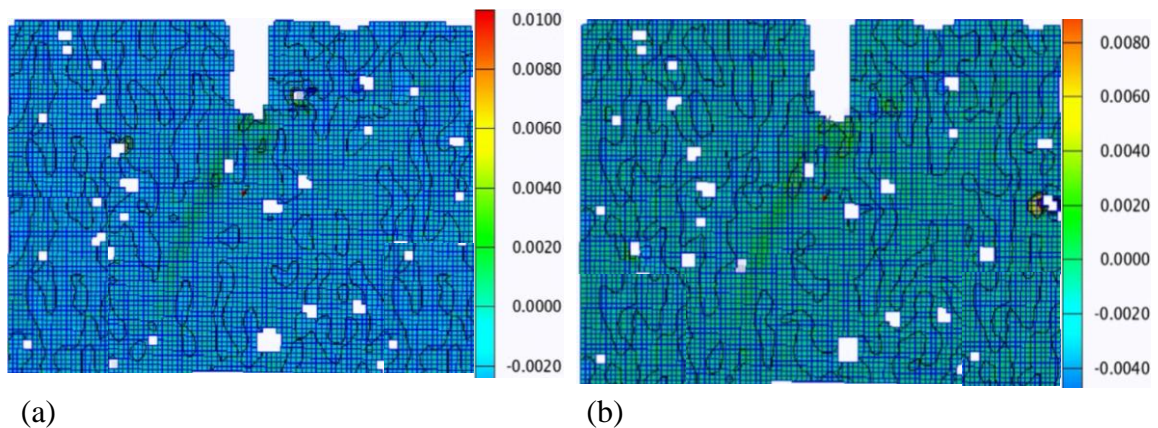


Figure 3.52: Strain distribution and initiation of damage localized on the WST-specimen's (WST6) surface, assessed using DIC: (a) at 82% of the peak-load ($P_{sp} = 13.4$ kN and CTOD = 0.019 mm), (b) at 85% of the peak-load ($P_{sp} = 14$ kN and CTOD = 0.02 mm)

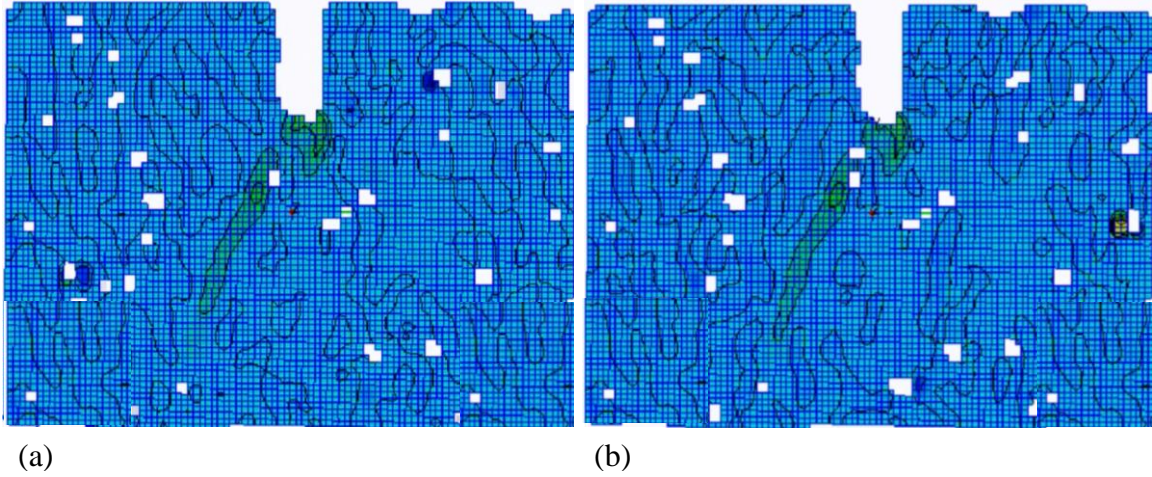


Figure 3.53: Strain distribution and damage localization on the WST-specimen's (WST6) surface, assessed using DIC at approximately 94% of the peak load: (a) ($P_{sp} = 15.4$ kN and $CTOD = 0.025$ mm), (b) ($P_{sp} = 15.5$ kN and $CTOD = 0.025$ mm)

When P_{sp} was increased to approximately 96% of the peak-load (Figure 3.54 (a)), the $CTOD$ was 0.027 mm and maximum strain was 0.0045 at the crack tip. At this point, the length of the *FPZ* was approximately 22 mm, and its width was 30 mm. Increasing P_{sp} to about 99% of the peak load, led to the appearance of a new micro-crack band on the right side of the WST-specimen's surface, as shown in Figure 3.54 (b). With increased loading, the strain within this new band increased also, and the band became clearly defined. However, this phenomenon was accompanied by decreasing strain within the first band of micro-cracks, indicating the closure of these micro-cracks. At this point (B: $P_{sp} = 99\%$ of peak load), the length of the *FPZ* was approximately 23 mm and its width was 28 mm, while the $CTOD$ was 0.031 mm with 0.005 maximum strain at the crack tip.

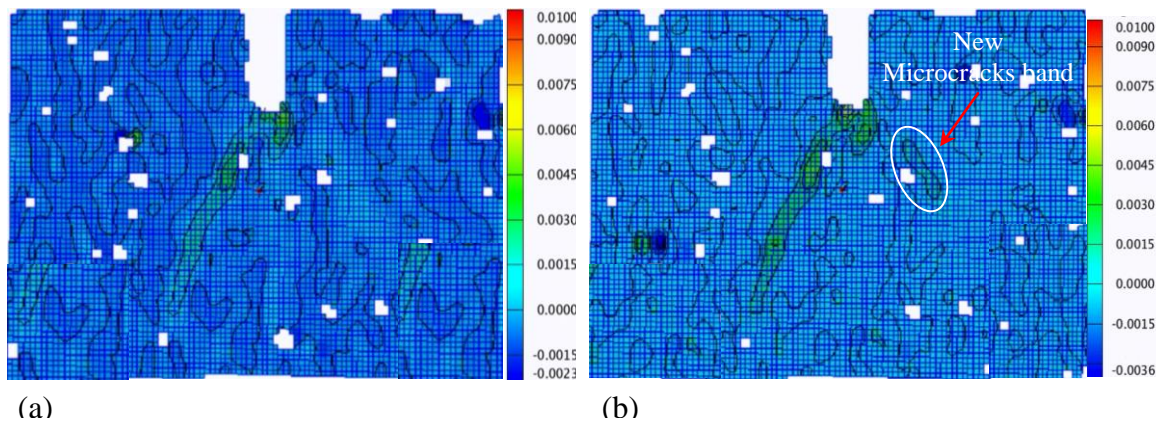


Figure 3.54: Strain distribution and damage localization on the WST-specimen's (WST6) surface, assessed using DIC at: (a) 96% of the peak load ($P_{sp} = 15.8$ kN and $CTOD = 0.027$ mm) – Point B in Figure 3.49, (b) 99% of the peak load ($P_{sp} = 16.2$ kN and $CTOD = 0.031$ mm)

Figure 3.55 illustrates the strain field measurements obtained for the peak-load of 16.4 kN represented by Point C in Figure 3.49. The maximum recorded strain was 0.006 at the crack tip, and the CTOD was 0.034 mm. Since the application of the peak-load was followed by the critical propagation of the major crack (softening stage), this CTOD represents the critical crack tip opening displacement ($CTOD_c$). At peak loading (Point C-Figure 3.49), the width of the *FPZ* continued decreasing, which may be associated with unloading of the material located farther away from the crack path. This phenomenon indicates that the softening stage was initiated without the occurrence of sudden failure because of the cohesion effect within the *FPZ*. When the peak-load was applied, the length of the *FPZ* was approximately 28 mm (21.5% of the ligament length); this increase in length was accompanied by a decrease in the width of the *FPZ* to approximately 22 mm.

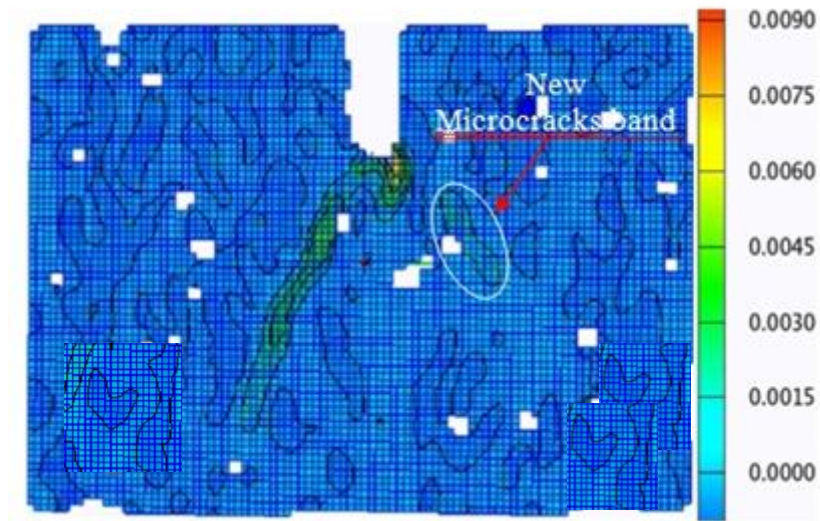


Figure 3.55: Strain distribution on the WST-specimen's (WST6) surface at the Peak-load assessed using DIC: ($P_{sp} = 16.4$ kN and CTOD = 0.034 mm) – Point-C (Figure 3.49)

Following the application of peak-load (i.e., loading Point-C in Figure 3.49), the area around the new band of microcracks exhibited an increase in strain as indicated by the appearance of more internal cracks around band, as shown in Figure 3.56(a). With a slight loading increase, the new band of microcracks started to localize, which indicates that a crack was initiated at the location of this band (Figure 3.56 (b)). This can happen when the main band (i.e., first band of micro-cracks) formed around a relatively strong aggregate, and/or when another group of micro-cracks with a weaker matrix or interface than the main band, is formed. This phenomenon is evident from the appearance of two small spots with a high level of strain at the location of the first band of micro-cracks (Figure 3.56 (a)), where a strong aggregate may exist between the two groups of micro-cracks; it is evident that the major crack changed the course of its path when a weaker path was found.

Moreover, the observed damage consisted of the major crack opening within the crack band that was associated with the unloading of the portion of the specimen lying outside of this band. However, this phenomenon was accompanied by the narrowing width of the *FPZ*, as well as increasing strain within the new crack band, but decreasing strain in the first band and the rest of the specimen (Figure 3.56 (b)). The length of the *FPZ* continued increasing after the peak load was applied; however, it was not possible to estimate its length, as the *FPZ* extended beyond the 50-mm field of view calibrated for the DIC system's cameras in this study.

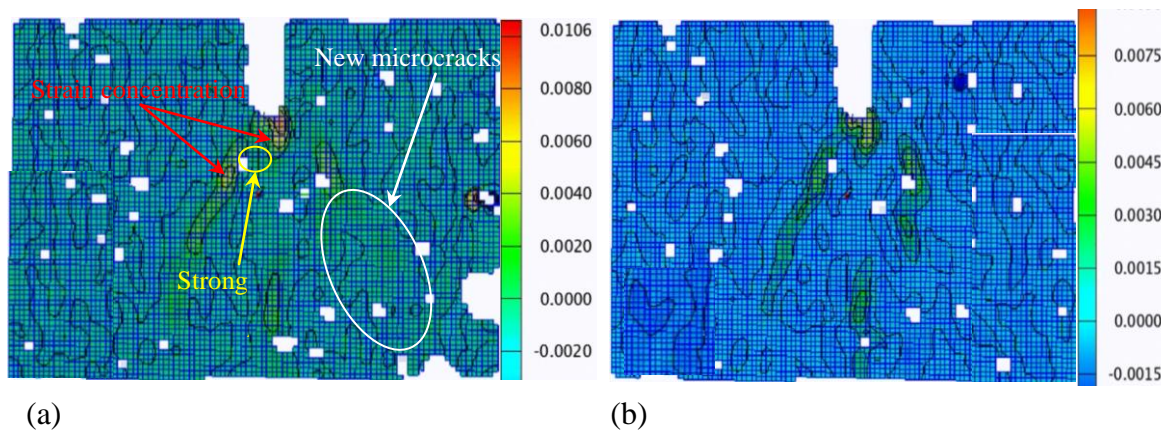


Figure 2.56: Strain distribution during the post-peak stage (at 99% of the peak-load) on the WST-specimen's (WST6) surface, assessed using DIC: (a) ($P_{sp} = 16.35$ kN and $CTOD = 0.039$ mm), (b) ($P_{sp} = 16.32$ kN and $CTOD = 0.04$ mm) Stage-D

The $CTOD$ continued increasing during the post-peak phase as the applied load continued, while the width of the band of microcracks near the crack/notch tip decreased, indicating the initiation of a traction-free region where the initial crack started to expand (Figure 3.57 (c)). Accordingly, the width of the *FPZ* continued to decrease, and the strain at the new crack path continued to increase while the strain at the original band of

micro-cracks decreased. As a result, the new band of micro-cracks continued to localize while the original band began to close during the post-peak phase.

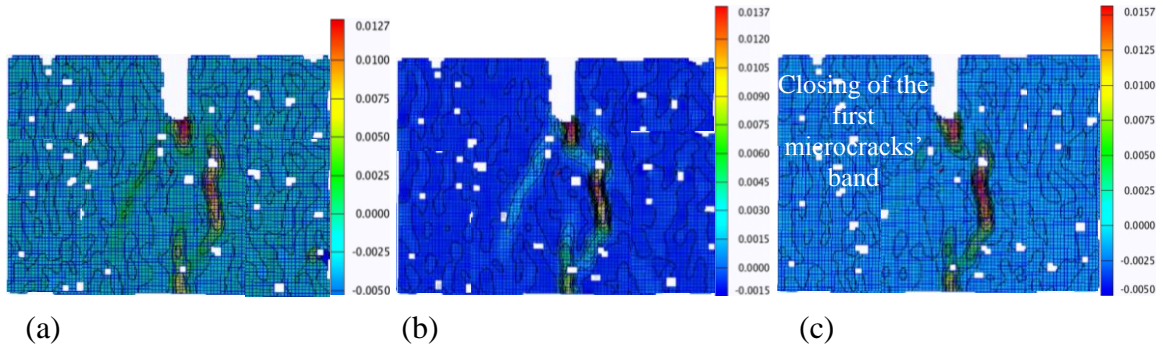


Figure 3.57: Strain distribution during the post-peak phase (Stage-D) on the WST-specimen's (WST6) surface assessed using DIC at: (a) 86% of the peak-load ($P_{sp} = 14.2$ kN and CTOD = 0.055 mm), (b) 85% of the peak-load ($P_{sp} = 13.99$ kN and CTOD = 0.06 mm), and (c) 79% of the peak-load ($P_{sp} = 13.00$ kN and CTOD = 0.069 mm) – Stage-D in Figure 3.49

Figure 3.58 illustrates the strain field corresponding to the post-peak phase (i.e., loading Stage-D in Figure 3.49) of the P_{sp} -CTOD curve. In this stage, the crack opening at the tip continuously increased at a constant rate. Moreover, the strain over the new crack path continued increasing, and was accompanied by gradual closing of internal cracks lying outside of the region containing the crack path, an indication that the width of the *FPZ* continued to decrease.

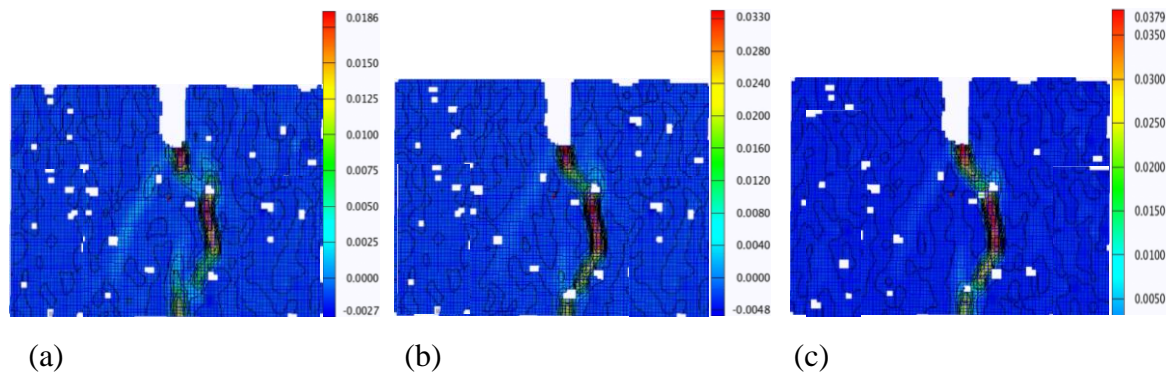


Figure 2.58: Strain distribution during the post-peak stage on the WST-specimen's (WST6) surface during the post-peak phase (Stage-D), assessed using DIC at: (a) 75% of the peak-load ($P_{sp} = 12.3$ kN and CTOD = 0.076 mm), (b) 50% of the peak-load ($P_{sp} = 8.0$ kN and CTOD = 0.12 mm), and (c) 40% of the peak-load ($P_{sp} = 6.5$ kN and CTOD = 0.13 mm) Stage-D in Figure 3.49

The results for the final stage of the softening curve, the tail of the curve shown in Figure 3.49 (Stage-E), are presented in Figure 3.59. The P_{sp} applied to the WST-specimen began to overcome the cohesive pressure, $\sigma(w)$, along the crack path until the end of testing; the test was stopped at a P_{sp} of 0.15 kN, and the CTOD at this point was 1.064 mm. During this post-peak stage (Stage-E), the change in CTOD was constant, and the specimen was under compressive strain except for the area around the crack path. The traction free zone appeared during the post-peak phase at 30% of the peak-load with a 1.5 mm crack extension and CTOD of 0.162 mm.

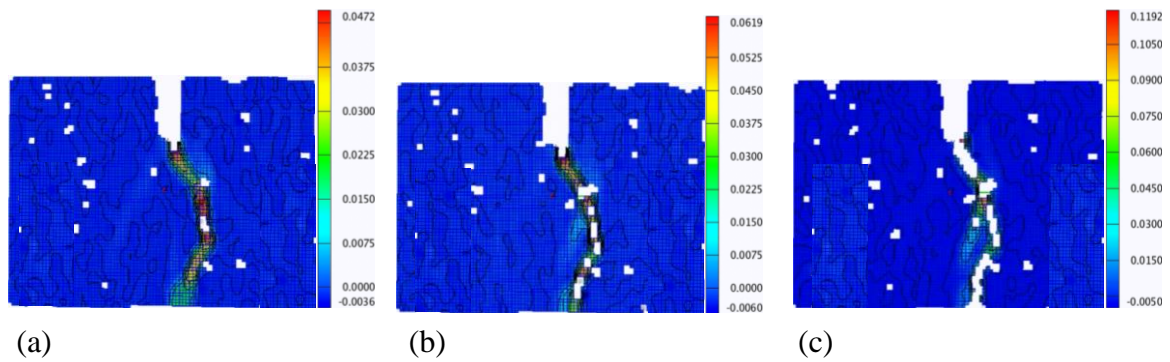


Figure 2.59: Strain distribution during the post-peak stage over the WST-specimen's (WST6) surface, assessed using DIC: (a) 30% of the peak-load ($P_{sp} = 5.0$ kN and $CTOD = 0.162$ mm), (b) 21% of the peak-load ($P_{sp} = 3.5$ kN and $CTOD = 0.215$ mm), and (c) 8% of the peak load ($P_{sp} = 1.3$ kN and $CTOD = 0.381$ mm) Stage-E

An interesting observation is that at the end of the test, the crack was not fully opened although it had appeared on the image of the specimen's surface. The maximum tensile strain along the crack path was 0.25, while the remaining surface was under compression. These observations could be interpreted as indicating that new crack surfaces that formed along the crack path might still be in contact along the specimen's width, and may have different paths because of the concrete's heterogeneity, as demonstrated in Figure 3.60. Accordingly, the WST-specimen may continue to sustain tensile stress that is characterized by the material's tensile stress-separation relationship; consequently, additional energy is needed to fully open the crack.

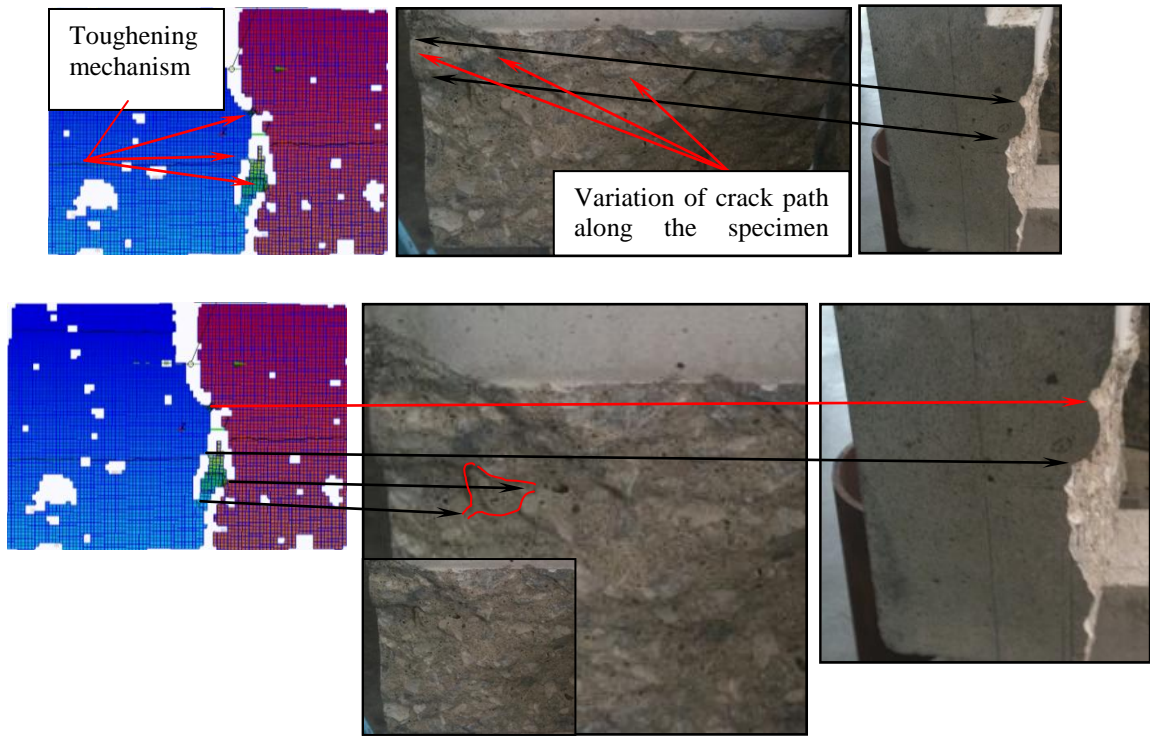


Figure 3.60: Variation in the crack path for the WST-specimen (WST6) along its width

3.10 Advantages of the DIC Technique

The traditional method for assessing fracture behaviour, particularly COD, in concrete relies on the use of a clip-gauge attached directly to the specimen to measure the displacement at the mouth of the opening crack (CMOD). This approach to the measurement of COD has several limitations. First, the point on the specimen where the displacement measurement takes place needs to be specified before running the test. Secondly, this experimental result (CMOD) needs to be calibrated to determine the displacement at the tip, rather than the mouth, of the opening crack. Third, the

measurement of crack propagation in terms of COD along the entire crack path and the complete crack profile cannot be assessed using a sensor, such as a clip-gauge, from a specified, fixed position. Finally, the data collected, using the traditional direct-contact method, are affected by vibration from the test-machine and/or instability of the concrete specimen during cracking.

In this study, a technique involving the comparison and correlation of digital images obtained under various loading conditions (DIC) was used to visualize the deformation of a concrete surface by post-test processing of successive digital images. DIC is a non-contact and non-disturbing method, which can be used to measure COD on the concrete surface, where the crack path can be tracked successfully without interfering with the fracture process. DIC enables the measurement of both displacements at the crack tip and at any other point on the concrete surface that lies within the field of view. Furthermore, the points of interest where displacement should be measured can be defined after the test is completed and the crack path has been defined. The only limitation to the number of points where displacement can be assessed is the resolution of the digital imaging device, which affects the distinctiveness of each image within a series of images that can be obtained during the creation of a virtually continuous displacement field in a test, such as the WST.

Tracking crack propagation during the fracture process is a complicated and demanding task. Optical measurements such as DIC, however, allow new possibilities for the analysis of the fracture process. Instead of measuring the deformation at discrete pre-

determined points, a displacement field can be recorded during testing and continuous features, such as the evolution of the crack profile or the crack tip position, can be measured after the completion of testing. Consequently, it is possible to examine the energy dissipation process and tensile damage along the crack path during loading. To the best of the author's knowledge, no previous research has been published that examines the rate of energy dissipation during crack formation in concrete structures.

In addition, and according to the literature, the G_F can be simply calculated by dividing the area under the P_{sp} -CMOD curve by the area of the fracture surface. However, according to the cohesive fracture model, G_F is defined as the energy required to overcome the cohesive stress when separating two surfaces, and can be calculated from the area under the P_{sp} -COD curve, measured at the initial crack tip (Shah et al, 1995). Consequently, the traditional method will overestimate the value of G_F if the P_{sp} -COD curve is based on the CMOD (the measure obtained with the traditional clip-gauge method) rather than the COD at the initial crack tip (CTOD); this can lead to a weak design. In addition, the clip-gauge method can be difficult to utilize for the assessment of real concrete structures conducted outside of controlled laboratory conditions. In contrast, DIC can be employed outside of the laboratory and the precise value of G_F can be found directly with the DIC system, without the need for calibration, and/or the use of expensive finite element analysis. Therefore, the DIC measurement technique, if used properly, leads to unambiguous analysis of COD and related parameters, and shows the promising possibility of avoiding the aforementioned disadvantages inherent to the traditional clip-gauge method of measuring displacement during concrete fracture.

The only disadvantage to this approach lies in its restriction to surface deformations that can be captured by photographic imaging. This limitation means that the DIC approach is suitable only for cases where cracking can be considered as uniform across the width of the specimen, as is typical of most Mode I fractures, and is also an implicit assumption of Hillerborg's fictitious crack model. The following chapter will consider whether the extraction of a stress-crack opening relationship, which leads to other fracture properties such as tensile strength, is possible using the experimental observations collected with the new DIC technique.

3.11 Summary of the Findings for the Application of DIC to the Study of the Fracture Behaviour of Plain Concrete

The traditional measurement technique for assessing displacement in the WST has many limitations, such as: (a) the clip-gauge must be attached directly to the specimen; (b) it is impossible to assess crack evolution and the *FPZ*; and (c) since the displacement is measured at the crack mouth, evaluation of the G_F from this measurement leads to overestimation compared to the determination of G_F based on displacement measurement at the crack tip. Consequently, other techniques have been used to measure COD in concrete structures. Optical fiber technology using fiber bragg grating detected the *FPZ* successfully; however, strain measurements obtained with this technique could be unreliable due to fiber damage or the presence of an adjacent aggregate that shielded the material from strains. Furthermore, a major drawback of this technology is that optical fibers are very sensitive to environmental temperatures, vibrations and air draft (Denarie et al., 2001). Therefore, the need for an accurate non-contact and non-disturbing

technique that is capable of monitoring the *FPZ* is recognised by many researchers. One of these non-contact methods determines crack tip position by acoustic emission, so provides a more accurate estimation of the dissipated energy; however, it failed to characterize the crack profile (Skocek and Stang, 2010).

To the best of the author's knowledge, most of the previous investigations included general study of the fracture processes in concrete and/or characterization of the *FPZ* (e.g. size, shape, and variation of the *FPZ*); however, no investigations focused on changes in concrete properties, such as crack opening or dissipated energy along the crack path, during various loading stages in a single test. The development of the *FPZ* (which is difficult to investigate using the traditional clip-on gauge technique) was successfully investigated in this study using DIC. Following proper surface preparation of the substrate, DIC was successfully applied in the WST to obtain the P_{sp} -COD relationship at any location on the surface of a concrete specimen.

The DIC optical technique is used to visualize surface deformations, and is based on the processing of data encapsulated in digital images. DIC is superior to other methods because it is more accurate and reliable. Some aspects of fracture development were examined in the current study with this technique that would not have been possible otherwise. DIC is a non-disturbing technique that has the ability to obtain undisturbed data during the fracture process from multiple locations; furthermore, the analysis can be planned or adjusted after testing is completed and the crack path is known. It is also a non-contact method (i.e., no gauges require attachment to the specimen); therefore, it is

possible to monitor the development of the *FPZ* and crack evolution without interference from the sensor during the fracture and/or when machine vibrations are present during testing. The DIC technique uses image recognition to analyze and compare digital images of the surface of a substrate at different stages of testing. This technique is not restricted to a single axis or to specific points on the surface because images of the entire surface of the specimen are recorded, and then processed conveniently after the test; so, DIC is capable of providing richer data than gauge-based measurement techniques. For all of the aforementioned reasons, the DIC technique was chosen to generate the P_{sp} -CTOD curves from the analysis of digital images of concrete specimens obtained while the *FPZ* was monitored during loading.

The research presented here deals with Mode I fracture behaviour of plain concrete. In this study, optical measurement of deformation and crack propagation in the *FPZ* was performed in conjunction with traditional methods, and the mechanical and fracture properties of concrete were determined experimentally. In particular, this experimental study examined the fracture behaviour of plain concrete using the WST; the DIC findings were compared to control data obtained with a traditional method using a clip-on gauge placed near the crack mouth. These control findings, CMOD and the P_{sp} -CMOD relationship, were used as a reference for the evaluation of the DIC technique using the ARAMIS system.

The following summary describes the findings and conclusions drawn from the experimental work presented in this chapter:

1. General outcomes:

- DIC was used to generate the softening curve (Psp-CTOD) for several concrete specimens during the WST. The softening curve demonstrates the degradation of the load-carrying capacity of concrete during the fracture process; this curve is directly linked to the G_F . As expected, the experimental findings were consistent with the load-crack opening diagram. The maximum load increased as the concrete specimen's age increased; however, the specimens constructed of high-strength material reacted in a more brittle manner, which is evident when comparing the brittleness number of each specimen and the descending part of the curve.
- The observed behaviour was essentially the same in each of the completed tests. The cracks were too small to be observed with the naked eye before application of the peak load. The first crack that appeared was very thin (i.e., a hairline crack) and occurred without producing an audible sound. In most specimens, a single crack formed; however, in a single specimen (WST6), the crack bifurcated into two branches. This could be the reason that this specimen produced the maximum levels observed for peak-load and G_F ; perhaps additional energy was absorbed when creating the new crack (although the age of this specimen could have been a factor since it was double the age of the other specimens).
- Concrete casting conditions and the W/C ratio play a large role in crack evolution and concrete fracture properties due to their impact on the hydration process,

which affects the presence of micro-cracks and the interaction between the aggregate and the matrix.

- A major factor affecting concrete properties is the W/C ratio of the concrete mixture. Although the W/C ratio specified was identical for all specimens, the evaporation of water plays a role in decreasing the actual W/C ratio according to the order in which each specimen was cast.

2. Fracture Process Zone (*FPZ*):

The *FPZ* is defined as the zone in which the material undergoes strain softening. The phenomena described in this chapter are consistent with an explanation for the behaviour of concrete caused by a complicated and relatively large *FPZ*, which deviates from the rest of the concrete structure in terms of linear elastic fracture mechanics. Investigation of the *FPZ* and COD are essential for characterizing the stability of a concrete structure.

- The length of the *FPZ* increased slowly as the load increased to 84% of maximum peak-load. With continuous loading, this rate increased until the load reached 100% of the peak load, and was followed by slow growth within the post-peak phase. The length of the *FPZ* was approximately 21% of the ligament length at peak load; however, Wu et al. (2011) found this value to be 25%. The current investigation was terminated at 80% of the peak load during the post-peak phase

(i.e., when the length of the *FPZ* exceeded the measurement volume, which was limited by the size of the calibration plate (~50 mm)).

- The *FPZ* width increased with increasing load, and reached its maximum width at the initiation of the localization of the micro-cracks (i.e., at about 96% of the peak load when the length of the *FPZ* started increasing rapidly); after that, the *FPZ* began to narrow. The maximum width of the *FPZ* was approximately three times the maximum grain size, which was also equal to two times the ligament length for the current work. This experimental finding is consistent with estimates of the crack band width during this loading stage (i.e., three times the maximum aggregate size; Bazant and Oh, 1983). During the post-peak descending (softening) phase, the tortuous crack ran along the ligament while the width of the *FPZ* remained constant and became smaller than the maximum aggregate size.
- This study provides experimental support for the popularity of using the bi-linear softening model to estimate the tension strain softening behaviour of concrete (Roelfstra and Wittmann, 1986; Guinea et al., 1994; Sousa and Gettu, 2003; RILEM, 2007). The shape of the P_{sp} -COD curve derived from the DIC data changed in the post-peak phase, so that two zones were distinguished. The first zone is due to micro-cracking ending at approximately 37% of the peak-load, and the second zone is due to aggregate interlock starting at 22% of the peak-load (i.e., after the initiation of a traction-free zone).

3. Crack Evolution

In this study, attention was paid to the changes in the crack tip position associated with the evolution of the crack path, toughening mechanisms in the *FPZ*, and variations in the dissipated energy along the crack path.

- During the cracking phase, the crack ran through the matrix, and sometimes ran through aggregate particles. High-strength concrete could have been the reason behind this observation as the matrix and the aggregates are mechanically very similar in this type of concrete.
- The traction free zone (or crack extension) initiated during the post-peak phase at 25%-30% of the P_{sp} . The rate of increase of the traction free zone was very small until the post-peak load declined to 10% of the P_{sp} , but increased rapidly after the load declined to 5% of the P_{sp} .
- Crack formation and G_F depend on the mechanical interaction between the aggregates and the cement-based matrix. Consequently, these findings confirm that material properties of concrete depend on the interfacial region.

4. Concrete Fracture Properties

Knowledge of the post-cracking parameters is necessary for any structural integrity assessment because these parameters contribute to crack initiation and propagation.

- Fracture energy (G_F) is a fundamental fracture parameter, which represents the cracking resistance and fracture toughness of concrete. It is generally considered as a material property in concrete fracture mechanics and cracking analyses. The study presented in this chapter demonstrates that the DIC technique is capable of generating the P_{sp} -CTOD softening curve, which directly provides a conservative estimate of G_F without the need for any further calibration. By comparison, the G_F obtained using the traditional clip-on gauge technique (based on the P_{sp} -CMOD curve) was over-estimated by 16% to 29%. Accordingly, the author proposes using the CTOD, instead of the CMOD, to directly calculate the G_F as the outcome is more reliable and less likely to lead to weak design and assessment.
- The fracture properties can be expressed by a single parameter called the characteristic length (l_{ch}) which is defined as $G_F E/f_t^2$. According to Shah et al. (1995), the l_{ch} of concrete is in the range of 200-400 mm. In this study, the l_{ch} was determined to be 374-462 mm when calculated using the data obtained from the traditional clip-on gauge method, compared to 291-378 mm calculated from the DIC results. Thus, the finding for l_{ch} based on DIC data corresponded more closely to the previously published value for the l_{ch} of concrete. This is an indicator that the accuracy of the DIC technique is superior to traditional methods.
- Characteristic length (l_{ch}) and brittleness number, rather than the peak-load, are the best and most informative properties that can be used for the assessment and monitoring of concrete structures.

3.12 Conclusions

The optical DIC non-disturbing, non-contact measurement technique proved to be valuable for characterizing concrete fracture properties. This study demonstrates the use of the DIC technique to generate the P_{sp} -COD softening curve for the crack opening at the crack tip; this curve is the main ingredient for identifying concrete fracture parameters. The study also demonstrates the utility of this novel technique for the investigation of crack evolution and the development of the *FPZ* zone.

The progression of the *FPZ* associated with crack evolution in the WST was monitored successfully with DIC, while these processes presented significant difficulties for a traditional assessment method. The experimental observations were discussed with particular attention to the detection of the evolution of the tortuous crack path and the impact of toughening mechanisms on the *FPZ*, the size of the *FPZ*, the traction free zone (crack extension), the position of the newly formed crack tip, and the variation of dissipated energy and tensile damage along the crack path.

In this study, the DIC technique was applied successfully to the assessment of concrete specimens in the WST and the following conclusions were successfully documented:

- The DIC technique can be used for the assessment of concrete structures since it is possible to monitor the development of the *FPZ* and crack evolution without interference during the fracture.

- This technique provides an accurate measurement of the crack opening displacement (COD) at the crack/notch tip and at any other position on the concrete surface.
- The variation of the dissipated energy and the crack opening displacement along the crack path can be estimated using DIC, while these processes presented significant difficulties for traditional methods.
- The experimental observations revealed that the development of the *FPZ* is slow until 84% of the peak load is applied, then immediate and sudden development of the *FPZ* occurs and continues until 100% of the peak load has been applied; this rapid development is followed by slow growth of the *FPZ* within the post-peak phase. These observations mean that the application of 84% of the peak-load is a critical stage in the loading history. In addition, according to the findings of this study, the length of the *FPZ* at peak-load is approximately 21% of the ligament length.
- The *FPZ* width increases with increasing load, and reaches its maximum width with the initiation of the localization of micro-cracks (at about 96% of the peak load when the length of the *FPZ* starts increasing rapidly). The maximum width of the *FPZ* is approximately three times the maximum grain size; this value was also equal to two times the ligament length of the WST-specimen. During the post-peak phase, the width of the *FPZ* continued decreasing and then remained constant as the crack ran along the ligament.
- The loading stress caused energy consumption in highly stressed regions, such as the *FPZ*. Therefore, energy dissipation is influenced by the size of this zone,

which changes during loading (i.e. the changing dimensions of the *FPZ* during loading influence energy dissipation so that it varies during the WST according to the state of the *FPZ*.)

- The dissipated energy is not equally distributed along the ligament; there is variation in the amount of tensile damage along the crack path, leading to a pronounced size effect.
- The toughening mechanisms in the *FPZ*, due to concrete heterogeneity and micro-cracks, are the main reasons for the softening behaviour that was observed during the WST. As a result of these toughening mechanisms, the energy released into the crack tip was reduced, preventing sudden failure.
- The findings from this study are in accordance with the bi-linear softening model, which is recommended to estimate the tension softening curve of concrete.
- The traction free zone (or crack extension) initiates at 25%-30% of the P_{sp} during the post-peak phase. The critical phase starts at 10% P_{sp} where the crack extension increases rapidly. These observations could not have been made without the use of DIC.
- Mechanical properties of concrete are affected by the interaction between aggregates and cement-based matrix.
- The DIC technique is capable of generating the P_{sp} -CTOD curve, which directly provides a conservative estimate of G_F without the need for any further calibration.
- Characteristic length and brittleness number, rather than the peak-load, are the best properties to use for monitoring and assessment of concrete structure.

The DIC technique met the experimental requirements for the WST and made it possible to study the dynamics of crack propagation by monitoring the evolution of the tortuous crack and energy dissipation during the fracture without the limitations of traditional methods. In the present work, the size of the area that was assessed was limited by the calibration plate size, which controls the field of view. The author suggests using a larger calibration plate to cover the whole ligament length; however, the displacement sensitivity increases with increasing the field of view. Consequently, the use of DIC is recommended for the study of the fracture behaviour of concrete structures, and can be used for both assessment and monitoring purposes.

CHAPTER IV

INVERSE ANALYSIS AND NUMERICAL SIMULATION

Experimentalists put most of their efforts into the characterization of the mechanical behaviour of materials and structures by deriving a set of constants or curves from test data, whereas theoreticians put most of their efforts into developing theories and models that are consistent with the curves and the constants found by the experimentalists. This is a unique time in the history of solid mechanics. Due to the exponential increase in computational power and the continual development of innovative experimental techniques in which model predictions and experimental outcomes can be compared directly, new prospects for characterizing the mechanical behaviour of complex systems and materials more precisely have opened. Indeed, it is now possible to deduce the values of parameters in models developed from theory directly from the results of experiments (Pierron and Lo, 2008). The problem of validating estimated parameters, which are used as primary information to conduct analysis using numerical model is referred to as an inverse analysis.

Bui and Tanaka (1994) noted that inverse problems often arise in the mechanics of materials. This is because the material parameters are not measured directly in the laboratory. These parameters have to be identified through computer simulations of test data, and the minimization of a suitably defined function that quantifies the discrepancy between experimental and computed quantities.

Inverse analysis is needed to develop the concrete *softening* (σ - w) curve as indirect tension tests (such as the WST or TPBT) are conducted instead of a direct uniaxial tension test (see Chapter Two for more details). In this dissertation, the DIC technique was successfully applied to the WST leading to the accurate measurement of the P_{sp} -CTOD directly from the opening at the crack tip. Thus, there is no compromise if this result is employed for the determination of the (σ - w) curve, which leads to an accurate estimation of the fracture properties of concrete such as the *tensile strength* (f_t) and *fracture energy* (G_F). The evaluation of f_t of concrete is of extreme importance for the accurate prediction of crack initiation and propagation. This parameter can be estimated using the splitting tensile strength of concrete cylinders; however, Herholdt et al. (1985) showed that doing so overestimates the true f_t of concrete, and should be reduced by an empirical factor in the range of 0.6 – 0.9.

The main objective of this chapter is to estimate the *softening curve*, which has two basic parameters (f_t and G_F), from experimental measurements. In other words, the principal concern is the possibility of extracting the *softening curve* from the WST results for the P_{sp} -CTOD relationship (obtained using DIC as described in Chapter Three). According to Bazant and Yu (2011), the combined impact of the work-of-fracture and size effect during testing can be avoided only if the fracture energy/initial fracture energy ratio (G_F/G_f) and the knee stress/tensile stress (σ_l/f_t) ratio when bi-linear softening is assumed (shown in Figure 4.1) are known a priori; estimation of these ratios is far too uncertain according to these authors' findings. In this chapter, however, these two ratios were estimated by employing the results of an inverse analysis.

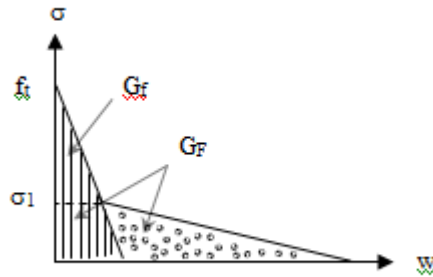


Figure 4.1: The bi-linear softening curve with four parameters

The identification of the fracture properties of concrete was carried out using a bilinear approximation of the *softening curve* (σ - w), and solving an inverse problem. Inverse analysis is known to be ill-posed in many circumstances, however, and the uniqueness of the solution may be an issue to consider. In fact, the feasibility of the inverse analysis is contingent not only on the specimen's geometry and boundary conditions, but also on its material properties (RILEM TC 187-SOC, 2007). In 1976, Bazant showed that localization of strain-softening damage into bands produced a size effect on the post-peak deflections and energy dissipation of concrete structures. Therefore, the *crack band model* was proposed as a solution. A modification of the *fictitious crack model* (FCM) was developed by Bazant and Oh (1983). The forward problem is based on the nonlinear *cracked hinge model* (CHM), which is capable of taking into account the softening phenomenon; the *CHM* is based on the fracture mechanics concepts of the *FCM*. The *FCM* is a simplified model for the quasi-brittle system of fracture where a crack is represented by a narrow band of partially broken material able to transfer stress between its two faces. This stress is defined by a unique function of the σ - w curve for mode I opening (no shear or rotation). The behaviour of the

material outside the cohesive zone is assumed to be linear elastic. This simplified model is viewed as the simplest model capable of capturing, although with limited accuracy, the main aspects of concrete fracture from a structural point of view; i.e., it provides a means for making reasonable predictions of the manner in which concrete structures undergo cracking (RILEM TC 187, 2007). In this model, a closed-form solution is presented for the moment rotation relationship of the hinge as a crack propagates. This approach approximates the behaviour observed during the WST, and allows an analytical solution.

This chapter presents two topics: 1) inverse analysis is carried out to determine the concrete fracture parameters using the non-linear *cracked hinge model* (CHM), and assuming a bi-linear σ - w curve; 2) the fracture parameters that were obtained in this way are confirmed using Finite Element Analysis (FEA) utilizing the coupled damage-plasticity model.

4.1 An Inverse Problem Formulation for the Identification of the Fracture Properties of Concrete

The WST is an indirect tension test which involves a complex state of stresses, strains, and crack opening. A major disadvantage of this test is that it requires a relatively complex data reduction or inverse analysis to generate the *softening curve* (σ - w) (RILEM TC 187-SOC, 2007), which governs the fracture process within concrete. An extension of methods used to estimate the σ - w relationship for concrete, in which the f_t was independently estimated, was described by Rossi et al. (1991). General methods for

inverse analysis are described by Østergaard, Olesen, Stang & Lange (2002). The analytical model for the current research work was derived by the inverse analysis of the results (P_{sp} -CTOD) obtained from direct measurements at the crack tip with DIC as described in the previous chapter. The outcomes of this analysis are interpreted and compared to the preliminary results from traditional indirect measures for the WST (P_{sp} -CMOD) using the same analytical model. The experimental results from the WST were interpreted using the non-linear *CHM* that was introduced by Ulfkjær et al. (1995) and further developed by Olesen et al. (2006). This model was adapted for the WST by Østergaard (2004), who developed an algorithm for an inverse analysis. The conceptual basis of the *CHM* is to consider the crack as a local discontinuity in the overall stress-strain field, which is assumed to disappear outside of a certain bandwidth, s , as shown in Figure 4.2b. Therefore, the non-linear deformation is assumed to be confined to this band while the rest of the structure is modelled using an appropriate elastic model. The simplified nature of the *CHM* provides an efficient method for evaluating the P_{sp} -COD curve.

Since the localized damage band can be physically simulated by a crack, the strain localization allows the use of fracture mechanics to describe the failure of concrete. In this chapter, an inverse analysis procedure for the non-linear *CHM*, based on the *FCM*, is described and applied to the identification of the four parameters of the σ - w curve using the WST results presented in the previous chapter.

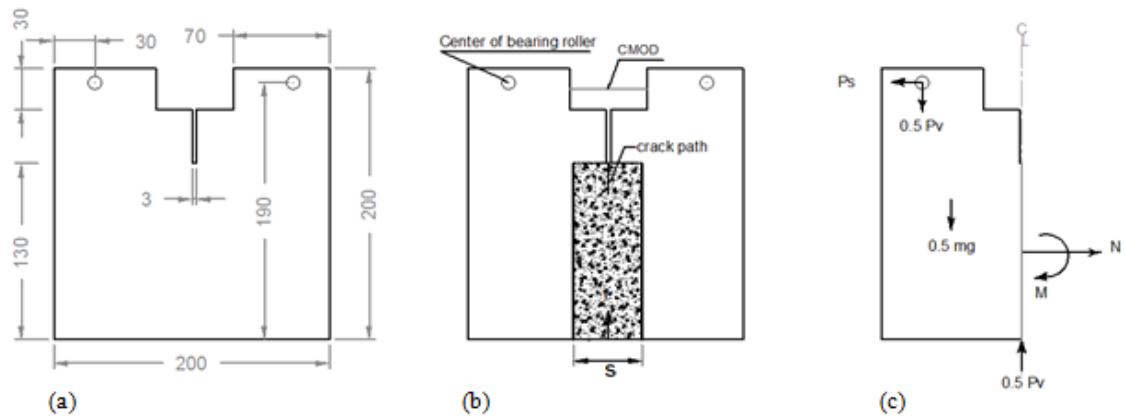


Figure 4.2: (a) Geometry of the WST-specimen, (b) Incorporation of the hinge model, (c) loading (CMOD: crack mouth opening displacement, P_v : vertical load, P_s : splitting load, mg : specimen weight) (All dimensions are in millimetres)

4.1.1 Fictitious Crack Model (FCM)

The fracture behaviour of concrete is influenced by the sizable *FPZ* where the material undergoes softening damage; as a result, the linear fracture mechanics (LEFM) cannot be applied to concrete (Shah and McGarry, 1971). In addition, aggregate-bridging and other toughening mechanisms that are associated with the difficulties involved in the calculation of the crack tip position, the tortuous crack path, and the variation of the *FPZ* along the thickness of the structure, make the application of fracture mechanics to concrete structures more complicated. The non-linear fracture response due to the presence of the *FPZ* was successfully applied to concrete using cohesive pressure (cohesive stress, $\sigma(w)$) acting on crack faces associated with quasi-brittle crack length. A major contribution made by Hillerborg et al. (1976), the first to suggest a *FCM* for concrete fracture, was inspired by the softening and plastic *FPZ* proposed by Barenblatt (1959, 1962) and Dugdale (1960). This model was the first non-linear fracture

mechanical (NLEM) model for concrete that considered energy dissipation in the *FPZ*. It is widely used and supported by reports in the literature, which assume that the energy produced by the applied load is completely balanced by the cohesive pressure. The *FCM* also assumes that the crack initiates and propagates when the tensile stress reaches f_t of the material.

In 1976, Hillerborg, Modeer and Petersson investigated the *FPZ* in front of a crack in a concrete structure and found that it was long and narrow. This observation led to the development of the *FCM* (Hillerborg et al. 1976), one of the simplest and most powerful NLEM models available for concrete. The *FCM* was the first nonlinear fracture mechanical model for concrete that included the *FPZ*. This model is now more commonly called the “*cohesive crack model*” (ACI 446.1 R-91). The *cohesive crack model* (CCM) has been widely accepted as the best compromise for the analysis of the fracture of concrete and other quasi-brittle materials. The softening stress-separation law of this model is best described as a bi-linear curve characterized by the four parameters shown in Figure 4.1: the *initial fracture energy* (G_f), the *total fracture energy* (G_F), the *tensile strength* (f_t), and the *knee point ordinate* (σ_1) (Bazan and Yu, 2010).

Thirty years after Hillerborg’s pioneering work (1976), there are still questions about the best way to determine the fundamental cohesive crack property (i.e., the *softening curve*) RILEM TC 187-SOC (2007).

In the current research, mode I concrete fracture is simulated using the *FCM* proposed by Hillerborg et al. (1976), and following the cohesive models of Barenblatt (1962) and Dugdale (1960). Jenq and Shah (1985), Kobayashi et al. (1991), Cook et al. (1987), and Cox and Marshall (1994) all studied the fracture of concrete and described the energy release rate for mode I quasi-brittle crack, G_q , using both of the terms G_{Ic} and G_σ . Shah et al. (1995) noted that if the energy dissipation, derived using the Dugdale-Barenblatt cohesive concept (G_σ), is constant because the FPZ is constant, then the energy release rate for a mode I quasi-brittle crack, G_q , is constant and satisfies the classical definition of ‘energy release rate’. In other words, the *FCM* assumes that cracked faces are in contact during stable crack propagation and the energy required to create the new surfaces is small compared to that required to separate them. Therefore, in this model, propagation of a quasi-brittle crack is approximated using the Dugdale-Barenblatt mechanism (i.e., energy dissipation mechanism - G_σ), which takes into account only the material traction, assuming that the Griffith-Irwin energy dissipation mechanism for mode I fracture (i.e., the energy rate consumed to create two surfaces, G_{Ic}) is equal to zero. Consequently, the new crack and corresponding *FPZ* are simulated by the monotonic decreasing function $\sigma(w)$ of crack propagation displacement (w). The cohesive stress-crack opening relationship (σ - w) is illustrated in Figure 4.3. In this model, the real traction-free part of the crack ends at the start of the fictitious crack.

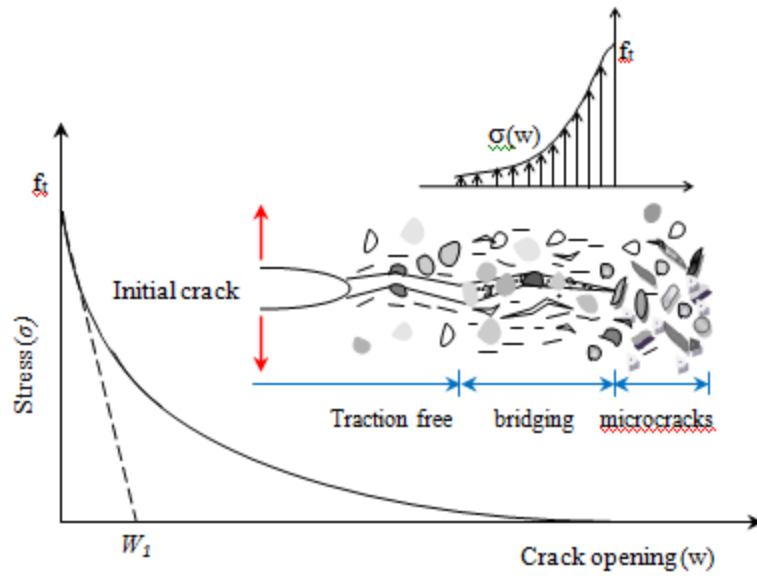


Figure 4.3: Cohesive crack in front of the notch and stress-crack opening curve

In the *FCM*, it is assumed that strain localization and crack initiation appear after the peak load is reached, but before this, the material exhibits linear elastic behaviour. After crack initiation, stresses can still be transmitted across the crack; therefore, the crack is termed a ‘fictitious’ crack. The softening takes place within a narrow zone (the FPZ or the damage zone), while simultaneously, the remainder of the specimen contracts elastically due to decreasing stress (Hillerborg, 1976). Consequently, the pre-peak tensile response of concrete can be characterized by a linear stress-strain curve, while the post-peak fracture behaviour (softening) within the damage zone can be described by a stress-crack opening function (σ - w). The area under σ - w curve represents the material fracture energy, G_F , and demonstrates the energy absorbed per unit area of the crack; G_F is regarded as a material fracture parameter (Figure 4.4(c)). In this model, the *softening curve* is assumed to be a material property that is independent of structural geometry and size; this curve can be constructed if the material properties, f_t and G_F , and the shape of

the σ - w curve are known as these three material parameters are required for this model. Hillerborg et al. (1976) combined f_t and G_F to determine another material property called characteristic length (l_{ch}), which is proportional to the *FPZ* length. In 1995, Shah et al. recognized that the l_{ch} based on the *FCM* is on the order of 2.00 to 3.33 times the length of the fracture process zone (l_{fpz}) at complete separation of the initial crack tip.

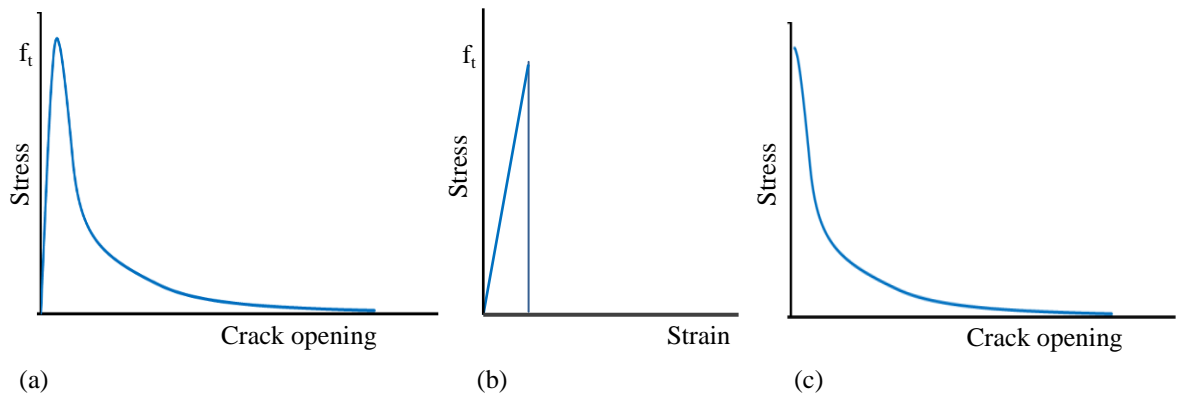


Figure 4.4: Principles of the fictitious crack model (FCM): (a) tensile stress-crack opening; (b) stress-strain curve for the whole specimen (c) stress-crack opening within the fracture zone

4.1.2 Description of the Cracked Hinge Model (CHM)

In 1995, the *CHM* was introduced by Ulfkjær et al., developed by Pedersen (1996) and Casanova and Rossi (1997), and then by Stang and Olesen (1998 and 2000). Application of the *CHM* to three point bending beams was investigated by Olesen (2001), and adapted to WST results by Østergaard (2003). The *CHM* assumes that the material is quasi-brittle (as expressed by the *fictitious crack model*).

The basic idea of the *CHM* is to model the part of the structure that is close to the crack as a local change in the global stress and strain field using incremental horizontal strips of independent spring elements attached at each end to the rigid boundary of the band, s , which can translate and rotate adjoining un-cracked elements outside of the band as shown in Figure 4.2. The constitutive relationship for each spring is assumed to be linear elastic in the pre-cracked state. Within the cracked hinge band, it is assumed that crack propagation changes the stress-strain relationship only locally while the rest of the specimen remains unaffected. These assumptions make the analysis more effective in terms of time and cost savings as the solution for only part of the structure needs to be calculated.

Yielding a closed-form analytical solution for the entire P_{sp} -COD curve is one advantage of the *CHM*, in addition to other features such as the ability to develop simple programs that can replace time-consuming FEA modelling, and which may be applied for rapid analysis of experimental results (Østergaard, 2003).

Crack opening displacement is sensitive to the shape of the $(\sigma-w)$ curve; many different shapes, such as linear, bilinear, tri-linear, exponential, and power functions, have been used (Shah et Al., 1995). The bi-linear softening curve is simple, has already been adopted by many researchers, and provides sufficiently accurate results for a wide range of materials; it is usually used to approximate the softening behaviour of cementation materials. It might be expected that refinement of the *softening curve* by using a greater number of lines would improve the accuracy of the WST simulation.

However, the inverse analysis becomes unstable because of the large amount of information to be determined (Skocek and Stang, 2008). The bi-linear shaped softening curve is also recommended by CEB-FIP Model Code. For all of the above reasons, as well as the experimental findings presented in Chapter Three showing that the bi-linear function captures the two major mechanisms responsible for the observed tension softening in concrete (micro-cracking and aggregate interlock), the bi-linear softening model was chosen for the current work.

According to the *FCM*, the constitutive relationship for each segment inside the hinge is assumed to be linear elastic in the pre-cracked state (phase 0), while the post-peak fracture behaviour (softening) within the damage zone is approximated by a bi-linear softening curve as shown in Figure 4.5 and Equation (4.1). The parameters in the bi-linear function are: f_t , a_1 , a_2 , b_2 , E as shown in Figure 4.5 where a_1 and a_2 are the normalized slopes of the σ - w relationship, and b_2 intersects the y-axis for the second part of the bilinear relationship. A simple Rankine criterion is used to detect crack initiation. This criterion states that a crack forms when the maximum principal tensile stress exceeds f_t of concrete. In other words, cracking occurs when $\sigma(w) = f_t$, which yields at $b_1=1$ as shown in the figure below.

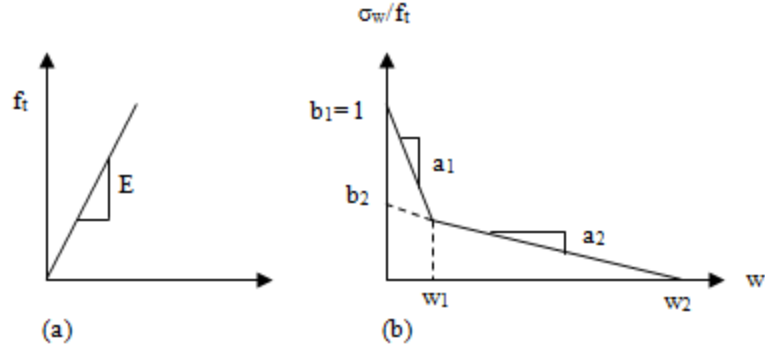


Figure 4.5: (a) Stress-strain relationship (pre-cracked state), (b) Stress-crack opening relationship (closing pressure for the fracture process zone) assuming a bi-linear softening curve for the cracked state

The stress-strain relationship in the *FCM* is given by:

$$\sigma = \begin{cases} E\varepsilon & \text{pre-cracked state} \\ \sigma_w = g(w) f_t & \text{cracked state} \end{cases} \quad (4.1)$$

where E stands for the Young's modulus, ε for elastic strain, $\sigma(w)$ for stress-crack opening relationship with w representing the crack opening, f_t for the uniaxial tensile strength, and $g(w)$ is a function representing the shape of the stress-crack opening relationship. Accordingly, for a bi-linear shape, $g(w)$ is given as:

$$g(w) = \begin{cases} b_1 - a_1 w & 0 \leq w \leq w_1 \\ b_2 - a_2 w & w_1 \leq w \leq w_2 \end{cases} \quad (4.2)$$

where $b_1 = 1$, and the limits w_1 and w_2 are given by the intersection of the two line segments and the intersection of the second line segment with the abscissa, respectively:

$$w_1 = \frac{1-b_2}{a_1-a_2}; \quad w_2 = \frac{b_2}{a_2} \quad (4.3)$$

The application of the *CHM* to a WST-specimen is shown in Figure 4.6, where the geometry, loading and deformation characteristics are illustrated with the ligament length of the hinge (h) equal to 130 mm. Analysis of the hinge element allows for the determination of the axial force, N , and bending moment, M , for any given value of the angular hinge deformation, 2ϕ .

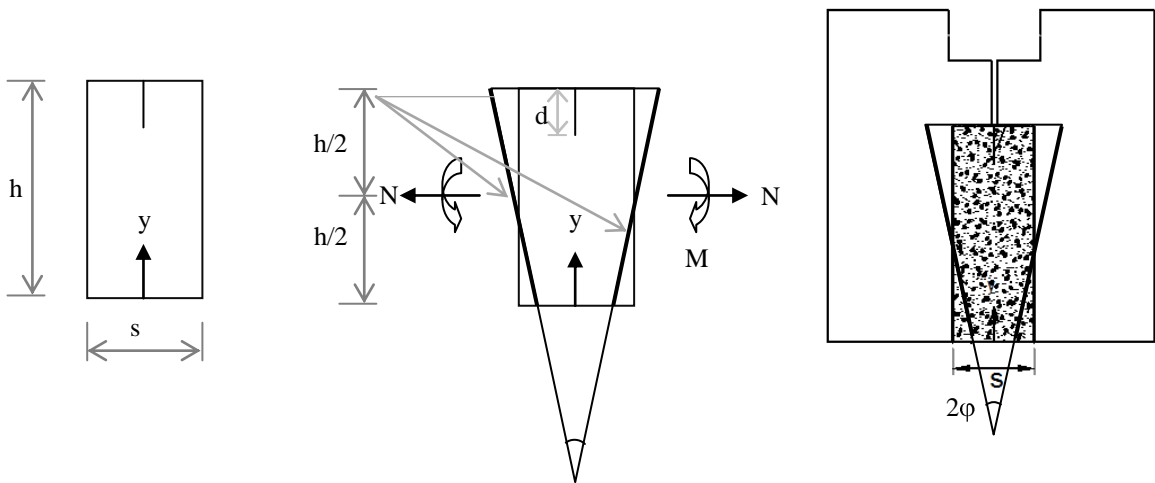


Figure 4.6: Geometry, loading and deformation characteristics with incorporation of the hinge element to a WST-specimen

The deformation of the hinge is described by half of the angular deformation (ϕ) and the depth of the neutral incremental strip (y_0) (Figure 4.7 and Equation 4.4). (See Oleson, 2001 for more details).

$$\left. \begin{aligned} w(y) &= \frac{2}{1-\beta_i} \frac{y-y_0}{\varphi-\xi_i} \frac{1-\beta_i}{1-\beta_i} \\ \sigma \quad w(y) &= \frac{\xi_i-2}{1-\beta_i} \frac{y-y_0}{\varphi\beta_i} \frac{E}{s} \end{aligned} \right\} \quad (4.4)$$

Where β_i and ξ_i are dimensionless parameters chosen according to the phase of crack propagation i and are defined by:

$$\beta_i = \frac{f_i a_i s}{E}, \quad \xi_i = \frac{f_i b_i s}{E}, \quad \text{while } 1 \leq i \leq 2 \quad (4.5)$$

As the crack propagates at the crack tip, the stress distribution changes through three distinctive phases. The σ - w profile is divided into different intervals that are governed by equation 4.4, and correspond to different values of i according to the actual crack propagation phase. These intervals are defined by y^* , y_1 , and y_2 parameters as shown in Figure 4.7 and Equation 4.6.

$$\left. \begin{aligned} y^* &= \frac{f_i s}{2\varphi E} \\ y_i &= y_0 + \frac{1}{2\varphi} \xi_i - \beta_i - 1 \quad w_i, \quad \text{while } 1 \leq i \leq 2 \end{aligned} \right\} \quad (4.6)$$

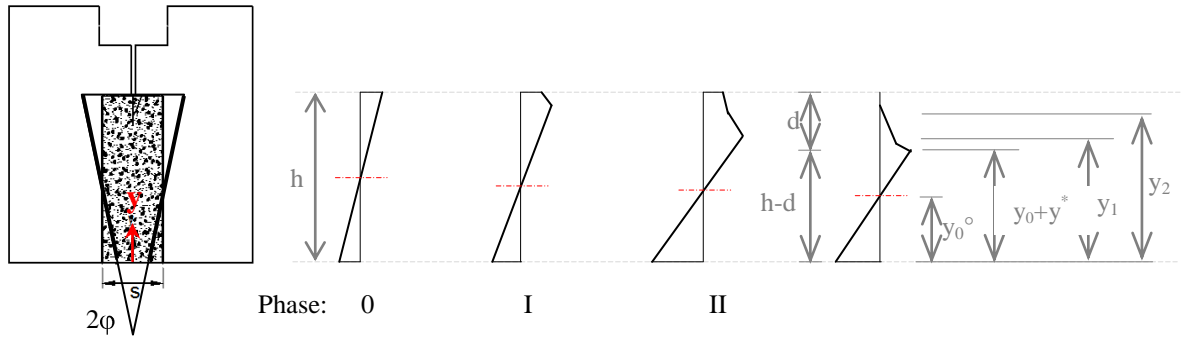


Figure 4.7: The phases of stress distribution in the hinge. Phase 0: Pre-cracking state of stress; Phases I to III: States of stress during crack propagation (adopted from Oleson 2001)

The complete stress distribution is established in all phases of the crack propagation during this step. Phase 0 represents the elastic state where no crack has formed, while phases I, II and III represent different stages of crack propagation (linear, bilinear and bilinear with a stress-free tail). The relationship between N , M , and φ can be obtained in each phase by balancing the sectional stresses with the external force N and the bending moment M . The following normalizations are introduced into the model:

$$\mu = \frac{6M}{f_t h^2 t}, \quad \rho = \frac{N}{f_t h t}, \quad \theta = \frac{h E \varphi}{s f_t}, \quad \alpha = \frac{d}{h} \quad (4.7)$$

where t is the width of the specimen (hinge), μ is the normalized moment, ρ is the normalized normal force, θ is the normalized hinge deformation, α is the normalized crack depth, and d is the depth of the fictitious crack (Figure 4.7). The pre-crack elastic

behaviour of the hinge is described by $\alpha = 0$ and $\mu = \theta$, while the cracking stage starts when $\theta = 1 - \rho$.

This analysis covers only the situations where the fictitious crack has not penetrated all the way through the depth of the hinge (i.e., the condition $\alpha < 1$ must hold), which implies that the solution is not valid for large positive values of the external normal force N .

The analysis is performed according to the state of crack propagation for four phases as shown in Figure 4.7:

- Elastic state where no crack has formed
- Linear
- Bilinear
- Bilinear with a stress-free tail

The hinge solution for the four phases is described as follows:

- Phase 0: The pre-crack elastic phase ($0 \leq \theta \leq 1 - \rho$)

$$\left. \begin{array}{l} \rho = 0 \\ \mu = 0 \end{array} \right\} \quad (4.8)$$

- Phase I: ($1 - \rho \leq \theta \leq \theta_{I-II}$)

$$\alpha = 1 - \beta_1 - \sqrt{1 - \beta_1 \left(\frac{1 - \rho}{\theta} - \beta_1 \right)} \quad (4.9a)$$

$$\mu = 4 \left(1 - 3\alpha + 3\alpha^2 - \frac{\alpha^3}{1 - \beta_1} \right) \theta + (6\alpha - 3)(1 - \alpha) \quad (4.9b)$$

➤ Phase II: $(\theta_{I-II} \leq \theta \leq \theta_{II-III})$

$$\alpha = 1 - \beta_2 - \frac{1 - b_2}{2\theta} - \sqrt{1 - \beta_2 \left(\frac{1 - b_2^2}{4\theta^2(\beta_1 - \beta_2)} - \beta_2 + \frac{b_2 - \rho}{\theta} \right)} \quad (4.10a)$$

$$\mu = 4 \left(1 - 3\alpha + 3\alpha^2 - \frac{\alpha^3}{1 - \beta_2} \right) \theta + (6\alpha - 3)(1 - \rho) - \frac{1 - b_2 \left(3\alpha^2 - \left(\frac{c}{2\theta} \right)^2 \right)}{1 - \beta_2} \quad (4.10b)$$

➤ Phase III: $(\theta_{II-III} \leq \theta)$

$$\alpha = 1 - \frac{1}{2\theta} \left(1 + \sqrt{\frac{1 - b_2^2}{\beta_1 - \beta_2} + \frac{b_2^2}{\beta_2} + 4\rho\theta} \right) \quad (4.11a)$$

$$\begin{aligned} \mu = & 4 \left(1 - 3\alpha + 3\alpha^2 - \alpha^3 \right) \theta + (6\alpha - 3)(1 - \rho) - 3\alpha^2 \\ & + \frac{1}{4\theta^2} \left(1 - \frac{b_2}{\beta_2} \right) \left(1 - \frac{b_2}{\beta_2} + c \right) \left(1 + \frac{\beta_1 c}{1 - \beta_1} \right) + \left(\frac{c}{2\theta} \right)^2 \end{aligned} \quad (4.11b)$$

where c is given by:
$$c = \frac{1 - b_2}{\beta_2 - \beta_1} \frac{1 - \beta_1}{\beta_2 - \beta_1}$$

The transition points between these phases are governed by the following equations:

➤ From Phase 0 to Phase I:

$$\theta_{0-I} = 1 - \rho \quad (4.12)$$

➤ From Phase I to Phase II:

$$\theta_{I-II} = \frac{1}{2} \left(1 - \rho - c + \sqrt{1 - \rho - c^2 + \frac{c^2}{\beta_1 - 1}} \right) \quad (4.13)$$

➤ From Phase II to Phase III:

$$\theta_{II-III} = \frac{1}{2} \left(\rho \beta_2 - 1 + \frac{b_2}{\beta_2} + \sqrt{\rho^2 \beta_2 - 1^2 + 2\rho \beta_2 - 1 \frac{b_2}{\beta_2} + \frac{1 - b_2^2}{\beta_1 - \beta_2} + \frac{b_2^2}{\beta_2}} \right) \quad (4.14)$$

The crack mouth opening displacement (CMOD) is a function of the ligament length, h , and is given by the crack opening at the crack tip (i.e., where $y = h$):

$$CMOD = w h = \frac{sf_i}{E} \frac{1 - b_i + 2\alpha\theta}{1 - \beta_i} \quad (4.15)$$

where:

$$b_i, \beta_i = \begin{cases} 1, \beta_1 & \text{Phase I} \\ b_2, \beta_2 & \text{Phase II} \\ 0, 0 & \text{Phase III} \end{cases} \quad (4.16)$$

The width of the hinge, s , is an essential parameter that influences the solution of the hinge model. Bazant and Oh (1983) proposed to model the *FPZ* with a band of uniformly and continuously distributed micro-cracks within a fixed width (h_c) called the

crack band, which was assumed to be a material fracture parameter for this model. An approximate estimation of the crack band is $h_c = n_a d_a$, where d_a is the maximum aggregate size and n_a is an empirical constant equal to 3 for concrete. However, Østergaard (2003) assumed that this band has a width of approximately 0.2 ligament length ($0.2h$). In this study, the band width was estimated to be 26 mm since both approaches give almost the same result as the maximum aggregate size used was 9 mm.

4.2 Application of Inverse Analysis to the Wedge Splitting Test (WST)

If the hinge model is applied successfully to the WST, it allows for an accurate determination of G_F and it also provides a fast and objective determination of the (σ - w) curve. This is due to the model's detailed analytical expression that includes phased analysis and inverse calculations. The major concern with use of the hinge element is whether the assumption about rigid vertical boundaries is acceptable. If deformations in the boundary planes play a significant role in the shape of the P_{sp} -COD curve, then the model might be too simple and thus, imprecise in its predictions. Østergaard (2003) addressed this concern by comparing hinge model results with FEA calculations.

In the current research, inverse analysis was carried out to determine the four parameters that control the proportions of the softening curve; the bilinear shape of the softening curve was assumed in advance (Figure 4.1). Splitting load-crack opening displacement (P_{sp} -COD) data from the WST, obtained using both classical and DIC techniques (see chapter three), is the main component of the inverse analysis that must be

performed in order to estimate the concrete fracture properties. After obtaining the data from the WST, two steps are necessary to perform the inverse analysis: 1) the parameters are determined for a solution that will simulate the experimental results; and 2) an optimization process based on the minimization of discrepancy or error in the fit between the experimental data and the corresponding data from the simulation is accomplished in the second step of the inverse analysis.

As mentioned, the *CHM* is the basis of the forward problem that is solved to determine the P_{sp} -COD curve from the softening curve parameter obtained from the inverse analysis (Figure 4.1). Figure 4.8 shows the loading on the WST-specimen; the normal force N and moment M can be determined from the equilibrium equation:

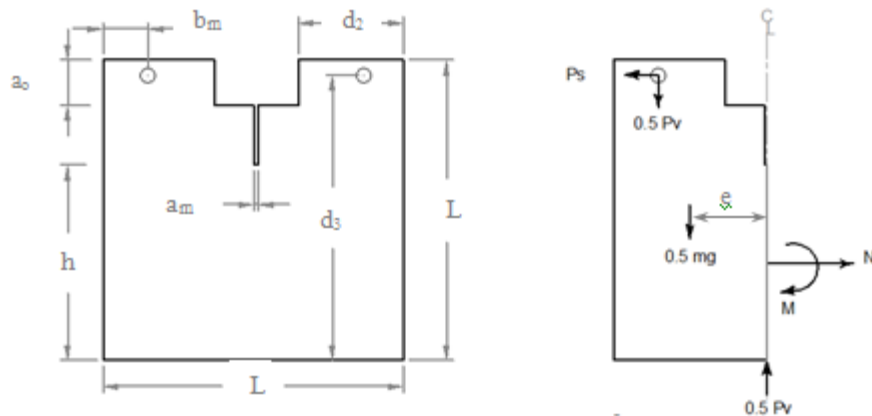


Figure 4.8: Geometry and loading of the WST-specimen

$$N = P_{sp} \quad (4.17)$$

$$M = P_{sp} \left(d_2 - \frac{h}{2} \right) + \frac{1}{2} P_v d_1 + \frac{1}{2} mge \quad (4.18)$$

where m is the WST-specimen's mass, and g is the gravity acceleration

The magnitude of load at which cracking initiates, (P_{sp}^0), at $\theta = 1 - \rho$ (see Section 4.1.2 for details related to the crack hinge model), can be estimated using Equations 4.8, 4.15 and 4.18, leading to:

$$P_{sp}^0 = \frac{f_t h^2 t - 3mge}{6d_2 + 3d_1 k - 2h} \quad (4.19)$$

The crack mouth opening displacement (CMOD) represents the opening at the line of loading, and where the crack opening displacement is traditionally measured experimentally in the WST using a clip-gauge as shown in Figure 4.2. The *CMOD* was determined from the summation of the opening due to the presence of the crack at the crack tip (δ_{CTOD}), the elastic deformation of the specimen (δ_e) and a geometrical amplification (δ_g) caused by the effect of the distance between the crack tip at h and the position of the clip gauge. In other words, δ_g represents the angle of rotation between the crack faces. The following equation is used to calculate the *CMOD*:

$$CMOD = \delta_e + \delta_{CTOD} + \delta_g \quad (4.20)$$

where:

$$\delta_e = \frac{P_{sp}}{Et} v_2 \quad [\text{Tada et al., 1985}] \quad (4.21)$$

$$v_2 = \frac{x}{1-x}^2 (38.2 - 55.4x + 33x^2) \quad (4.22)$$

where v_2 is a function of the ratio between the length of the initial crack and the distance from the loading line to the bottom of the specimen (given by $x=l-h/b$), while the effect of the vertical force, P_v , on the elastic opening is ignored as it is very small compared to the opening due to cracking.

$$\delta_{COD} = \frac{f_t s}{E} \frac{1 - b_i + 2\alpha\theta}{1 - \beta_i} \quad \text{while } 1 \leq i \leq 2 \quad (4.23)$$

where i refers to the phase of crack propagation as explained previously in section 4.1.2 (*cracked hinge model*).

Olesen (2001) calculated the opening due to the distance between the load line and the bottom of the crack using another equation:

$$w_{y,\varphi} = \frac{(y - y_0)\varphi - \xi_i}{1 - \beta_i}, \quad \xi_i = \frac{f_t b_i s}{E} \quad (4.24)$$

The crack angle, φ_{cr} , can be calculated with the following equation, which can be applied to all of the cracking phases:

$$\varphi_{cr} = \frac{\delta_{COD}}{2\alpha h} \quad (4.25)$$

When cracking begins, the angle of the crack faces does not equal zero. This was found from the differentiation of equation (4.24):

$$\varphi_{cr} = \frac{1}{2} \frac{\partial w(y, \varphi)}{\partial y} = \frac{\varphi}{1 - \beta_i} \quad (4.26)$$

When the crack is initiated at the angular deformation of φ_{0-I} , the crack angle is given by:

$$\varphi_{cr}^0 = \frac{\varphi_{0-I}}{1 - \beta_1} \quad (4.27)$$

Accordingly, the corrected crack angle is given by:

$$\bar{\varphi}_{cr} = \varphi_{cr} - \varphi_{cr}^0 \quad (4.28)$$

Thus, the geometrical amplification, δ_g , using the normalized angle, θ , instead of crack angle, φ , is given by:

$$\delta_g = 2\bar{\varphi}_{cr}(b-h) = 2(b-h) \left(\frac{\delta_{COD}}{2\alpha h} - \frac{f_t s}{hE} \frac{\theta_{0-I}}{1-\beta_1} \right) \quad (4.29)$$

The numerical approach must be applied using an iterative scheme to determine the actual load, P_{sp} , for a given $CMOD$; these data are presented in Chapter Three for the WST. This solution can be obtained using two non-linear equations describing the restraints on the load, P_{sp} , and the crack opening displacement, $CMOD$:

$$\mu_{ext} P_{sp} - \mu_{int}^j \theta, P_{sp} = 0 \quad (4.30)$$

$$CMOD^{obs} - CMOD P_{sp}, \theta = 0 \quad (4.31)$$

where $\mu_{ext} P_{sp}$ stands for the external loading of the hinge (given by Equation 4.19), $\mu_{int}^j(q, P_{sp})$ is the internal normalized moment capacity of the hinge, j is the actual crack phase, $CMOD^{obs}$ is the experimental observation for $CMOD$, and $CMOD P_{sp}, \theta$ is the determined $CMOD$ from Equation 4.20.

The above steps describe the forward analysis, which is required to obtain the P_{sp} - $CMOD$ curve for a known σ - w relationship (a bilinear function). This analysis is a necessary step towards minimizing the function that describes the error between the experimental results and the simulation results obtained using the parameters determined from the inverse analysis results during the optimization process.

To obtain the σ -w relationship from the experimental P_{sp} -COD relationship, inverse analysis is required. The inverse analysis consists of identifying the concrete fracture parameters that are compatible with the specimen's response. The approach is based on the finite element method developed by Roelfstra and Wittmann in 1986. These authors assumed that the essential fracture properties are those that minimize a function describing the error between the finite element curve and the experimental curve. In 1993, Ulfkjaer and Brincker investigated an optimization scheme that could be used for inverse analysis; however, this formulation had problems with local minima. The technique presented in the current work is based on the research of Olesen (2001) and Østergaard et al. (2004); the non-linear *cracked hinge model* described previously. The optimization problem is solved in steps corresponding to the different phases of crack propagation. This incremental technique was chosen to reduce the risk of reaching local minima. It requires the introduction of some of the material parameters in advance of the analysis, to obtain the remaining parameters; in addition, the type of the estimated softening curve needs to be defined prior to the analysis. A global optimization process involving several measured points is conducted. This global optimization process can be done through the determination of a series of sub-optimizations; selected variables are calculated one after the other as will be explained in this section. This approach to inverse analysis is more robust due to a lower risk of reaching local minima (Østergaard, 2003).

From the P_{sp} -CMOD curve, a minimization problem can be formulated to obtain the best *softening curve* that also produces the least discrepancy between the

experimental and the modelled results. The bi-linear softening curve shown in Figure 4.5 can be obtained from the output of the inverse analysis, which can be used to approximate the softening behaviour of concrete. To arrive at an accurate result when conducting an inverse analysis, the experimental data points must be spaced equidistantly along the curve so that each segment has the same weight in the computation. Otherwise, the segment with the most weight will have an excellent fit with experimental observations, which would influence the results and affect the accuracy of the remaining segments leading to a poor fit for the rest of the curve. Accordingly, data reduction was applied to the WST results before the analysis, and then the inverse analysis was carried out in three steps related to the different crack propagation phases (according to the non-linear *cracked hinge model* explained previously in Section 4.1.2).

Since the assessment of the fracture behaviour of a concrete structure can be influenced by the form of the $\sigma(w)$ function, reasonable and accurate determination of the $\sigma-w$ curve and the corresponding parameters are critical for the assessment of *cohesive crack* propagation (Shah et al., 1995). According to the bi-linear model adopted in this dissertation and illustrated in Figure 4.5, the pre-crack behaviour is assumed to be linear-elastic until the tensile strength, f_t , is reached. Then, the concrete cracks according to the bilinear $\sigma-w$ relationship. Using the following stepwise approach, each crack propagation phase has free parameters that govern the response of that particular phase while the other parameters are fixed. The material parameters of the hinge model can be established through an inverse analysis of the test results by minimizing the difference between the experimental results for the WST and the hinge model predictions for the splitting load.

Step I - (Determination of Young's modulus – E)

The first phase, the linear elastic phase, assumes that no crack has formed; Young's modulus is the only parameter that has influence on the P_{sp} -COD curve (Figure 4.5a). Therefore, it is the only free parameter that is determined in this step, while the other parameters are estimated and fixed during this step. It is important to mention here that the initial estimation of the *tensile strength* controls the number of observations that are conducted during the optimization process, using the mean square of differences between observations and predictions of the splitting load (P_{sp} and \hat{P}_{sp}) as an error norm:

$$\min_E \left(\frac{1}{N_{\max}^0} \sum_0^{N_{\max}^0} P_{sp} - \hat{P}_{sp}^2 \right) \quad E > 0 \quad (4.32)$$

where N_{\max}^0 is the last observation made in phase 0.

The optimization strategy for the cracked phases is conducted after estimating Young's modulus. Because the bi-linear shape of the σ -w was assumed in advance of the analysis, the optimization of the cracked phase is divided into two steps: f_t and a_1 are determined first, and then a_2 and b_2 are determined in the last step. This approach was adopted by Østergaard (2004) who claimed that this detailed analytical model is very robust when the local minima can be avoided during the optimization process.

Step II - (Determination of the tensile strength, f_t , and initial slope, a_1)

In this step, the initial phase of crack propagation (Figure 4.5 (b)), Young's modulus (E), tensile strength (f_t), and initial slope (a_1) are the only parameters governing the response of the *softening curve*. However, because E was determined during Step 1 and is fixed, the optimization is performed with only f_t and a_1 as free parameters.

$$\min_{(f_t, a_1)} \left(\frac{1}{N_{\max}} \sum_0^{N_{\max}} P_{sp} - \hat{P}_{sp}^2 \right) \quad f_t > 0 \quad (4.33)$$

where N_{\max} is the total number of observations made for this step.

Step III - (Determination of the second slope, a_2 , and its intersect with the y-axis, b_2)

This is the last step of optimization; all of the parameters, except for a_2 and b_2 , were determined in Steps 1 and 2 and are fixed

$$\min_{(a_2, b_2)} \left(\frac{1}{N_{\max}} \sum_0^{N_{\max}} P_{sp} - \hat{P}_{sp}^2 \right) \quad (4.34)$$

where N_{\max} is the total number of observations made for this step.

The three equations described above are solved by an iterative process. After inverse analysis was used to determine the bi-linear softening function, the fracture test was simulated numerically using the initial inverse analysis result (the bi-linear softening diagram) by means of forward analysis based on the non-linear *CHM*. The calculated P_{sp} -COD curve following minimization was compared to the experimental curve; if the two curves were not close, the process was repeated, and the optimization cycle continued until a good convergence was reached. By globally reiterating the optimization process for all steps, the number of observations can be minimized, since the global iterations will converge at the true phase change point. The softening diagram leading to good agreement between the experimental and predicted outcomes is considered to be the *softening curve* of the tested concrete. Empirical observations found that the accuracy of the estimation of the tensile strength is critical.

The inverse analysis procedure was implemented in MatLab by adopting the set of programs prepared by Østergaard (2003). Using the experimental observations (see Chapter Three), the loop incorporates all observations and returns corresponding values for P_{sp} for a given estimate of the parameters in the σ - w relationship and a set of CMOD values. This approach was utilized in the algorithm for the inverse analysis, which applies the simplex algorithm, included in the Matlab Optimization Toolbox, to solve Equations 4.32 to 4.34.

This algorithm was conducted first with the WST's experimental data presented in Chapter Three for the traditional method of deriving the P_{sp} -CMOD curve by attaching

a clip-gauge at the crack mouth. As mentioned in the introduction to this chapter, the DIC results for the WST can likewise be used for the determination of the *softening curve* using the same procedure.

The main objective of this chapter is to approximate the concrete fracture parameters from the DIC experimental data. In other words, the possibility of extracting the σ - w relation from the WST results measured at the crack tip (rather than the crack mouth) with DIC techniques was examined. Consequently, Østergaard's algorithm was modified for use with experimental data extracted using DIC, where the crack-opening displacement was recorded at the crack tip during loading (see Chapter 3; Figure 3.17). As mentioned, the calculated CMOD consisted not only of the real crack opening and elastic deformation of the WS-specimen, but also the deformation caused by the rotation of the crack faces (geometrical amplification deformation, δ_g) due to the distance between the actual crack tip and the position of the clip gauge at the line of loading. In the case of DIC, the CTOD can be calculated directly as this last factor (δ_g) was not required for the analysis of the DIC data; accordingly, Equation 4.21 was modified as follows:

$$CTOD = \delta_e + \delta_{CTOD} \quad (4.35)$$

4.3 Inverse Analysis Results

In the previous section, a minimization problem was formulated to obtain the optimal softening curve that produces the least discrepancy between the experimental data and the predictions of the numerical model. The inverse analysis consists of identifying the concrete fracture parameters, including the bi-linear softening curve. The results of the inverse analysis are used to approximate the concrete softening behaviour, compatible with the test specimen's actual response.

Most approaches to inverse analysis investigate the response of only one test specimen to obtain the corresponding (σ - w) curve (RILEM TC 187-SOC, 2007). However, to improve the inverse analysis results, some researchers compare the results obtained from different types of tests. Guinea et al. (1994) and Abdala and Karihaloo (2004) used the notched beam test response together with the splitting tension test to improve the tensile strength estimation. Other researchers repeated the same test with specimens of different sizes (Gettu et al., 1998). Bolzon and Maier (1998) used more than one data set from tests using specimens of the same size; this was the method chosen for the current research work, so the same steel molds were reused to produce the test specimens. The inverse analysis was applied using the experimental results for specimens WST5 and WST6 (see chapter three). First, the analysis was conducted utilizing the experimental results obtained with the traditional technique where the CMOD was measured with a clip-gauge, and then the algorithm was modified to adapt it for the CTOD measurements obtained with the DIC technique.

The numerical results were compared with the experimental findings for both the DIC and the traditional clip-gauge measures from the WST. Figures 4.9 and 4.10 illustrate a comparison between the experimental P_{sp} -CTOD curve and the corresponding curve obtained from the inverse analysis of the DIC data for specimens WST 5 and WST 6. In addition, these figures depict the bi-linear σ - w relationship extracted from the output parameters of the inverse analysis (Tables 4.1 and 4.2) including the *tensile strength* (f_t) and the *softening curve* parameters (a_1 , a_2 , and b_2) when b_1 is equal to one. The results of the inverse analysis using traditional CMOD measurements are shown in Figures 4.11 and 4.12. Figure 4.12 illustrates the bi-linear σ - w relationship extracted from the output parameters of the inverse analysis summarised in Tables 4.3 and 4.4.

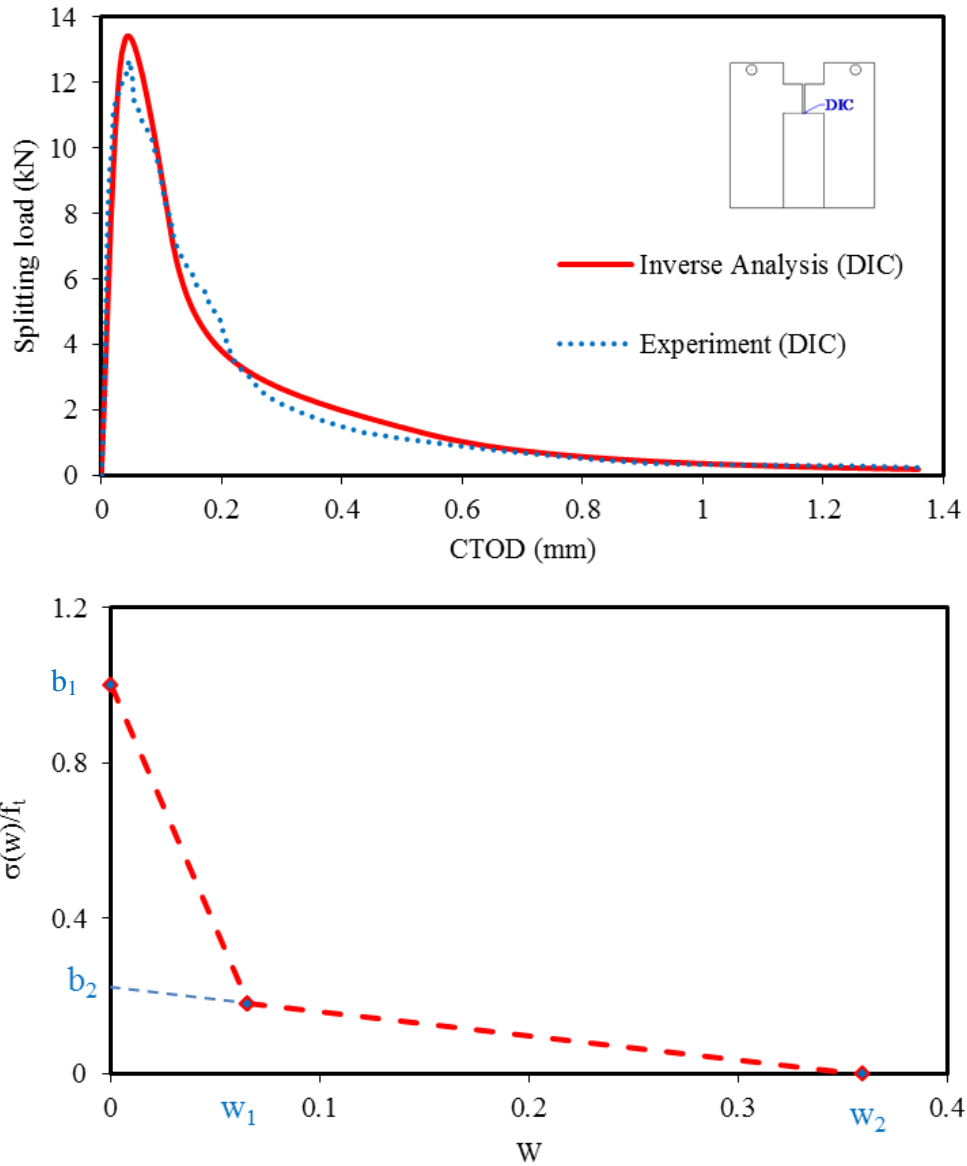


Figure 4.9: (a) Load-crack tip opening displacement curve (Psp-CTOD) and (b) normalized stress-crack opening displacement curve, extracted from inverse analysis using experimental DIC data for WST5

Table 4.1: Comparison between the input and output bilinear softening parameters of the inverse analysis for WST5 using the DIC experimental data

Softening curve parameters & E	f_t (MPa)	a_1	a_2	b_2	E (MPa)
Estimated Data (input data)	2.6	11.0	0.4	0.10	31,500
Inverse Analysis Result (output data)	2.1	13.0	0.5	0.18	40,000

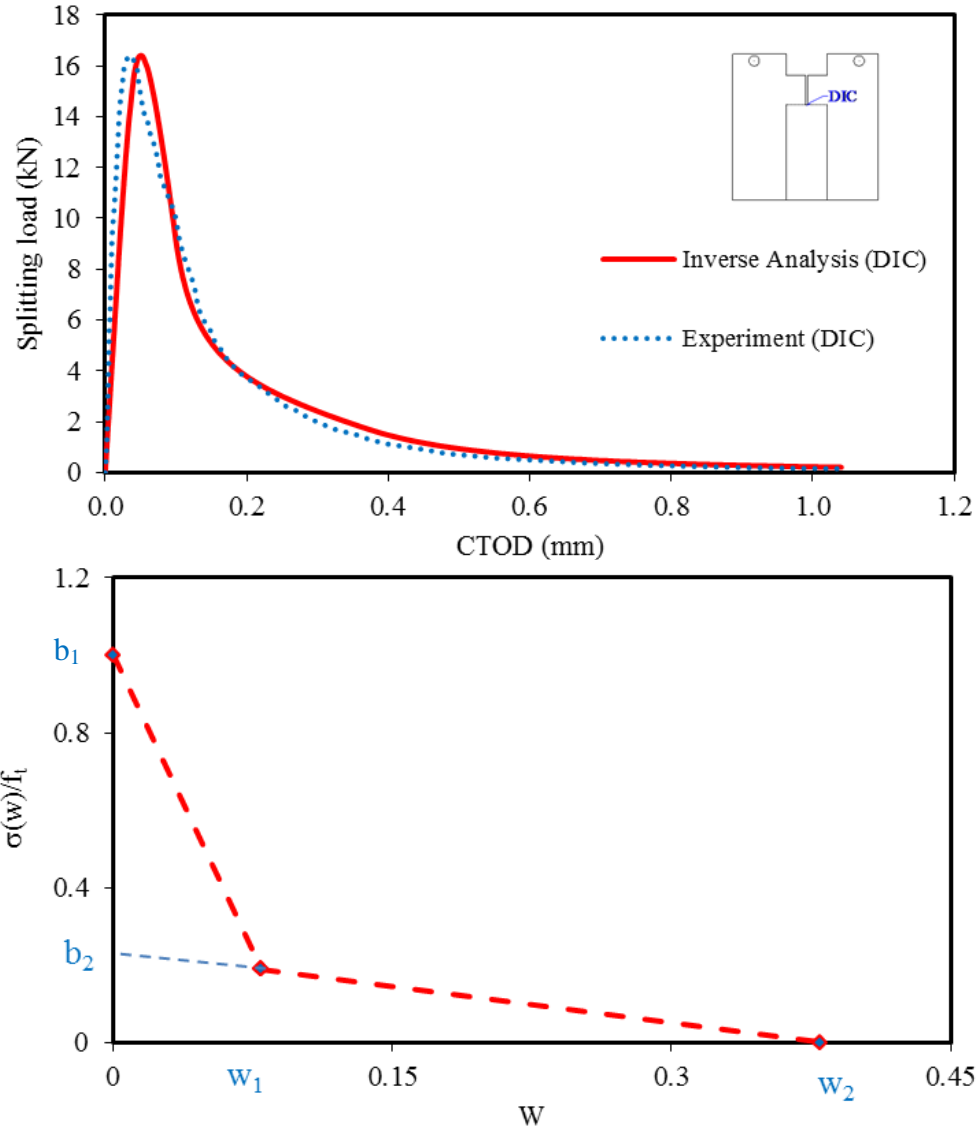


Figure 4.10: (a) Load-crack tip opening displacement curve (P_{sp} -CTOD) and (b) normalized stress-crack opening displacement curve, extracted from inverse analysis using experimental DIC data for WST6

Table 4.2: Comparison of the input and output parameters of the inverse analysis for WST-6 using the experimental DIC data

Softening curve parameters & E	f_t (MPa)	a_1	a_2	b_2	E (MPa)
Estimated Data (input data)	3.17	10	0.4	0.10	32,450
Inverse Analysis Result (output data)	2.60	10.7	0.5	0.188	35,000

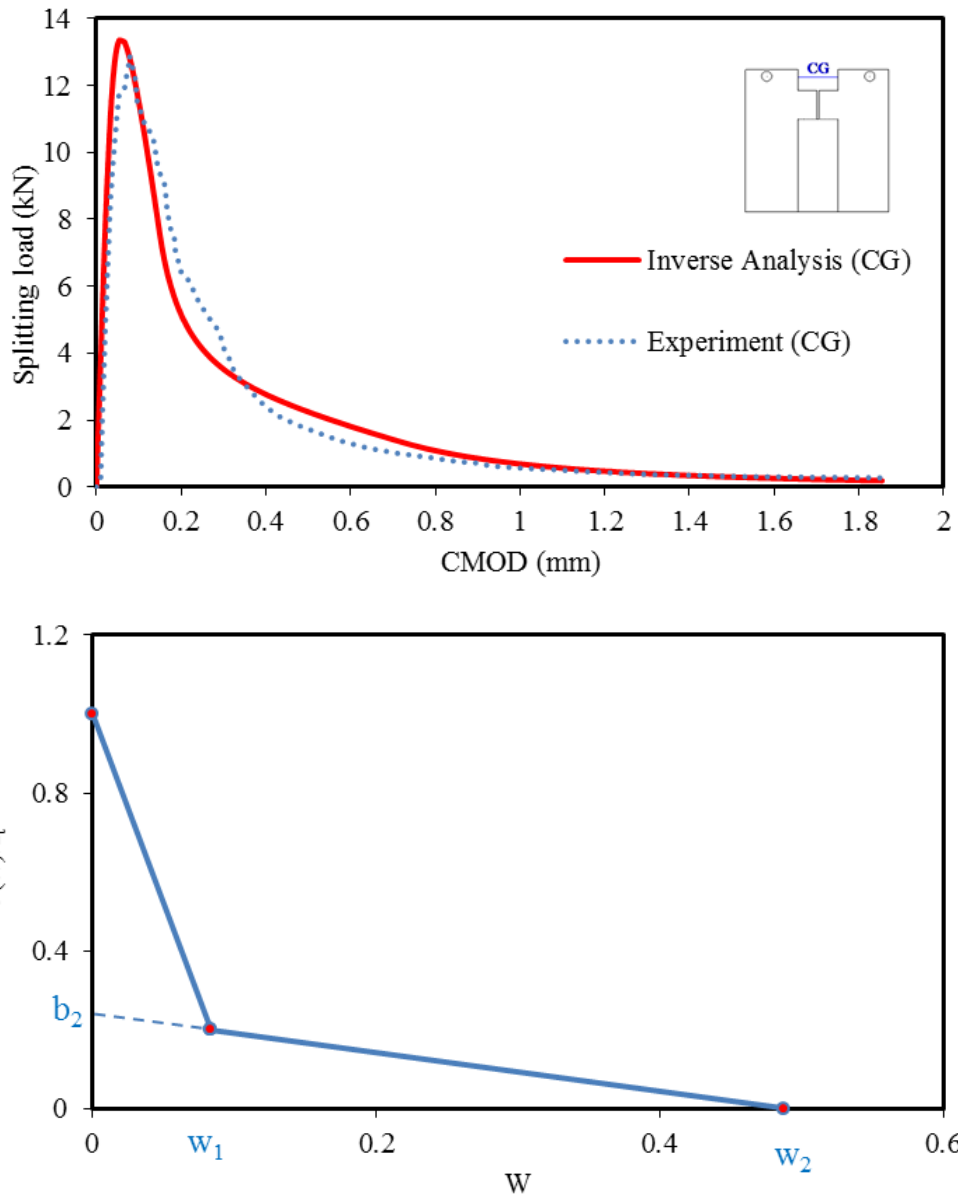


Figure 4.11: (a) Load-crack mouth opening displacement curve (P_{sp} -CMOD) and (b) Normalized stress-crack opening displacement (σ - w) curve, extracted from inverse analysis of traditional (CG) experimental data for WST5

Table 4.3: Comparison of the input and output parameters of the inverse analysis of the classical (clip-gauge) experimental data from WST5

Softening curve parameters & E	f_t (MPa)	a_1	a_2	b_2	E (MPa)
Estimated Data (input data)	2.6	11.0	0.40	0.10	31,500
Inverse Analysis Result (output data)	2.1	10.0	0.41	0.20	30,000

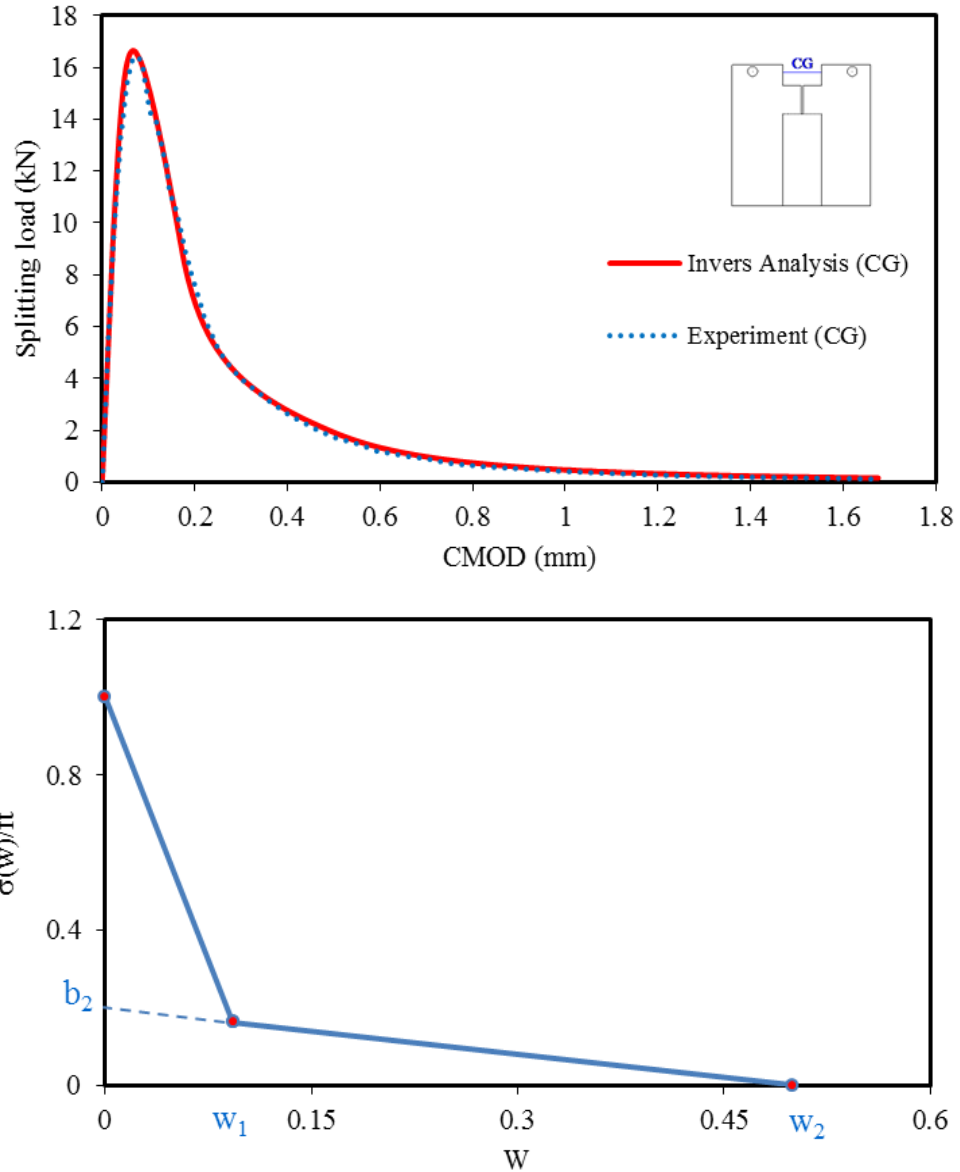


Figure 4.12: (a) Load-crack mouth opening displacement curve (P_{sp} -CMOD) and (b) Normalized stress-crack opening displacement curve (σ - w), extracted by inverse analysis of the traditional (CG) experimental data for WST6

Table 4.4: Comparison of the input and output parameters of the inverse analysis for WST6 using the classical (clip-gauge) experimental data

Softening curve parameters & E	f_t (MPa)	a_1	a_2	b_2	E (MPa)
Estimated Data (input data)	3.17	10	0.4	0.1	32,450
Inverse Analysis Result (output data)	2.62	9	0.4	0.2	32,277

Figures 4.9 to 4.12 show that the curves obtained with data collected using both experimental techniques, the traditional clip-gauge (CMOD) and the DIC (CTOD), fit well with the curves derived from inverse analysis based on the *CCM*. It can be seen that the curves obtained with this numerical technique are smoother since the data has less noise than the experimental one. Furthermore, the figures above demonstrate that the predictions fit well with the peak load, the area under the curve, and the tail on the right. Taking into account that a bi-linear curve is an approximation of the actual softening curve, the comparison shows that the model's fit is excellent for data from both of the experimental techniques investigated in this study. The results of the inverse analysis demonstrate the ability of the *CHM* to capture the WST behaviour observed using the DIC and traditional techniques. In addition, Tables 4.1 to 4.4 show that the error norm resulting from optimization based on minimization of the error in fit (mean square difference between observed and predicted data) was very low and was similar for both techniques (classical and DIC); however, the value for DIC was lower.

The parameters of the bilinear softening diagram were also computed as shown in Table 4.5. This includes: the fictitious crack width at the break point (w_1), the maximum fictitious crack width (w_2), and the intercept of the second part of the bi-linear relationship with the y-axis. The peak stress was normalized by measured f_t versus measures of specimen size and geometry. The ratio of computed peak stress to tensile strength measured per the ASTM standard C496, f_t , varies between 1 and 1.24.

Table 4.5: Softening curve parameters extracted from inverse analysis of experimental data

WST specimen	WST 5		WST 6	
	Classical Technique	DIC Technique	Classical Technique	DIC Technique
w ₁	0.08	0.07	0.10	0.08
w ₂	0.49	0.36	0.34	0.38
b ₂	0.20	0.18	0.17	0.19

Figures 4.13 and 4.14 depict a comparison between the normalized σ -w curves extracted from the inverse analysis of experimental data measured traditionally (CG) and the digital image correlation data (DIC) for WST5 and WST6 respectively. The σ -w curve obtained through inverse analysis corresponds satisfactorily with the experimentally obtained curve presented in the previous chapter (Figure 3.29). The main reason for the gap between the CG and DIC curves is that the DIC data was assessed directly at the crack tip while the CG data was derived from measures taken at the crack mouth, as discussed in Chapter Three.

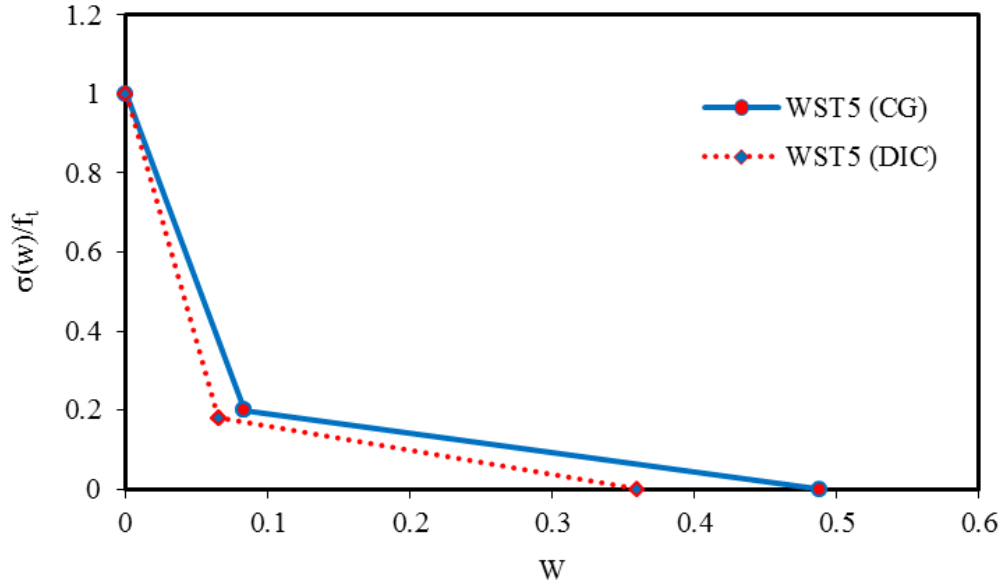


Figure 4.13: Normalized stress-crack opening displacement (σ - w) curves for WST5, extracted from inverse analysis of data obtained using traditional (CG) experimental and digital image correlation (DIC) techniques

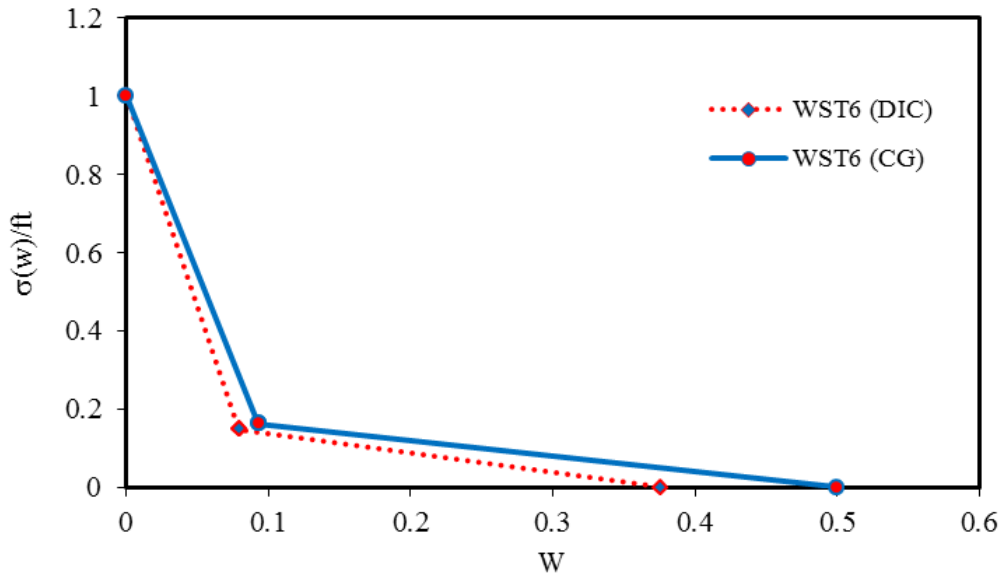


Figure 4.14: Normalized stress-crack opening displacement curves (σ - w) for WST6, extracted from inverse analysis of data obtained using traditional (CG) experimental and digital image correlation (DIC) techniques

It is important to note that fracture mechanics theory states that crack propagation is governed by the fundamental material properties of energy dissipation. Computational results show that the maximum loads of normally-sized concrete structures depend mainly on G_f and f_t . However, to obtain the maximum load of a very large structure or the post-peak response of any structure, which is important for determining the energy absorption capability of dynamic loading, the total fracture energy, G_F , and the knee point, σ_I , must also be identified (Bazant and Yu, 2010). Therefore, the parameters identified from the experimental work are also compared to those obtained by inverse analysis, which are based on the global response measurements used by both DIC and traditional techniques. Table 4.6 illustrates the results for G_F and G_f obtained from experimental work and inverse analysis simulation based on both techniques. G_F was calculated from the area under the P_{sp} -COD curve divided by the fracture area (130 mm X 200 mm), while G_f was calculated from the area under the initial steep part of the softening curve as shown in Figure 4.2. By obtaining f_t and σ_I , all four of the *softening curve* parameters were estimated in addition to the G_F/G_f and σ_I/f_t ratios.

Table 4.6: The fracture energy (G_F) and initial fracture energy (G_f) obtained from experimentation and inverse analysis simulation using both traditional clip-gauge and DIC techniques.

WST	WST 5				WST 6			
Result	Classical Technique		DIC Technique		Classical Technique		DIC Technique	
	Experiment	Inverse Analysis	Experiment	Inverse Analysis	Experiment	Inverse Analysis	Experiment	Inverse Analysis
G_F (N/mm)	0.119	0.128	0.099	0.092	0.131	0.127	0.092	0.085
G_f (N/mm)	0.077	0.053	0.048	0.038	0.088	0.066	0.052	0.04
G_F/G_f	1.5	2.4	2.1	2.4	1.5	1.9	1.8	2.1
σ_1/f_t	0.17		0.15		0.12		0.14	

Table 4.6 shows that there is a discrepancy between values of fracture energy obtained from experimental work and from inverse analysis simulation, with the latter generally being less (with the exception of the G_F for WST 5 obtained with the classical clip-gauge technique). In addition, the G_F/G_f and σ_1/f_t ratios were calculated as shown in the above table: the σ_1/f_t ratio calculated from inverse analysis findings was between 0.12 to 0.17 while the ratio of G_F/G_f obtained from the experimental data was between 1.5 and 2.1 or between 1.9 and 2.4 from the results of the inverse analyses. Previous reports (Wittmann et al. 1988, Rokugo et al. 1989, CEB 1991) found that for normal concrete the ratio σ_1/f_t is usually less than 0.25 and G_F/G_f is less than 5.

Table 4.7 shows that the ratio of $G_{F(IA)}/G_{F(Ex)}$ is greater than the ratio for initial $G_{f(IA)}/G_{f(Ex)}$. Review of the P_{sp} -COD curves indicates that the tails of the curves are similar, but that the initial steep part of the curve diverges. The deviation between the

results for experimentation and inverse analysis could be related to closure of an open crack during testing, which is not included in the *CHM*.

Table 4.7: Comparison of the fracture energy (G_F) and initial fracture energy (G_i) obtained from the experimental studies and inverse analysis simulations.

WST specimen	WST 5		WST 6	
Result	Classical Technique	DIC Technique	Classical Technique	DIC Technique
$G_{F(IA)}/G_{F(Ex)}$	1.08	0.93	0.97	0.92
$G_{i(IA)}/G_{i(Ex)}$	0.69	0.79	0.75	0.77

The sources of error in the evaluation of fracture energy in the WST were investigated previously by Guinea et al. (1992), Planas et al. (1992), and Elices et al. (2002). The main sources of error were: the friction between the support and the specimen, crushing near the supports, the energy dissipation in the bulk of the materials near the crack, and the energy enclosed in the unmeasured tail of the load-deformation curve, which was estimated (see Chapter Three). The authors found that the observed dependence of the fracture energy on the size of the specimen (about 40% of the G_F) was caused by these sources of error. Most of the error, more than 30% of the observed size dependence of 40%, originated from the neglected energy in the tail part of the load-deformation curve. The authors stated that when these sources of error are considered in the calculation of the fracture energy for the beam tests, it is not clear whether the resulting size dependence (20–30%) is a fundamental feature of concrete material or if it was caused by inevitable test error. Therefore, more attention was paid to the *initial*

fracture energy, G_f , when considering the discrepancy in the total *fracture energy*, G_F , in regard to the stage that the WST was terminated; this affected the estimate of the area under the tail of the load-deformation curve. The discrepancy found for $G_{f(IA)}/G_{f(Ex)}$ was lower when data obtained with the DIC technique was used. Wittmann (2002) found that G_F depends on deviations of a real crack from an idealized crack plane, and also found that G_F and strain softening depend on the composite structure of the material. These properties are essentially governed by the mechanical interaction of the aggregates with the cement-based matrix. Wittmann also found that the maximum aggregate size influences G_f .

Despite the discrepancies seen in the results from the inverse analysis, there is no doubt that it is possible to determine realistic fracture parameters by applying inverse analysis to the DIC experimental results; the results obtained with inverse analysis of DIC experimental data are useful and similar to the experimental results calculated in chapter three.

4.4 Finite Element Analysis (FEA)

In the previous section, inverse analysis was conducted using the *non-linear cracked hinge concept (CHM)* based on the *fictitious crack model (FCM)*. To confirm that the result obtained from the inverse analysis arrived at the best possible determination, finite element analysis (FEA), using the commercially available program, ABAQUS, was applied to the concrete fracture parameters obtained from inverse

analysis of data collected with both techniques (the DIC and the traditional clip-gauge techniques). Through the FEA, the P_{sp} -COD curve was obtained and the associated concrete fracture parameters were determined. A study comparing the results of the experimental, inverse analysis and finite element analysis procedures is conducted in this chapter. This comparison serves to challenge or validate the inverse analysis methods presented in the previous section as well as the DIC measurement technique presented in the previous chapter.

4.4.1 Finite Element Modeling and Concrete Fracture Behaviour

The low tensile strength of concrete leads to cracking, which is usually controlled by providing steel reinforcement in the tension zones. In structures such as massive concrete dams, providing steel reinforcement is uneconomical and the accurate modelling of cracking is important for assessing the structure's behaviour. FE method is a powerful tool for structural analysis, but requires the use of advanced material modelling to simulate cracking behaviour.

Fracture is an important form of deformation and damage in both plain and reinforced concrete structures. To accurately predict fracture behaviour using FEA, it is essential to choose a consistent and accurate fracture model of the material's properties. The finite element model (FEM) when first used was expected to model and solve any problem; however, even this powerful numerical tool has proven to be difficult to apply when the strength of a structure or structural element is controlled by cracking. When

early applications of FEA were studied in light of current understanding of fracture mechanics, FEA was found to be non-objective or incorrect (ACI Committee 446.3R-97).

FEA was first applied to the cracking of concrete structures by Clough (1962). In 1967, Ngo and Scordelis modeled discrete cracks, but did not address the problem of crack propagation. In the same year, Nilson introduced propagation of discrete cracks in concrete structures into the analysis by using a strength-based criterion. However, the stress singularity that occurs at the crack tip was not modeled. Thus, since the maximum stress at the crack tip depends on element size, the result of the analysis was mesh-dependent. Since then, much of the research and development in discrete numerical modeling of the fracture of concrete structures has been carried out by Ingraffea and his coworkers (1977 to 1991) and also by Hillereborg and his coworkers (1976 to 1985). Ingraffea introduced fracture mechanics principles to model linear elastic crack propagation. Although the *FCM* was utilized in the development of a FEM for the analysis of non-linear discrete fracture, the *FCM* appeared to be inadequate for modelling realistic concrete behavior in the FPZ in some situations. Therefore, a smeared crack model, introduced by Rashid in 1968, was necessary (ACI 446.3R-97). In this model, cracks are modeled by changing the constitutive (stress-strain) relations of the solid continuum in the vicinity of the crack instead of changing the FE mesh. Once the calculated stress exceeded the tensile capacity of the concrete, the material stiffness dropped to zero in the direction of the principal tensile stress. At the same time, the stress was released and reapplied as residual loads. Although this approach contains strain localization problems (mesh sensitivity), it became the most widely used method

after various localization limiters were developed (such as the crack band model and nonlocal continuum). In 1976, Bazant realized that concrete cannot be modeled as a pure continuum because of the softening behaviour of concrete caused by the localized FPZ, which is on the order of the maximum aggregate size; therefore, the size of the heterogeneous structure must be taken into account.

4.4.2 Application of Finite Element Analysis (FEA)

The determination of the direction of a crack is based on the reasonable assumption that the crack will propagate when the maximum principal tensile stress at the crack tip reaches the strength of the material (Petersson 1981, Gustafsson 1985, Hillerborg and Rots 1989, Bocca et al. 1991, Gerstle and Xie 1992) and that the direction of crack propagation will be perpendicular to the maximum principal tensile stress. In the current study, the energy-based approach for determining crack propagation was incorporated. The basis for such an approach was developed by Li and Liang (1992). Promising results have been obtained using energy release rate approaches to determine both the direction and the load level at which a fictitious crack will propagate (Xie, Gerstle and Rahulkumar, 1995).

In FEA where cracking behaviour is modeled, including the strain-softening response, the use of a strength criterion for failure yields results that are inadequate with respect to the size of the FE mesh used (Bazant et al., 1980). Many of the problems related to the service state and strength state design may be addressed by using energy

criteria based on fracture mechanics. The energy criteria of fracture mechanics provide the control necessary to assure stable and convergent solutions. Therefore, from a numerical modeling standpoint, the fracture mechanics approach is needed when a concrete structure is analyzed.

Concrete is a quasi-brittle material, and its modelling requires the inclusion of a specific characteristic length corresponding to the dimensions of the inhomogeneities in the microstructure of the material. In this study, the whole WS-specimen was chosen, so that the crack path will accord with the analysis and the distributed load was applied according to the experimental set up. The 2D analyses were carried out utilizing the *plasticity-damage coupled model* available in ABAQUS to ensure that the *fracture energy* dissipation was independent of the mesh size through visco-plastic regularization. The *plasticity-damage coupled model* implemented in ABAQUS was developed for concrete by Lee and Fenves (1998). The Drucker-Prager hyperbolic function was used as a flow potential defined by the *dilation angle* (ψ), the uniaxial compressive stress at failure (σ_{c0}), and a parameter ϵ characterising the flow potential eccentricity. This model must be used in conjunction with functions for concrete *tension softening*, concrete *tension damage*, and concrete *compression hardening*.

In order to verify the applicability of the non-linear *CHM* to the WS-specimens, the parameters obtained from the inverse analysis were used as the inputs for the ABAQUS analysis. The elastic properties of concrete were defined by the *elastic modulus* (E) and *Poisson's ratio* (ν). The concrete tension softening option was used to

model the post-cracking behaviour of concrete; the *tensile strength* (f_t) and *fracture energy* (G_F) are the parameters that characterized the fracture process. The concrete tension damage, characterized by the *tensile damage* (d_t) and *direct cracking displacement* (u_t^{ck}), was used to specify the tensile damage evolution associated with the stiffness degradation. In addition, the concrete compression behaviour was defined by the concrete *compressive stress capacity* (f_c) and the *crushing strain* (ϵ_c^{in}).

A simple *Rankine criterion* was used to detect crack initiation. This criterion states that a crack forms when the maximum principal tensile stress exceeds the material tensile strength. Crack detection was based purely on Mode I fracture considerations. As soon as the Rankine criterion for crack formation had been met, it was assumed that the first crack had formed. The crack surface was taken to be perpendicular to the direction of the maximum principal tensile stress. Since the behaviour of a plain concrete specimen is unstable during crack propagation, exhibiting softening, the Riks method was used to control the solution process and ensure convergence after the peak load was reached. The Riks method uses the load magnitude as an additional unknown parameter, so solves simultaneously the parameters for loads and displacements. Therefore, another quantity must be used to measure the progress of the solution; ABAQUS/Standard uses the “arc length”, l , along the static equilibrium path in load-displacement space. This approach provides a solution regardless of whether the response is stable or unstable. The Riks method is generally used to predict the unstable collapse of a structure in order to speed convergence of ill-conditioned or snap-through problems that do not exhibit instability (ABAQUS, 2010).

To the best of the author's knowledge regarding previous work reported in the literature, researchers chose to conduct the FEA with one-half of the specimen while a concentrated load was applied at the position of the roller bearing. Using this geometry, the crack path is assumed to be straight, while in reality and as was proved experimentally, the concrete crack is tortuous, which consumes more energy.

4.4.3 Damage-based Mechanics Model (ABAQUS, 2010)

A transfer of the principles of fracture mechanics to continuum elements is the key to the model of the WST used in this study. For this purpose, the *plasticity-damage coupled model*, which includes the degradation of the elasticity caused by loading (such as the loss of elastic stiffness), was chosen for employing energy principles. The *plasticity-damage coupled model* provides general capability for the modeling of concrete. It is a continuum model based on the assumption of scalar isotropic damage in combination with isotropic tensile and compressive plasticity to represent the inelastic behaviour of concrete. Although concrete is an isotropic and heterogeneous material consisting of matrix and aggregate, it is generally accepted that it may be treated as an approximately uniform material if the minimum dimension of the concrete structure is more than 5 times the maximum size of the aggregate used (Shah et al., 1995).

Utilizing the *plasticity-damage coupled model* in ABAQUS allows the flow potential and yield surface for concrete to be defined. The effective cohesion stresses determine the size of the yield (or failure) surface. The *concrete damaged plasticity*

option must be used in conjunction with the *concrete tension stiffening* and the *concrete compression hardening* options. In addition, the *concrete tension damage* and/or the *concrete compression damage* options can be used to specify tensile and/or compressive stiffness degradation damage. This model is used for the following reasons (ABAQUS, 2010):

1. Provides a general capability for the modeling of concrete and other quasi-brittle materials in all types of structures (beams, trusses, shells, and solids)
2. Uses the concepts of isotropic damaged elasticity in combination with isotropic tensile and compressive plasticity to represent the inelastic behaviour of concrete
3. Can be used for plain concrete, even though it is intended primarily for the analysis of reinforced concrete structures
4. Designed for applications in which concrete is subjected to monotonic, cyclic, and/or dynamic loading under low confining pressures
5. Consists of the combination of non-associated multi-hardening plasticity and scalar (isotropic) damaged elasticity to describe the irreversible damage that occurs during the fracturing process
6. Assumes that the two main failure mechanisms are tensile cracking and compressive crushing of concrete. The evolution of the yield surface is controlled by two hardening variables: the tensile and the compressive equivalent plastic strain
7. The tensile softening stress-strain response induces strain localization.

This model assumes that the uniaxial tensile and compressive response of concrete is characterized by damaged plasticity, as shown in Figure 4.15.

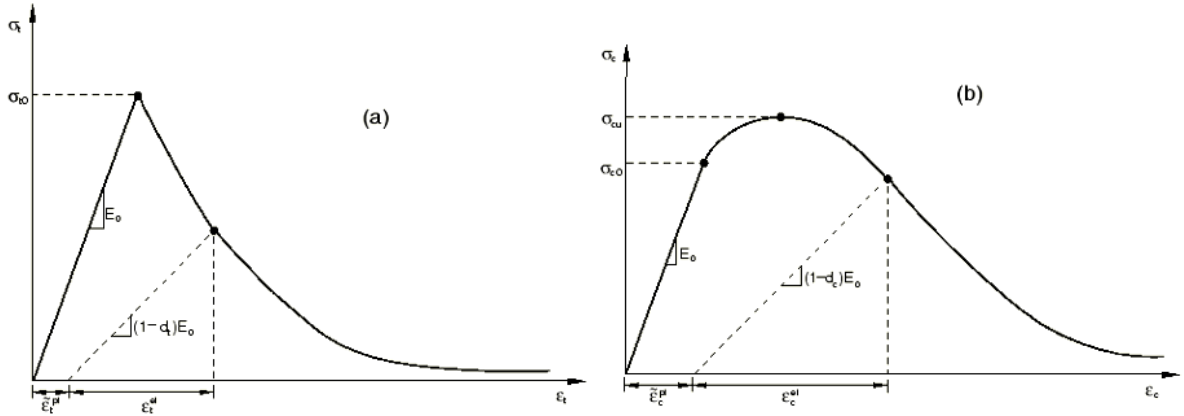


Figure 4.15: Response of concrete to uniaxial loading in (a) tension and (b) compression (ABAQUS, 2010).

where σ_{t0} is the tensile failure stress, σ_{c0} is the initial compressive yield stress, σ_{cu} is the ultimate stress; ϵ_t^{pl} , ϵ_c^{pl} are the tensile and the compressive equivalent plastic strain; ϵ_t^{el} , ϵ_c^{el} are the tensile and the compressive elastic strain; E_0 is the initial (undamaged) elastic stiffness of the material; and d_t and d_c are the degradation of the tensile and compressive elastic stiffness.

Under uniaxial tension, the stress-strain response follows a linear elastic relationship up to the point where the failure stress, σ_{t0} , corresponds to the onset of micro-cracking in the concrete material. Beyond the failure stress point, the formation of micro-cracks is represented macroscopically with a softening stress-strain response, which induces strain localization in the concrete structure. Under uniaxial compression, the response is linear up to the value of initial yield, σ_{c0} . In the plastic system, the

response is typically characterized by stress hardening followed by strain softening after the ultimate stress, σ_{cu} . This representation is simplistic; however, it captures the main features of the concrete response. As shown in Figure 4.15, when the concrete specimen is unloaded at any point on the strain softening branch, the elastic stiffness of the material appears to be damaged or degraded. The degradation of the elastic stiffness is characterized by two damage variables, d_t and d_c , which are assumed to be functions of the plastic strains. The damage variables can take values from zero, representing the undamaged material, to one, which represents total loss of strength. The concrete *plasticity-damage coupled model* defines the reduction of the elastic modulus in terms of a scalar degradation variable d as:

$$E = (1-d) E_o$$

Tension stiffening is used to simulate load transfer across the crack through the cohesive pressure, which enables definition of the strain softening behaviour of cracked concrete. The tension stiffening parameter introduces unreasonable mesh sensitivity in the absence of reinforcement into the results from the concrete model; however, Hilleborg's (1976) fracture energy proposal adequately allays this concern for many practical purposes. As the WS-specimen will crack under tension, the concrete's brittle behaviour is characterized by a stress-displacement response with this approach. The fracture energy cracking model is invoked by using the G_F option to define the failure stress, σ_{to} , as a tabular function of the associated fracture energy. This model assumes a

linear loss of strength after cracking as shown in Figure 4.16. The cracking displacement, at which complete loss of strength takes place, is $u_{t0} = 2 G_F/\sigma_{t0}$.

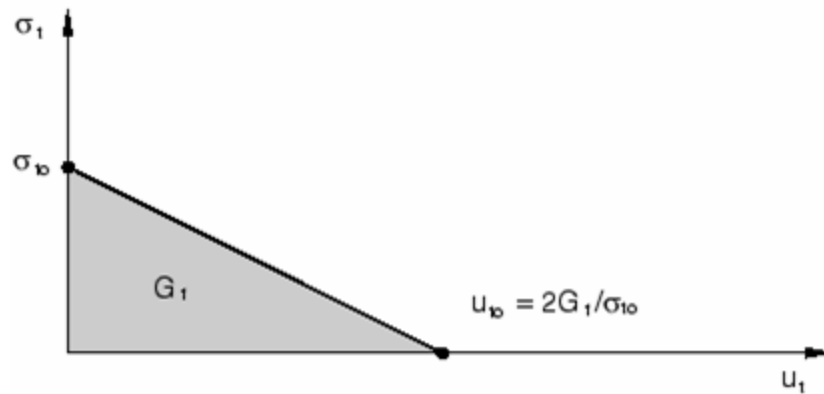


Figure 4.16: Concrete tension stiffening with G_F option (ABAQUS, 2010)

The implementation of the stress-displacement concept in a finite element model requires the definition of a characteristic length associated with an integration point. The characteristic crack length is based on the element geometry and formulation. For the current study, four-noded plane-stress continuum elements were chosen (CPS4R). Consequently, for this type of solid element, the square root of the area associated with the integration point was used. This model can accurately simulate the behaviour of concrete under static loading, and can consider the degradation of stiffness and strength in combination with the nature of stiffness recovery, due to crack propagation and crack closure under tension and compression.

4.4.4 The Application of FEA to the WST

The WS-specimen was modeled using ABAQUS to conduct a 2D plane stress analysis where a plasticity-damage coupled model simulated concrete behaviour. The constitutive behaviour was described by a linear elastic model in combination with a Mohr-Coulomb yield criterion. In the current study, the angle of friction for concrete may be set to 38° , and consequently the cohesion was given by $c = f_c/4$, where f_c is the concrete compressive strength. The concrete compressive and tensile strength as well as Young's modulus were chosen according to the experimental and inverse analysis results with the yield strength assumed to be 70% of the compressive strength. The G_F , which was experimentally and then numerically calculated using inverse analysis, was transferred to a continuum body by employing energy principles and used in continuum damage mechanics. Concrete parameters extracted from the inverse analysis were used as input properties for this model. Table 4.8 and Table 4.9 summarize the material properties used in the plasticity-damage coupled model. For concrete compression hardening and concrete tension damage, two points on the associated curve were taken as shown in Figure 4.15.

Table 4.8: Material properties of the plasticity-damage coupled model (traditional method)

Concrete Model Option	Concrete Properties *	1 st point	2 nd point
Concrete Damaged Plasticity	ψ	38°	-
Concrete Compression Hardening	f_c (MPa)	36.4**	52***
	ε_c^{in}	0	0.00186
Concrete Tension Stiffness	f_t (MPa)	2.6	-
	G_F (N/mm)	0.127	-
Concrete Tension Damage	d_t	0	0.9
	u_t^{ck}	0	0.0977

* ψ : dilatation angle, f_c : concrete compressive strength, ε_c^{in} : inelastic crushing strain, f_t : tensile strength, G_F : concrete fracture energy, d_t : concrete tension damage, u_t^{ck} : direct tensile cracking strain
 ** compression yield stress; *** ultimate compression stress

Table 4.9: Material properties of the plasticity-damage coupled model (DIC technique)

Concrete Model Option	Concrete Properties *	1 st point	2 nd point
Concrete Damaged Plasticity	ψ	38°	-
Concrete Compression Hardening	f_c (MPa)	36.4**	52***
	ε_c^{in}	0	0.002
Concrete Tension Stiffness	f_t (MPa)	2.6	-
	G_F (N/mm)	0.0852	-
Concrete Tension Damage	d_t	0	0.9
	u_t^{ck}	0	0.066

* ψ : dilatation angle, f_c : concrete compressive strength, ε_c^{in} : inelastic crushing strain, f_t : tensile strength, G_F : concrete fracture energy, d_t : concrete tension damage, u_t^{ck} : direct tensile cracking strain
 ** compression yield stress; *** ultimate compression stress

To achieve further insight into the WST and to validate the inverse analysis results, an extensive FEA of the tested specimens was undertaken by applying a fine mesh to the expected crack path and within the crack band width. Figure 4.17 depicts the finite element meshing applied to the WS-specimen, which was found to perform satisfactorily.

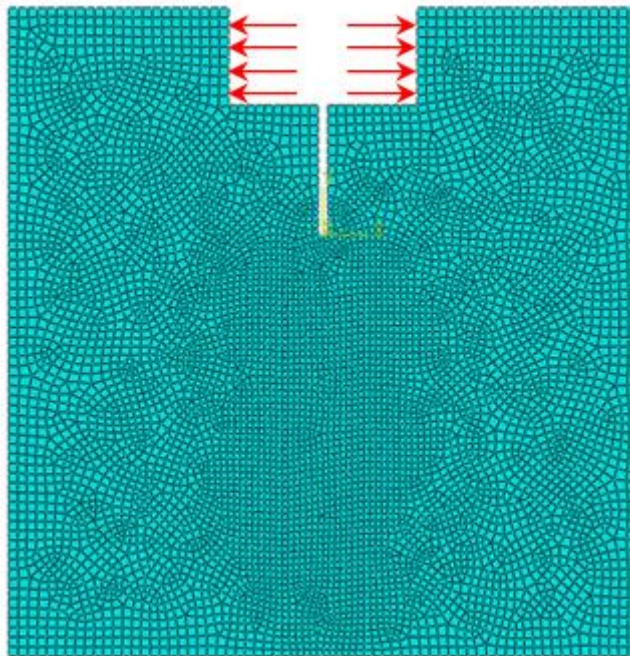


Figure 4.17: Finite element meshing on the WST model

4.5 Finite Element Analysis (FEA) Results

As noted earlier, FEA was used for validation and comparison purposes. Figure 4.18 (a) depicts the P_{sp} -CTOD extracted from the FEA of the DIC inverse analysis results. Comparison of the FEA, experimental, and inverse analysis DIC results is

illustrated in Figure 4.18 (b), which show that the 2D model closely approximates the experimental and the inverse analysis results. However, the FEA solution was unable to produce a stable solution when the load decreased below 2.6 kN (the descending portion or tail of the curve).

The FEA and DIC curves show a high degree of correlation. Prior to the material localization at 87% of the peak load, where only the tensile strain hardening accounts for the non-linearity of the P_{sp} -CTOD response, the results are essentially identical. However, after the initiation of the material localization and after the peak load, the inverse analysis results are identical to the FEA up to 37% of the peak load during the post-peak phase. As depicted in Figure 4.18(b), the correlation during the post-peak phase is not as good after 37% of the peak load; this can be attributed to the effect of aggregate interlock, which is not included in the FEA model (see conclusions of Chapter Three).

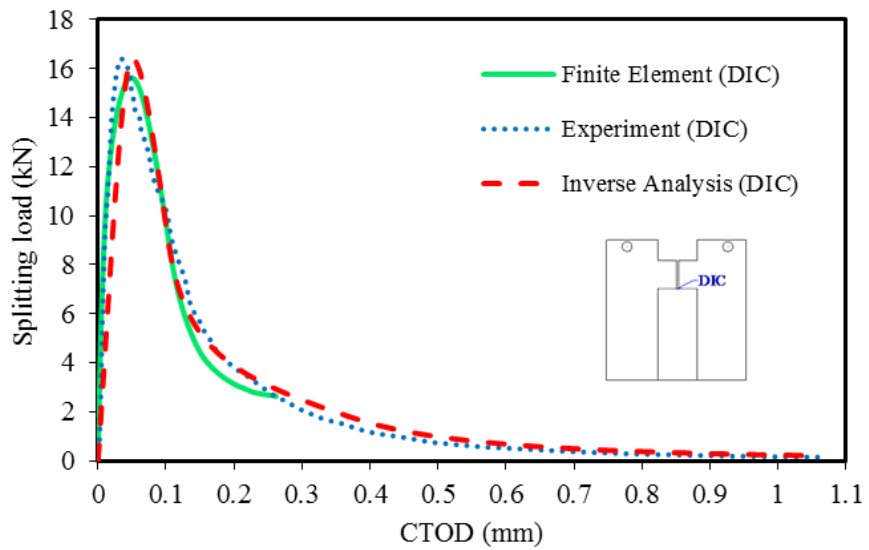
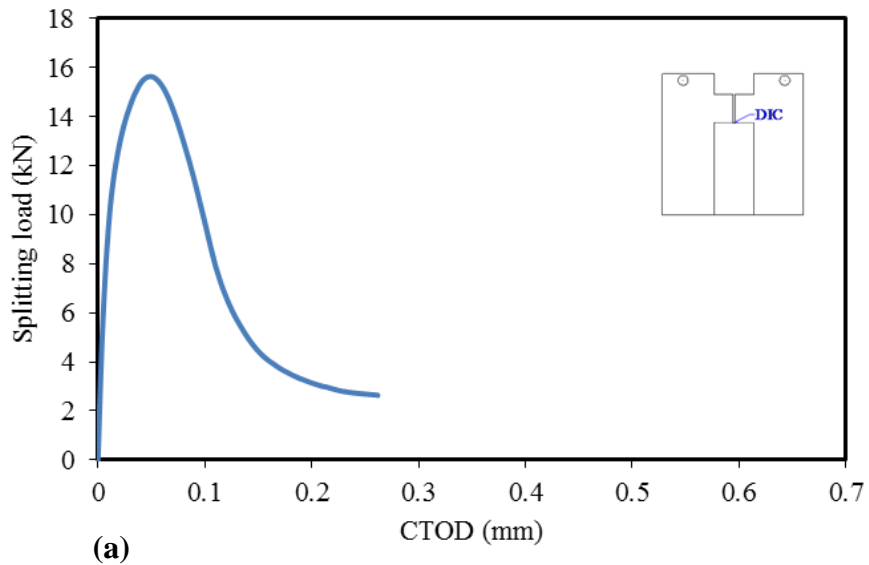


Figure 4.18: Load-crack tip opening displacement curve (P_{sp} -CTOD): (a) FE result using DIC extracted from inverse analysis output (b) comparison of experimental and analytical results

The crack path and the tensile damage (damage pattern) are shown in Figure 4.19. The crack is almost straight although it is well known that cracks in concrete are tortuous as was illustrated in Chapter 3 (see Figures 3.13, 2.26 and 3.27); tortuous crack paths are caused by toughening mechanisms and the heterogeneity of concrete material in addition to the thickness effect. The first crack initiated at 3.07 kN when the principal stress (S_p)

reached 2.6 MPa, the material tensile strength and the strain was equal to 0.00013 (Figure 4.20). At this stage, a small amount of tensile damage appears (0.0014) as shown in the figure below; the CTOD and CMOD were recorded as 0.0022 and 0.008 respectively.

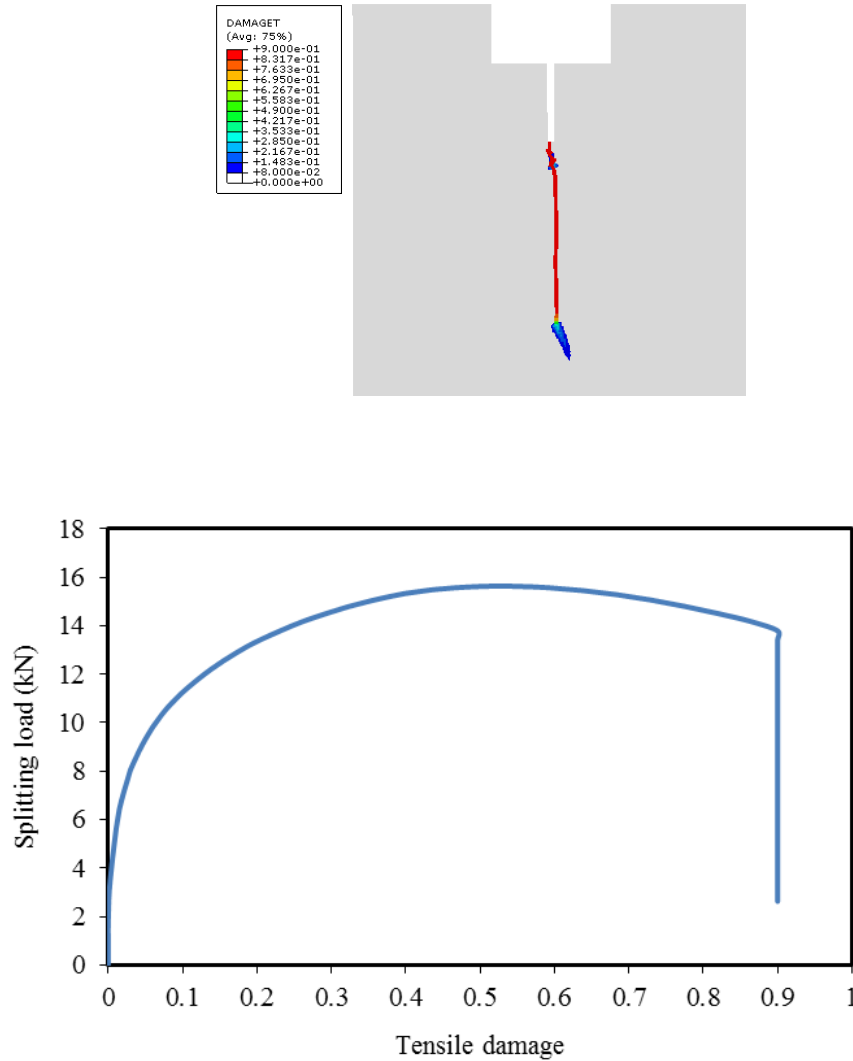


Figure 4.19: Tensile damage (d_t) in the cracked specimen and the crack's path derived using DIC output

At the peak load, 15.64 kN, the principal stress and strain at the crack tip were equal to 1.115 MPa and 0.0022, respectively. The CTOD and CMOD were recorded to be 0.048 mm and 0.098 mm, respectively and the tensile damage (d_t) was equal to 0.517.

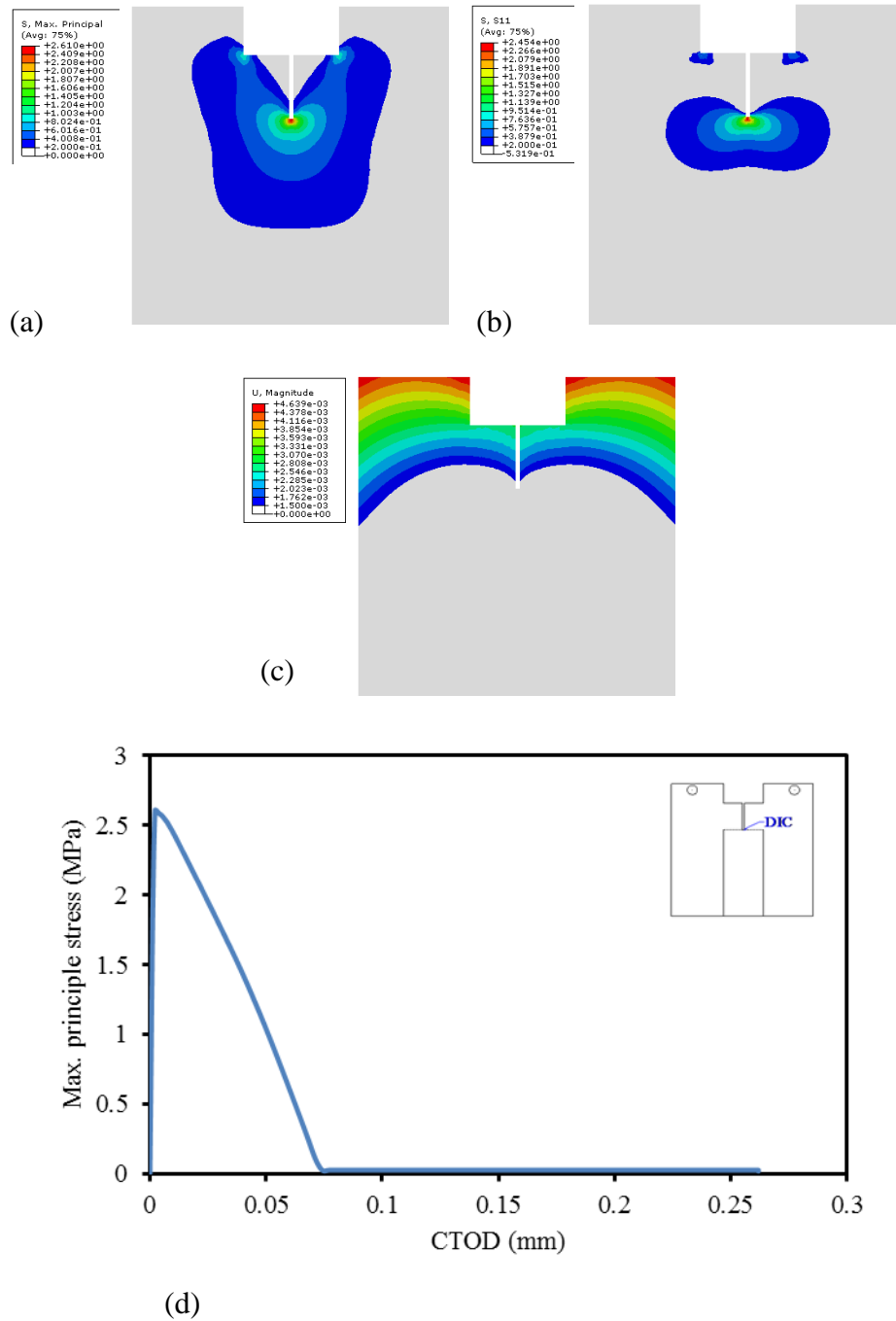


Figure 4.20: FEA result: (a) maximum principal stress (S_p), (b) S_{11} , (c) displacement, (d) principal stress-CTOD curve at the first crack (3.07 kN) using DIC output

Because of the straight crack path on the modeled cracked specimen, it is interesting to see that S_{11} (S_{xx}) is close to the principal stress of 1.11 MPa. After the peak load, the stress and strain start decreasing at the crack tip. At 13.8 kN, during the

post peak phase, the stress was reduced to 0.026 MPa, and tensile damage reached its maximum value (0.9). Both values were constant until failure, when the stress value jumped suddenly to 0.018 MPa (Figure 4.21). It is obvious from the stress and strain distribution along the contour of the WS-specimen that the crack band (s) is larger than was depicted using DIC experimental data.

Figure 4.22 (a) shows the P_{sp} -COD relation for various locations along the crack path. The energy required to propagate the crack to distance, y , from the crack/notch tip along the crack path is shown in Figure 4.22 (b). The dissipated energy was calculated by dividing the area under the P_{sp} -COD curve at each position, y , by the fracture surface as shown in Figure 3.4. *The tensile damage* (d_t) defined as the ratio between the dissipated energy at each point along the crack and the G_F is depicted in Figure 4.23 along with the experimental results obtained with the DIC technique. Despite the difference shown between the two curves, the results are clearly correlated. The fracture energy is sensitive to the crack band width; it increases when the elastic energy stored in the crack band increases, yielding a lower peak value. The overall curve shape is unchanged except between 20 and 40 mm from the crack/notch tip, where the result shows a different scenario. With reference to Chapter 3 (Figure 3.54 to 3.58) where the new micro-crack band appeared on the right side of the surface of the WST 6 specimen along with the existing band, at this stage more energy was dissipated as additional energy was absorbed when the new crack band was created and then the energy was reduced while closing the first band of micro-cracks. This phenomenon does not occur in the FEA.

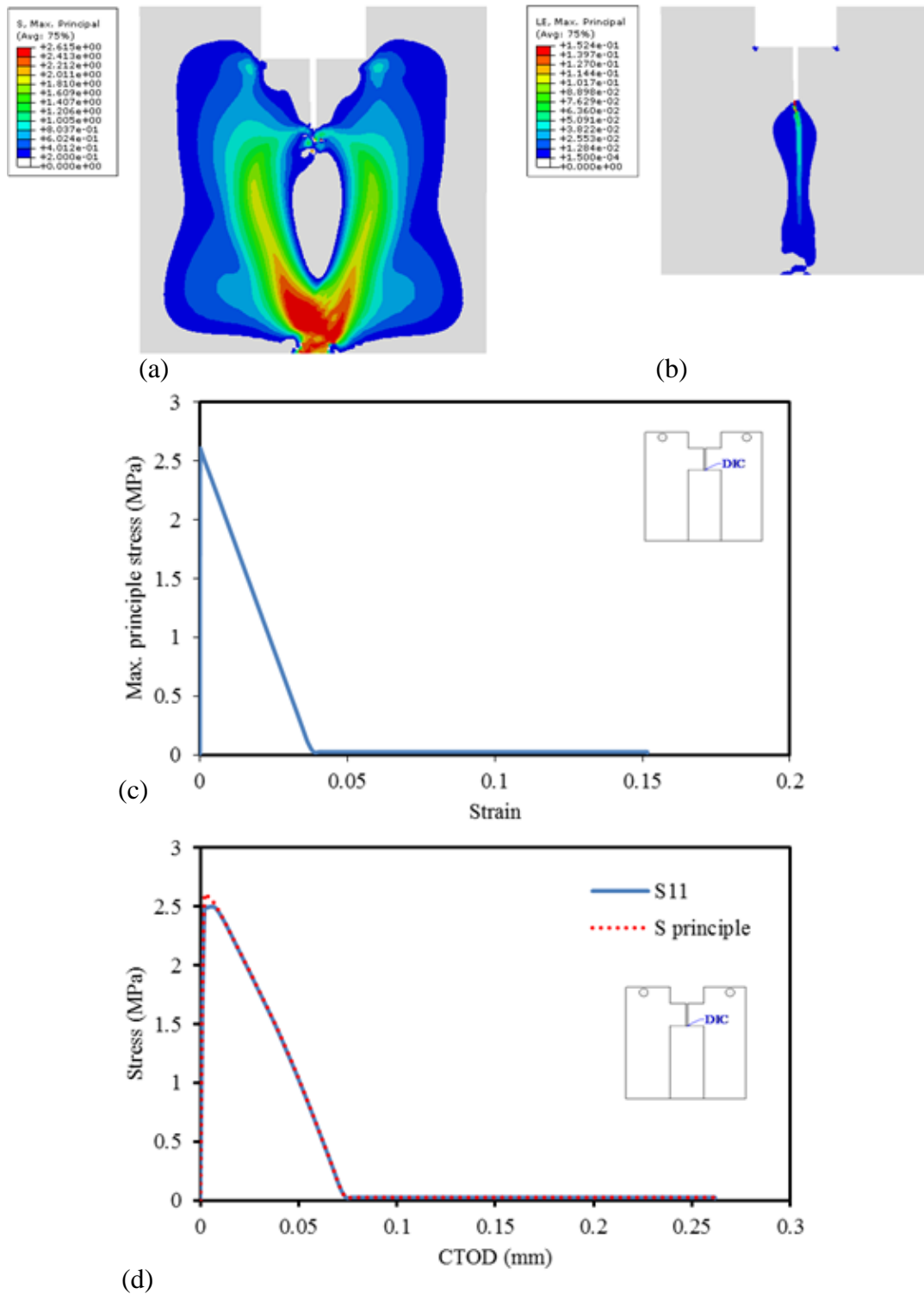
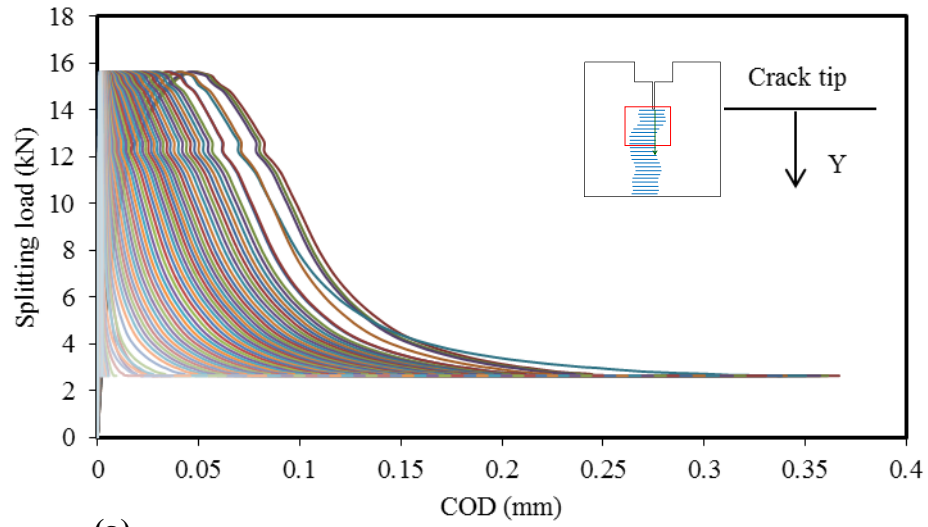
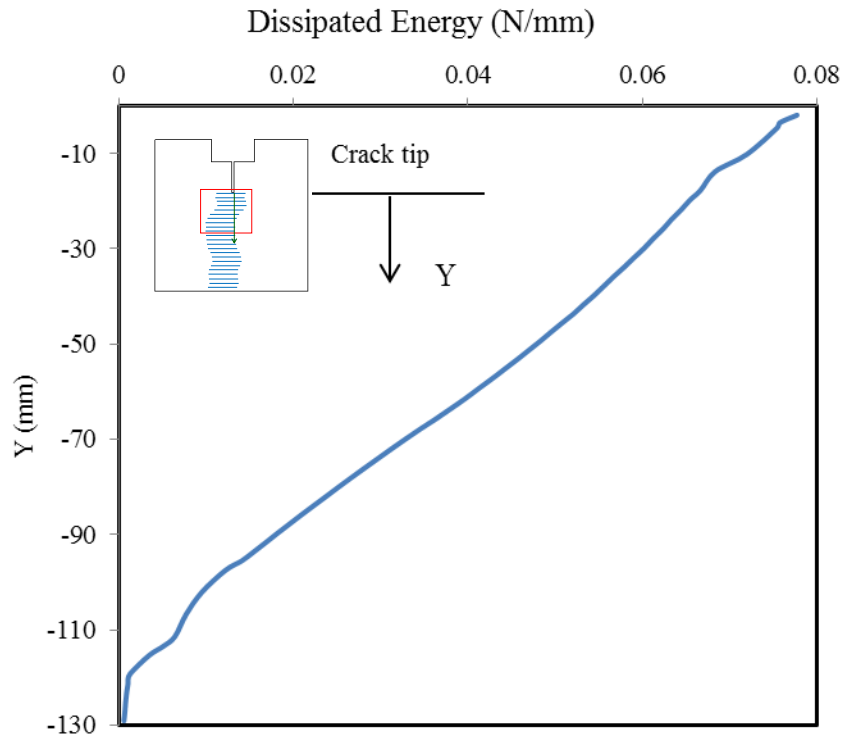


Figure 4.21: Maximum principal stress (S_p) and strain (ϵ_p) at failure using DIC output



(a)



(b)

Figure 4.22: FEA results using DIC output: (a) Splitting load-crack opening displacement (P_{sp} -COD) for various positions along the crack path, calculated at a distance y from the crack tip, (b) the dissipated energy along the crack path

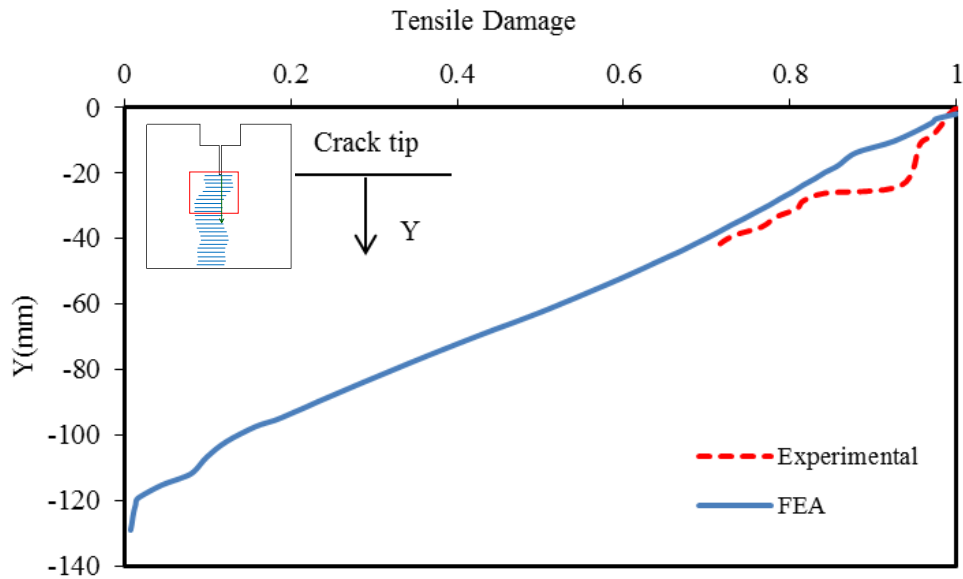


Figure 4.23: The dissipated energy along the crack path (comparison study between the FEA results of the DIC output and the experimental results from the DIC technique)

The WST-specimen was also modeled using concrete properties extracted by applying inverse analysis to the experimental data obtained with the traditional method (clip-on gauge). The results are shown in Figures 4.24 to 4.29. While the overall behaviour is unchanged, the crack opening displacement is greater (Figure 4.24) to keep the fracture energy, G_F , close to the value used as the FEA input.

The first crack initiated at 3.07 kN when the principal stress (S_p) reached 2.6 MPa, which is equal to the material tensile strength, f_t ; the strain was equal to 0.00014 (Figure 4.26). At this stage, a small amount of tensile damage appears (0.0014), and the CTOD and CMOD were recorded as 0.0024 and 0.0087, respectively. At the peak load, 16.32 kN, the principle stress and strain were equal to 1.134 MPa and 0.00277,

respectively. The CTOD and CMOD were 0.06 and 0.12 respectively, and the tensile damage was equal to 0.44 (half of the total damage). The S_{11} (S_{xx}) is close to the principal stress (S_p), which was equal to 1.34 MPa. After the peak load, the stress and strain began to decrease at the crack tip/notch. At 13.8 kN, post-peak phase, the stress was reduced to 0.026 MPa and the tensile damage reached its maximum value (0.9). Both values were constant until failure when the stress value jumped suddenly to 0.0177 MPa at 2.27 kN.

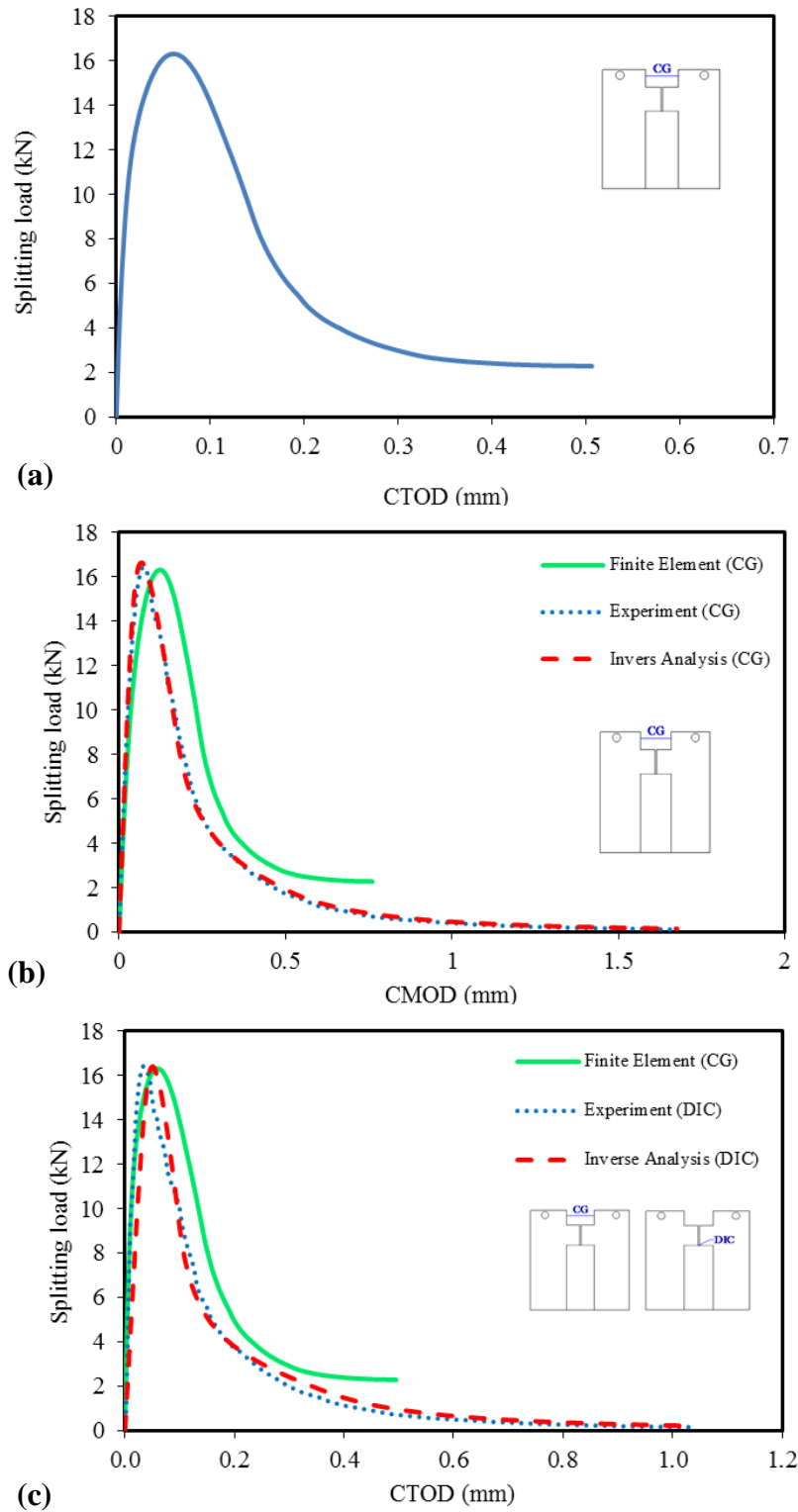


Figure 4.24: Load-crack tip opening displacement (P_{sp} -CTOD) curve: (a) FEA result from data obtained using the traditional method (clip gauge, CG) extracted from the inverse analysis output; (b) and (c) comparison of experimental and analytical

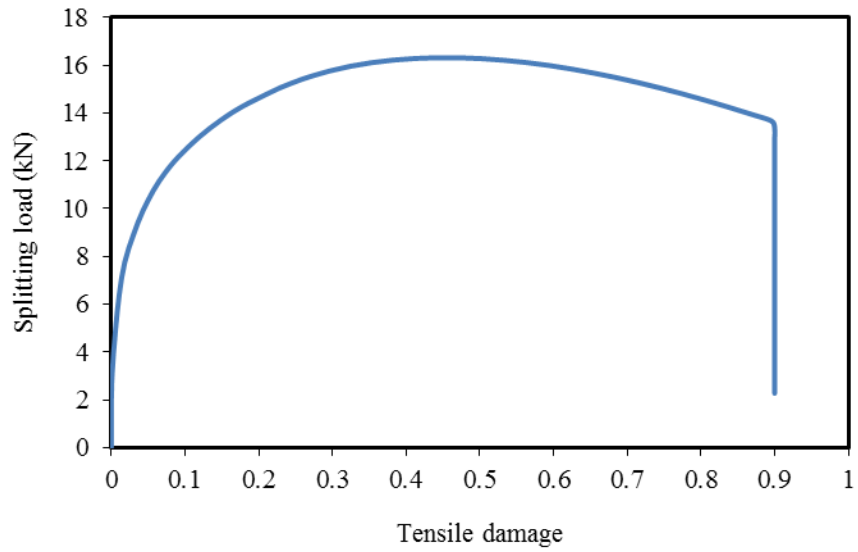
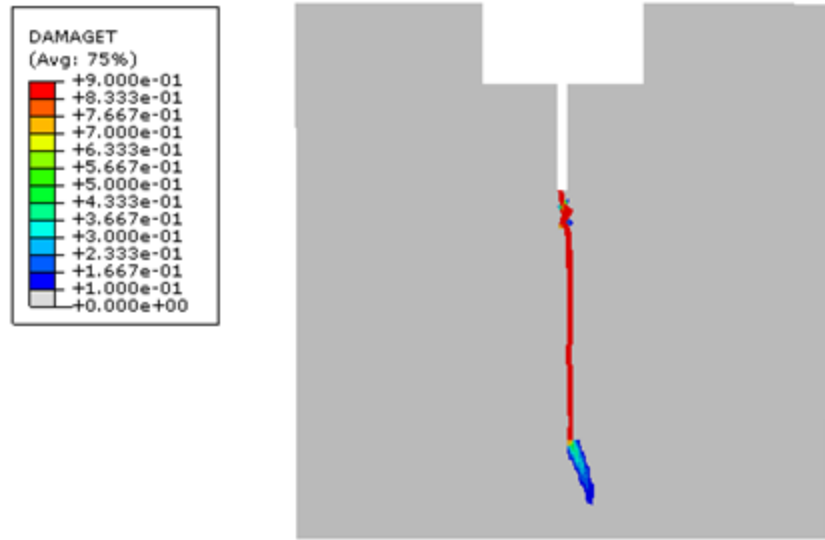


Figure 4.25: Tensile damage in the cracked specimen and the crack's path based on CG output

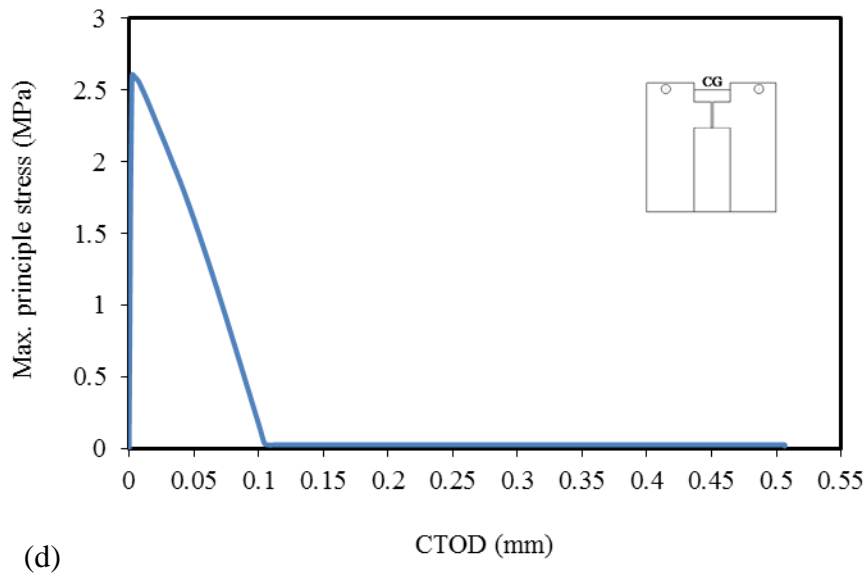
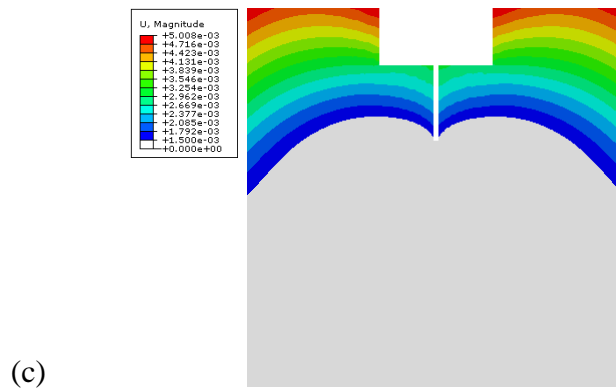
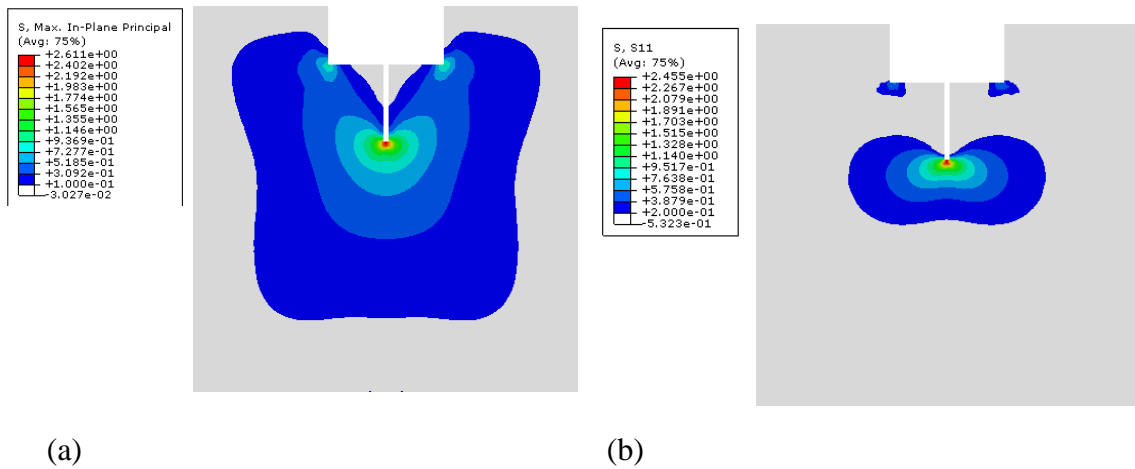
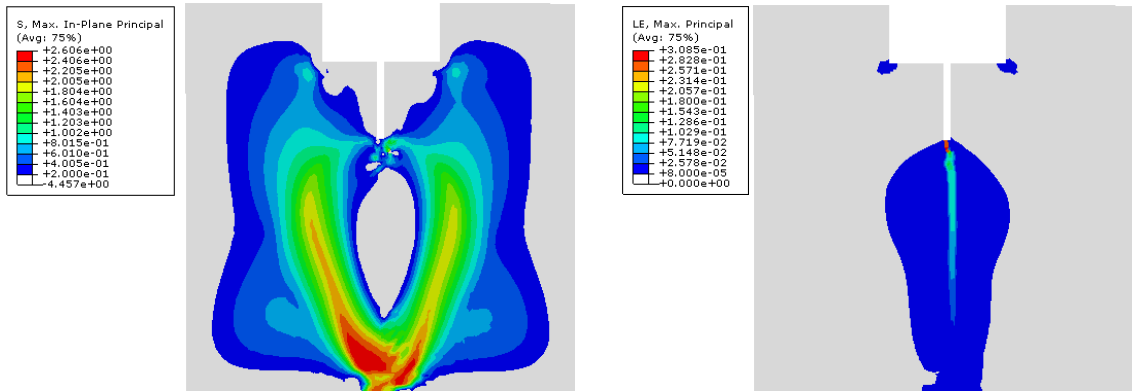
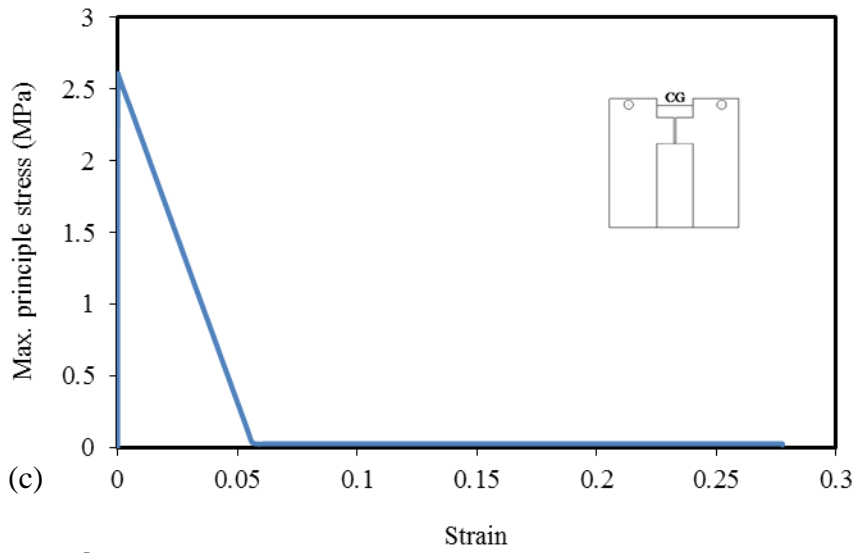


Figure 4.26: Finite Element results: (a) Maximum principal stress (S_p); (b) S_{11} ; (c) displacement; (d) principal stress-CTOD curve at the first crack (3.07 kN) using CG inverse analysis output

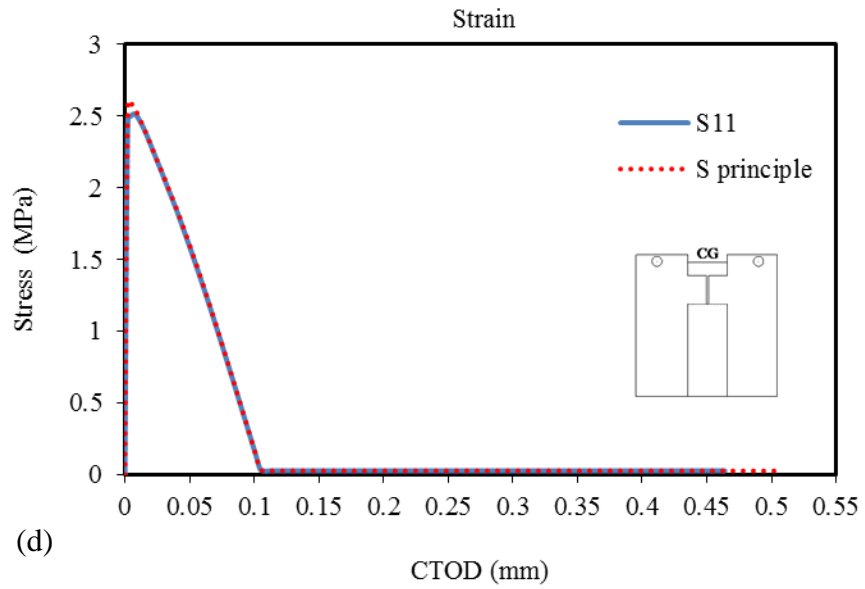


(a)

(b)



(c)



(d)

Figure 4.27: Finite Element results: (a) Maximum principal stress (S_p); (b) strain (ϵ); (c) S_p - ϵ curve; (d) S-CTOD curve at failure using CG output

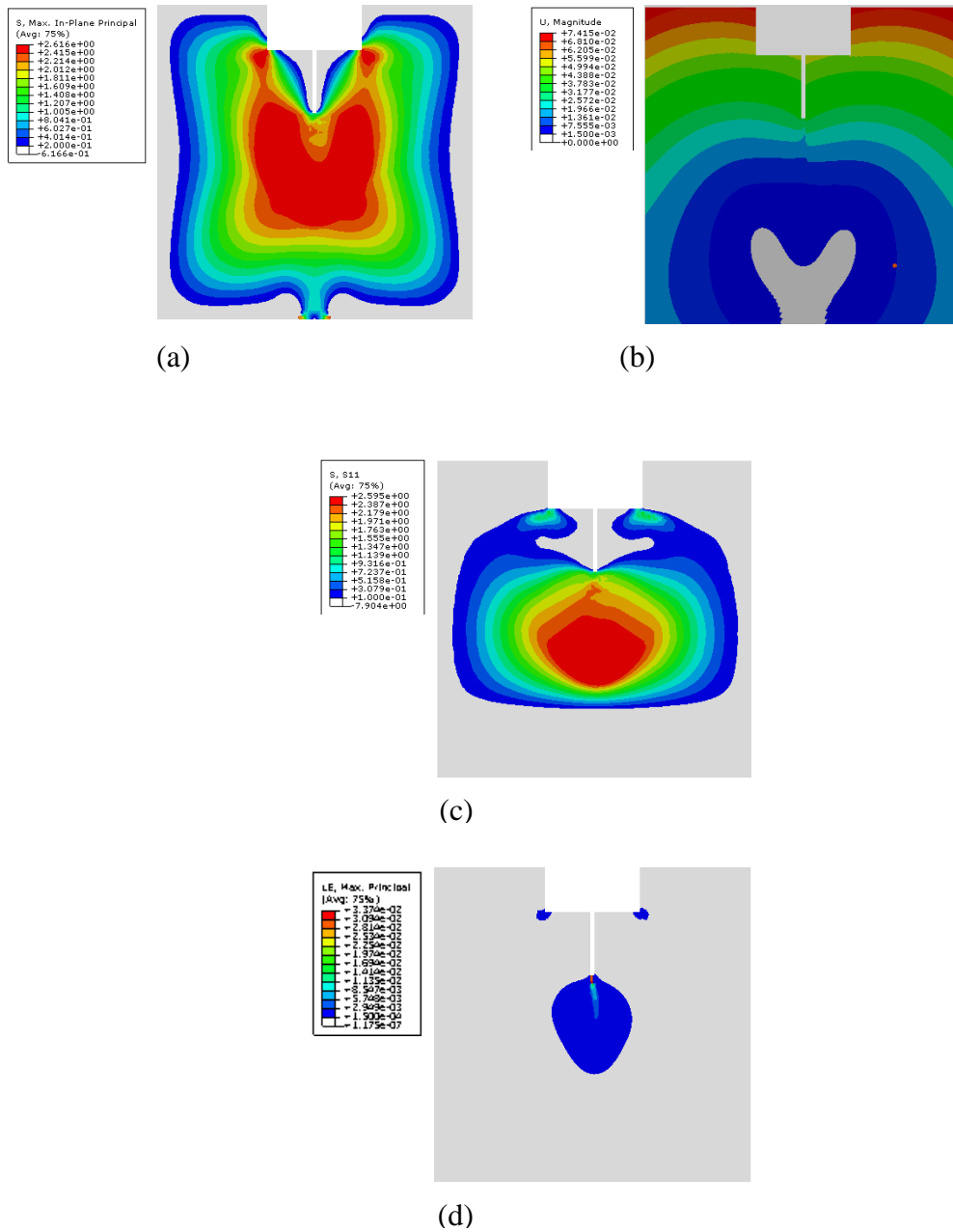


Figure 4.28: Finite Element results: (a) Maximum principal stress (S_p), (b) displacement, (c) stress S11, (d) Maximum principal strain at the peak load using CG inverse analysis output

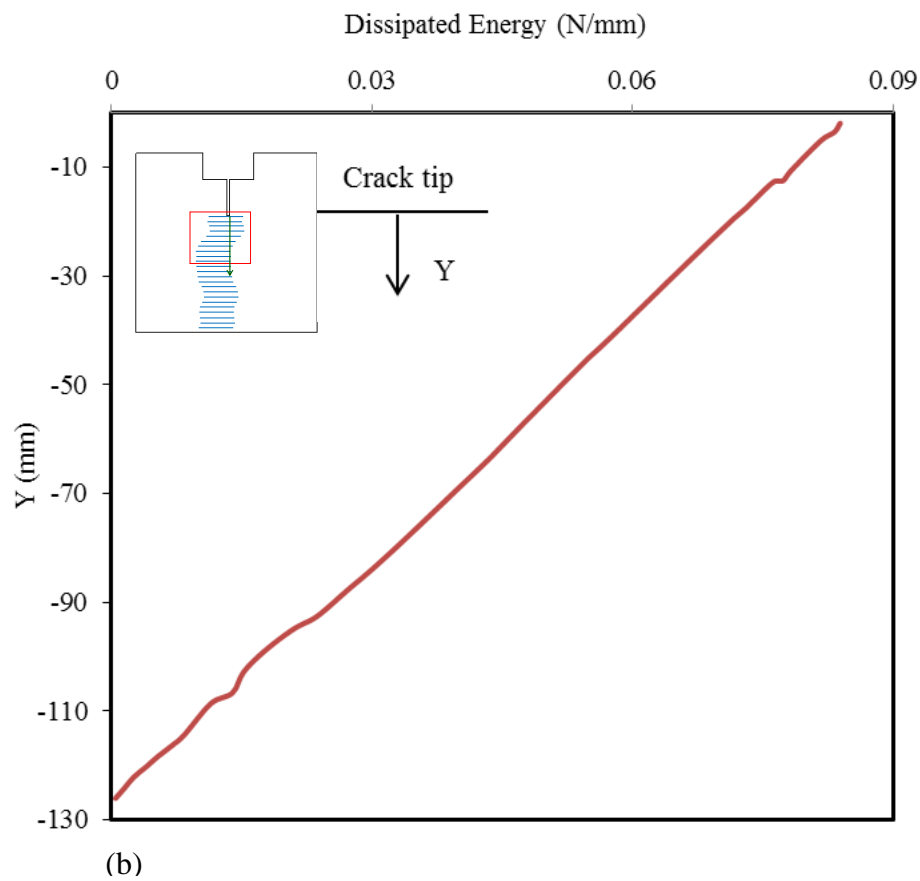
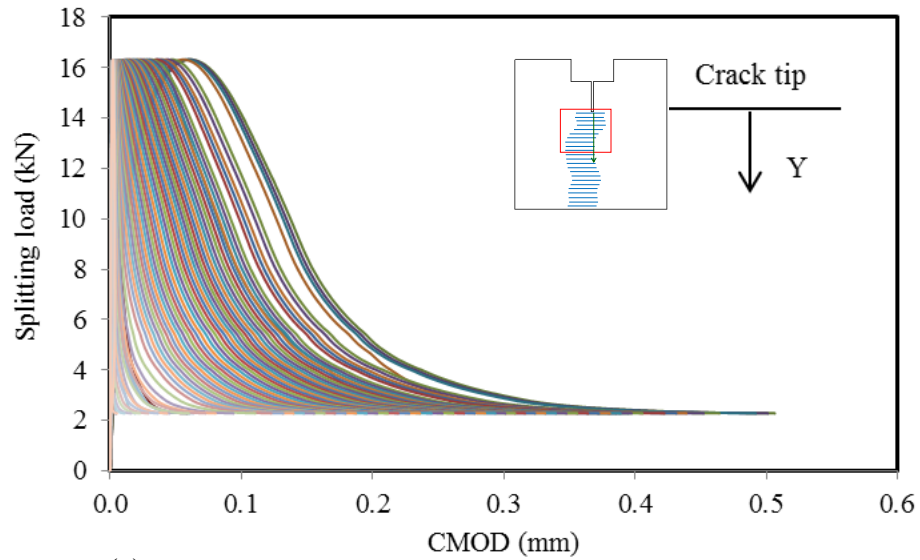


Figure 4.29: FEA results using CG output: (a) splitting load-crack opening displacement (P_{sp} -COD) for various positions along the crack path, calculated at a distance (y) from the crack tip, (b) the dissipated energy along the crack path

Table 4.10 and Figure 4.30 depict a comparison between the FEA results obtained using the traditional method (CG) and the DIC technique. G_F/G_f ratio was calculated as shown in Table 4.10, the G_F/G_f ratio obtained was between 1.2 and 2.1. Comparing this result to previous reports in the literature, researchers (Wittmann et al. 1988, Rokugo et al. 1989, CEB 1991) stated that for normal concrete, if the ratio G_F/G_f is less than 5, then the result is considered to be satisfactory. According to Bazant and Yu (2011), the estimation of G_F/G_f and the knee σ_I/f_t ratios is too uncertain; however, when the combination of the work-of-fracture and size effect testing are not needed when these ratios are known a priori.

Figure 4.30 (a) shows the P_{sp} -COD as it was described in Chapter Three; the discrepancies between the two experimental curves are affected by the distance between the CG position (located near the crack mouth) and the crack tip (where the data for the DIC was extracted). In fact, the degree of variation between the curves increases as the crack opening widens because of the angle of rotation formed between the two locations (mouth and tip) on the opening crack (see Figure 3.17). Figure 4.31 depicts the variation in tensile damage between 6 kN and 13.8 kN, which is greater when DIC was used. This could be related to variation in the fracture energy or to variation in the dissipated energy along the crack path.

Table 4.10: Concrete fracture energy (comparison study)

WST Technique	DIC			CG		
	Experiment	Inverse Analysis	FE	Experiment	Inverse Analysis	FE
G_F (N/mm)	0.092	0.085	0.078	0.131	0.127	0.1
G_f (N/mm)	0.052	0.04	0.051	0.088	0.066	0.086
G_F/G_f	1.8	2.1	1.5	1.5	1.9	1.2

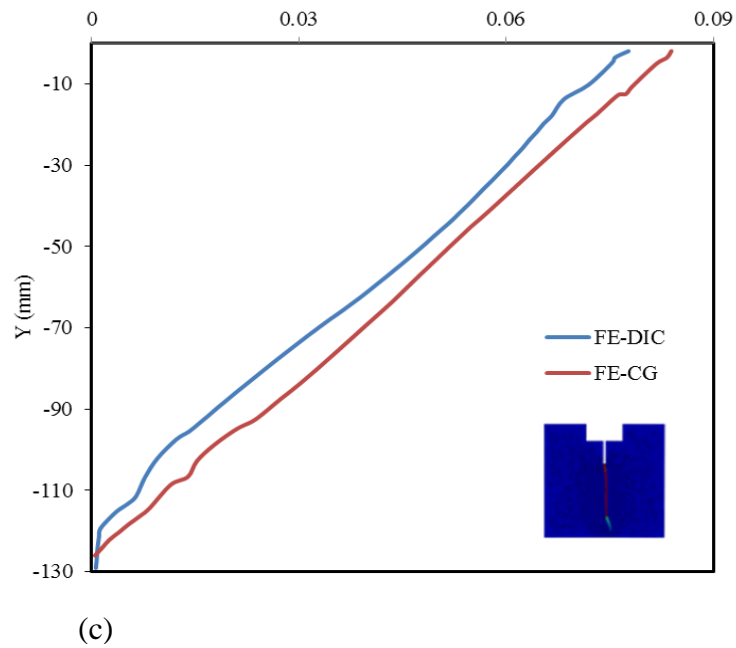
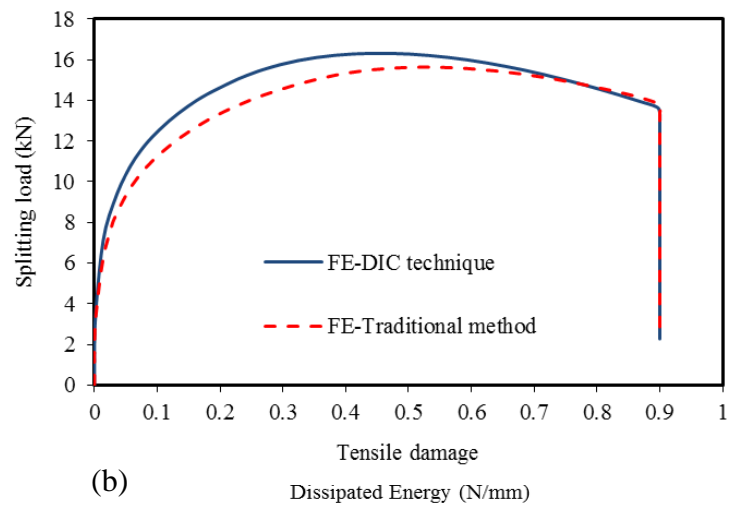
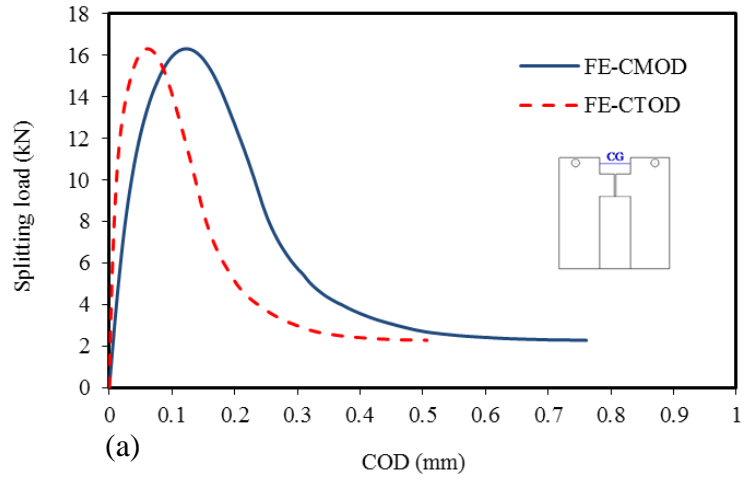


Figure 4.30: Comparison of FEA results for the CG and DIC experimental data: (a) P_{sp} -COD curve; (b) P_{sp} - d_t curve; (c) Dissipated energy-Y curve

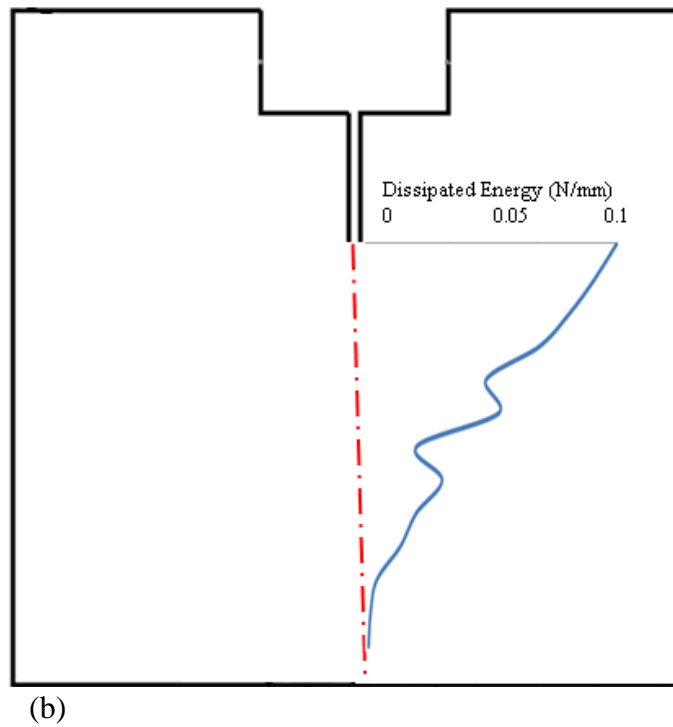
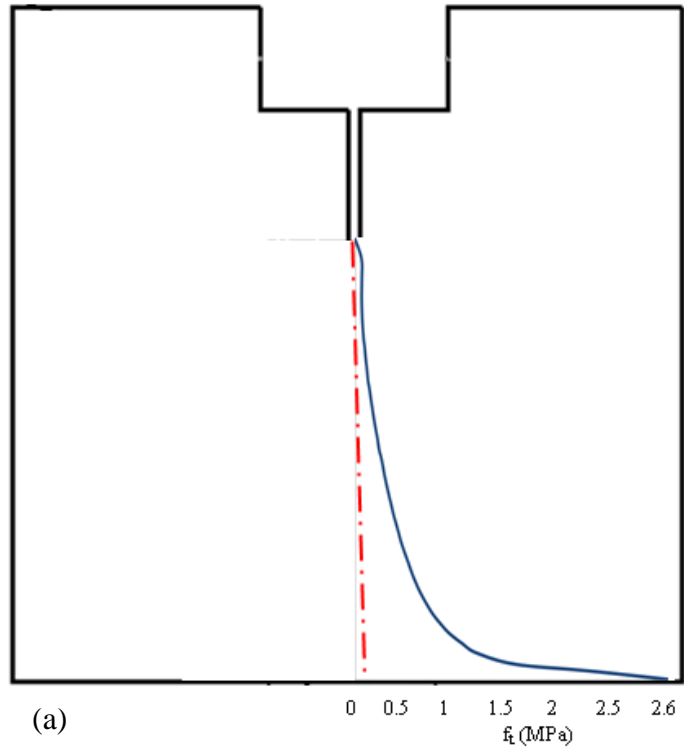


Figure 4.31: FEA results: (a) variation in the tensile strength on the WST-specimen; (b) variation in the dissipated energy along the crack path on the WST-specimen

4.6 Conclusion

The present work integrates inverse and finite element analytical models to analyze the outcomes of the Wedge Splitting Test (WST). The results show that concrete properties extracted from inverse analysis can be used to calibrate a Finite Element Analysis that implements a plasticity-damage coupled model, and which validates the inverse analysis. The results obtained by experimental methods, inverse analysis and FEA agreed reasonably well.

A nonlinear cracked hinge model can model the crack propagation in a WST assessed using the DIC technique. The modelled DIC results were compared to the results modelled for the traditional CG technique, and both sets of predictions for crack propagation were compared to the experimental observations. The nonlinear cracked hinge model permits the stress-crack opening relationship to be modeled by a bilinear curve using the Østergaard algorithm (2004), which has been modified for use with the DIC data. This method, which is attractive in its simplicity, is based on the cohesive crack (fictitious crack) model proposed in a simplified form by Barenblatt (1959, 1962), and later developed in detail and applied to concrete by Petersson (1981) and Hillerborg et al. (1983 and 1985). The study presented here has resulted in new insights into the behaviour of concrete, and how the four fracture mechanical parameters of the softening bilinear curve (σ - w) for concrete can be determined.

The numerical approach used in this study revealed that a plasticity-damage coupled model is able to capture the evolution of strain localization in the WST. These results validate the inverse analysis formulation of the DIC results for the WST. The discrepancies between the experimental observations and/or the inverse and the finite element analytical results can probably be attributed to the different cracking patterns known to occur during FEA that is associated with the mesh pattern of the specimen. Nevertheless, these meshes were found to perform satisfactorily.

This research supports the proposed use of a combination of experimental, numerical and simulation tools to assess the integrity of concrete structures. A method for the determination of the fracture mechanical properties of concrete material has been developed. The conclusions are based on analytical models describing the fracture mechanical behaviour of concrete, and on FE models that confirmed the analytical results, and are comparable to the experimental results obtained with both traditional CG and DIC techniques. This model and the inverse analysis formulation established in the current study demonstrate applicability to concrete; in addition, good supporting evidence was obtained and presented here.

CHAPTER V

CONCLUSIONS AND RECOMMENDATIONS

5.1 General Observations

The presence of cracks is not an indication of the end of a concrete structure's service life; however, an investigative approach is required for structural integrity assessment, the most critical demand in the industrialized world, to ensure added protection under conditions involving severe loading.

Studying the performance of concrete, particularly its fracture properties, is essential for assessing the integrity of existing structures. The identification and accurate estimation of concrete fracture mechanics parameters are also needed to reliably model concrete structures subjected to extreme loading, such as earthquakes, flood, wind, and storm. The research presented in this thesis investigated the feasibility of applying a new non-contact methodology for the identification of fracture parameters that is based on Digital Image Correlation (DIC), and which was applied to the wedge splitting test (WST) to measure crack extension and propagation and to investigate the characteristics of the *FPZ* under loading in a comprehensive manner.

Since the assessment of the WST by DIC is an indirect experimental procedure, inverse analysis of the data collected was required to generate the *softening* (σ - w) *curve* and to derive other fracture parameters. The associated forward problem was based on

the cracked hinge model, which is capable of accounting for the softening phenomena. This approach approximates the behaviour of the WST, and allows an analytical solution for the identification of the fracture parameters. The results of the identification procedures were confirmed using finite element analysis (FEA) along with the value of the fracture energy that was obtained by using the concrete damaged-plasticity coupled constitutive law to simulate the progressive accumulation of mechanical damage in the WST-specimen. As this 2D model is fully capable of representing the WST (Østergaard et al., 2003), the current research modelled the WST-specimen in 2D.

Characteristics other than the displacement field were determined successfully using DIC; the concrete fracture process scenario was also recorded successfully during a single test without interfering with the fracture process. This characterization included: the properties of the *FPZ*, toughening mechanisms, crack profile evolution, changes in crack tip position and in the traction free zone. These processes typically present significant difficulties when other assessment techniques are used.

Simulation models can be used to predict the fracture process in concrete materials; however, since homogeneity is generally assumed in these models, this analytical approach fails to track the impact of toughening mechanisms, such as bridging between different faces of concrete cracks. Crack branching and crack deflection processes are caused by concrete heterogeneity, which aids in the creation of tortuous cracks; however, these mechanisms are not integrated into the FE model. Since a tortuous crack has a longer path, the fracture energy derived from an FE model tends to

be underestimated; however, this leads to a more conservative assessment of the structure's integrity as the law governing fracture energy indicates that less energy is required for crack propagation. In addition, due to the varying influence of several factors, including the chemical composition of cement paste, environmental conditions, the mechanisms that are active in various settings, and hardening, concrete properties keep changing within infrastructure; therefore, modeling of existing concrete structures under various conditions is necessary.

5.2 Conclusions

The non-contact non-disturbing DIC measurement technique proved to be valuable not only for generating the P_{sp} -COD curve, but was also able to successfully monitor the fracture processes in the *FPZ* that are associated with crack evolution in WST-specimens. The experimental observations revealed the impact of toughening mechanisms within the *FPZ*, the size of the *FPZ*, the traction free zone (crack extension), the orientation of the newly formed crack tip, and the variation of dissipated energy and tensile damage along the crack path. Particular attention was paid to the detection of the evolution of the crack path; accordingly, the following conclusions were successfully documented from the experimental observations obtained using the DIC technique:

- The evolution of the *FPZ* associated with cracking in the WST was monitored successfully with DIC, which has previously proved to be difficult when other techniques were adopted. This work has resulted in new insights into the

behaviour of concrete structures during fracture, and aided in the determination of the fracture parameters for concrete.

- The experimental observations revealed that the development of the *FPZ* is slow until 84% of the peak load is applied, then immediate and sudden development of the *FPZ* occurs and continues until 100% of the peak load has been applied; this rapid development was then followed by slow growth of the *FPZ* during the post-peak phase. These observations mean that the application of 84% of the peak-load is a critical stage in the loading history of a concrete structure. In addition, according to the experimental data collected during this study, the length of the *FPZ* at peak-load was approximately 21% of the crack ligament length. The *FPZ* width increased with loading, and reached its maximum width with the initiation of the localization of micro-cracks (at about 96% of the peak load when the length of the *FPZ* started increasing rapidly). The maximum width of the *FPZ* was approximately three times the maximum grain size, which was also equal to two times the ligament length of the WST-specimen. In addition, during the post-peak phase, the width of the *FPZ* continued decreasing, and then remained constant as the crack ran along the ligament.
- The traction free zone (or crack extension) was initiated at 25%-30% of the P_{sp} during the post-peak phase. The critical phase started at 10% P_{sp} at the point where the crack extension increased rapidly. These observations could not have been made without the use of DIC.

- The l_{ch} , which depends on the interfacial strength between aggregate and matrix, increased with the presence of aggregates along the crack path. Accordingly, the best way to increase the G_F is by increasing the aggregate-matrix interface.

In the second stage of this research, the DIC results and the results of the inverse analyses were integrated to obtain the $\sigma-w$ curve. Concrete fracture parameters extracted from inverse analysis were used as input parameters for the FEA. Accordingly, the following conclusions were successfully documented in the current work:

- The FEA was found to perform better in the pre-peak stage, whereas the hinge-model performed better for the experimental results obtained during the post-peak stages with both techniques; however, regarding the FEA results, more discrepancy was found during the second part of the softening curve, when aggregate interlock began.
- The fracture energy/initial fracture energy (G_F/G_f) ratio obtained in this study using the DIC results was between 1.8 and 2.4. According to Wittmann et al. (1988), Rokugo et al. (1989), and CEB (1991), this result is considered satisfactory as the value of the ratio is less than 5. However, the optimization studies conducted by Bazant et al. (2011) indicated that $G_F/G_f = 2.5$ is statistically nearly optimum, and displays no systematic dependence on tensile strength, maximum aggregate size, or water/cement ratio.
- The estimation of tensile damage extracted using FEA agreed reasonably with the experimental results obtained using the DIC technique; this outcome is not possible using traditional techniques.

The outcomes of this research support the proposed use of a combination of experimental, numerical and simulation tools to assess the integrity of concrete structures. A method for the determination of the fracture properties of concrete material was developed. The results of inverse identification were confirmed using finite element analytical techniques along with the value obtained for fracture energy. This research enables the application of the proposed combined experimental simulation tool to assess the integrity of concrete structures, in which the *FPZ* and crack pattern can be monitored by non-contact optical methods throughout loading.

5.3 Recommendations for Future Research

The DIC technique made it possible to study the dynamics of crack propagation in concrete by monitoring the evolution of the tortuous crack, and also energy dissipation during the fracture process without the limitations of traditional methods. Consequently, the use of DIC is recommended for the comprehensive study of the fracture behaviour of concrete structures, and this technique can also be used for assessment and monitoring purposes.

The recommendations for future research can be summarized as:

- Study of the development of the *FPZ*, which is difficult to investigate using the traditional clip-gauge technique, but was successfully investigated in this study

using the non-contact DIC technique, following proper preparation of the surface of the specimen. However, this study was limited to only part of the entire surface area of the concrete specimen because of the limitations imposed by currently available optical lenses. Accordingly, the author suggests using different lenses, so that the whole *FPZ* can be captured in digital images for investigation; thus, the *FPZ* and l_{ch} could be evaluated experimentally. Nevertheless, the use of different lenses that can extend the field of view may also affect the accuracy of the results obtained for crack opening displacement.

- Since this study demonstrated the accuracy of the DIC findings, now possible with the development of the ARAMIS system, future fracture tests could be controlled through closed-loop testing machines without the use of a clip-gauge to control the loading process.
- Current successful and extensive research on the fracture mechanics of a concrete field includes detailed investigation of the microstructure of concrete material. Actions to improve the classic concrete material that produces a large amount of CO₂ is urgently needed. This issue could be solved by replacing a portion of Ordinary Portland Cement with smart materials. However, codes provide information about the analytical relationships between the measured properties and other important properties of concrete, and are based primarily on experience with traditional concrete. Therefore, the effects of new material on concrete fracture properties need to be investigated, so as to create lighter, greener and sustainable concrete that is able to reduce CO₂ emissions.

- From an experimental point of view, the author of the present work suggests casting the WST-specimen from the un-notched side where the steel loading device becomes more stable on the concrete surface. In the current study, the initial plan was to also determine the P_{sp} -CMOD function with the DIC technique, for comparison purposes; however, as the steel loading device covered the crack mouth area, this objective was not attained. With the use of a stable loading device, DIC data can be recorded using the pattern of the steel wedge part at the position of the clip-gauge.
- Based on the laboratory experiences arising from the present study, in which a major objective was to compare the results obtained from multiple specimens, the author recommends casting all WST-specimens to be used in a study simultaneously, as the W/C ratio has a great effect on the experimental results.
- The tail of the P_{sp} -COD curve, which depends on the time that the WST ends, has a great influence on G_F . According to the RILEM TC 187 report (2007), the WST can be stopped when the CMOD reading reaches $4D/300$ mm, where D is the specimen's depth.
- The influences of low W/C ratio, loading rate, and various curing conditions (high or low temperature curing) on the fracture properties of concrete need to be investigated. Essentially, these factors need to be controlled and applied consistently in order to produce reliable and reproducible results.

BIBLIOGRAPHY

- Abdalla & Karihaloo. (2004). A method for constructing the bilinear tension softening diagram of concrete corresponding to its true fracture energy. *Magazine of Concrete Research*, 56(10), 597-604.
- Alfaiate. J & Sluys L. J. (2007). Strong discontinuity formulations: A comparative study. *Proceedings of the 6th International Conference on Fracture Mechanics of Concrete and Concrete Structures - Fracture Mechanics of Concrete and Concrete Structures*, 1, 147-154.
- Auer, T., Gruber, D., Harmuth, H., & Triessnig, A. (2006). *Numerical investigations of mechanical behaviour of refractories*. pp. 985-989.
- Baluch, M. H., Rahman, M. K., & Al-Gadhib, A. H. (2002). Risks of cracking and delamination in patch repair. *Journal of Material for Civil Engineering*, 14(4), 294-302.
- Bažant, Z. & Yu, Q. (2011). Size-effect testing of cohesive fracture parameters and nonuniqueness of work-of-fracture method. *Journal of Engineering Mechanics*, 137(8), 580-588.
- Bažant, Z. P. (2005). *Scaling of structural strength*. Elsevier Butterworth-Heinemann, Oxford.
- Bažant, Z. P. (1996). Analysis of work-of-fracture method for measuring fracture energy of concrete. *Journal of Engineering Mechanics*, 122(2), 138-144.
- Bažant, Z. P. – Ed. (1992). *Fracture Mechanics of Concrete Structures*. Proceedings of the First International Conference on Fracture Mechanics of Concrete Structures, Colorado, USA, Elsevier Applied Science, London and New York.
- Bažant, Z. P. and Oh, B. H. (1983). Crack band theory for fracture of concrete. *Materials and Structures*, 16(3), 155-177.
- Bažant, Z. P. (1988). Nonlocal continuum damage and measurement of characteristic length. *Mech. of Composite Materials*, G. J. Dvorak and N. Laws, eds., AMD, 92, ASME, 79-85 (presented at Joint ASME/SES Appl. Mech. and Eng. Sci. conf., Berkeley, Calif.
- Becq-Giraudon, E. F. (2000). Size effect on fracture and ductility of concrete and fiber composites. *Ph.D., Northwestern University*.
- Bolzon, G., Fedele, R., Maier, G. (2002). Parameter identification of a cohesive crack model by Kalman filter. *Computer Methods in Applied Mechanics and Engineering*, 191(25-26), 2847-2871.
- Bolzon G, Cocchetti G. (1998). On a case of crack path bifurcation in cohesive materials. *Archive of Applied Mechanics*, 68, 513-523.
- Borges, R. F. (1981). Crack patterns of reinforced concrete slab. *Ph.D., The University of Hong Kong*.
- Brocca, M. (1999). Material modeling and structural analysis with the microplane constitutive model. *Ph.D., Northwestern University*.
- Broek, D. (1986). *Elementary engineering fracture mechanics*. The Hague, Netherlands; Hingham, Mass Martinus Nijhoff; Kluwer Academic Publishers, Boston.

- Bruggi, M. (2009). Modeling cohesive crack growth via a truly-mixed formulation. *Computer Methods in Applied Mechanics and Engineering*, 198(47-48), 3836-3851.
- Brühwiler, E; & Wittmann, F.H. (1990). The wedge splitting test, a new method of performing stable fracture mechanics tests. *Engineering Fracture Mechanics*, 35(1-3), 117-125.
- Bui H.D., Tanaka M. (Eds), 1994. Inverse Problems in Engineering Mechanics. *Balkema, Rotterdam*.
- Becq-Giraudon, E. F. (2000). Size effect on fracture and ductility of concrete and fiber composites. *Ph.D. Dissertation, Northwestern University*.
- Cal, Q., Robberts, J.M. Van, R. (2006). Cracking in concrete using smeared cracking finite element modeling. *South African Journal of Science*, 102(11-12), 548-556.
- Cedolin, L. (2008). Identification of concrete fracture parameters through size effect experiments. *Cement Concrete Composites*, 30(9), 788-797.
- Dabbagh & Foster. (2006). A smeared - fixed crack model for FE analysis of RC membranes incorporating aggregate interlock. *Advances in Structural Engineering*, 9(1), 91-102.
- De Borst, R., Remmers, J., Needleman, A., Abellan, M. (2004). Discrete vs smeared crack models for concrete fracture: Bridging the gap. *International Journal for Numerical and Analytical Methods in Geomechanics*, 28(7-8), 583-607.
- De Borst. (1997). Some recent developments in computational modeling of concrete Fracture. *International Journal of Fracture*, 86, 5–36
- De Borst. (1987). Smeared cracking, plasticity, creep, and thermal loading-A unified approach. *Computer Methods in Applied Mechanics and Engineering*, 62, 89-110.
- Duan, K. (2006). Scaling of quasi-brittle fracture: Boundary and size effect. *Mechanics of Materials*, 38(1-2), 128-141.
- Elices, M., Guinea, J., Gomez, J.& Planas J. (2002). The cohesive zone model: Advantages, limitations and challenges. *Engineering Fracture Mechanics*, 69(2), 137-63.
- Gettu, R. (2006). Determining the tensile stress-crack opening curve of concrete by inverse analysis. *Journal of Engineering Mechanics*, 132, 141.
- Gettu, R. (1992). Concrete and rock fracture, and the influence of loading rate. *Ph.D., Northwestern University*.
- Granger, S. (2009). Monitoring of cracking and healing in an ultra high performance cementitious material using the time reversal technique. *Cement and Concrete Research*, 39(4), 296-302.
- Grassl, P. (2004). Plasticity and damage mechanics for modeling concrete failure. *Chalmers tekniska högsk*, (2186)
- Guinea, G. V. (1996). Stress intensity factors for wedge-splitting geometry. *International Journal of Fracture*, 81, 113-124.
- Guo, L. (2008). Latent crack path and service life predictions for unnotched concrete under bending by digital speckle correlation method. *Fatigue Fracture of Engineering Materials Structures*, 31(1), 29-37.
- Guo, Z. (2004). Size effect analysis of materials and structures from micro scale to macro scale. *Ph.D., Northwestern University*.

- Guo, Z. K., Kobayashi, A. S., & Hawkins, N. M. (1993). Further studies on fracture process zone for mode I concrete fracture. *Engineering Fracture Mechanics*, 46(6), 1041-1049.
- Hadjab, H., Thimus, J. F., & Chabaat, M. (2010). Comparative Study of Acoustic Emission and Scanning Electron Microscope to Evaluate Fracture Process Zone in Concrete Beams. *Journal of Materials in Civil Engineering*, 22(11), 1156-1163.
- Hadjab-Souag, H., Thimus, J. F., & Chabaat, M. (2007). Detecting the fracture process zone in concrete using scanning electron microscopy and numerical modelling using the nonlocal isotropic damage model. *Canadian Journal of Civil Engineering*, 34(4), 496-504.
- Haidar, K., Dubé, J. F., & Pijaudier-Cabot, G. Modelling crack propagation in concrete structures with a two scale approach. *International Journal for Numerical and Analytical Methods in Geomechanics*, 27(13), 1187-1205.
- Hillerborg, A., Modéera, M., & Petersson, P. (1976). Analysis of crack formation and crack growth in concrete by means of fracture mechanics and finite elements. *Cement and Concrete Research*, 6(6), 773-782.
- Hordijk, D. A., & Reinhardt, H. W. (1989). Macro-structural effects in a uniaxial tensile test on concrete. In *Brittle Matrix Composites 2* (486-495). Springer Netherlands.
- Hornain, H. (1996). Microscopic observation of cracks in concrete - A new sample preparation technique using dye impregnation. *Cement and Concrete Research*, 26(4), 573-583.
- Hu, H. T., Lin, F. M., & Jan, Y. Y. (2004). Nonlinear finite element analysis of reinforced concrete beams strengthened by fiber-reinforced plastics. *Composite Structures*, 63(3), 271-281.
- Huang, H. (2009). Prediction of slant ductile fracture using damage plasticity theory. *The International Journal of Pressure Vessels and Piping*, 86(5), 319-328.
- Ince, R. (2012). Determination of concrete fracture parameters based on peak-load method with diagonal split-tension cubes. *Engineering Fracture Mechanics*, 82, 100-114.
- Jeeho Lee, & Gregory L. Fenves. (1998). A plastic-damage concrete model for earthquake analysis of dams. *Earthquake Engineering Structural Dynamics*, 27(9), 937-956.
- Jirasek, M. (1993). Modeling of fracture and damage in quasibrittle materials. *Ph.D., Northwestern University*.
- Kaplan, M. F. (1961). Crack propagation and the fracture of concrete. *ACI Journal*, 58(11), 591-610.
- Karihaloo, B. L., Abdalla, H., & Xiao, Q. Z. (2003). Coefficients of the crack tip asymptotic field for wedge splitting specimens. *Engineering Fracture Mechanics*, 70(17), 2407-2420.
- Kim, J. H. (1998). Failure mechanism and size effect of quasi-brittle materials: Ice, steel-reinforced concrete, and fiber composite. *Ph.D., Northwestern University*.
- Kim, J., Lee, Y., & Yi, S. (2004). Fracture characteristics of concrete at early ages. *Cement and Concrete Research*, 34(3), 507-519.
- Kumar, S., & Barai, S. V. (2009). Effect of softening function on the cohesive crack fracture parameters of concrete CT specimen. *Sadhana*, 34(6), 987-1015.

- Kwak, H.G., Filippou, F.C. (1997). Nonlinear FE analysis of R/C structures under monotonic loads. *Computers & Structures*, 65(1), 1-16.
- Lamond, J. F. (2006). Significance of tests and properties of concrete and concrete-making materials (Vol. 169). *Astm International*.
- Lee, J. (1998). Plastic-damage model for cyclic loading of concrete structures. *Journal of Engineering Mechanics*, 124(8), 892-900.
- Lee, J. (1998). A plastic-damage concrete model for earthquake analysis of dams. *Earthquake Engineering Structural Dynamics*, 27(9), 937-956.
- Li, C. (2011). 3-D mesoscopic numerical simulation of concrete damage and fracture. *Zhong Nan Da Xue Xue Bao (Zi Ran Ke Xue Ban)*, 42(2), 463-469.
- Li, G., & Cheng, J. (2007). A generalized analytical modeling of grid stiffened composite structures. *Journal of Composite Materials*, 41(24), 2939-2969.
- Lysak, M. V. (1996). Development of the theory of acoustic emission by propagating cracks in terms of fracture mechanics. *Engineering Fracture Mechanics*, 55(3), 443-52.
- Martin, J. (2007). Experimental testing to determine concrete fracture energy using simple laboratory test setup. *ACI Materials Journal*, 104(6), 575-584.
- Moes N. & Belytschko T. (2002). Extended finite element method for cohesive crack growth. *Engineering Fracture Mechanics*, 69(7):813-833
- Muralidhara, S. (2010). Fracture process zone size and true fracture energy of concrete using acoustic emission. *Construction and Building Materials*, 24(4), 479-486.
- Muralidhara Rao, T. (2009). Fracture parameters of high strength concrete - an experimental study. *Journal of Structural Engineering*, 35(6), 397-403.
- Murthy, A. R. C. (2010). Fracture analysis of concrete structural components accounting for tension softening effect. *Computers, Materials Continua*, 19(2), 135-154.
- Murthy, A. R. C. (2009). State-of-the-art review on fracture analysis of concrete structural components. *Sādhanā, India*, 34(2), 345-367.
- Murthy, A. R. C. (2007). Remaining life prediction of cracked stiffened panels under constant and variable amplitude loading. *International Journal of Fatigue*, 29(6), 1125-1139.
- Navalurkar, R. K. (1996). Fracture mechanics of high-strength concrete members. *Ph.D., New Jersey Institute of Technology*.
- Neville, A. M. (1981). Properties of concrete (3rd ed.). Pitman, London.
- Niu, Z., Cheng, C., Ye, J., & Recho, N. (2009). A new boundary element approach of modeling singular stress fields of plane V-notch problems. *International journal of solids and structures*, 46(16), 2999-3008.
- Belinha, J., Kinis, L.M.J.S. (2007). Nonlinear analysis of plates and laminates using the element free galerkin method. *Composite Structures*, 78(3), 337-350.
- Olesen, J. F. 1. (2007). Nonlinear fracture mechanics and plasticity of the split cylinder test. *Materials and Structures*, 39(4), 421-432.
- Olesen, J. F. (2001). Fictitious crack propagation in fiber-reinforced concrete beams. *Journal of Engineering Mechanics*, 127(3), 272-280.
- Olesen, J F., Østergaard, L., Stang, H. (2006). Nonlinear fracture mechanics and plasticity of the split cylinder test. *Materials and Structures*, 39(288), 421-432.
- Optical Measuring Techniques (GOM) mbH. (2005). ARAMIS user manual.

- Orteu, J. J., Cutard, T., Garcia, D., Cailleux, E., & Robert, L. (May 2007). Application of stereovision to the mechanical characterization of ceramic refractories reinforced with metallic fibers. *Strain*, 43(2), 96–108.
- Ostergaard, L., Walter, R., & Olesen, J. F. (2005). Method for determination of tensile properties of engineered cementitious composites (ECC). *Proceedings of ConMat'05*.
- Østergaard, L., Lange, D., & Stang, H. (2004). Early-age stress–crack opening relationships for high performance concrete. *Cement and Concrete Composites*, 26(5), 563-572.
- Østergaard, L., Damkilde, L., & Stang, H. (2003). Early age fracture mechanics and cracking of concrete: Experiments and Modelling. *Technical University of Denmark Danmarks Tekniske Universitet, Department of Structural Engineering and Materials Institut for Bærende Konstruktioner og Materialer*.
- Ouyang, C., Landis, E., & Shah, S. P. (1991). Damage assessment in concrete using quantitative acoustic emission. *Journal of Engineering Mechanics*, 117(11), 2681-2698.
- Petroski, H. J., OJDROVIC, R.P. (1987). The concrete cylinder: Stress analysis and failure modes. *International Journal of Fracture*, 34(4), 263-79.
- Petersson, PE. (1981). Crack growth and development of fracture zone in plain concrete and similar materials. Report TVBM-1006, *Lund Inst. of tech., Lund, Sweden*
- Planas, J., & Elices, M. (1990). Fracture criteria for concrete: mathematical approximations and experimental validation. *Engineering fracture mechanics*, 35(1), 87-94.
- Planas, J. (1999). Size effect and inverse analysis in concrete fracture. *International Journal of Fracture*, 95(1/4), 367-378.
- Planas, J., Elices, M., Guinea, G. V., Gómez, F. J., Cendón, D. A., & Arbillá, I. (2003). Generalizations and specializations of cohesive crack models. *Engineering fracture mechanics*, 70(14), 1759-1776.
- Ponson, L., Bonamy, D., Bouchaud, E., Cordeiro, G., Toledo, R., & Fairbairn, E. (2007). Path and dynamics of a crack propagating in a disordered material under mode I loading. *Proceeding FRAMCOS-6*, 63-67
- Que, N. S., & Tin-Loi, F. (2002). Numerical evaluation of cohesive fracture parameters from a wedge splitting test. *Engineering Fracture Mechanics*, 69(11), 1269-1286.
- Rocco, C., Guinea, G. V., Planas, J., & Elices, M. (2001). Review of the splitting-test standards from a fracture mechanics point of view. *Cement and concrete research*, 31(1), 73-82.
- Rolfe, S. T., & Barsom, J. M. (1977). Fracture and fatigue control in structures : Applications of fracture mechanics. *Englewood Cliffs, N.J.: Prentice-Hall*.
- Rots, J.G, Kuster, G.M.A, Blaauwendraad, J. (1984). The Need for fracture mechanics options in finite element models for concrete structures. *Proceedings of the International conference on Computer Aided Analysis and Design of Concrete Structures, Split*, 19-32.
- Schlangen, E. (2008). Crack development in concrete, part 1: Fracture experiments and CT-scan observations. *Key Engineering Materials*, 385-387, 69-72.

- Shah, S. P., Swartz, S. E., & Ouyang, C. (1995). Fracture mechanics of concrete: applications of fracture mechanics to concrete, rock and other quasi-brittle materials. *New York: Wiley*.
- Shah, S. P., & Carpinteri, A. Eds. (1989). Fracture mechanics test methods for concrete. *Chapman and Hall*.
- Shayanfar, M. A., Kheyroddin, A., & Mirza, M. S. (1997). Element size effects in nonlinear analysis of reinforced concrete members. *Computers & structures*, 62(2), 339-352.
- Skoček, J., Stang, H. (2010). Application of optical deformation analysis system on wedge splitting test and its inverse analysis. *Materials and Structures*, 43(S1), 63-72.
- Skoček, J., Stang, H. (2008). Inverse analysis of the wedge splitting test. *Engineering Fracture Mechanics*, 75(10), 3173-3188.
- SIMULIA Dassault System. ABAQUS 6.9 documentation.
- Skaryński, L. (2010). Calculations of fracture process zones on meso-scale in notched concrete beams subjected to three-point bending. *European Journal of Mechanics.A, Solids*, 29(4), 746-760.
- Sukumar, N., Moran, B., Black, T., & Belytschko, T. (1997). An element-free Galerkin method for three-dimensional fracture mechanics. *Computational Mechanics*, 20(1-2), 170-175.
- Sundara Raja Iyengar, K. T. (2002). Analysis of crack propagation in strain-softening beams. *Engineering Fracture Mechanics*, 69(6), 761-778.
- Theiner, Y. (2009). Numerical prediction of crack propagation and crack widths in concrete structures. *Engineering Structures*, 31(8), 1832-1840.
- Tikhomirov, D., & Stein, E. (2002). Continuum damage growth in plain and reinforced concrete: Theory and finite element applications. *Proceedings in Applied Mathematics and Mechanics*, 1(1), 201-202.
- Ulfkjær, J., Krenk, S. & Brincker, R. (1995). Analytical model for fictitious crack propagation in concrete beams. *Journal of Engineering Mechanics*, 121(1), 7-15.
- Van Mier, J. G. M. (1991). Mode I fracture of concrete: Discontinuous crack growth and crack interface grain bridging. *Cement and Concrete Research*, 21(1), 1-15.
- Wang, T., & Hsu, T. T. (2001). Nonlinear finite element analysis of concrete structures using new constitutive models. *Computers & Structures*, 79(32), 2781-2791.
- Wittmann, F. H., Mihashi, H., & Nomura, N. (1990). Size effect on fracture energy of concrete. *Engineering Fracture Mechanics*, 35(1), 107-115.
- Wright, P. J. F. (July 1995). Comments on an indirect tensile test on concrete cylinders. *Magazine of Concrete Research*, 7(20), 87-96.
- Wu, Z., Rong, H., Zheng, J., Xu, F., & Dong, W. (2011). An experimental investigation on the FPZ properties in concrete using digital image correlation technique. *Engineering Fracture Mechanics*, 78(17), 2978-2990.
- Wu, Z., Yang, S., Hu, X., & Zheng, J. (2006). An analytical model to predict the effective fracture toughness of concrete for three-point bending notched beams. *Engineering Fracture Mechanics*, 73(15), 2166-2191.

- Xia, P. X., Zou, G. P., & Tang, L. Q. (2011). Numerical simulation on the compound crack propagation process in concrete. *Advanced Materials Research*, 250, 1139-1142.
- Xiang, Y. (1996). Modeling of fractures and scaling in quasi-brittle materials. *Ph.D., Northwestern University.*
- Xin-She Yang, Janet M. Lees and Chris T. Morley. (2008). Modelling crack propagation in structures: *Comparison of numerical methods*. vol.24(iss.11), pg.1373 -1392.
- Xu, S., & XU. (2008). Determination of fracture parameters for crack propagation in concrete using an energy approach. *Engineering Fracture Mechanics*, 75(15), 4292-4308.
- Yang, X. S., Lees, J. M., & Morley, C. T. (2008). Modeling crack propagation in structures: Comparison of numerical methods. *Communications in Numerical Methods in Engineering*, 24(11), 1373-1392.
- Yang, Z. J. (2007). Modelling cohesive crack growth using a two-step finite element-scaled boundary finite element coupled method. *International Journal of Fracture*, 143(4), 333-354.
- Zhao, T.Y.T.L.L. (2009). The contacting computation method for simulating the model I crack propagation process in concrete under cyclic loading. *Chinese Journal of Solid Mechanics*, 5, 010.
- Zhi. (1993). Further studies on fracture process zone for mode I concrete fracture. *Engineering Fracture Mechanics*, 46(6), 1041-1049.
- Zhou, Y. (2005). Size effect on strength of fiber composites and rigid foams. *Ph.D., Northwestern University.*
- Zi, G. (2002). Size effect of quasibrittle materials and simulation of concrete decontamination using microwave heating. *Ph.D., Northwestern University.*

VITA AUCTORIS

NAME: Wafa Habib Polis Asmaro

PLACE OF BIRTH: Mosul, Nineveh, Iraq

YEAR OF BIRTH: 1966

EDUCATION: Kourtoaba High School, Mosul, Nineveh, Iraq
1981 - 1984

University of Mosul, Nineveh, Iraq
1984 - 1988 B.A.Sc. Science in Civil Engineering

University of Windsor, Windsor, Ontario
2004 - 2007 M.A.Sc. Civil Engineering/Structural

University of Windsor, Windsor, Ontario
2007 - 2013 Ph.D. Civil Engineering/Structural